AASERT contract #F49629-92-J-0331
AFOSR grant AFOSR-91-0269
ARO contract #DAAL03-86-K-0175

THE IMPACT OF A TWO-MOMENT CLOUD MODEL ON THE MICROPHYSICAL STRUCTURE OF TWO PRECIPITATION EVENTS

by Michael Patrick Meyers

William R. Cotton, P.I.

Colorado State University

DEPARTMENT OF ATMOSPHERIC SCIENCE

PAPER NO. 575

THE IMPACT OF A TWO-MOMENT CLOUD MODEL ON THE MICROPHYSICAL STRUCTURE OF TWO PRECIPITATION EVENTS

by

Michael Patrick Meyers

Department of Atmospheric Science

Colorado State University

Fort Collins, CO 80523

Research Supported by

Augmentation Awards for Science and Engineering Research Training

under Contract F49629-92-J-0331

Air Force Office of Scientific Research

under Grant AFOSR-91-0269

Army Research Office

under contract #DAAL03-86-K-0175

April 25, 1995

Atmospheric Science Paper No. 575

ABSTRACT

THE IMPACT OF A TWO-MOMENT CLOUD MODEL ON THE MICROPHYSICAL STRUCTURE OF TWO PRECIPITATION EVENTS

A new two-moment microphysical parameterization is described. The proposed scheme predicts the mixing ratio and number concentration of rain, pristine ice crystals, snow, aggregates, graupel and hail. The general gamma distribution is the basis function used for each hydrometeor. Preliminary sensitivity testing of the new microphysical scheme in an idealized convective simulation shows that the two-moment prediction scheme allows more freedom on the size distribution enabling the diameter to evolve more realistically than in a 1-moment scheme. Sensitivity to the prescribed input parameters such as cloud droplet concentrations and the shape parameter ν is demonstrated in the model results.

Model verification is performed on two separate case studies which occurred in very diverse environments. A wintertime shallow post-frontal upslope case from the Winter Icing and Storm Project (WISP91) and a strong summertime convective storm from Cooperative Convective Precipitation Experiment (CCOPE81) are investigated. In these case studies, the kinematic evolution of the two-moment and one-moment simulations is very similar, however, the microphysical structure shows differences between the two schemes. In the two-moment simulation, the diameters of each hydrometeor are allowed to evolve depending on the environmental conditions, and these fields compare well to the observed measurements. In the one-moment simulations, with either the mean diameter or the slope intercept parameter fixed, the results show the unrealistic constraint of not allowing variations in the hydrometeor spectra. Comparisons to aircraft measurements for both cases show that the microphysical structure is predicted well by the two-moment scheme compared to the observations. Peak reflectivities are predicted close to the observed values using

the two-moment scheme, while the one-moment scheme with the mean diameter specified over-predicts reflectivities due to the larger prescribed diameters. In the simulation where N_0 is specified, reflectivity are similar to the observations, however, other microphysical parameters such as graupel and rain are not simulated well. In both one moment simulations, the ratio of hail precipitation to rain is grossly over–predicted. Sensitivity to variations in the ν parameter are demonstrated in the summertime case. These sensitivity experiments show the need for more measurements of the size and shape of the hydrometeor spectra for various weather environments. There is also a need to numerically examine the effects of varying ν in a variety of environments and storms.

Michael Patrick Meyers
Department of Atmospheric Science
Colorado State University
Fort Collins, Colorado 80523
Spring 1995

ACKNOWLEDGEMENTS

I would like to thank my advisor, Dr. William Cotton for his support, guidance and patience during my many years as a graduate student. I would like to thank Dr. Roger Pielke for his valuable suggestions and assistance throughout the course of my study. The comments and participation of my other committee members, Drs. Steven Rutledge and V. Bringi are also appreciated.

I am especially indebted to Dr. Robert Walko who spent countless hours helping me with the code and supporting me through the struggle. I am very grateful to Jerry Harrington who helped me a great deal developing the code for the two-moment scheme. I extend my thanks to Dr. Paul DeMott who provided the foundation for our ice nucleation work and several joint articles. Many thanks are extended to Ben Bernstein who provided me with WISP data and to Scot Randell, both of whom provided valuable suggestions and comments to the manuscript. I am grateful to Dr. Johannes Verlinde who helped me lay the framework for the two-moment scheme. I would like to acknowledge Dr. Russell De Souza for his undergraduate guidance and encouragement to pursue graduate studies in Atmospheric Science.

I would like to specifically acknowledge Drs. James Bossert, Ed Brandes, Piotr Flatau, Mel Nicholls, Peter Olsson, Roy Rasmussen, David Rogers, Jerome Schmidt, Craig Tremback, Joe Turk, Michael Weissbluth, Doug Wesley, and Lewis Grasso, Rolf Hertenstein, Dan Johnson, Ray McAnelly, Greg Poulos, and Bjorn Stevens. I extend a special thanks to Brenda Thompson who helped me keep my sanity through all of this with her encouragement and humor. Brenda Thompson and Abby Hodges are also thanked for helping me with all my annoying questions associated with the manuscript. I am grateful to Donna Chester for helping me with all my computer problems. I would also like to thank everyone in the Cotton and Pielke groups whom I left out. Members of the WISP91 and CCOPE81

field projects are also appreciated. Thanks are extended to Judy Sorbie-Dunn who drafted some of the figures for the manuscript.

I like to thank Leann Walters for her unconditional friendship and supporting me emotionally through all my highs and lows. I would also like to thank Cara DelVecchio for helping me maintain my focus and for her encouragement as I finished my dissertation. Finally I would like to thank my family for their endless support and encouragement and never doubting that I would get my Ph.D.

This research was supported by the DoD Augmentation Awards for Science and Engineering Research Training under grant F49620-92-J-0331M and the Air Force Office of Scientific Research under grant AFOSR-91-0269 and by the Army Research Office under contract #DAAL03-86-K-0175. Some computations were performed at the National Center for Atmospheric Research (NCAR). NCAR is sponsored by the National Science Foundation.

TABLE OF CONTENTS

LIST OF FIGURES

LIST OF TABLES

Chapter 1

INTRODUCTION

1.1 Cloud Models

With the advancing state of computer technology, atmospheric modelers are now able to incorporate more sophisticated physics into their models in the hope of gaining a better understanding of the physical controls on atmospheric processes. Cloud models specifically need to adequately represent the hydrometeor evolution over a wide variety of conditions to accurately predict the microstructure of cloud systems. Cloud modelers have two options to represent the hydrometeor spectra, explicit bin-resolving or bulk microphysical models.

Explicit bin-resolving models (Young 1974; Hall 1980; Kogin 1991; Feingold et al. 1988; 1994) discretize the hydrometeor categories into specific bins, which facilitates keeping track of the different processes and interactions affecting the hydrometeor spectra. Since bin models require large amounts of memory and computation time, they have predominantly been applied to an assumed or prescribed kinematic structure. The expense of an explicit bin-resolving model can be tremendous as evidenced by a simulation performed by Stevens (personal communication, 1994) of a 9 km^2 stratus topped boundary layer cloud, which is 800 m deep, with a 60X60X60 domain and 60 prognostic equations. The simulation takes about one day of wall clock time to simulate 5 minutes of cloud evolution with a 2 second timestep on an IBM RS6000/370 high performance workstation.

Bulk microphysical schemes employ more simplistic assumptions than the explicit microphysical models and therefore require much less memory and computation time. In a bulk microphysical scheme, the water class is categorized into different species, and a certain basis function of the size distribution is assumed for each category, such as a gamma type (Walko et al. 1995; hereafter referred to W95). Simplified formulas represent all interactions between each of the hydrometeor classes which result from the integration of the

hydrometeor spectra. Different types of bulk schemes have been reported. Rutledge and Hobbs (1983; 1984) developed a diagnostic kinematic model with bulk microphysics, where the kinematic field was derived from Doppler radar data and microphysics were integrated in time while holding the wind field constant until a steady state structure was attained. Lin et al. (1983) and Cotton et al. (1986) both used a bulk microphysical scheme but coupled with a dynamical model instead of a kinematic model. All of these models incorporated a three-class ice parameterization. McCumber et al. (1991) compared two-class and three-class ice parameterizations and found that the three-class system was superior to the two-class system for a specific squall line simulation due to the added flexibility of the additional hydrometeor category. All of these models incorporated graupel/hail as the third category category which, depending on the spatial characteristics of the specified hydrometeor greatly impacted the overall microphysical structure of the simulation (McCumber et al. 1991). The focus of this current study is simulating mesoscale precipitation events, consequently, a bulk microphysical scheme is desired.

Another capability of bulk microphysical schemes is the degree of sophistication used in representing the hydrometeor size spectra. In the previous three models discussed, only one moment of the distribution is predicted (usually mixing ratio) while the other moments are diagnosed or prescribed. An improvement in the representation of the hydrometeor spectra has been to predict two moments of the hydrometeor distribution, namely, the mixing ratio and the number concentration, and to diagnose the mean diameter. Srivastava (1978) noted the advantages of predicting on 2 parameters of the hydrometeor size spectra especially in precipitation processes. Prediction of two moments of the distribution should allow the hydrometeor spectra of each category to evolve more realistically, improving prediction of complex microphysical processes. Improvements should also be expected in radar reflectivity and radiative transfer calculations which are both dependent on the size and the number concentration of the hydrometeors. Ziegler (1985) used his 2-moment model in a three-dimensional kinematic framework to simulate a severe Oklahoma thunderstorm. Assuming a gamma distribution for cloud droplets and rain, and an exponential distribution for other hydrometeors, the mixing ratio and number concentration of cloud droplets,

rain, hail, and the mixing ratios of cloud ice and snow were predicted. Some highlights of the microphysical scheme included stochastic coalescence effects in warm clouds as well as wet and variable density dry hail growth processes. Nickerson et al. (1986) developed a warm rain microphysical scheme to examine orographic precipitation processes. Number concentrations of rain as well as mixing ratio of cloud droplets and rain were predicted based upon a log-normal distribution. Murakami (1990) developed a three-dimensional anelastic cloud model to simulate a severe thunderstorm over Montana. The mixing ratio and number concentrations of cloud ice and snow were predicted as well as the mixing ratio of water vapor, cloud water, rain, and graupel/hail. More recently, Wang and Chang (1993) developed a three-dimensional cloud model which includes a chemistry scheme to examine a severe thunderstorm in Montana. Both the mixing ratio and number concentration of cloud water, rainwater, ice crystals, snowflakes, graupel and hail are predicted in the model assuming an exponential distribution. Ferrier (1994) also developed a bulk microphysical model to examine hydrometeor profiles of convective and stratiform precipitation in large scale environmental conditions. This scheme includes prediction of the mixing ratios and number concentrations of ice crystals, snow, graupel, and hail; the mixing ratios of cloud drops and rain are also predicted assuming an exponential distribution. Some highlights of this scheme include prediction of wet precipitation ice (for radar applications), more efficient collection formulations, and the treatment of aggregation processes.

1.2 Objectives

A two-moment hydrometeor prediction scheme is implemented into the Regional Atmospheric Modeling System (RAMS) to examine two diverse precipitation events. The two-moment scheme should provide better prediction of more diverse weather systems (eg. MCS) which have a spatial and temporal variability of the hydrometeor structure within the storm. Implementation of the two-moment scheme should also provide the background for remote sensing comparisons (eg. Zdr) and retrieval of parameters for future studies. One of the tasks includes updating all the previously existing microphysics based on the most recent observations and parameterizations (Chapter 2). This scheme predicts on

the mixing ratio and number concentration of rain, pristine ice crystals, snow, aggregates, graupel, and hail categories. The added features of this new microphysical scheme include:

- the use of a generalized gamma size-spectrum where the ν parameter can be prescribed by the user as opposed to a fixed Marshall Palmer spectrum
- the introduction of ice-liquid mixed phase graupel and hail categories categories with non-thermal equilibrium for the rain, graupel and hail classes
- new heterogeneous and homogeneous ice nucleation parameterizations
- approximate solutions to the stochastic collection equation rather than the continuous accretion model approach
- breakup of rain droplets is formulated into the collection efficiency
- analytical flux equations predict mixing ratio and number concentration conversion from pristine ice crystals to snow due to deposition (no riming)
- predictive equations for ice nuclei (IN)
- crystal habit is diagnosed dependent on temperature and saturation
- evaporation and melting of each species assumes that the smallest particles completely disappear first
- more complex shedding formulations which take into account the amount of water mass on the coalesced hydrometeor.

After testing the new scheme, two case studies are examined, a wintertime orographic precipitation event, and a summertime convective case. These cases will allow comparisons between the two-moment predictive scheme and the one-moment predictive scheme, which has been recently formulated and subjected to some preliminary testing (W95). This study is especially challenging since emphasis is placed on verification of the microphysical scheme using radar data, and ground-based and aircraft hydrometeor observations. Mesoscale verification of the spatial distribution of precipitation and the kinematic structure of the

storms is also considered. These experiments demonstrate some of the potential benefits and shortcomings of the two-moment scheme.

The current version of RAMS which includes recent modifications made to the single-moment prediction scheme as well as the model development of the two-moment microphysical version of RAMS is described in the next chapter. Sensitivity testing of the new two-moment scheme is detailed in Chapter 3. In Chapter 4 the wintertime orographic precipitation case study is discussed, and the convective case study is discussed in Chapter 5. Chapter 6 summarizes the major conclusions of this study and suggestions for further research.

Chapter 2

THE MICROPHYSICAL MODEL

In the past, the hydrometeor size spectra in RAMS (Walko et al., 1995; hereafter referred to as W95) was controlled by a user-specified mean hydrometeor diameter. The mixing ratio of each hydrometeor category was predicted while the concentration was diagnosed [see Cotton et al., 1982; 1986 (which also predicted on the number concentration of pristine ice crystals)]. The two-moment scheme predicts the concentration and mixing ratio of the distribution function for each hydrometeor category making the determination of each hydrometeor size spectra less arbitrary. With more complex physics the model should better capture the evolution of the hydrometeor spectra. The microphysical scheme is discussed in this chapter, and details the water categories, size distribution, and the model formulations of the mixing ratio and concentration tendencies of each hydrometeor species.[1]

2.1 Categories of water

RAMS has seven water categories: vapor, cloud droplets, rain, pristine ice, snow, aggregates, graupel, and hail. Cloud droplets and rain are of course liquid, but may be supercooled. Pristine ice, snow, and aggregates are assumed to be completely frozen, while graupel and hail are mixed-phase categories, capable of consisting of ice only or a mixture of ice and liquid.

All hydrometeor categories except cloud droplets are assumed large enough to fall. Cloud droplets and pristine ice are the only categories to nucleate from vapor. All other

---

[1]The existing framework for the RAMS microphysical model was initiated by Flatau et al. (1989) and W95. This dissertation is a continuation of the research initiated by these authors.

categories form from existing hydrometeors, but once formed, may also grow by vapor deposition. Pristine ice and snow categories are distinctly defined due to a size criteria. The criterion is based on the bimodal structure observed in some stratified clouds (Arnott et al., 1993), and the negligible riming rates of small ice crystals. The conversion of pristine ice crystals to snow is due only to deposition since riming at these sizes may be neglected. The onset of riming is also dependent on the habit of the crystal. Pitter (1977) found that hexagonal plates must grow by vapor deposition to sizes larger than 300 μm before riming commences. Schlamp et al. (1975) found the minimum size for columns to start riming is close to 50 μm. Theoretical computations of Schlamp and Pruppacher (1977) showed that needles started riming around 40 μm. Consequently, pristine ice crystals are defined as small ice crystals which may continue to grow by vapor deposition, but are not permitted to grow by any other process. Harrington et al, (1995) have determined different cutoff diameters between pristine ice crystals and snow in a cirrus case, and therefore this threshold diameter is easily modified by the user. The snow category is defined in RAMS as relatively large ice crystals which have grown from the pristine ice category due to vapor deposition and may continue to grow by riming. Aggregates are defined as ice particles that have formed by collision and coalescence of pristine ice, snow, and/or other aggregates. Like snow, aggregates are allowed to retain their identity with moderate amounts of riming (large amounts of riming converts these snow and aggregates to graupel). Pristine ice, snow, and aggregates are all low-density ice particles, having relatively low mass and fall speed for their diameters.

Hail and graupel can have many criteria which set the two species apart. Some researchers have used a size constraint. For instance Heymsfield (1983) defined diameter, $D < 1.0$ cm to be graupel and hail to be $D \geq 1.0$ cm. Fraile et al. (1992) assumed stones $D < 0.5$ cm were not hail. Another criterion which can distinguish graupel from hail is the density of the particle. List and Schemenauer (1971) found graupel densities close to 0.6 g cm^{-3}. More recently, Heymsfield (1978) found graupel densities over Northeastern Colorado were typically below 0.5 g cm^{-3} and conical graupel densities were nearly constant at 0.45 g cm^{-3}. Pflaum et al. (1978) found graupel densities near 0.21 g cm^{-3} for particles

with a mean size of 1.1 mm and temperatures near -15°C. Pflaum and Pruppacher (1979) found graupel densities for small graupel (0.4 mm) to be near 0.3 g cm^{-3}. Graupel characterized by low densities required surface temperatures between -10 and -15°C, as found by Heymsfield (1978) . The lower density graupel was characterized by a rougher exterior, while the higher density graupel formed when the surface temperature of the particle was 0°C and had a smooth exterior. These observations followed Macklin's (1962) work which stated that the riming density increases with increasing cloud droplet diameter, surface temperature of the ice sphere, and cloud droplet impact velocity. Hail densities for the most part have been observed closer to 0.9 g cm^{-3} by various studies (Vittori and di Caporiacco 1959; List and Schemenauer, 1971; Matson and Huggins, 1980; Ulbrich and Atlas, 1982) . Prodi found mean values of hailstone density lie between 0.82 and 0.87 g cm^{-3}. In a comparatively lower LWC (liquid water content) spring storm in Boulder, Colorado, Knight and Heymsfield (1983) observed hail densities between 0.31 and 0.61 g cm^{-3} for hail diameters ranging from 0.63 to 1.54 cm. A problem with some of the measurements is that they are ground-based observations which include melting hailstones. Rasmussen and Heymsfield (1987a,b) suggested that measurements of hail at the ground may lead to higher densities than occur aloft due to meltwater soaking into the hailstone's lower density interior.

A fixed density for rain, graupel and hail, is assumed in RAMS since these hydrometeors are assumed to be spherical in shape. Farley (1987) made comparisons between a fixed and a variable density scheme in a severe supercell type storm. He found only minor relative differences in larger scale features such as storm structure and movement between the two schemes. In RAMS graupel is an intermediate density hydrometeor and is approximately spherical in shape. It is formed by moderate to heavy riming and/or partial melting of snow or aggregates. Graupel is allowed to carry up to half of its mass as liquid. If the percentage becomes larger, by either melting, riming or collection by rain, a graupel particle is re-categorized as hail. Hail, or frozen drops (also includes sleet), is a high density hydrometeor considered spherical in shape. It is formed by freezing of rain drops or by riming or partial melting of graupel. Hail is allowed to carry any fraction of

liquid water up to but not including 100%, however, at these high liquid percentages the hail will subsequently convert to rain. This treatment which puts melted hydrometeors into the graupel and hail categories is done as a bookkeeping measure. Note that these definitions of graupel and hail emphasize their composition and density more than their method of formation. For example, a snowflake or aggregate undergoing gradual melting in this scheme first converts to graupel, then to hail, and finally to rain, although hail is more traditionally assumed to form from the collection of supercooled water onto a hail embryo (graupel or aggregate) or from freezing of supercooled rain. The hail category in RAMS therefore, extends to include all "observed hail" (defined as $D > 0.5$ cm), and additionally may include "observed high density graupel", and ice hydrometeors produced by raindrop freezing, regardless of size. The purpose of this approach is to more accurately model a hydrometeor's fall velocity and consequent rates of ventilation and collision as it undergoes transformation to different densities. As will be discussed, fall velocity is a function of diameter and category only, so changing categories is the means for changing the velocity of a given diameter particle.

2.2 The gamma distribution and its moments

RAMS is set up to use the generalized gamma function or as it is more commonly known in radiative transfer, the *modified gamma* distribution. It is defined as

$$f(x) = \frac{c}{s} x^{c\nu-1} \exp\left(-x^c\right), \tag{2.1}$$

where c and ν define the shape of the distribution, and s is a normalization factor to ensure that the integral of the distribution over the interval of definition is equal to 1. Other distributions can be obtained by simplifying this distribution. The *gamma* distribution can be obtained by setting $c = 1$ in this equation, and the *exponential* distribution may be obtained by setting $c = 1$ and $\nu = 1$. The *half-normal* distribution is another one of the family of gamma distributions, and it can be obtained by setting $c = 2$ and $\nu = \frac{1}{2}$.

The distribution function (2.1) can be transformed into a more useful form for atmospheric applications, but first, the probability density function needs to be defined. The

variation of the size spectra of each hydrometeor category can be described by the changes in the moments of the assumed distribution. The spectral density function $n(D)$ is defined such that $n(D)dD$ is the total number of particles with diameters between D and $D+dD$, per unit volume of air. Therefore, $N(D_x)$, the zeroth moment of the distribution,

$$N(D_x) = \int_0^{D_x} n(D)dD, \tag{2.2}$$

is the total concentration per unit volume of air of particles with diameters less than D_x. To describe a size spectrum we choose a suitable probability density function $f(D)$ defined over the interval (D_{min}, D_{max}). For our applications assume $D_{min} = 0$ and $D_{max} = \infty$. The form of the probability density function $f(D)$ has to meet a few simple criteria. It must be of an analytical form amenable to integration in a closed form so that the resulting mathematics is manageable. Also it must be a normalized function, with only a few degrees of freedom, all of which should be diagnostic, based on bulk or spectral field measurements or model predictions (Flatau et al., 1989). The particle size distribution spectrum can then be represented by

$$n(D) = N_t f(D), \tag{2.3}$$

where N_t is the total concentration of particles per unit volume of air.

It is sometimes practical to define a new probability density function through a transformation of variables. From Flatau et al. (1989),

$$f(D) = f(x)\frac{dx}{dD}, \tag{2.4}$$

where the variable x is an arbitrary function of D, i.e. $x = h(D)$, and h is a arbitrary function. The distribution function (2.1) can now be transformed with the aid of (2.4) by letting

$$x = \frac{D}{D_n}, \tag{2.5}$$

where D is the diameter of a particle and D_n is the *scaling* diameter. D_n is the non-physical scaling diameter used to present the spectral distribution function in a non-dimensional form. The scaling diameter will be related to physical quantities such as the mean diameter

of the distribution, however these relations will differ with the chosen spectral parameters. In our generalized scheme it is convenient to use scaling diameter rather than a specific physical quantity since this leads to simpler and general mathematics.

After some simple algebra and noting that the normalization can be obtained by setting $s = \Gamma(\nu)$ where $\Gamma(\nu)$ is the complete gamma function and $c = 1$, the form for the gamma distribution will be

$$f_{gam}(D) = \frac{1}{\Gamma(\nu)} \left(\frac{D}{D_n}\right)^{\nu-1} \frac{1}{D_n} \exp\left[-\left(\frac{D}{D_n}\right)\right], \tag{2.6}$$

where the hydrometeor diameter D may range from zero to infinity. The shape parameter ν controls the breadth of the distribution, and may be any real number greater than or equal to 1, Fig. 2.1 shows the sensitivity of the distribution to ν.

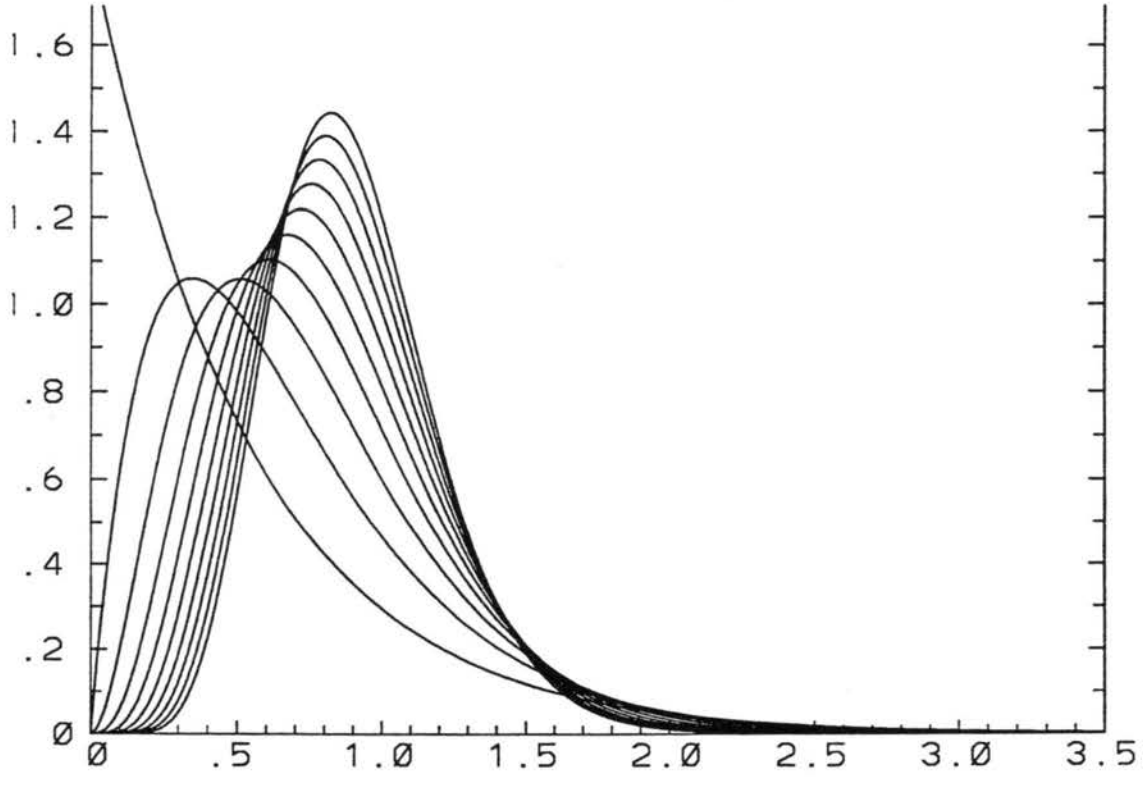

Figure 2.1: Set of gamma distribution curves for integer values of the shape parameter ν from 1 to 10. The peaks of the curves shift progressively to the right as ν increases. The ordinate provides the values of f given by 2.6. The abscissa presents the hydrometeor diameter D, where D_m is held fixed at 1.0 for all curves, and β_m is set to 3. (W95)

When considering the size distribution of various hydrometeor categories, the averaged properties of different species can be defined as

$$\overline{g} = \int_{D_{min}}^{D_{max}} g(D)n(D)dD. \tag{2.7}$$

The function g often exhibits a power law dependence, such that

$$g(D) = c_g D^{p_g} \tag{2.8}$$

where c_g and p_g are constants. Mass m and the terminal velocity v_t may be expressed in a power law relationship with diameter:

$$m = \alpha_m D^{\beta_m} \tag{2.9}$$

$$v_t = \alpha_{vt} D^{\beta_{vt}}, \tag{2.10}$$

their integrals become

$$\overline{m} = N_t \alpha_m D_n^{\beta_m} \frac{\Gamma(\nu + \beta_m)}{\Gamma(\nu)}, \tag{2.11}$$

and

$$\overline{v}_t = N_t \alpha_{vt} D_n^{\beta_{vt}} \frac{\Gamma(\nu + \beta_{vt})}{\Gamma(\nu)}. \tag{2.12}$$

Hydrometeor density is related to mass by

$$\rho_h \equiv \frac{\overline{m}}{Volume} = \frac{\alpha_m D^{\beta_m}}{\frac{\pi}{6} D^3} = \frac{6\alpha_m}{\pi} D^{\beta_m - 3}. \tag{2.13}$$

Next, the generalized moment of the distribution is found. The p^{th} moment of the distribution $f_{gam}(D)$, defined over the interval $(0, \infty)$ is

$$I(p) = \int_0^\infty D^p f_{gam}(D)dD = D_n^p \frac{\Gamma(\nu + p)}{\Gamma(\nu)}. \tag{2.14}$$

With the generalized moment of the distribution, the specific moments of the gamma distribution can easily be found. The first moment of the distribution, the mean diameter, is defined as

$$D_{mean} = \frac{\Gamma(\nu + 1)}{\Gamma(\nu)} D_n = \nu D_n. \tag{2.15}$$

The effective diameter D_{eff}, the ratio of the third moment to the second moment is

$$D_{\text{eff}} = \frac{\Gamma(\nu+3)}{\Gamma(\nu+2)} D_n. \tag{2.16}$$

The mode diameter D_{mode}, where the peak of the distribution is located, can be obtained by differentiating the gamma function (2.6) and setting it equal to zero, which gives

$$D_{mode} = (\nu - 1) D_n. \tag{2.17}$$

The scaling diameter can be diagnosed from the third moment of the distribution, the liquid water content. The liquid water content for a spherical particle is defined as

$$l = \int_0^\infty m(D) n(D) dD. \tag{2.18}$$

Substitution of (2.11) into (2.18) and dividing by by air density ρ_a gives an expression for the mass mixing ratio of the hydrometeor category

$$r = \frac{N_t}{\rho_a} \alpha_m D_n^{\beta_m} \frac{\Gamma(\nu+\beta_m)}{\Gamma(\nu)}. \tag{2.19}$$

This equation gives a relation between the mixing ratio r, the total concentration N_t, and the scaling diameter, and the width parameter ν.

In RAMS, ν, α_m, β_m, α_{vt}, and β_{vt} of each category can be changed at the user's discretion, but these parameters are held fixed in time and space for the duration of the simulation for each hydrometeor class with the exception of the pristine ice and snow categories, where α_m, β_m, α_{vt}, and β_{vt} may change at each grid location depending on the diagnosed habit of the crystal (see Section 2.6.2). Once these parameters are specified, there remain two free parameters from the set (r, N_t, D_n) to be determined for each category, the third parameter being obtained from the other two and (2.19). In the one-moment scheme, D_n is usually specified while r is predicted and N_t is diagnosed. In the two-moment scheme both r and N_t are predicted and D_n is diagnosed. The spatial and temporal dependence of the two free parameters defines the model solution for each category. In the next section, the equations governing the two free parameters are discussed.

2.3 The continuity equations

With the exception of cloud water and vapor, the mixing ratios and number concentrations of all water categories are governed by conservation equations of the form

$$\frac{\partial}{\partial t}(\rho_0 A) = \mathrm{ADV}(\rho_0 A) + \mathrm{TURB}(A) + \mathrm{SEDIM}(\rho_0 A) + \rho_0 \mathrm{SOURCE}(A) \qquad (2.20)$$

where A represents the mixing ratios and number concentrations of rain, pristine ice, snow, aggregates, graupel, and hail, plus an additional "total water" category consisting of the sum of the mixing ratios of all categories including cloud water and vapor (r_c and r_v). ADV (A) and TURB (A) represent advective and turbulent transport of A by the resolved and subgrid velocities in the model. SOURCE (A) represents source (and sink) terms for the categories which consist of all types of conversion of water substance from one category to another. SEDIM (A) represents local losses and gains of A due to gravitational sedimentation. Eq.(2.20) is integrated forward in time from initial values (except for r_t, initial values are usually zero) to obtain prognostic mixing ratios for each model grid cell and each timestep.

The ice liquid potential temperature (θ_{il}) is governed by an equation of the same form as Eq.(2.20), where SOURCE represents external heat sources such as radiative flux convergence, and SEDIM represents local sources or sinks due to sedimentation of ice or liquid water (Tripoli and Cotton, 1981). θ_{il} is conservative in the absence of sedimentation and external heating.

2.4 Diagnosed variables

The cloud droplet mixing ratio (r_c) and the water vapor mixing ratio (r_v) are diagnosed from (r_T), (r_{liq}) and (r_{ice}) by using the saturation mixing ratio (r_{sl}) over water,

$$r_v = \max(0, r_T - r_{liq} - r_{ice}) \qquad (2.21)$$

and

$$r_c = \max(0, r_T - r_{liq} - r_{ice} - r_{sl}) \qquad (2.22)$$

This set of equations can be solved iteratively to produce a diagnosis of T, θ, r_{sl}, r_v, and r_c from predictions of θ_{il}, Exner function π, r_T, r_r, r_i, r_s, r_a, r_g, and r_h.

The sum of the mixing ratios of cloud and vapor is determined as a difference of the prognostic mixing ratios:

$$r_{c+v} = r_t - (r_r + r_p + r_s + r_a + r_g + r_h). \tag{2.23}$$

The cloud mixing ratio r_c is then diagnosed as the amount, if any, by which the sum exceeds the saturation mixing ratio r_s with respect to liquid water:

$$r_c = \max\left[0, r_{c+v} - r_{sl}\right], \tag{2.24}$$

while r_v is diagnosed from

$$r_v = r_{c+v} - r_c. \tag{2.25}$$

Vapor mixing ratio r_v is thus not allowed to exceed r_{sl}. Saturation mixing ratio r_{sl} is given by

$$r_{s\ell} = \frac{0.622 e_{s\ell}}{p - e_{s\ell}}, \tag{2.26}$$

where $e_{s\ell}$ is evaluated from an 8th order polynomial in air temperature T_a (Flatau et al., 1992). T_a is itself diagnosed from the prognostic ice-liquid potential temperature $\theta_{i\ell}$ and from the mixing ratios of all liquid and ice categories by the equation (Tripoli and Cotton, 1981)

$$T_a = \theta_{i\ell}\left(\frac{p}{p_{oo}}\right)^{R/c_p}\left[1 + \frac{Q_{lat}}{c_p max(t, 253)}\right], \tag{2.27}$$

where Q_{lat} is the total latent heating and is given by,

$$\begin{aligned} Q_{lat} &= \left[r_r + r_c + (1 - i_g) r_g + (1 - i_h) r_h\right] L_{\ell v} \\ &\quad + (r_p + r_s + r_a + i_g r_g + i_h r_h) L_{iv}, \end{aligned} \tag{2.28}$$

and i_g and i_h are the fractional amounts of ice in the mixed-phase graupel and hail categories, respectively. Eqs.(2.24– 2.28) and the equation for $e_{s\ell}$ are solved iteratively until convergence occurs.

2.5 Recent modifications made to the single moment scheme

This section describes some recent structural and microphysical changes which are described in detail in W95. These updates were originally made to the one-moment version of RAMS, but are also included in the two-moment version of the code.

2.5.1 The hydrometeor heat budget

The hydrometeor heat budget used in RAMS is thoroughly summarized in W95. The heat budget equations for rain, graupel, and hail hydrometeor species allow for non-thermal equilibrium (eg. heat storage on the hydrometeors is allowed). The other non-mixed-phase hydrometeors such as pristine ice, snow, and aggregates assume thermal equilibrium which is defined here as the latent heating exactly balancing the sensible heat diffused from the hydrometeor. A heat storage term does not occur for these non mixed-phased hydrometeors. Non-thermal equilibrium effects allows for mixed-phase hydrometeors in the cases of graupel and hail and supercooling of rain. These are formulated by noting that the temperature of any given hydrometeor can differ from that of the surrounding ambient air temperature due to latent heat release or absorption in the hydrometeor and sensible heating by collisions with other hydrometeors. The temperature of the hydrometeor controls the rates of heat and vapor diffusion, and the amount of sensible heat transfer which occurs during hydrometeor collection. A heat budget equation for each category is used to compute the hydrometeor temperatures. For convenience a category reference energy is defined

$$\begin{aligned} Q = &\quad 0.5T_c \quad \text{for ice} \\ Q = &\quad T_c + 80 \quad \text{for liquid} \end{aligned} \tag{2.29}$$

where T_c is the mean category temperature in °C, and Q represents the internal energy in cal/g of the category relative to a reference state of ice at 0°C. The factor of 0.5 represents the lower specific heat of ice compared with water, and the 80 reflects the higher energy state of liquid water due to the latent heat of fusion. A value of Q less than or equal to

0 implies that the hydrometeor is total ice and a value of Q greater than or equal to 80 implies a liquid hydrometeor. A value of Q between 0 and 80 implies that the category is either supercooled liquid or contains a mixture of ice and liquid. An energy equation for each ice and liquid category may be written in terms of Q as

$$\frac{dQ}{dt} = S_{vd} + S_{hd} + S_{conv}, \tag{2.30}$$

where the three terms on the right represent sources or sinks associated with vapor diffusion, heat diffusion, and sensible heat transfer from mass conversion between categories. Melting or freezing of a hydrometeor does not create an external heat source or sink of Q, however it can affect the hydrometeor temperature and therefore any of the source terms. The definition of Q in Eq. (2.29) provides a convenient means for evaluating the third source term in Eq. 2.30. For a given amount of mixing ratio r_1 and energy Q_1 converted from one ice or liquid category to another (eg. collection or melting), both r_1 and $Q_1 r_1$ are subtracted from the old category and added to the new. Thus, by balancing these terms it is possible to describe the amount and energies associated with both the ice and water phases of a mixed-phase hydrometeor. It should be noted that in the older version of the RAMS microphysical module, temperature differentials between the hydrometeor surfaces and the ambient environment were allowed, however latent heat release was assumed to be always in balance with the sensible heat transfer (i.e. diffusion).

The Q value gives not only the surface temperature of the hydrometeor, but also the fraction of liquid present. The diagnosis of the fraction of liquid present allows for convenient decisions regarding conversions during collection, melting and shedding. The decisions behind those conversion processes are discussed in Sections 2.6.5, 2.6.8 and 2.6.9. Another advantage of allowing mixed-phase hydrometeor categories is that it allows for more accurate radar reflectivity calculations.

2.5.2 Stochastic collection equation

Differential fall speeds between individual hydrometeors of the same or different categories enable some of them to collide and coalesce. The categories, masses, and temperatures (or Q values) of the two colliding hydrometeors, determine where the mass of

coalesced hydrometeor is transferred. The rate at which the mixing ratio r_x of species x is collected into coalesced hydrometeors due to collisions with hydrometeors of species y is given by the stochastic collection equation (Verlinde et al. 1990)

$$\frac{dr_x}{dt} = \frac{N_{tx}N_{ty}\pi F_\rho}{4\rho_a} \int_0^\infty \int_0^\infty m(D_x)(D_x + D_y)^2 \left|V_{tx}(D_x) - V_{ty}(D_y)\right| \\ f_{gamx}(D_x) f_{gamy}(D_y) E(x,y) dD_x dD_y \qquad (2.31)$$

where f_{gam}, m, and v_t are defined in Eqs. (2.6), (2.9), and (2.10), respectively. The collection efficiency E(x,y) is the product of collision efficiency and coalescence efficiency. The additional factor F_ρ not appearing in Verlinde et al. is equal to $(\rho_{00}/\rho_a)^{0.5}$ and accounts for the air density effect on the terminal fall velocities. This collection equation is different from earlier versions of RAMS (see Cotton et al. 1986) as well as other microphysics models (Lin et al 1983, Rutledge and Hobbs, 1984) which assume that collection can be approximated by a continuous collection equation.

Verlinde et al. (1990) assumed that $E(x,y)$ is independent of D_x and D_y so that it can be moved outside the integrals; a reasonable assumption for all hydrometeor classes but cloud droplets, where E varies strongly over the cloud droplet spectrum. Verlinde et al. (1990) found analytic solutions to Eq. (2.31) in terms of known functions, but W95 found it more computationally expedient to solve only the integral over D_y analytically while numerically computing the integral over D_x. W95 restructured the code accordingly, and further reduced the computational effort during model runtime, by implementing a large number of tabulated solutions to the integral in the form of a three-dimensional table. Two of the table dimensions are the characteristic diameters D_{nx} and D_{ny} which occur in f_{gamx} and f_{gamy}. The third dimension was the pair (x,y) of interacting categories ranging over 32 of the 49 total possible pairs that can be formed from the 7 liquid and ice categories. Sixty table entries were spaced in uniform increments of $ln(D_{nx})$ and $ln(D_{ny})$, over four orders-of-magnitude range of each of the characteristic diameters. During model runtime, for any given pair (x,y), values were interpolated from the table bi-linearly over $ln(D_{nx})$ and $ln(D_{ny})$ to efficiently obtain a value for the double integral in Eq. 2.31. Any change in the width parameters of the hydrometeor species requires a re-calculation of the

lookup tables before a cloud simulation is begun. Multiplying the equation by Δt gives the amount of r_x coalescing with category y over a timestep

$$\Delta r_x = \frac{N_{tx} N_{ty} \pi F_\rho E(x,y) \Delta t}{4 \rho_a} J\left((x,y), D_{nx}, D_{ny}\right) \tag{2.32}$$

where J is the interpolated table value. In some cases (for large Δt) Eq. 2.32 may result in a value of Δr_x which is greater than r_x. This unphysical result is prevented by limiting Δr_x from all conversions to be less than or equal to the amount of r_x available.

Hydrometeor collections are divided into five classes, each with its own basic rules for determining the destination category or categories of Δr_x. These interactions as well as the number concentration discussion are thoroughly described in Section 2.6.5.

2.6 Model formulations of two-moment scheme

This next section describes the SOURCE and SEDIM terms in Eq.(2.20) as applied to all prognostic mixing ratios and number concentrations for each categories.

2.6.1 Autoconversion

Autoconversion refers to the transition from cloud droplets to rain drops due to collision and coalescence of cloud droplets. Berry and Reinhardt (1974a,b) discretized the droplet distribution into precipitating and non-precipitating size categories (a radius $r = 41 \mu m$ cutoff). They then evaluated the stochastic coalescence equation (SCE) analytically and integrated to obtain tendency equations for concentration and mixing ratio.

In RAMS the cloud droplets are distributed according to the gamma distribution and based on the diagnosed liquid water content and prescribed number concentration, a mean diameter is diagnosed. From Berry and Reinhardt (1974b) a characteristic water content L and time scale τ is defined for the autoconversion process where $\frac{L}{\tau}$ represents an average autoconversion rate.

$$L = 2.7 \times 10^{-2} r_c \left(\frac{1}{16} \times 10^{20} D_m^4 (1+\nu)^{-0.5} - 0.4\right) \tag{2.33}$$

and

$$\tau = \frac{3.7}{\rho r_c} \left(0.5 \times 10^6 D_m (1+\nu)^{-0.5} - 0.75\right)^{-1}. \tag{2.34}$$

The mixing ratio tendency can then be calculated

$$\frac{dr_r}{dt} = \frac{\rho_w}{\rho}\frac{L}{\tau} \tag{2.35}$$

and the concentration tendency

$$\frac{dn_r}{dt} = 3.5 \times 10^6 \frac{L}{\tau}. \tag{2.36}$$

According to Lupkes et al. (1989), Berry and Reinhardt's formulation (1974b) for autoconversion also includes the action of droplet selfcollection and accretion. Comparisons of Berry and Reinhardt's formulas (1974a-d) with the SCE revealed that the increase of the autoconversion rate, being characteristic in the initial stage of rainwater formation, is underestimated by Berry's parameterization. Berry and Reinhardt's description has not taken into account a spectral distribution of cloud droplets so their treatment is incomplete (Doms and Beheng, 1986) .

Beheng (1993) has developed a parameterization for autoconversion and cloud water sel-fcollection. In this parameterization the width parameter n occurs in a cloud droplet distribution asuming a gamma-function form $f(r) = Ar^n e^{-Br}$. For $5 \leq n \leq 15$, $50 \leq N_c(t=0) \leq 300$ cm^{-3} and $0.5 \times 10^{-6} \leq L_c \leq 2.0 \times 10^{-6}$ g cm^{-3}, the following rate equations have been found.

$$\frac{\partial}{\partial t}L_c = -6.0 \times 10^{25} n^{-1.7} N_c^{-3.3} L_c^{4.7} - \alpha L_c^{4.7} \tag{2.37}$$

for rate change of cloud water content due to autoconversion where α has to be interpolated from a table for $N_c > 100$ cm^{-3} and $n > 5$. The cloud and raindrop number density autoconversion expression is,

$$\frac{\partial}{\partial t}N_c = 7.7 \times 10^6 (\frac{\partial}{\partial t}L_c)_{aut}. \tag{2.38}$$

The formulation for the selfcollection of cloud droplets which do not convert to rain is,

$$\frac{\partial}{\partial t}N_c = -5.5 \times 10^{10} n^{-0.63} L_c^2. \tag{2.39}$$

Since RAMS does not predict cloud water concentrations, the parameterizations by Berry and Reinhardt (1974a,b) are used. However, when prediction of cloud water concentrations is implemented into RAMS, these more recent formulations should be considered.

2.6.2 Diagnosis of crystal habit

To account for the variability of crystal type in different environmental conditions, the capacitance and mass-dimensional relations of pristine ice crystals and snow are allowed to vary. Since the model doesn't keep track of the history of all crystals, a simple diagnostic check of the ambient temperature and saturation conditions at each grid location is performed during each timestep. RAMS allows two different options in the diagnosis of pristine ice and snow crystal habit. The first scheme, which is intended for orographic and shallow layer clouds, assumes that the cloud top temperature dictates the crystal type throughout the layer of the cloud. The model integrates down from the model top until the liquid or ice cloud is reached. A crystal habit is diagnosed at the cloud top of each cloud layer dependent on temperature and saturation conditions and is assumed for the cloud layer down to the bottom of the cloud. If another cloud layer is encountered below the upper cloud, it would assume a crystal type of the cloud top temperature of that particular cloud layer. This process is repeated until the ground is reached for each vertical column. A more simplistic scheme is also formulated in RAMS where the crystal type is diagnosed at each grid location based on the local temperature and saturation conditions. This scheme allows variability of the crystal type in the cloud layer unlike the first scheme. These schemes are compared in Chapter 3.

The habit diagnosis impacts the model in several ways. The capacitance is dependent on the crystal type and may change the growth characteristics of the crystals. For instance, needles tend to grow more quickly than plates for the same environmental conditions.. Different types of crystals fall at different speeds which is determined by the V_t-D relationship in (2.10). The crystal-dependent terminal velocities impact the sedimentation of the hydrometeors but these velocities are not used in the collection formula. The crystal type information, however, is used to determine the amount of conversion to graupel due to hydrometeor collection of cloud water by pristine ice crystals and snow. The deposition scheme may be simplified for convective type clouds to assume a specific crystal type, since collection processes are dominant over depositional growth.

2.6.3 Ice Nucleation and IN Prediction

Nucleation of pristine ice crystals may occur by a variety of physical mechanisms. These may be divided into two general categories: heterogeneous nucleation, in which an ice nucleus (IN) is responsible for initializing an ice crystal structure from vapor or liquid, and homogeneous nucleation where an IN is not involved. Parameterizations representing both heterogeneous and homogeneous nucleation are described here.

Heterogeneous ice nucleation

Deposition nucleation is a form of heterogeneous nucleation in which vapor molecules attach to an IN, and may occur anytime the ambient vapor mixing ratio exceeds saturation over ice, and the temperature is below $-5°C$. Condensation-freezing nucleation occurs when an aerosol has the properties of both a cloud condensation nucleus (CCN) and an IN. Vapor molecules attach as liquid to the aerosol due its hygroscopicity, and then freeze because of its IN property. Condensation-freezing nucleation requires supersaturation with respect to liquid water, and temperatures below $-2°C$. The deposition nucleation and condensation-freezing nucleation mechanisms are combined to form one expression due to their sensitivity to vapor concentration (Meyers et al., 1992). This parameterization is based on data from continuous flow diffusion chambers (Rogers, 1993; Al-Naimi and Saunders, 1985) which indicate an exponential variation of ice nuclei concentrations with ice supersaturations. This parameterization of the measured ice nucleus concentrations on the ice supersaturation is given by

$$(N_t)_d = exp(a + b((S_i - 1) * 100))) \tag{2.40}$$

where $(N_t)_d$ is the number of nucleated crystals per liter and the coefficients a and b are dependent on the environmental conditions and are shown in Table 2.1. The number $(N_t)_d$ is given as a total number of crystals which can nucleate under the given environmental conditions, and is not dependent on time or on the length of the model timestep. The square of the correlation coefficient for this fit is 0.82. This method predicts pristine ice crystal concentrations an order of magnitude or greater than those measured by previous methods

(Fletcher, 1962) at temperatures warmer than –20°C. This form of the equation can be adapted for other types of airmasses (personal communication, Paul DeMott 1994) such as for the proposed High Plains wintertime upslope event and the High Plains summertime convective case. The coefficients are modified for these cases.

Contact freezing nucleation occurs when an IN comes into contact with an existing supercooled cloud water droplet. Transport of the IN to the droplet results from a combination of diffusiophoresis, thermophoresis, and Brownian motion. Diffusiophoresis occurs in supersaturated environments where droplets are growing by condensation, and is a process in which the net vapor mass flux toward the droplet carries IN in the flow. In RAMS, since exact saturation is assumed when diagnosing an amount of cloud water, a separate estimate of supersaturation is obtained by computing Δr_{vd} as a residual of the net change in cloud water mixing ratio over a timestep minus all source terms (such as collection) other than vapor deposition, and taking r_v in the equation as the ambient supersaturation. Thermophoresis occurs in subsaturated environments when cloud droplets exist but are evaporating. It is a flux of aerosols toward the droplet resulting from the gradient of air molecular speed (temperature) when the droplet is evaporatively cooled below the environmental temperature. As for diffusiophoresis, the separate estimate of subsaturation is used. Thermophoresis dominates over diffusiophoresis for submicron sized aerosols, so their net effect is to increase contact nucleation in subsaturated conditions and decrease it in supersaturated conditions. Brownian motion is a random-movement transport of aerosols due to collisions with air molecules, and results in some IN colliding with cloud droplets.

Parameterizations of the numbers of crystals produced by contact nucleation due to diffusiophoresis, thermophoresis, and Brownian motion are described in Cotton et al (1986)

Table 2.1: Coefficients for heterogeneous nucleation for different environmental conditions

source of data	a	b
Meyers et al., 1992	–0.639	0.1296
High Plains Wintertime (Rogers et al. 1995)	–2.53	0.158
High Plain Summertime (DeMott et al., 1995)	0.35	0.1

and follow Young's (1974b) model and are given by, respectively,

$$\left(\frac{dN_t}{dt}\right)_v = F_1 F_2 \frac{R_v T_a}{L_{lv}\rho_a} \tag{2.41}$$

$$\left(\frac{dN_t}{dt}\right)_t = \frac{F_1 F_2 f_t}{\rho_a}, \tag{2.42}$$

and

$$\left(\frac{dN_t}{dt}\right)_b = F_1 D_{ar}, \tag{2.43}$$

where D_{ar} is the aerosol diffusivity. The expressions F_1, F_2 and f_t are defined by

$$F_1 = 2\pi D_c N_c N_a, \tag{2.44}$$

$$F_2 = \frac{k}{p}(T - T_c), \tag{2.45}$$

and

$$f_t = \frac{0.4[1 + 1.45K_n + 0.4K_n \exp(-1/K_n)](k + 2.5K_n k_a)}{(1 + 3K_n)(2k + 5k_a K_n + k_a)}, \tag{2.46}$$

where R_c is the cloud droplet radius, N_c is the cloud droplet concentration, N_a is the concentration of active contact nuclei, k is the thermal conductivity, k_a is the aerosol thermal conductivity, K_n is the Knudsen number, T_c is the cloud droplet temperature and T the environment temperature while p is the environmental pressure. The Knudsen number K_n is defined as

$$K_n = \frac{\lambda_{a0} T p_0}{T_0 p R_a} \tag{2.47}$$

where $\lambda_{a0} = 6.6 \times 10^{-8}$ m is the mean free path at reference temperature $T_0 = 293.15K$ and reference pressure $p_0 = 1013.25$ HPa, and R_a is an assumed aerosol radius. The aerosol diffusivity D_{ar} is defined by

$$D_{ar} = \frac{7.32 \times 10^{-18} T_c}{R_a \mu}(1 + K_n). \tag{2.48}$$

A parameterization for the number of IN per cubic meter available for contact freezing nucleation is described in Meyers et al (1992), and is given by

$$N_{ic} = exp\,(4.11 - 0.262T_c)\,, \tag{2.49}$$

where a contact nuclei size of 0.1 μm is assumed.

Ice nuclei prediction

To account for spatial variations of ice nuclei (IN) and depletion due to nucleation, the model predicts on both deposition/condensation freezing nuclei and contact-freezing nuclei. The number concentration of IN is governed by the conservative equation shown in (2.20). The Source term represents loss due to heterogeneous ice nucleation and the model assumes no sedimentation of IN. These heterogeneous nucleation equations (Eqs. 2.40 and 2.49) are representative of lower tropospheric conditions and do not account for number loss due to nucleation. To account for advection, diffusion, sinks due to nucleation, and spatial variability of the IN distribution, a non-dimensional pre-factor is defined to account for the modified IN profile, where

$$IN_{\%avail} = \left(\frac{IN_{pred}}{IN_0}\right). \tag{2.50}$$

IN_{pred} is the number concentration of crystals predicted to be available at a grid location (which is initially set to $IN_0 * F_{IN}$), IN_0 is the number concentration available under maximum realistic ice supersaturated conditions (typically $6.05 \times 10^5 - 1.0 \times 10^6 \mathrm{m}^{-3}$), and $IN_{\%avail}$ is the pre-factor defining the percent available to be nucleated and is multiplied by the heterogeneous equations. Due to the lack of soundings of IN, their vertical profile is assumed to decrease with height based on the relative decrease of total aerosol concentrations with altitude in the free atmosphere (DeMott et al., 1994). Here, it is assumed that there is a relationship between the total aerosol concentration and IN concentration. The decrease is nearly log linear in height, except in the mixed boundary layer. The IN population is assumed to be initially set to $1.0 \times 10^6 m^{-3}$ in the boundary layer and decrease an order of magnitude per 5 km in a standard atmosphere. This polynomial expression fit for this decrease is given by

$$F_{IN} = -215.736(\rho_a \times 10^{-3}) + 1.528 \times 10^6(\rho_a \times 10^{-3})^2$$
$$-3.455 \times 10^9(\rho_a \times 10^{-3})^3 + 2.857 \times 10^{12}(\rho_a \times 10e{-}3)^4. \tag{2.51}$$

where F_{IN} is the fraction of ice nuclei available at any height with respect to the number available at the ground level, and ρ_a is the air density (kg m^{-3}). However, this prescribed IN field can be modified both horizontally and vertically by the user. In subsequent simulations IN_{pred} has an initially prescribed horizontally-homogeneous structure and is a function of IN_0 and ρ_a. This IN structure may be modified in time by advection, diffusion, and nucleation.

Homogeneous ice nucleation

Homogeneous freezing of cloud water can be described by a single equation with dependencies on temperature and cloud droplet volume, which can be integrated over the cloud droplet distribution (DeMott et al., 1994). This type of nucleation is due to the spontaneous freezing of water molecules to an ice latice structure. Based on empirical data for activated cloud droplets where the solute and curvature effects are negligible, the following expression represents the number of cloud droplets freezing in a timestep

$$(N_t)_c = N_t \int_0^\infty \left[1 - exp\left(-10^y \frac{\pi D^3}{6} \Delta t\right) n(D)\right] dD \tag{2.52}$$

where

$$y = -606.3952 - 52.6611 T_c - 1.7439 T_c^2 - 0.0265 T_c^3 - 0.0001536 T_c^4. \tag{2.53}$$

This nucleation formula is applied in the temperature range $-50°C < T_c < -30°C$. At colder temperatures, the value at $-50°C$ is applied, which is essentially nucleation of all cloud droplets. For a given Δt and cloud distribution shape parameter, both of which are constant for a specific time integration in RAMS, the integral in Eq. (2.52) is a function of T and D_n only. For computational efficiency, the integral is computed prior to time integration for many values of T and D_n to create a two-dimensional table of values, and required values are bi-linearly interpolated from the table during model execution. RAMS also considers homogeneous freezing of raindrops in a similar manner, extending the parameterization over ranges of D_n typical of raindrops. A two-dimensional lookup table is also formulated for this process.

DeMott et al (1994) derived an equation describing fractional number of haze particles freezing in one second due to homogeneous freezing. This expression includes dependencies on temperature, relative humidity, CCN mass and vertical velocity which is integrated over a specific size distribution of CCN,

$$f_{nuc} = \int_0^{D_{max}} exp\left(-\frac{D}{D_n}\right)\left(1 - exp\left(\frac{D}{D_e}\right)^b\right)\frac{dD}{D_n}, \tag{2.54}$$

D and D_n refer to the CCN spectrum, which we have generalized to follow a gamma distribution as in Eq. (2.6). The quantity D_e and b are complicated functions of atmospheric temperature and relative humidity, and the type of solute, assumed to be ammonium sulfate in this work, and $D_{max} = 1.02\mu m$. Assuming a fixed background CCN spectrum, the integral in Eq. (2.54) is a function of only temperature and relative humidity. As is done for evaluating the number of nucleating cloud droplets, the integral values are computed and stored in a two-dimensional table, from which required values are later interpolated. The fraction of haze particles freezing in a model timestep Δt is approximated by the bracketed term in the following equation, and is of a form which cannot exceed unity. The actual number freezing is given by

$$(N_t)_h = N_h\left[1 - exp\left(-f_{nuc}\Delta t\right)\right], \tag{2.55}$$

where N_h is the number concentration of haze particles. Plans are underway to predict on aerosols and CCN (personal communications, R. Walko) rather than prescribing these parameters as is done in the current model. In addition to more realistic prediction of warm rain process, prediction of aerosols and CCN would greatly improve homogeneous ice nucleation prediction with a more realistic aerosol profile.

The total number of nucleating ice crystals is given by

$$\Delta N_t = max(0., (N_t)_d + (N_t)_c + (N_t)_h + \left[\left(\frac{dN_t}{dt}\right)_v + \left(\frac{dN_t}{dt}\right)_t + \left(\frac{dN_t}{dt}\right)_b\right]\Delta t - {N_t}^{t-1}), \tag{2.56}$$

which is added to the number concentration N_t for pristine ice. The *max* function is included so not to overpredict ice crystals concentrations by comparing the number concentration to number concentration at the beginning of the modeling timestep. The nucleation

contribution to mixing ratio is evaluated from the expression

$$\Delta r_p = \Delta N_t M_n / \rho_a \tag{2.57}$$

where M_n is an assumed initial mass of a nucleated particle.

2.6.4 Secondary production of ice crystals

Cotton et al. (1986) discussed secondary ice production due to riming following the work of Gordon and Marwitz (1981), who developed a parameterization for the Hallet-Mossop ice multiplication theory. Two basic models were discussed in the Cotton et al. (1986) paper, and they questioned whether both these processes are independent processes or just different steps in interpretation of the Hallet-Mossop experiments. If this is the case, then both equations would possibly lead to double counting the same process. Cotton et al. (1986), argued that in that case it would be desirable to chose only one multiplication process. It was decided to use the following scheme, since these equations are formulated in a structure more conducive to the present model for both single moment and double moment prediction.

- Approximately 350 ice splinters are produced for every milligram of rime accreted onto each graupel particle at $-5°C$ ((Hallet and Mossop, 1974)). This mechanism was formulated using

$$P_p(I) = 3.5 \times 10^5 \mathrm{g}^{-1} \frac{dm}{dt}\Big|_{RM} f_1(T_s) \tag{2.58}$$

where $(dm/dt)|_{RM}$ is the riming rate for any of the ice categories and the function f_1 of surface temperature of the ice particle T_s represents the temperature dependence of the process. The Hallet-Mossop mechanism is thought to peak at $-5°C$, and be about zero above $-3°C$ and below $-8°C$. Linear interpolation then yields (Cotton et al., 1986):

$$f_1(T_s) = \begin{cases} 0; & T_s > 270.16 \\ [(T_s - 268.16)/2]; & 270.16 \geq T_s \geq 268.16 \\ [(T_s - 268.16)/3]; & 268.16 \geq T_s \geq 265.16 \\ 0; & 265.16 \geq T_s \end{cases} \tag{2.59}$$

2.6.5 Collection

The impact of collection on mixing ratio tendency was discussed in Section 2.5.2. Collection impacts number concentration in a similar manner to the mixing ratios, however, by predicting number concentration, other physical processes are possible, such as self-collection of like-hydrometeors and raindrop breakup. Using (2.31), the rate at which the number concentration n_x of species x is collected into coalesced hydrometeors due to collisions with species y may be written as,

$$\frac{dn_x}{dt} = \frac{N_{tx}N_{ty}\pi F_\rho}{4} \int_0^\infty \int_0^\infty (D_x + D_y)^2 \left|V_{tx}(D_x) - V_{ty}(D_y)\right| f_{gamx}(D_x) f_{gamy}(D_y) E(x,y) dD_x dD_y. \quad (2.60)$$

A large number of the solutions to the integral are computed and tabulated in three-dimensional lookup tables similar to the technique used for mixing ratio as described in Section 2.5.2.

The collecting hydrometeors are characterized by five different types of interactions depending on the specific impacts on the mixing ratios and number concentration tendencies of the hydrometeors. The first group of interactions is due to hydrometeor self–collection which only impacts the number concentration of the self–collecting hydrometeor. This type of interaction tends to move the distribution to larger sizes with the exception when breakup occurs during self-collection of rain. The second type of hydrometeor interaction treats ice collisions where pristine ice crystals and or snow collect to form aggregates. This class of interactions results in a number concentration and mixing ratio tendency for each involved hydrometeor. As mentioned earlier, a quantity of energy $Q_x r_x$ accompanies the mixing ratio r_x during each transfer. Another class of ice-phase interactions occurs when the destination of collection between the collecting hydrometeor and the collected hydrometeor is the collecting hydrometeor. An example of this type of interaction is aggregate collection of snow. This class of collection results in a number and mass tendency for the collected hydrometeor and a mass tendency for the collecting hydrometeor.

The next two types of collection involve ice-liquid interactions. In these collection processes the destination may be a third hydrometeor category, rain, graupel or hail.

In interactions involving an ice category with the cloud droplet or rain categories, three factors determine the destination of the collection: the type of collecting ice hydrometeor, the amount of rain or cloud mixing ratio collected, and if the collection process results in a mixed-phased hydrometeor. The amounts of mixing ratio, number concentration, and energy produced by the collisions are divided between the input ice category and a secondary ice category, which is graupel when the interaction involves cloud water, and hail when the interaction involves rain. A simple diagnostic scheme was devised to determine the amount of collected mass retained by the collecting ice category:

$$r_{ret} = max(0., r_{colt} - \zeta \times r_{\%liq} - \chi \times r_{coll}) \tag{2.61}$$

where r_{ret} is the amount of mass being retained by the collecting ice category, r_{colt} is the amount of collected mass, $r_{\%liq}$ is the mixing ratio of the liquid portion of the coalesced hydrometeor after the two contributors reach thermal equilibrium with each other, and r_{coll} is the amount of collected mass of either the cloud or rain categories. The ζ and χ values for each hydrometeor interaction are given in Table 2.1 and 2.2. For example, a dendritic snowflake will continue to keep its identity after collecting cloud water in a dry-growth regime, but a columnar snowflake will more likely be converted over to graupel especially in a wet growth regime. Ice-rain interactions usually result in most of the collected mass and number being converted to the hail category. A similar diagnostic calculation is done for the number concentration tendency due to collection:

$$n_{conv} = max(0., (r_{colt} - r_{ret})/r_{colt}) \times n_{colt}) \tag{2.62}$$

where n_{conv} is the number concentration tendency that is converted to the third hydrometeor category, and n_{colt} is the number of collected hydrometeors.

One of the major differences between the two-moment and one-moment schemes, besides the fact that number concentration tendencies due to collection are calculated, is the importance of D_n on the collection kernel. In the one-moment scheme the characteristic diameter of the distribution is prescribed by the user so all collection processes are based on that fixed diameter. With the two-moment scheme, the characteristic diameter is diagnosed based on the mixing ratio and concentration of the distribution allowing for varying

Table 2.2: Collection weighting factors for interactions involving ice categories and cloud droplets.

Collecting Hydrometeor	ζ	χ
snow(spatial)	1	0
snow(columnar)	1	1
aggregates	1	0
graupel	.5	0
hail	0	0

values of D_n of each species. Implicit in the diagnosis of D_n is the possibly wide variability of v_t for each species. These changes should produce greater flexibility and a more realistic depiction of the collection process.

Collisional breakup

The collisional breakup parameterization assumes that filament breakup is the only active mode (Brazier-Smith et al., 1973; Low and List, 1982; Srivastava, 1978). Verlinde (1993) parameterized the breakup coalescence efficiency into the self-collection equation. A similar approach used in RAMS (Verlinde and Cotton, 1993) by modifying the collection efficiency by

$$E_c(D_m) = \begin{cases} 0 & for D_m < D_{cut} \\ Aexp(D_m) & D_m > D_{cut} \end{cases} \tag{2.63}$$

This formulation allows the $E_c = 1.0$ for $D_m \leq 600\mu m$ and decreases to $E_c < 0.0$ for $D_m > 900\mu m$. Raindrop breakup results in a number concentration tendency for the rain category.

Table 2.3: Collection weighting factors for interactions involving ice categories and rain drops.

Collecting Hydrometeor	ζ	χ
pristine ice crystals	0	10
snow	0	5
aggregates	0	5
graupel	1	1
hail	0	0

2.6.6 Deposition

Depositional growth for all hydrometeors follows from the vapor diffusion equation for a single hydrometeor (Pruppacher and Klett, 1978)

$$\frac{dm}{dt} = 2\pi D\psi f_{Re}(\rho_{va} - \rho_{vsh}). \tag{2.64}$$

where ψ is the vapor diffusivity. The ventilation coefficient f_{Re} is given by (Cotton et al. 1982)

$$f_{Re} = \left[1.0 + 0.229\left(\frac{v_t D}{V_k}\right)^{0.5}\right] S, \tag{2.65}$$

where S is the shape parameter. Multiplying by the distribution function (Eq. 2.6) and integrating over the distribution gives the mass diffusion rate per cubic meter of atmosphere:

$$\frac{d\bar{m}}{dt} = N_t 2\pi\psi F_{Re}(\rho_{va} - \rho_{vsh}), \tag{2.66}$$

where

$$F_{Re} \equiv \int_0^\infty D f_{Re} f_{gam}(D) dD \tag{2.67}$$

is the integrated product of ventilation coefficient and diameter. It is assumed that ρ_{vsh} and therefore hydrometeor temperature is independent of diameter. All hydrometeors (with the exception of pristine ice crystals which may be transfered to the snow category) are assumed to grow by deposition and maintain their identity in a saturated environment.

The interaction between pristine ice crystals and snow are considered a special case since the distinction between the two species is due to the size of the crystals. Both pristine ice and snow distributions may occur in either ice supersaturated or ice subsaturated conditions (Harrington et al., 1995). During conditions of ice supersaturation, pristine ice number concentration and mass mixing ratio are transferred to the snow category by vapor depositional growth. This transfer is consistent with our definition of snow; snow is the larger ice crystal class which is initiated only by vapor-grown pristine ice crystals. During ice subsaturated conditions, transfer of number concentration and mass mixing ratio from the snow category to pristine ice is conversely, calculated. The mean size of the pristine ice crystals are bounded by a size, D_b, which is set to $60\mu m$ for reasons discussed in Section 2.1. The mean size of pristine ice is not allowed to grow beyond this size while the

snow mean size is not allowed to become less than D_b. Since, pristine ice and snow conform to the generalized gamma distribution functions both implicitly contain crystals of all sizes. Therefore, the transfer of crystals from pristine ice to snow is calculated by considering the change of mass mixing ratio and number concentration in the range $D_b \rightarrow \infty$ of the pristine ice distribution. Similarly, the snow transfer of mass mixing ratio and number concentration is calculated by considering the change in the region $0 \rightarrow D_b$ of the snow distribution. These equations may be written as,

$$\left(\frac{dr}{dt}\right)_{p\rightarrow s} = \frac{d}{dt}\left\{\frac{1}{\rho_a}\int_{D_b}^{\infty} \alpha_m D^{\beta_m} n(D)dD\right\}_{vp} \tag{2.68}$$

$$\left(\frac{dN_t}{dt}\right)_{p\rightarrow s} = \frac{d}{dt}\left\{\frac{1}{\rho_a}\int_{D_b}^{\infty} n(D)dD\right\}_{vp} \tag{2.69}$$

for the pristine ice to snow transfers where the subscripts v and p refer to the vapor-depositional process and the pristine ice category, respectively. Similarly, the snow transfer can be written,

$$\left(\frac{dr}{dt}\right)_{s\rightarrow p} = \frac{d}{dt}\left\{\frac{1}{\rho_a}\int_{0}^{D_b} \alpha_m D^{\beta_m} n(D)dD\right\}_{vs} \tag{2.70}$$

$$\left(\frac{dN_t}{dt}\right)_{s\rightarrow p} = \frac{d}{dt}\left\{\frac{1}{\rho_a}\int_{0}^{D_b} n(D)dD\right\}_{vs}. \tag{2.71}$$

By applying Leibniz' rule and some chain differentiation the following forms of the above equations can be derived (Harrington et al., 1995),

$$\left(\frac{dr}{dt}\right)_{p\rightarrow s} = \left\{\frac{D_b^2 n(D_b)}{\beta_m I(1)} + \frac{T(1,\frac{D_b}{D_n})}{I(1)}\right\}_p \left(\frac{dr}{dt}\right)_{vp}, \tag{2.72}$$

$$\left(\frac{dN_t}{dt}\right)_{p\rightarrow s} = \left\{\frac{\rho_a D_b^{2-\beta_m} n(D_b)}{\alpha_m \beta_m I(1)}\right\}_p \left(\frac{dr}{dt}\right)_{vp}, \tag{2.73}$$

where $I(1)$ is the first moment of the complete gamma distribution, and $T(1,\frac{D_b}{D_n})$ is the first moment of the incomplete gamma distribution described in general as,

$$T(P,X) = \int_X^{\infty} D^P n(D)dD. \tag{2.74}$$

The equations for the snow to pristine ice transfers are written similarly as,

$$\left(\frac{dr}{dt}\right)_{s\rightarrow p} = \left\{-\frac{D_b^2 n(D_b)}{\beta_m I(1)}\right\}_s \left(\frac{dr}{dt}\right)_{vs}, \tag{2.75}$$

$$\left(\frac{dN_t}{dt}\right)_{s\rightarrow p} = \left\{\frac{\rho_a D_b^{2-\beta_m} n(D_b)}{\alpha_m \beta_m I(1)}\right\}_s \left(\frac{dr}{dt}\right)_{vs}. \tag{2.76}$$

The first term in Equation (2.72) describes the mass mixing ratio of crystals in the region $0 \rightarrow D_b$ that grow larger than D_b; the second term describes the vapor depositional growth of crystals in the region $D_b \rightarrow \infty$. Since we are describing all hydrometeors with the complete gamma distribution function, there is an amount of overlap of the pristine ice distribution into the snow region. In order to put a constraint on the artificial growth of pristine ice crystals in the region $D_b \rightarrow \infty$, this second term in Equation (2.72) is quantified as a source for snow mass mixing ratio. Equation (2.73) describes the number concentration of pristine ice in the region $0 \rightarrow D_b$ that grow beyond the D_b size. For the snow transfer process, note that Equation (2.75) is similar to Equation (2.72) except for the second term in Equation (2.72). This term is dropped since it describes the mass mixing ratio that is lost to the vapor category due to sublimation of crystals in the region $0 \rightarrow D_b$. Equation (2.75), thus, describes the mass of crystals that are transferred from the snow to pristine ice category due to sublimation. For number concentration transfer processes in ice subsaturated conditions, Equation (2.76) describes the number concentration of snow that sublimates to sizes less than D_b.

2.6.7 Evaporation

During subsaturated conditions, the mass mixing ratio that evaporates/sublimates from the water/ice classes is described by integrating the mass vapor depositional growth equation over the distributions as described in W95. There is the possibility, however, that the smallest ice hydrometeors in the distribution will disappear completely into vapor in a given timestep. Therefore, a parameterization of number concentration loss due to evaporation/sublimation was formulated (Harrington et al., 1995). This is accomplished by considering the fractional number concentration loss (N_f) from the distribution to be a strong function of the fractional mixing ratio lost (R_f) in a timestep, the distribution shape parameter (ν), and for pristine ice and snow categories, the crystal habit (H). The equation may be written as,

$$N_f = F_e(R_f, \nu, H), \tag{2.77}$$

where

$$N_f = \frac{\Delta N_t}{N_t}, \tag{2.78}$$

and

$$R_f = \frac{\Delta r}{r} \tag{2.79}$$

where r is the mass mixing ratio of a given species, N_t is the total number concentration of a given species, and ΔN_t is the change in number concentration due to evaporational/sublimational loss of a given species. Formulation of an analytical function, F_e, in Equation (2.77), however, was not obvious. One solution was to calculate values of the fractional number concentration loss using a bin model representation of the distribution function, $n(D)$. In this bin model, an initial, normalized distribution was slowly evaporated in a subsaturated environment. During every time-step the mass loss from each bin is calculated, if the mass loss to evaporation/sublimation was greater than the mass in the bin then the crystals are assumed to have completely disappeared into vapor which constituted a number concentration sink. By adding up the values of mass and number concentration lost to sublimation, tables can be created of N_f and R_f for a given ν and H. These tables were constructed for each category for number loss ratio for ranges of mass loss from 0.1 to 1.0, for prescribed values of ν, and for all crystal habits. This method was tested for pristine ice crystals and snow against variations in external parameters such as temperature, pressure, and ice saturation ratio. It was found by Harrington (1994) that these parameters have little effect on the tabulation of these ratios.

2.6.8 Melting

The ice distributions can be greatly modified depending on which type of melting and shedding physics is incorporated into the model. It has been observed that the air temperature must be warmer than –8°C for melting to occur (Heymsfield and Hjelmfelt, 1984). Melting is strongly affected by the relative humidity profile. Rasmussen and Heymsfield (1987b) stated that melting may not commence until 5 to 8°C in dry, evaporative conditions. Another problem concerned with melting is that during melting of low density graupel the particle completely soaks with water (Kidder and Carte, 1964; Prodi, 1970;

and Rasmussen and Heymsfield, 1987a), effectively transforming the particle into a higher density hail particle which would lead to a conversion to the hail category. In melting regions, small stones should melt first leaving the larger stones. Initial attempts by Lin et al. (1983) and Rutledge and Hobbs (1984) kept the intercept of the distribution constant during melting, but Orville and Kopp (1977) and Kopp et al. (1983) showed that this method produced unrealistically large decreases in the ratio of large to small particles and consequently lowered melting rates. Ferrier (1994) attempted a more realistic approach by melting the smallest ice particles completely within a timestep while assuming an exponential hydrometeor distribution. His model produced the opposite effect to holding the intercept constant since many more of the smaller particles were removed from the distribution. This scheme resulted in unrealistically large mean particle diameters below the melting level with substantially smaller melting rates than in the constant intercept approach.

A more detailed description of the mass mixing ratio tendency due to melting used in RAMS can be found in W95. Since pristine ice crystals are assumed to be all ice, any melt mass is converted to cloud water. A corresponding percentage of the number concentration of the crystal is assumed to be lost during melting. The snow and aggregate categories also assume all melt mass is lost by the crystal. Since the melted mass is converted to the graupel category an equal amount of ice mass is assumed to be lost to maintain a mixed-phased converted hydrometeor. To determine the number concentration tendency lost by snow and aggregates, an explicit bin model was used similar to the technique used for evaporation (see Section 2.6.7). This is accomplished by considering the fractional number concentration loss (N_f) from the distribution due to melting to be a strong function of the fractional mixing ratio lost (R_f) in a timestep, the distribution shape parameter (ν), and for pristine ice and snow categories, the crystal habit (H). Number concentration and mixing ratio tendencies due to melting of graupel and hail is more complicated due to the mixed-phased capabilities of these species. Graupel is able to maintain a small percentage of liquid before converting to the hail category. Once the fraction of water in graupel reaches 50% the graupel particle is assumed to be transformed into a high density

hail particle. A look-up table is used to produce a mass and number tendency conversion to rain assuming that the smallest graupel particles completely melt into rain. Hail is assumed to be a mixed phase hydrometeor, where a mass and number tendency conversion to rain, similar to graupel, is assumed. Another source for rain from the hail category is due to shedding (see Section 2.6.9).

2.6.9 Shedding

Shedding from hail can produce a significant number of liquid particles which can be a significant source of rain and potential hail embryos. Lesins and List (1986) describe that the shedding process represents an instantaneous conversion of cloud to rain. Rasmussen and Heymsfield (1987c) also point out that the concentration of shed drops in a moderate updraft may be 10^3 higher than the number of shedding hail. Graupel and hail must be large enough to shed liquid water. Observations indicate sizes (D) between 0.5 cm (Heymsfield and Hjelmfelt, 1984) and 0.8 cm are necessary (Rasmussen et al., 1984b). Chong and Chen (1974) determined the critical amount of water carried by an ice core based on the radius of an ice core. Lesins and List (1986) observed 5 growth regimes and determined a ice fraction minimum to be 0.5. Rasmussen et al. (1984b) observed much more water being retained than Chong and Chen (1974). They devised an expression for the critical mass of water on the ice core's surface before shedding occurs (M_{Wcrit}) dependent on the mass of the ice M_i.

$$M_{Wcrit} = 0.268 + 0.1389 M_i. \tag{2.80}$$

Since the model predicts hail as a mixed-phased hydrometeor, the ice mass portion of hail can be calculated ($M_i = M(D) * fracice$). Integrating 2.80 over the hail distribution results in an expression for the mass loss due to shedding,

$$M_{loss} = \int_{0.5}^{\infty} ((M(D) * fracliq) - M_{Wcrit}) n(D) dD \tag{2.81}$$

with the solution for mixing ratio loss due to shedding,

$$r = 1/\rho_0 \frac{\pi}{6} N_t \frac{\gamma(\nu + 3, Dcut/D_n)}{\Gamma(\nu)} (\rho_l D_n^3 fracliq - (0.268 + 0.1389 \rho_i D_n^3 fracice)). \tag{2.82}$$

Rasmussen and Heymsfield (1987a) stated that shedding is independent of altitude for non-tumbling hail. The size of the drops shed by hail and graupel are observed to be between 0.5 and 2.0 mm with a 1 mm modal size (Rasmussen et al., 1984b and Lesins et al., 1980). The mixing ratio of the mass shed by the ice spheres is calculated, and the number of raindrops shed is determined by assuming that the shed size is $D_{shed} = 1.0$ mm,

$$N_{shed} = \left(\frac{r_{shed}}{\pi/6 D_{shed}^3} \right). \tag{2.83}$$

where r_{shed} is the mixing ratio of the rain shed, and D_{shed} is the size of the shed drops.

It would be possible to integrate this formula over the entire hail distribution to obtain a maximum allowable value of liquid to mass ratio for the category, and to shed drops when the category liquid content exceeds this value. However, there are physical situations where, due to differential melting and liquid collection rates with hail size, some hail sizes will be below the threshold for shedding while others will exceed it; thus, this effort seems unwarranted. Furthermore, other authors (e.g., Chong and Chen, 1974) have observed significantly different liquid water retention amounts. We therefore take the simple approach of applying Eq. (2.80) directly to the mean mass $\overline{m}$ of the hail distribution, and shedding when the fractional liquid water content exceeds the maximum allowed for that mass.

2.6.10 Sedimentation

Gravitational settling of hydrometeors causes them to fall relative to air. In RAMS, transport of hydrometeors due to resolved and subgrid air motions in the model is evaluated elsewhere (see Eq.(2.20)); sedimentation only deals with the mass-weighted relative fall velocity between the hydrometeor class and air, which is given by Eq.(2.12). After evaluating Eq.(2.20) without the SEDIM(A) term, and updating mixing ratio r and concentration n based on all other terms, sedimentation is then carried out on the updated mixing ratios and number concentrations to obtain a final value for the timestep.

Following W95, a Lagrangian scheme is used to transport the mixing ratio from any given grid cell to a lower height in the vertical column. Before sedimentation, the mixing ratio is identified as a collection of volumes each corresponding to a grid cell bounded by

a top height z_{top} and bottom height z_{bot}. The volume is assumed to fall at speed $\overline{v}_t$ for the timestep, resulting in new heights of the top and bottom surfaces of the volume given by

$$z_{topnew} = z_{top} - \overline{v}_t \Delta t, \tag{2.84}$$

and

$$z_{botnew} = z_{bot} - \overline{v}_t \Delta t. \tag{2.85}$$

We then identify which grid cell or cells are overlapped by the displaced volume, and in what proportion. The mixing ratio is transferred from the original grid cell to the new ones in the given proportions. This scheme allows sedimentation which can be more rapid than one grid level per timestep (a limiting velocity of explicit Eulerian methods), and can often occur when vertical grid stretching is used to provide high resolution near the ground.

In evaluating the SEDIM term for number concentration for each hydrometeor, it is assumed that N_t is transported in the same proportion as mixing ratio. This procedure ensures that the mixing ratio and number concentration of each hydrometeor does not fall into separate grid volumes due to sedimentation.

2.6.11 Equation closure

There is always the potential that in some situations the model may predict unrealistic number concentrations or mixing ratios and this may result in the diagnosis of extreme hydrometeor diameters. As a precaution, a check on the diameter of each hydrometeor category is made to make sure that the values are in bounds when the diameter is diagnosed in the 2-moment scheme. If the diagnosed diameter is smaller than D_{nmin} or D_{nmax}, it is assumed that the diameter is out of bounds and the concentration is re-diagnosed based on that diameter (see Table 2.4). Tests are performed in (see Chapter 3) to show how frequently this diameter readjustment is needed.

Table 2.4: Diameter bounds for each of the hydrometeors with D_{nmin} and D_{nmax}.

Hydrometeor	D_{nmin} (m)	D_{nmax} (m)
cloud droplets	1.0e-6	4.0e-5
rain	4.0e-5	0.01
pristine ice crystals	1.0e-6	6.0e-5
snow	6.0e-5	0.01
aggregates	1.0e-6	0.01
graupel	1.0e-6	0.005
hail	1.0e-6	0.01

Chapter 3

SENSITIVITY TESTING OF MICROPHYSICS

Sensitivity of the 2-moment microphysical scheme of RAMS to selected parameters such as the shape parameter (ν), number concentration (N_t) of cloud droplets, and ice nuclei (IN) are tested and examined in this section. Comparisons are made only between simulations performed here; no attempt is made in this work to compare with results from previous model versions or with observations. Verification of the microphysical model is conducted in Chapters 4 and 5.

3.1 Model setup

For simplicity, the model is configured similarly to W95 with a two-dimensional computational domain over flat terrain, with no surface fluxes of heat or moisture. A deep convective cell which produces large amounts of both liquid and ice is simulated. The computational domain is 24 km deep and 50 km in horizontal extent, with grid spacing of 500 m in the horizontal and 300 m in the vertical. Initial conditions consist of zero winds, potential temperatures of 306 K and 218 K at the surface and 11 km, respectively, with a constant lapse rate between and a constant potential temperature above. The water vapor mixing ratio is set to 15.0 g kg^{-1} below 2 km and very dry air (0.01 g kg^{-1}) was initialized above 3 km. A Rayleigh friction absorbing layer is used above 18 km to prevent gravity wave reflection off of the rigid upper lid. Convection is initiated by a domain centered bubble in the horizontal, 10 km wide and 3 km deep, with a temperatures 5 K warmer and 2 g kg^{-1} moister than the environment. This simulation is quite explosive (2600 J kg^{-1}), and it is done purposely to exercise the microphysical scheme to a point which is near the physically-expected limits of a convective storm.

Table 3.1: Sensitivity tests and setup

Experiment	moments	ν	N_c	crystal habit
EXP1	2	1	300 cm^{-3}	hexagonal plates
EXP2	1 except for PI	1	300 cm^{-3}	hexagonal plates
EXP3	2	1	60 cm^{-3}	hexagonal plates
EXP4	2	1	1500 cm^{-3}	hexagonal plates
EXP5	2	3	300 cm^{-3}	hexagonal plates
EXP6	2	1	300 cm^{-3}	variable habits
EXP7	2	1	300 cm^{-3}	variable habit with vertical dependence

The sensitivity experiments are summarized in Table 2.1. These experiments test the sensitivity of the model to the 1-moment scheme, and the parameters ν, N_t of cloud droplets, and the different pristine ice crystal and snow habit schemes in the model. All experiments assume pristine ice crystals and snow are hexagonal plates, except for Experiments 6 and 7. Two-moments are predicted in every experiment except EXP2 (where only pristine ice crystals have a 2-moment prediction), and the cloud droplet number concentration (N_t) is set to 300 cm^{-3}, and ν=1 for all categories except in EXP5 (ν=3).

Convection develops nearly identically in the first several minutes for all experiments. Bouyancy is dominated by the initial warm bubble in the first few minutes, and by latent heat release for several minutes afterward. Significant differences in most fields become readily apparent by 15 minutes, and these differences grow rapidly. Variations of microphysical fields across experiments due to different values of microphysical parameters strongly impact the convective motions, which in turn feed back upon the evolving microphysical fields. At 30 minutes into the simulations, convective scale motions are still present in all cases, but the kinematic fields have diverged significantly. A simulation time of 15 minutes was chosen to present and discuss some of the differences between the experiments since the differences are not a direct result of the kinematics at this time and precipitation was starting to reach the ground. The two-moment scheme adds nearly 15% to the time integration of the model, however, optimization is currently being implemented to make the code more efficient.

3.2 Model results

Some of the model fields from EXP1 are shown in Fig. 3.1. The cloud water field shows locally high amounts being injected into the updraft core (Fig. 3.1a), with peak values close to 5.0 g kg^{-1}. These peak cloud water mixing ratios highlight the relatively slow conversion of cloud water to the ice categories in the main core of the updraft. The total mixing ratio field (Fig. 3.1b) shows very moist boundary layer air being transported into the middle-troposphere via the updraft core. The predicted N_{in} distribution shown in Fig. 3.1c displays a similar structure to the total water mixing ratio field with the high N_{in} air being advected into the upper troposphere. Figure 3.1d shows the vertical velocity for EXP1 at 15 minutes. The updraft peak velocities approach 52 m s^{-1} with weaker updrafts situated away from the center of the grid on both sides initiated by gravity waves excited by the initial convective pulse. Figure 3.2 shows the predicted hydrometeor mixing ratio fields for EXP1. Rain mixing ratio is displaced away from the storm center in secondary updrafts near 4 km AGL, with peak values of 2.5 g kg^{-1}. The rainwater which is produced in the updraft core is quickly converted to hail higher above the melting level due to collection processes. The low density ice categories are located high in the troposphere producing the anvil cloud. Glaciation is initiated by pristine ice crystals which are heterogeneously produced above 5 km AGL. These crystals grow by vapor deposition and convert to snow, which initiates the riming process, enabling larger crystals such as the aggregates, graupel and hail to be produced. In the presence of liquid water, most of this ice mass is converted to hail due to collection, and consequently, hail mixing ratios peak at nearly 6 g kg^{-1}. Pristine ice crystals dominate the anvil mass with peak values of 3 g kg^{-1}, nearly 5 times greater than snow and aggregate mixing ratio values. Later in the simulation, however, snow and aggregate mass dominate pristine ice crystal mass due to deposition and collection sources. Graupel mixing ratios are relatively small due to the high LWC in the storm which quickly converts much of the graupel mass over to the hail category.

The hydrometeor concentration fields are shown in Fig. 3.3. The rain concentration field shows peak rain number concentrations are found in the updraft core near 6 km

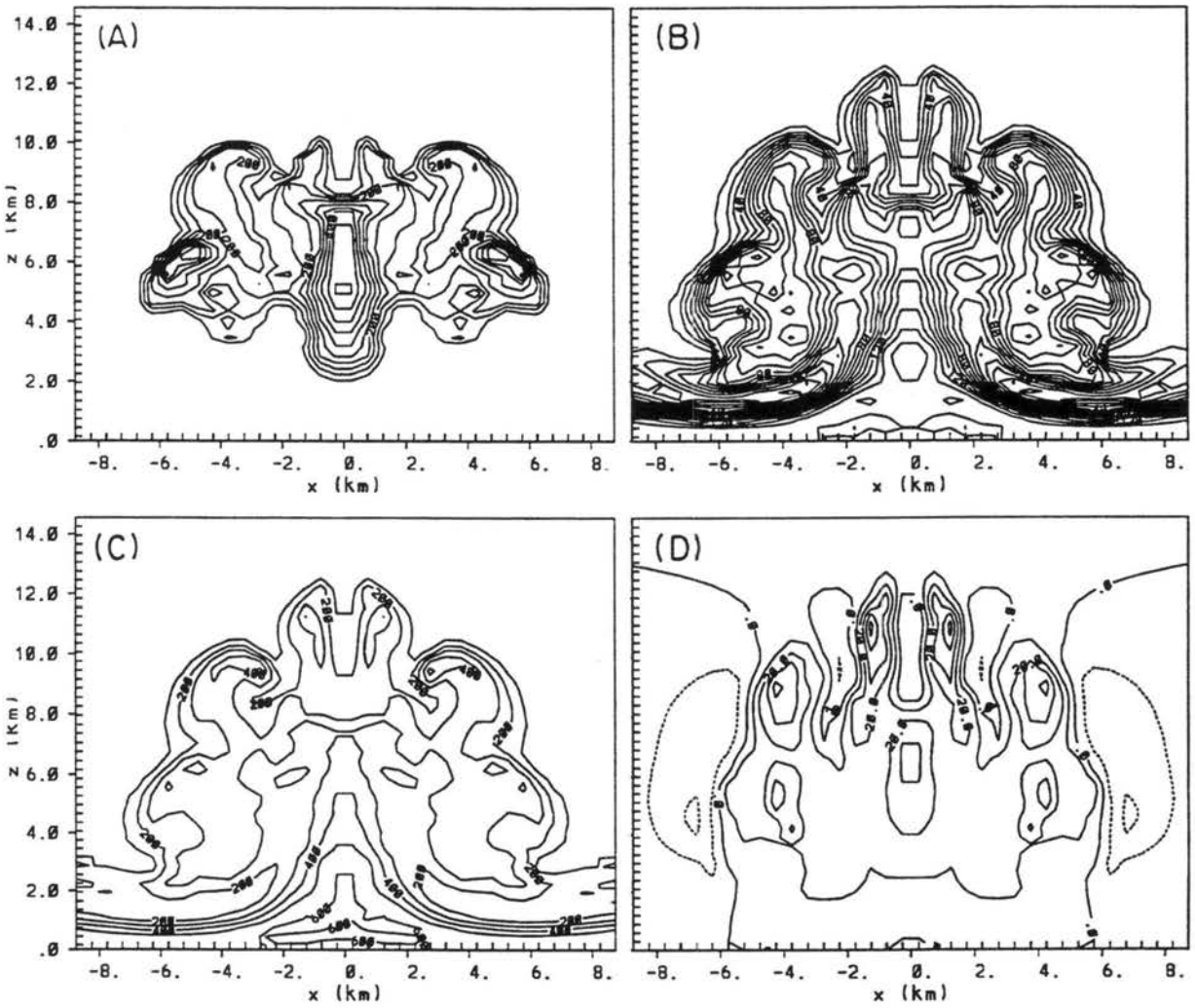

Figure 3.1: EXP1 simulated fields at 15 minutes. Contour intervals and maxima are shown in brackets. These and subsequent figures are "windowed in" to focus on the area of interest: (A) $r_c\,[0.5gkg^{-1}, 5.0gkg^{-1}]$, (B) $r_t\,[1.0gkg^{-1}, 15.0gkg^{-1}]$, (C) $N_{in}\,[1\times10^4m^{-3}, 6\times10^5m^{-3}]$, (D) $w\,[10.0ms^{-1}, 50.0ms^{-1}]$.

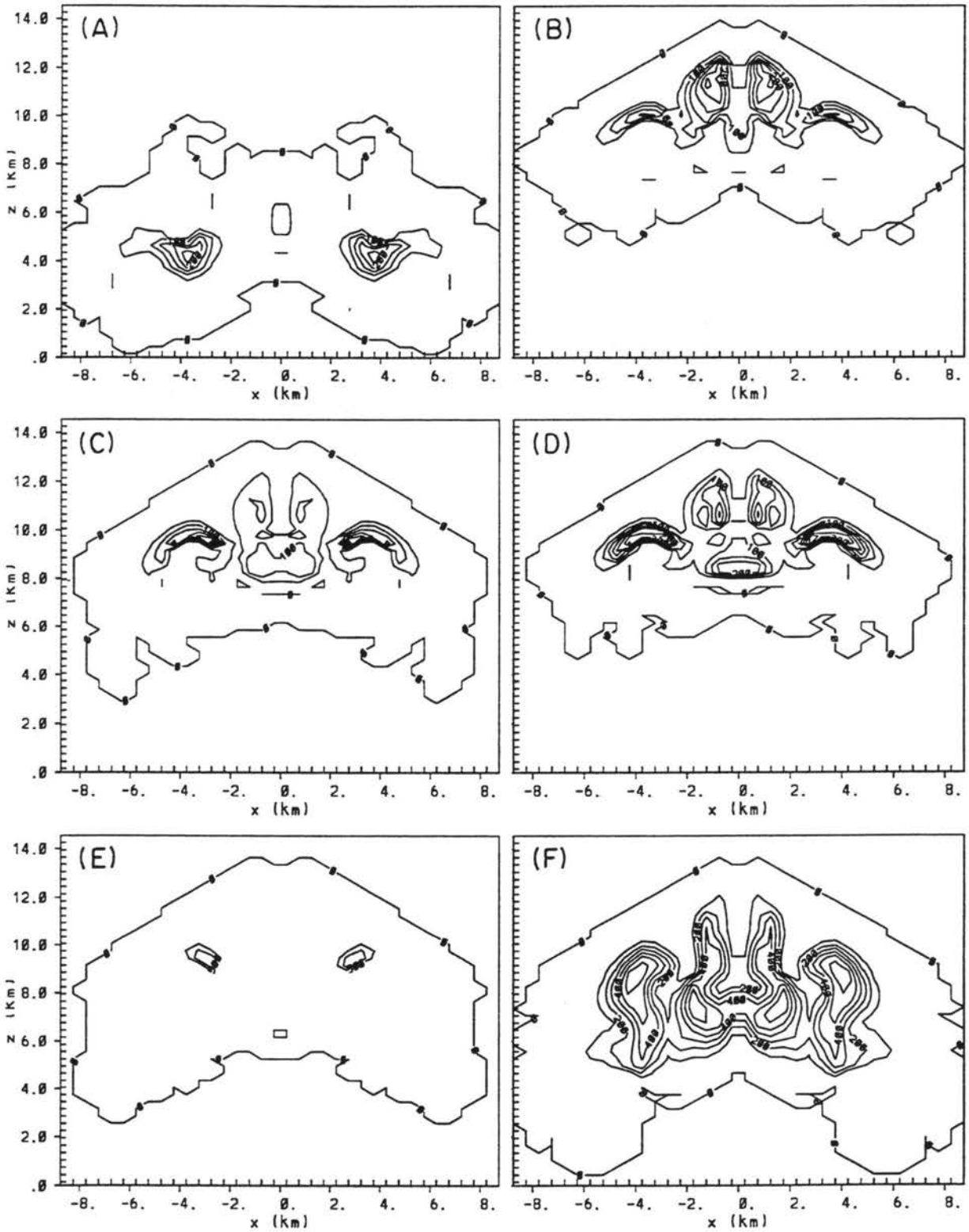

Figure 3.2: EXP1 microphysical fields at 15 minutes. Contour intervals and maxima are shown in brackets. Units are $[g\,kg^{-1}]$ for mixing ratios: (A) $r_r\,[0.5, 2.5]$, (B) $r_p\,[0.5, 3.0]$, (C) $r_s\,[0.05, 0.35]$, (D) $r_a\,[0.05, 0.4]$, (E) $r_g\,[0.05, 0.1]$, (F) $r_h\,[1.0, 6.0]$.

(peak values of 2 l^{-1}). This location is not colocated with maxima found in the rain mixing ratio fields. These high values of rain concentration found in the updraft core are produced from autoconversion of cloud droplets. Most of the "large" raindrops in the updraft are quickly converted to hail as a result of hydrometeor collisions resulting in smaller raindrops (see Figure 3.4a). The ice categories show a structure similar to their mixing ratio fields with peak number concentrations located in the upper troposphere. The pristine ice number concentrations peak values are $0.9x10^4$ l^{-1} at temperatures colder than -40°C. These crystals are produced by homogeneous freezing of the entire cloud droplet and part of the haze population. This type of simple simulation may produce higher number concentrations due to weak ambient flow which minimizes the flux of the pristine ice crystals out of the region. Snow and aggregate concentrations in the anvil reach 500 and 100 l^{-1}, respectively, due to conversion of pristine ice crystals by vapor deposition and aggregation. Graupel and hail number concentrations peaked near 0.5 and 0.2 l^{-1}.

The 2-moment prediction scheme diagnoses the hydrometeor mean diameter, and these are shown in Fig. 3.4. These diameters are the mean diameters of the hydrometeor distribution in a bulk microphysical sense and should be understood in this context. The rain field shows diameters ranging from 0.3 mm to 1.5 mm, with the largest mean raindrop diameters found near 4 km AGL, 5 km on either side of the domain center. This is a prime location for long residence times for rain since it is just below a cloud droplet source region, and other ice categories do not exist here which negates the potential sink due to collection. Pristine ice crystals, snow, and aggregates exist primarily in the upper regions of the cloud. The sizes of these low density ice categories are especially small due to the small LWC found high in the cloud. These crystals do exist at lower altitudes, but they are quickly collected by rain and converted to hail in these regions. Most of the pristine ice crystals diameters are near 10 μm and the modal diameter of snow near 100 μm. The mean diameters of aggregates and graupel are a bit larger with peak sizes near 1.0 mm. The hail category exists over a broad range of sizes with large diameters found near the center of the grid. Maximum sizes of hail are nearly 2.5 mm. The mean diameter of hail is smaller than would be expected for "observable" hail but the hail category in RAMS also

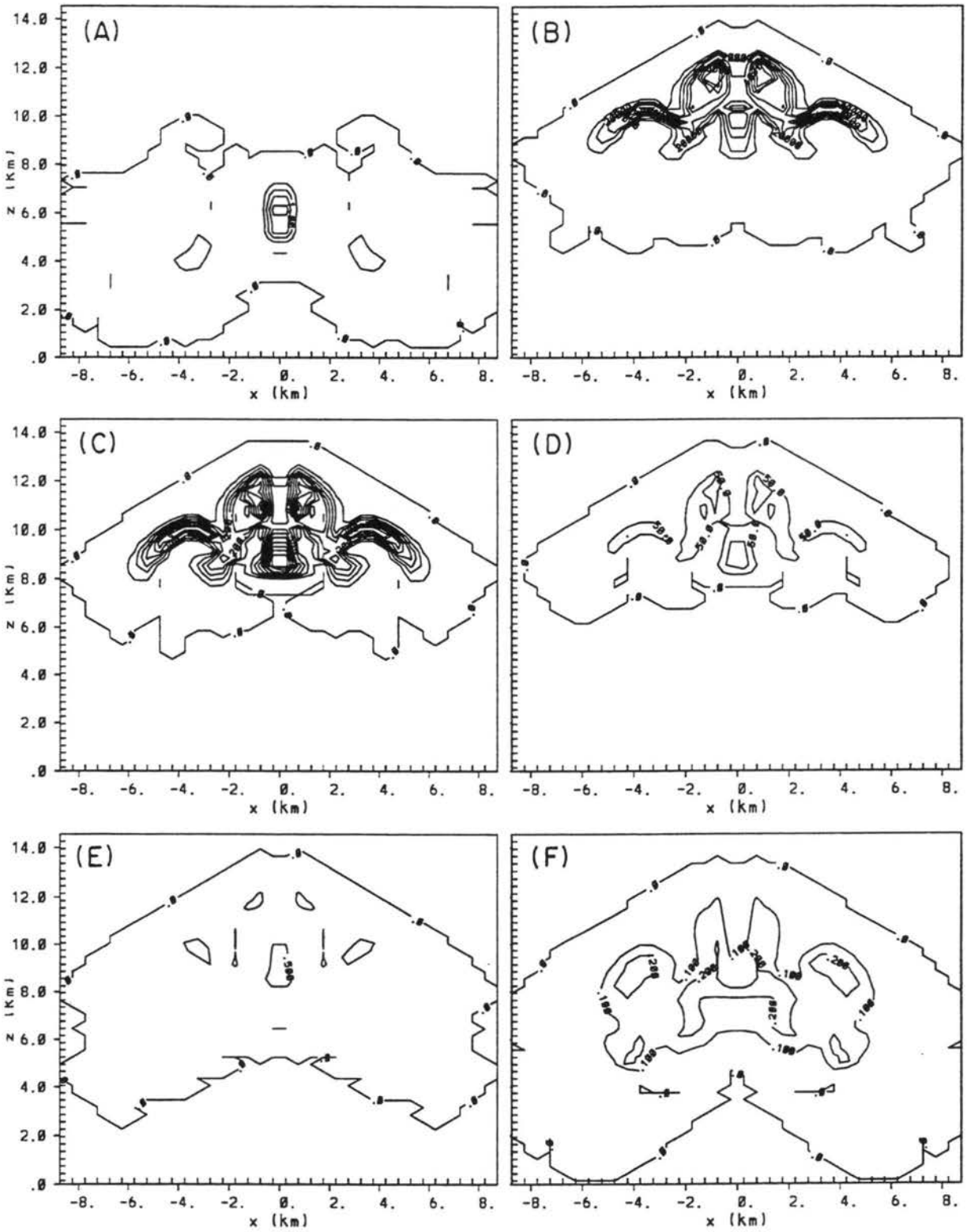

Figure 3.3: EXP1 microphysical fields at 15 minutes. Contour intervals and maxima are shown in brackets. Units are $[l^{-1}]$ for concentrations: (A) $n_r\,[0.5, 2.0]$, (B) $n_p\,[1\times10^4, 9\times10^4]$, (C) $n_s\,[50.0, 500.0]$, (D) $n_a\,[50.0, 100.0]$, (E) $n_g\,[0.5, 0.5]$, (F) $n_h\,[0.1, 0.2]$.

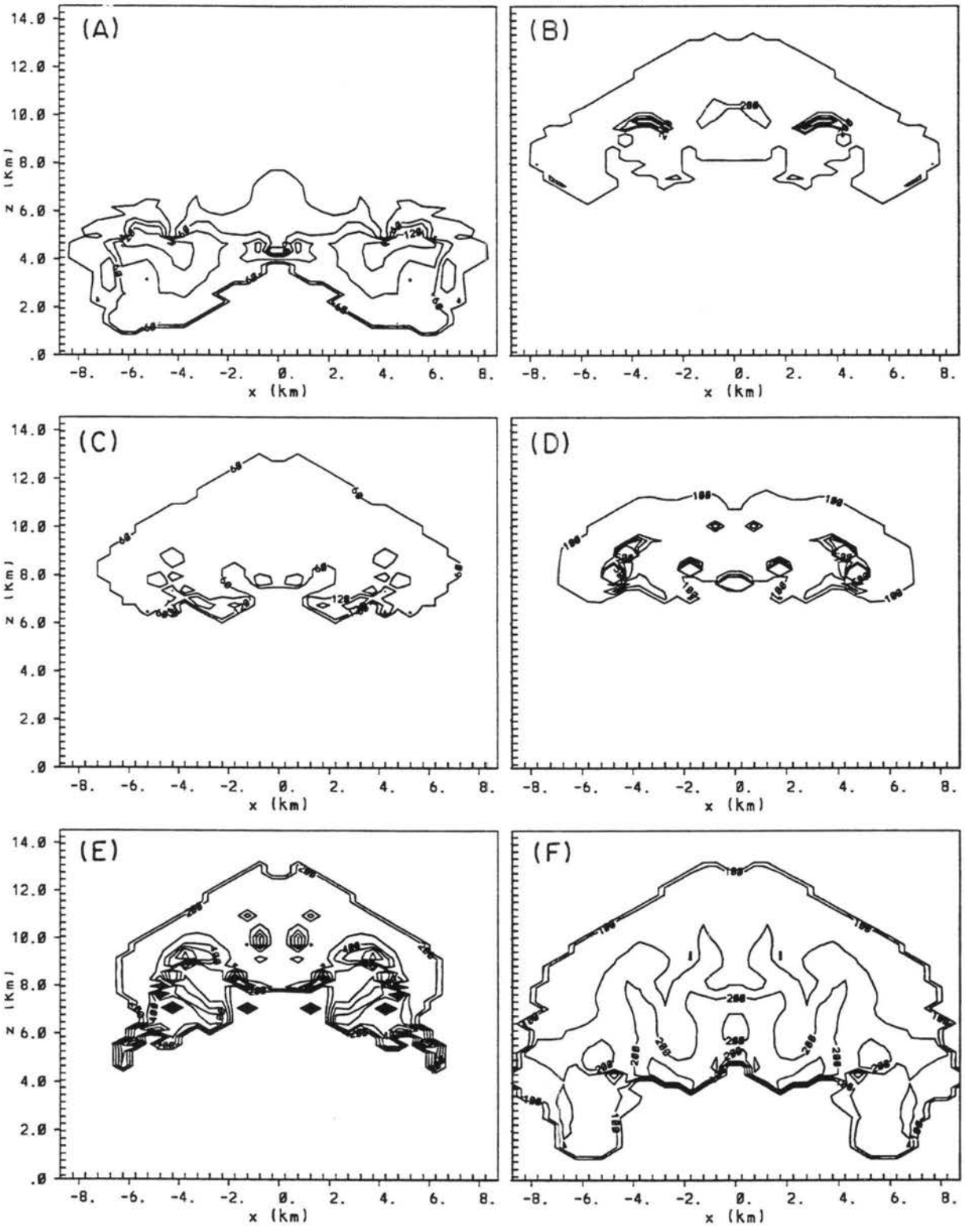

Figure 3.4: EXP1 microphysical fields at 15 minutes. Contour intervals and maxima are shown in brackets. Units are diameter in $[m]$: (A) $d_r\,[0.3 \times 10^{-3}, 0.15 \times 10^{-2}]$, (B) $d_p\,[0.1 \times 10^{-4}, 0.5 \times 10^{-4}]$, (C) $d_s\,[0.6 \times 10^{-4}, 0.18 \times 10^{-3}]$, (D) $d_a\,[0.2 \times 10^{-3}, 0.1 \times 10^{-2}]$, (E) $d_g\,[0.1 \times 10^{-3}, 0.8 \times 10^{-3}]$, (F) $d_h\,[0.5 \times 10^{-3}, 0.25 \times 10^{-2}]$.

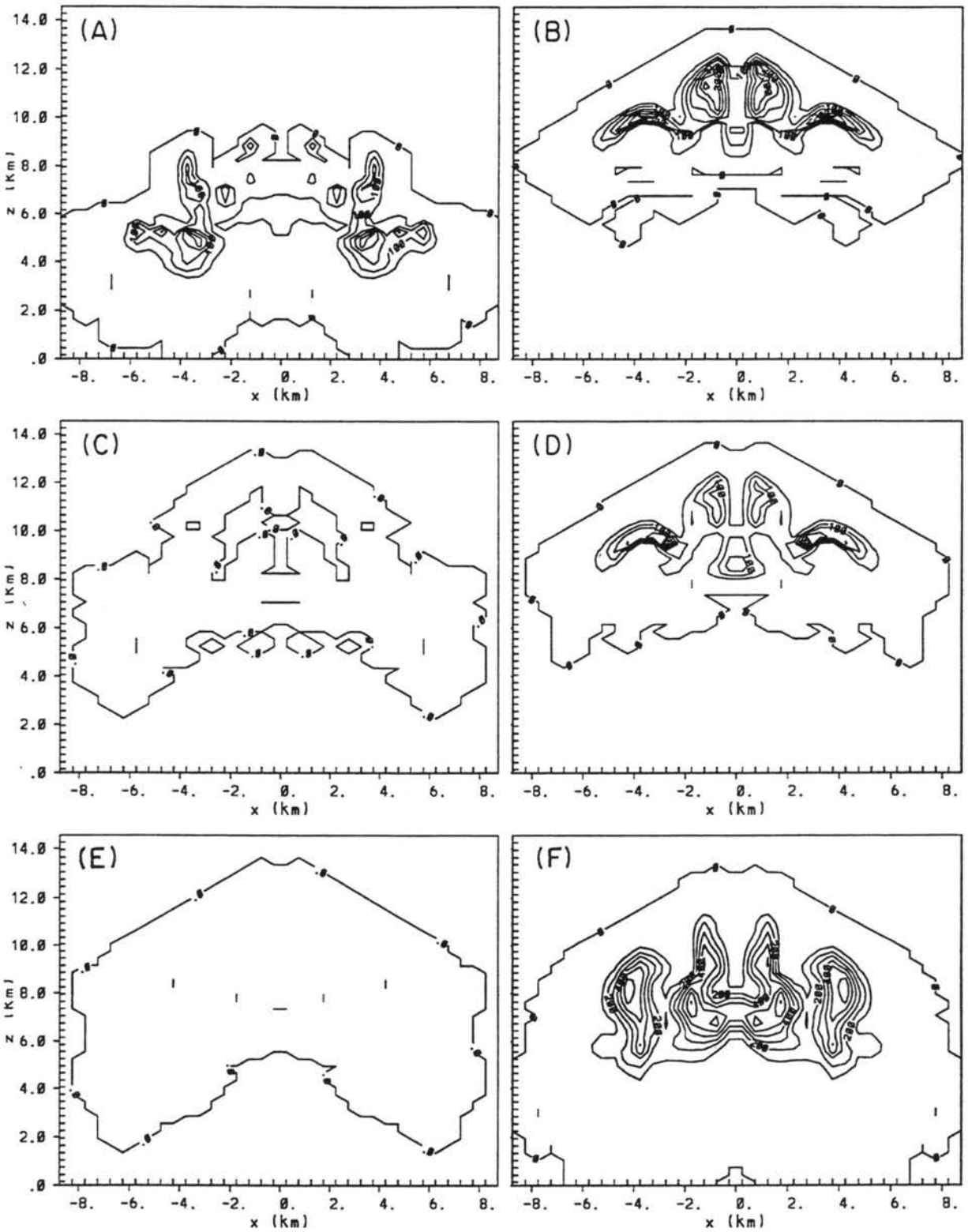

Figure 3.5: EXP2 microphysical fields at 15 minutes. Contour intervals and maxima are shown in brackets. Units are $[g\,kg^{-1}]$ for mixing ratios: (A) $r_r\,[0.5, 2.5]$, (B) $r_p\,[0.5, 3.5]$, (C) $r_s\,[0.05, 0.05]$, (D) $r_a\,[0.05, 0.35]$, (E) $r_g\,[0.05, 0.05]$, (F) $r_h\,[1.0, 7.0]$.

takes into account frozen drops, which will tend to push the distribution towards smaller sizes. Also, since a gamma distribution is assumed, hail diameters much greater than the mean diameter exist. One question raised in Chapter 2 was the importance of closing the physics with D_{nmin} and D_{nmax}. A check to determine the amount of time these limits were exceeded showed that it occurred less than 5% of the time which is very acceptable. The bounds were exceeded usually in tight gradient regions of the cloud where mixing ratios were low, and evaporation was taking place.

The mixing ratio fields from EXP2 are shown in Fig. 3.5. This experiment predicts on one moment of each hydrometeor category (except 2-moments for pristine ice crystals), the mixing ratio, and assumes a fixed mean diameter for each species. The mean particle mass has a diameter of 0.1 cm for rain, snow, and aggregates, 0.3 cm for graupel, and 0.5 for hail. The rain mixing ratio category (Fig. 3.5a) exhibits a more widespread structure from the EXP1, with rain mixing ratio values greater than 1.0 g kg^{-1} extending up to 8 km AGL. The low density ice categories show pristine ice mixing ratios nearly a 1.0 g kg^{-1} greater than EXP1 run, but this surplus results at the expense of snow, aggregate and graupel categories which are much less than found in EXP1. With the constraint of specifying the mean diameter of the hydrometeor category, the one-moment scheme effectively limits the amount of snow, aggregates and graupel. The prescribed diameters of these categories are relatively large, which decreases the residence time in regions in the presence of liquid water due to enhanced collection efficiencies and conversion to hail. As a consequence, rain extends to higher altitudes in this simulation than EXP1 due to the lack of ice hydrometeors at the 5-8 km AGL level. Hail mixing ratios are relatively unchanged from EXP1.

EXP3 is the same as the EXP1 except that N_t of the cloud droplets is decreased to 60 cm^{-3} in an attempt to simulate clean maritime conditions. This effectively increases the auto-conversion of cloud water to rain as compared to the EXP1. This is evident by Fig. 3.6a which shows a decrease of 4 g kg^{-1} in the cloud water mixing ratio field (peak values near 1 g kg^{-1}). As evidenced by the mixing ratio fields (Fig. 3.7), significantly more rain mass is produced in the center of the domain by autoconversion of cloud droplets to

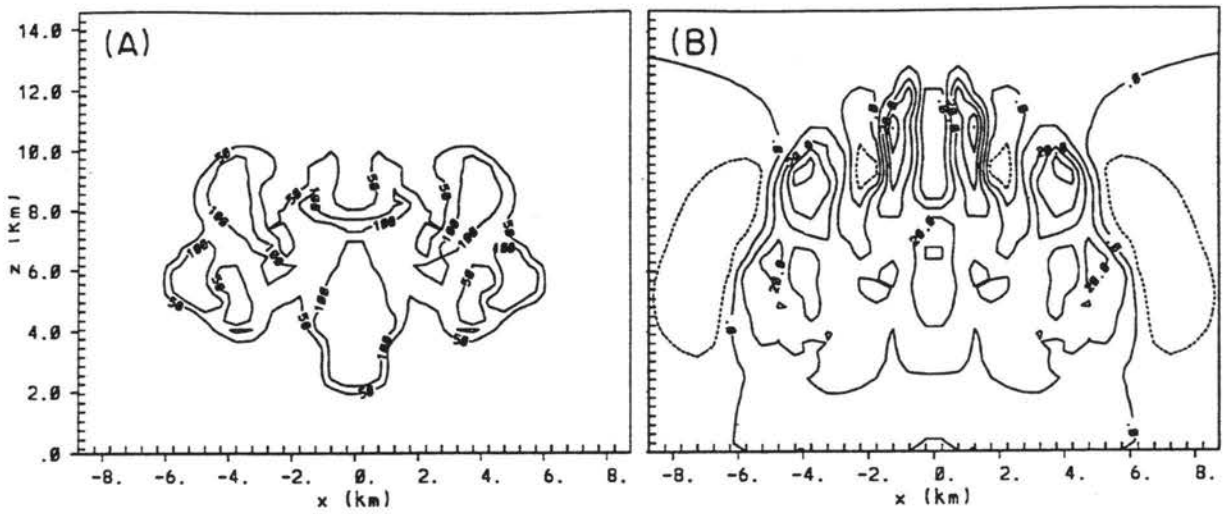

Figure 3.6: EXP3 simulated fields at 15 minutes. Contour intervals and maxima are shown in brackets: (A) $r_c\,[0.5gkg^{-1}, 1.0gkg^{-1}]$, (B) $w\,[10.0ms^{-1}, 50ms^{-1}]$.

rain (peak value 5 g kg^{-1}) in a location where relatively low amounts were found in EXP1. Significantly less low density ice mass is found at higher altitudes in the storm due to the greater amounts of rain mass being produced lower in the domain. Peak pristine ice crystal mixing ratios are 1.5 g kg^{-1}; nearly half that produced in EXP1. Snow, aggregate, and graupel mass display only negligible amounts. Hail, on the other hand, is produced more efficiently with the increased collection kernel of rain. Peak values of hail mixing ratio are nearly 9 g kg^{-1}. The number concentrations for the hydrometeors (Fig. 3.8) show much higher values for rain and hail (7 l^{-1} and 4.5 l^{-1}, respectively) and much lower values for snow, aggregates, and graupel as compared to the control run.

EXP4 is identical to the EXP1 except that N_t of the cloud droplet is increased to 1500 cm^{-3}, consistent with very polluted continental air. Fig. 3.9a shows the cloud water mixing ratio field reaching 8 g kg^{-3}, nearly 3 g kg^{-3} greater than the EXP1. Fig. 3.10 shows the mixing ratio fields for EXP4. Since the cloud droplet concentrations are increased, the droplet diameter is reduced, resulting in a shut-down of warm rain processes, as evidenced by negligible rain mixing ratios. Later in the simulation, more significant rain mass is produced by the melting of the ice categories. All the low density categories, however, have increased dramatically. Pristine ice mass is up to 7.0 g kg^{-1} with snow and graupel increasing 300% (peak values 1.0 g kg^{-3} and 3.9 g kg^{-3} respectively). With negligible

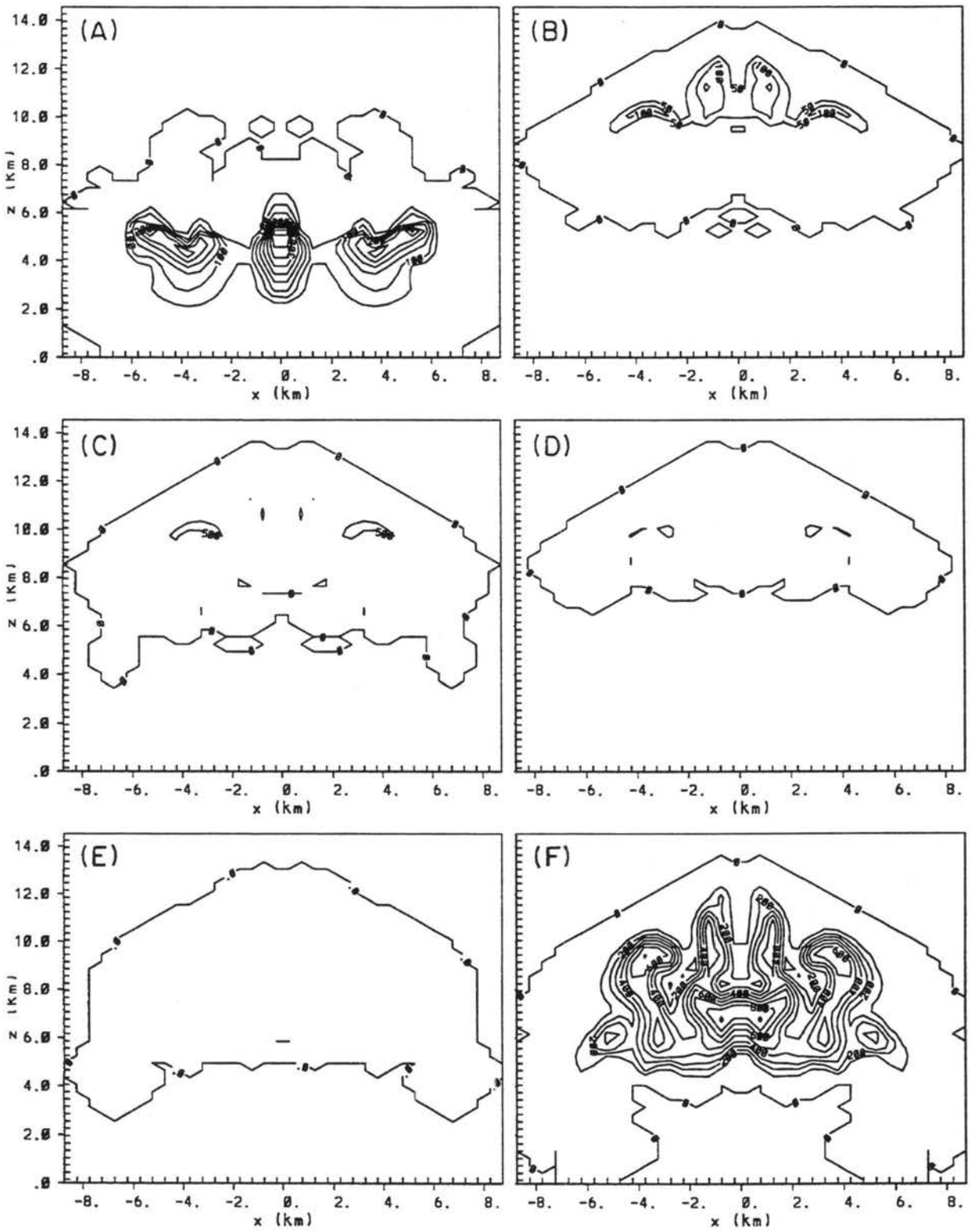

Figure 3.7: EXP3 microphysical fields at 15 minutes. Contour intervals and maxima are shown in brackets. Units are $[g\,kg^{-1}]$ for mixing ratios: (A) $r_r\,[0.5, 4.5]$, (B) $r_p\,[0.5, 1.5]$, (C) $r_s\,[0.05, 0.05]$, (D) $r_a\,[0.05, 0.05]$, (E) $r_g\,[0.05, < 0.05]$, (F) $r_h\,[1.0, 9.0]$.

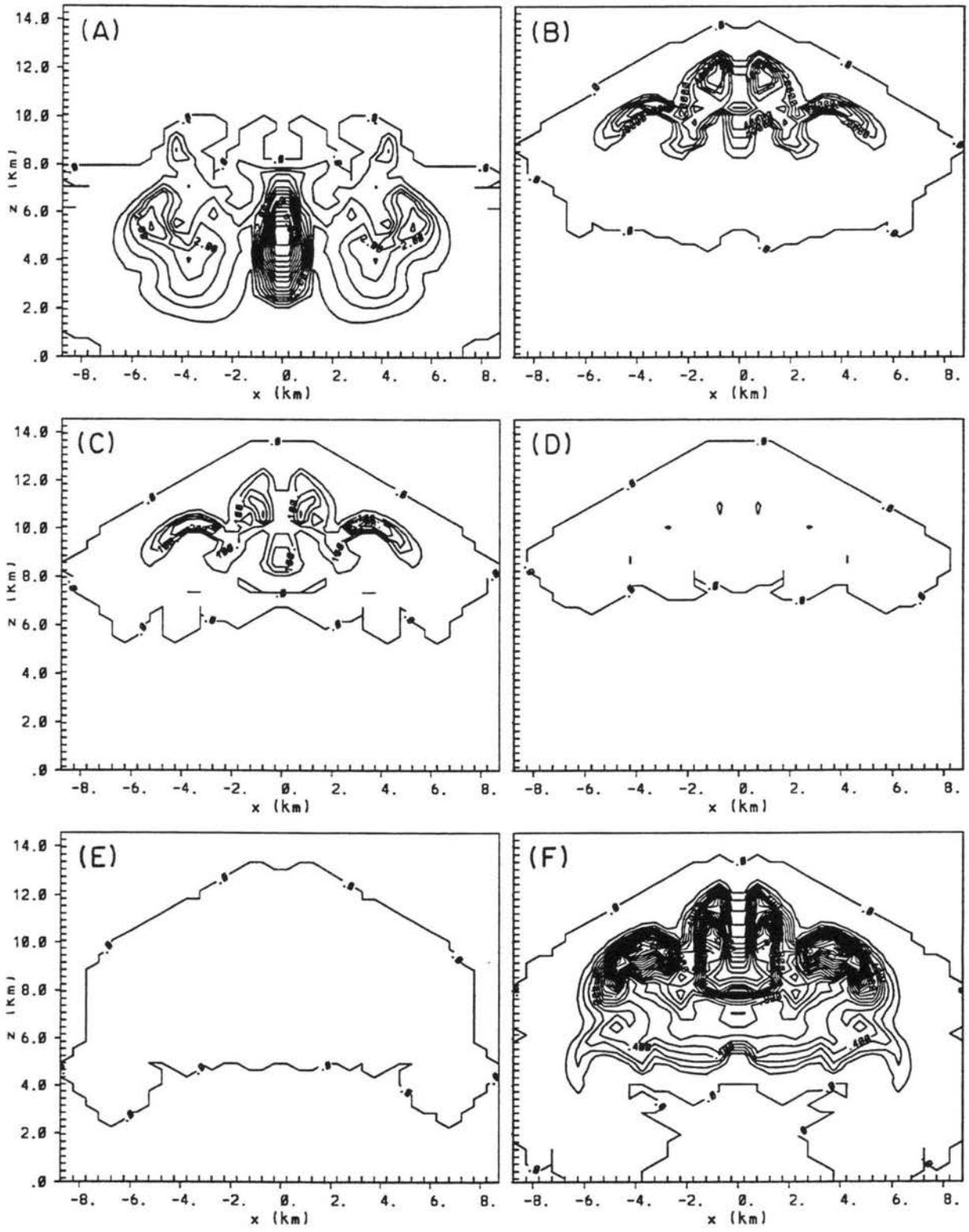

Figure 3.8: EXP3 microphysical fields at 15 minutes. Contour intervals and maxima are shown in brackets. Units are $[l^{-1}]$ for concentrations: (A) n_r [0.5, 7.5], (B) n_p [1×10^4, 9×10^4], (C) n_s [50.0, 300.0], (D) n_a [50.0, 50.0], (E) n_g [0.5, 0.05], (F) n_h [0.1, 2.3].

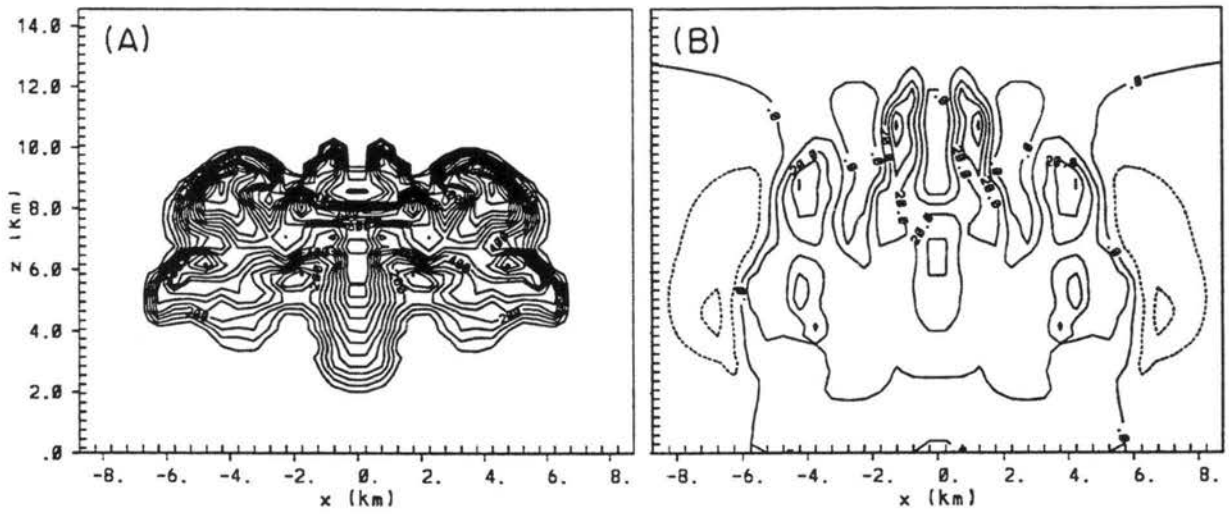

Figure 3.9: EXP4 simulated fields at 15 minutes. Contour intervals shown in brackets: (A) $r_c[0.5gkg^{-1}, 8.5gkg^{-1}]$, (B) $w[10.0ms^{-1}, 50.0ms^{-1}]$.

rain mixing ratios, conversion processes to hail are severely limited, resulting in peak hail mixing ratio values of 2.0 g kg^{-3}. The primary source for hail in this simulation is due to riming of graupel. The number concentrations for EXP4 are shown in Fig. 3.10. In addition to the concentrations of the low density categories increasing similarly to the mixing ratio field, the other highlight of this experiment is the increased concentrations of the hail category as compared to the EXP1. Most of this increase in the hail number concentration is due to collection of cloud water by the graupel particles and conversion to hail which results in smaller hail diameters than in EXP1.

EXP5 is identical to EXP1 except that $\nu = 3$ for each hydrometeor. The cloud water mixing ratio (not shown) is much less than EXP1 with peak values near 0.5 g kg^{-1}. Rain mixing ratios (Fig. 3.12) are dramatically higher with peak values near 7 g kg^{-1} and the rain structure shows highest values near the center of the grid where only low rain mixing ratios were found in EXP1. The increased rain mixing ratios are due to the increase in ν which increased the mean diameter of cloud water. This, in turn, sharply increases the autoconversion to rain. With so much rain mass occupying the lower troposphere, much less low density ice mass is produced higher in the cloud. Most of the low density crystals are quickly collected by rain and converted to hail. Hail mass, as a result, is nearly 3.0 g kg^{-1} greater than EXP1. Many more raindrops are produced in EXP5 with peak

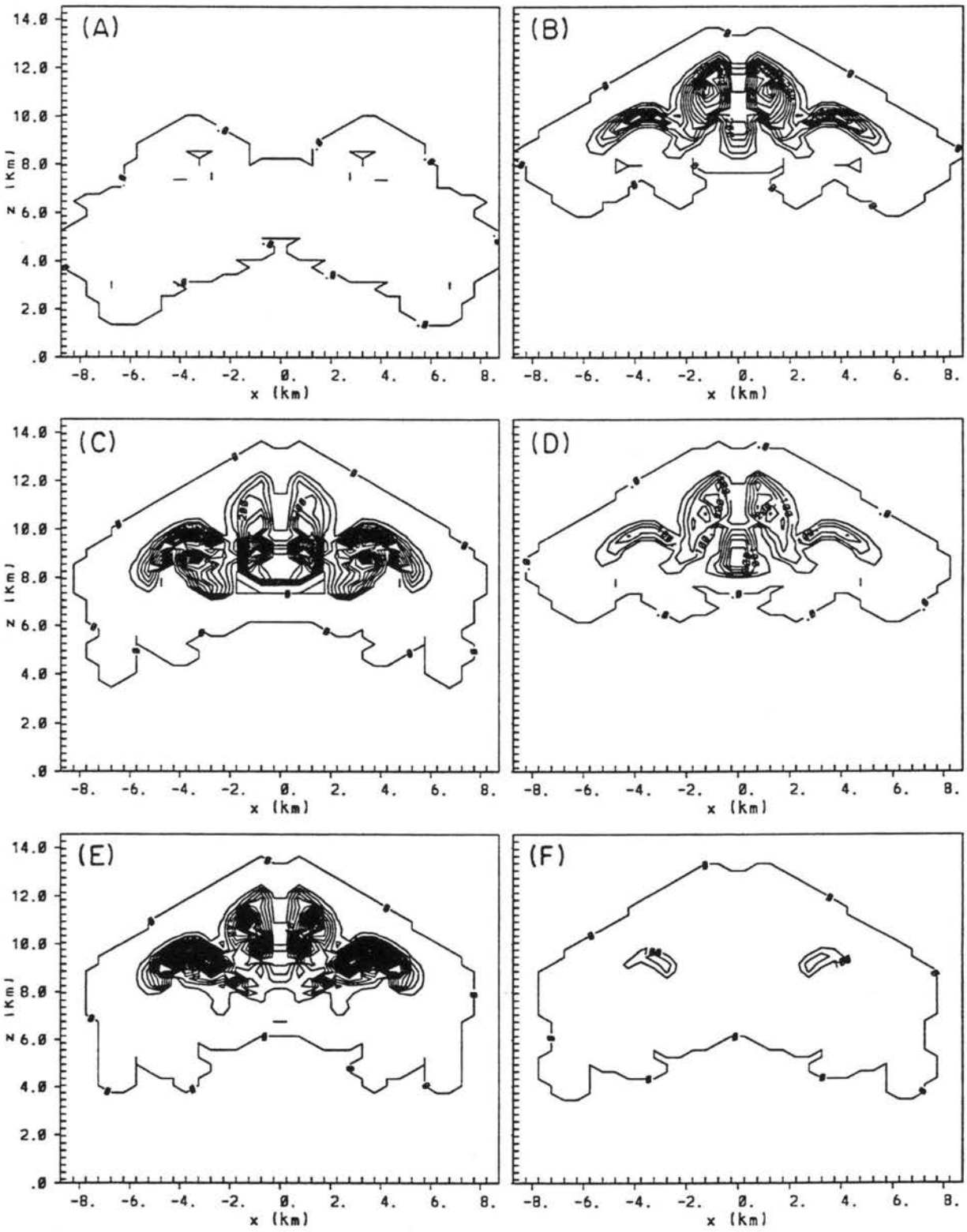

Figure 3.10: EXP4 microphysical fields at 15 minutes. Contour intervals and maxima are shown in brackets. Units are $[g\,kg^{-1}]$ for mixing ratios: (A) $r_r\,[0.5, < 0.5]$, (B) $r_p\,[0.5, 7.0]$, (C) $r_s\,[0.05, 1.0]$, (D) $r_a\,[0.1, 2.2]$,(E) $r_g\,[0.1, 3.9]$, (F) $r_h\,[1.0, 2.0]$. Note the different contour intervals for r_a and r_g from previous figures.

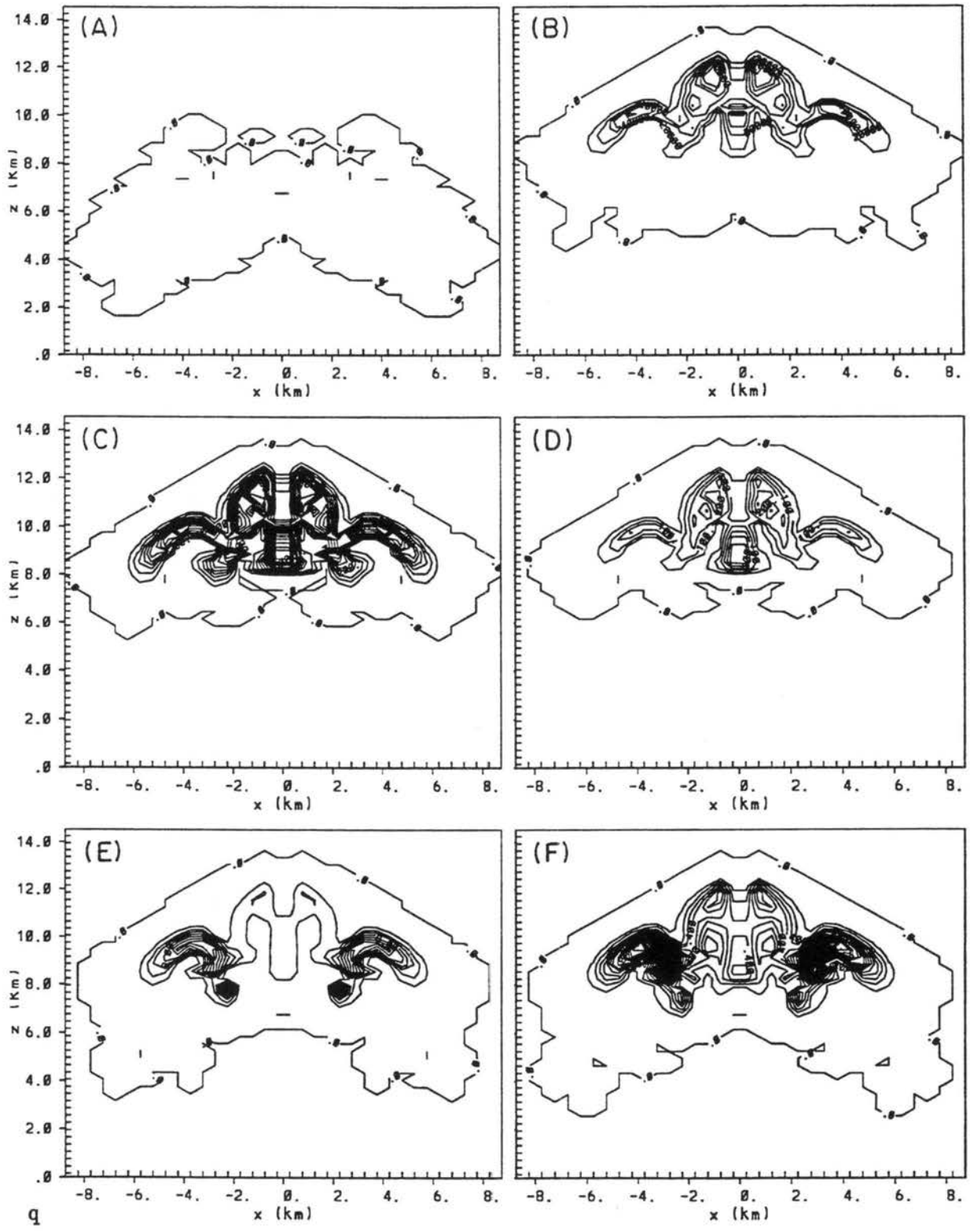

Figure 3.11: EXP4 microphysical fields at 15 minutes. Contour intervals and maxima are shown in brackets. Units are $[l^{-1}]$ for concentrations: (A) $n_r\,[0.5, 0.0]$, (B) $n_p\,[1 \times 10^4, 9 \times 10^4]$, (C) $n_s\,[50.0, 900.0]$, (D) $n_a\,[50.0, 300.0]$, (E) $n_g\,[2.0, 24.0]$, (F) $n_h\,[0.1, 3.1]$. Note the different contour intervals for n_g from previous figures.

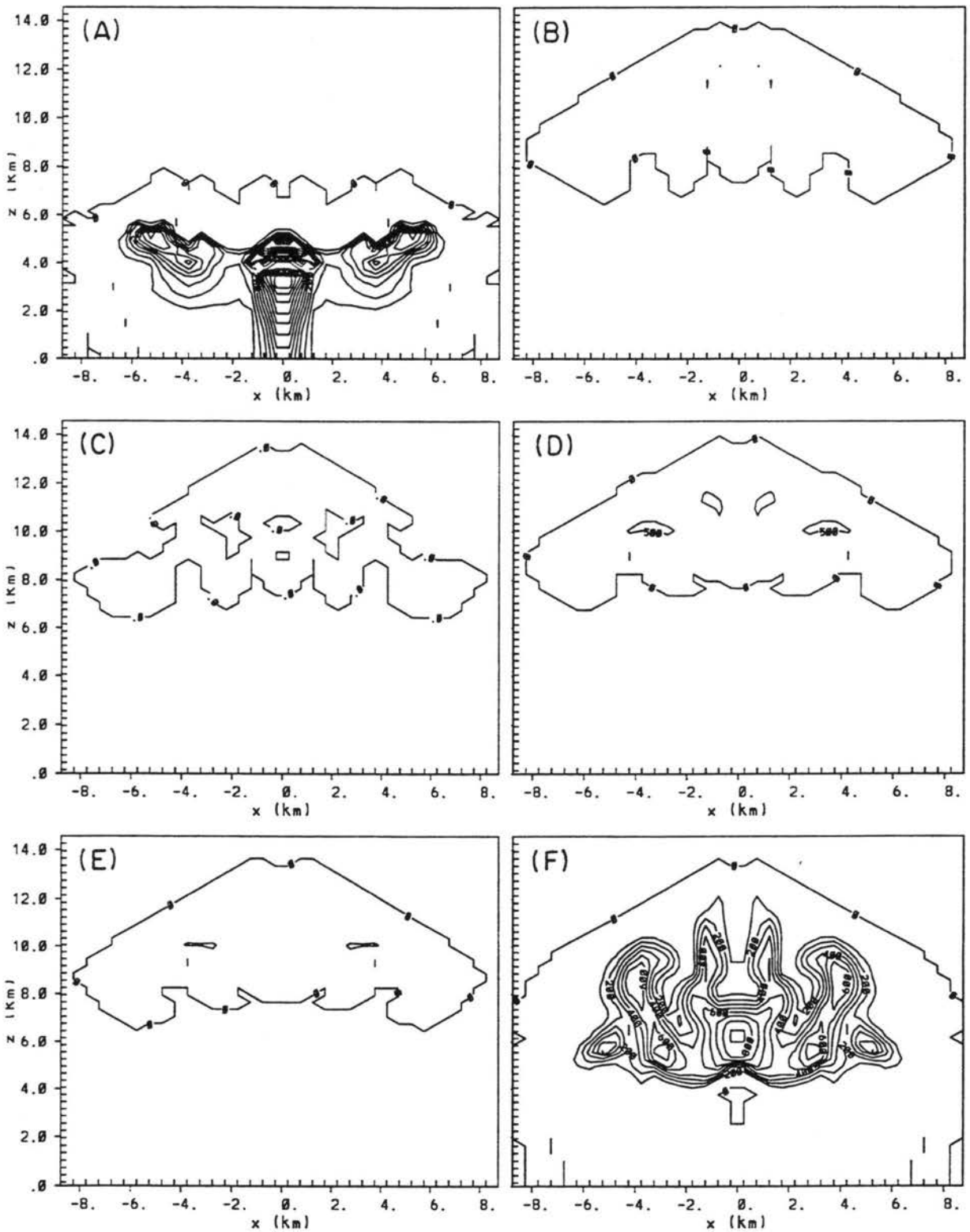

Figure 3.12: EXP5 microphysical fields at 15 minutes. Contour intervals and maxima are shown in brackets. Units are $[g\,kg^{-1}]$ for mixing ratios: (A) $r_r\,[0.5, 6.0]$, (B) $r_p\,[0.5, 0.5]$, (C) $r_s\,[0.05, 0.0]$, (D) $r_a\,[0.05, 0.05]$, (E) $r_g\,[0.05, 0.05]$, (F) $r_h\,[1.0, 9.0]$.

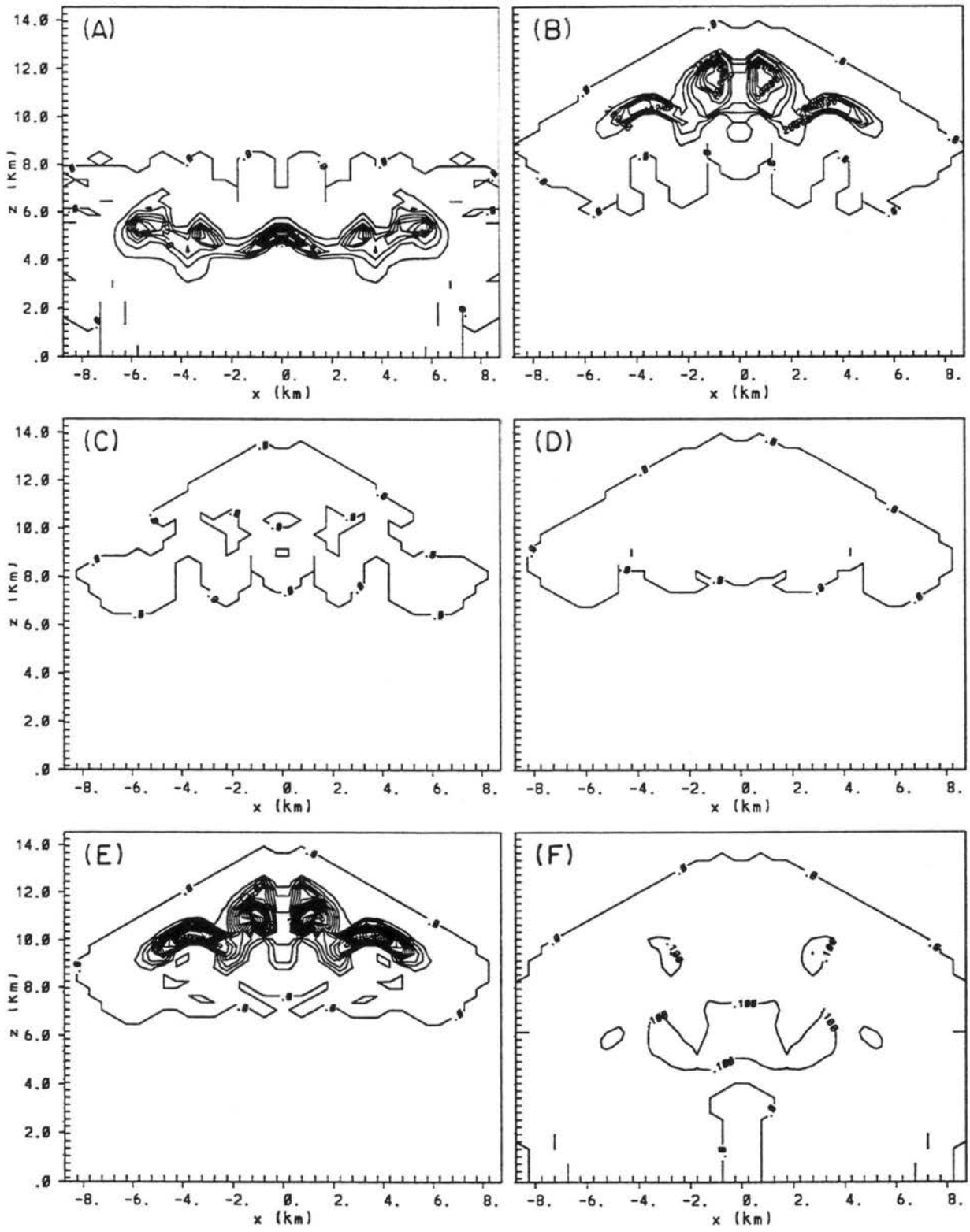

Figure 3.13: EXP5 microphysical fields at 15 minutes. Contour intervals and maxima are shown in brackets. Units are $[l^{-1}]$ for concentrations: (A) $n_r\,[3.0, 30.0]$, (B) $n_p\,[1 \times 10^4, 9 \times 10^4]$, (C) $n_s\,[50.0, 0.0]$, (D) $n_a\,[50.0, 0.0]$, (E) $n_g\,[3.0, 72.0]$, (F) $n_h\,[0.1, 0.2]$. Note the different contour invervals for n_r and n_g from previous figures.

values nearly 30 l^{-1}. Pristine ice crystals concentrations are nearly the same as the EXP1, however, snow and aggregate number concentrations are neglible. Graupel concentrations are much higher than in the EXP1, with peak values 72 l^{-1}. Hail concentrations are smaller than the EXP1 with peak values near 0.2 l^{-1}.

EXP6 shows a profound sensitivity to variable habit diagnosis in the model as described in Section 2.6.2 . Fig. 3.14 shows the mixing ratio fields for EXP6. Much less pristine ice mass compared to the EXP1 exists in the upper cloud levels where the habits of the crystals are dominated by rosettes and needles. Another dramatic difference between the two runs is the increase in the graupel category. Graupel mass peaks at 1.8 g kg^{-1} which is much greater than in EXP1. The reason for this increase is due to the dependence of the riming conversion process on habit. The habit of the crystal in EXP1 was a hexagonal plate which does not convert to graupel as easily as the columns and needles that prevail in this sensitivity experiment. The number concentrations for each of these categories are dramatically different than EXP1. Pristine ice crystals are nearly half that found in the EXP1, however, the number concentrations of snow, aggregates and graupel are significantly increased (2100 l^{-1}, 400 l^{-1}, and 950 l^{-1} respectively). Hail is much higher with peak values near 1.4 l^{-1}.

EXP7 which utilizes the vertical dependent variable habit diagnosis as described in Section 2.6.2 shows only slight differences to EXP6. Slight increases in the number concentrations of pristine ice crystals and snow are found in EXP7. Slight decreases are found in the graupel concentrations as compared to EXP6. The overall mass fields are unaffected.

3.3 Discussion

These experiments show the sensitivity of the model to the user specified input parameters for an idealized cumulus cloud initialized with a hot bubble. A summary of the maximum mixing ratios and concentrations from the sensitivity tests are shown in Table 3.2 and 3.3. First, the tables highlight the high sensitivity of the model to the number of moments which are predicted. The overall maximum mixing ratio field shows more mass going into hail at the expense of the snow, aggregates, and graupel categories. This result

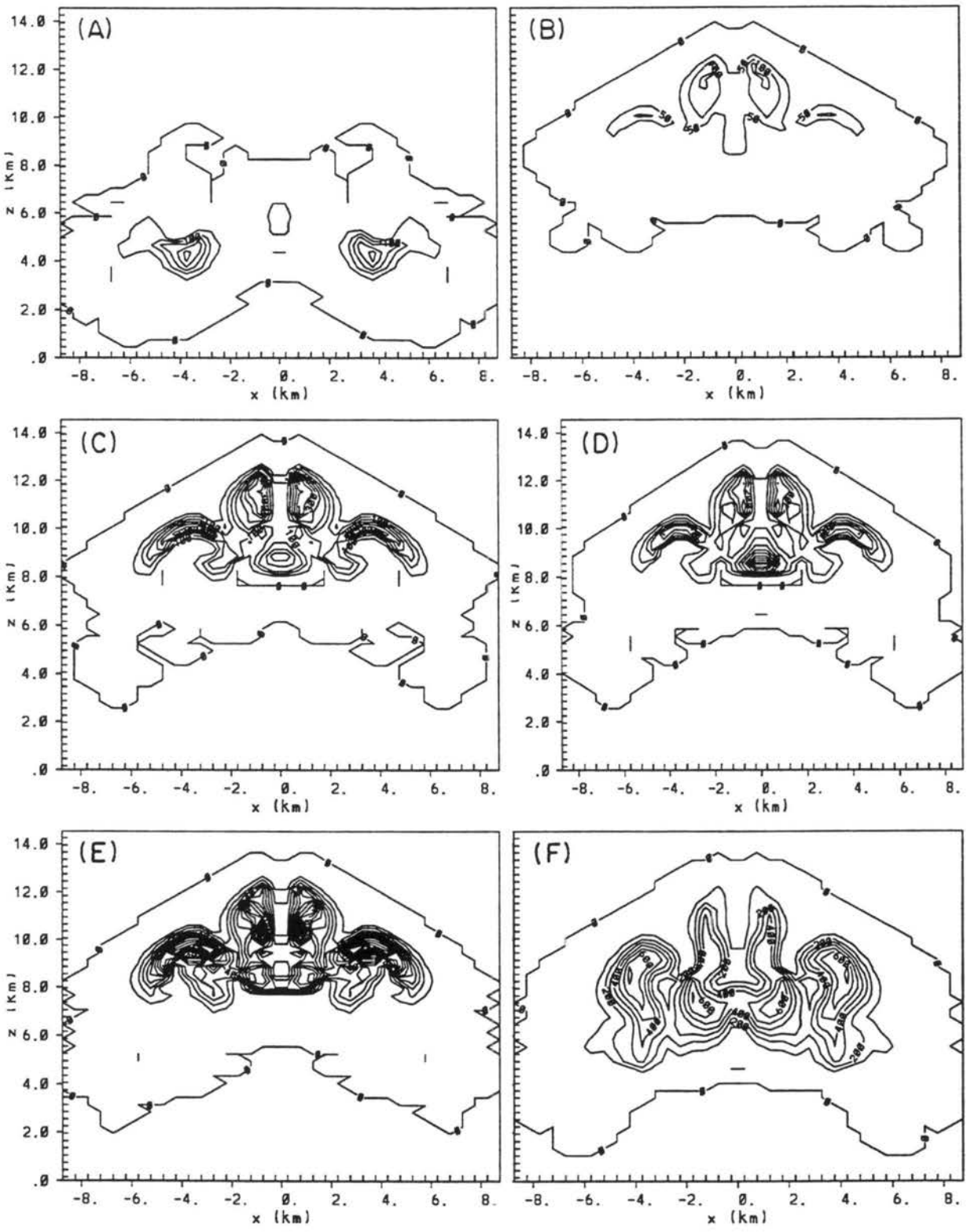

Figure 3.14: EXP6 microphysical fields at 15 minutes. Contour intervals and maxima are shown in brackets. Units are $[g\,kg^{-1}]$ for mixing ratios: (A) $r_r\,[0.5, 2.5]$, (B) $r_p\,[0.5, 1.5]$, (C) $r_s\,[0.05, 0.4]$, (D) $r_a\,[0.05, 0.5]$, (E) $r_g\,[0.1, 1.8]$, (F) $r_h\,[1.0, 7.0]$.

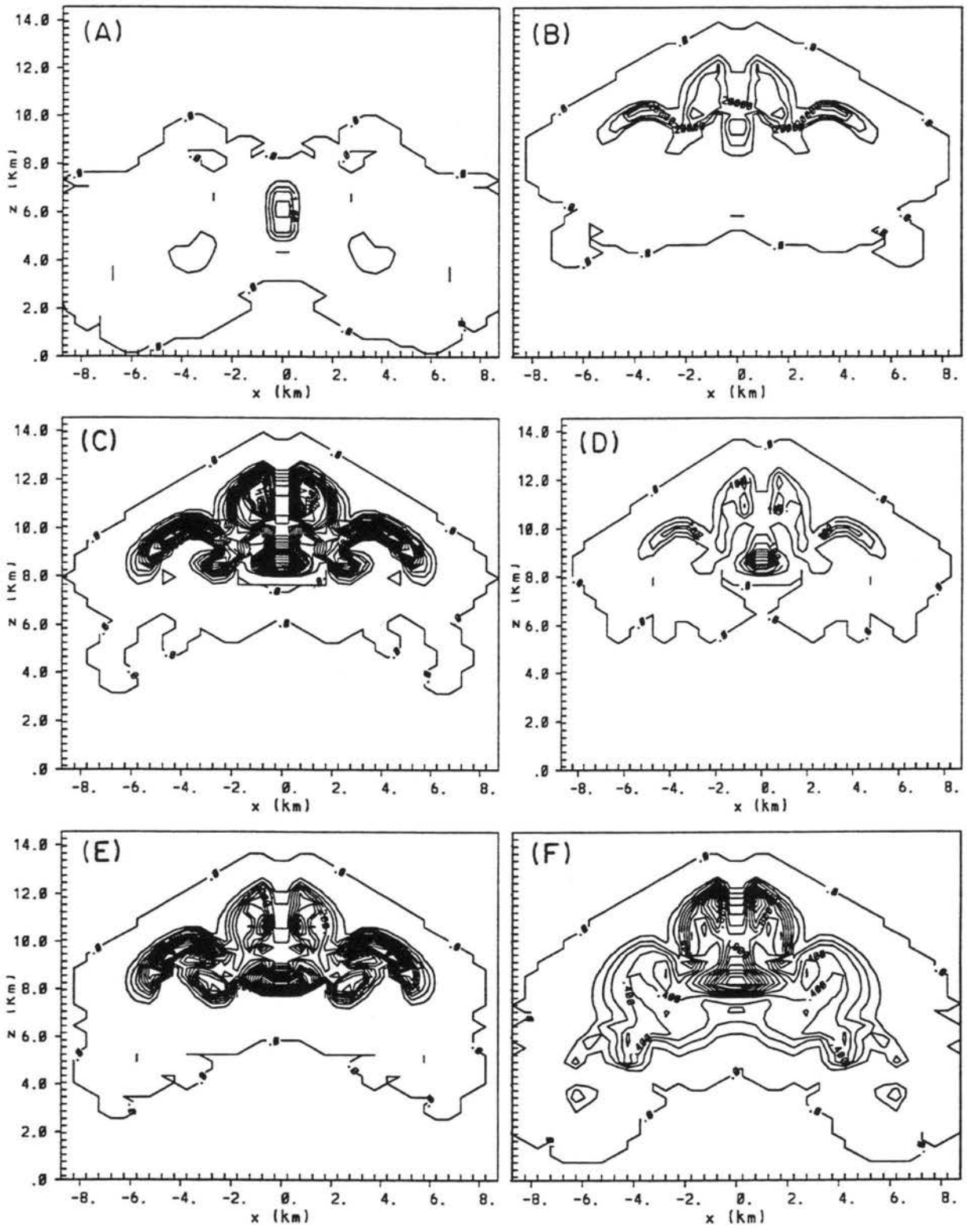

Figure 3.15: EXP6 microphysical fields at 15 minutes. Contour intervals shown in brackets. Units are $[l^{-1}]$ for concentrations: (A) $n_r\,[0.5, 2.0]$, (B) $n_p\,[1 \times 10^4, 4 \times 10^4]$, (C) $n_s\,[100, 2100]$, (D) $n_a\,[50.0, 400.0]$, (E) $n_g\,[50.0, 950.0]$, (F) $n_h\,[0.1, 1.4]$. Note the different contour invervals for n_s and n_g from previous figures.

Table 3.2: Maximum mixing ratios (g kg^{-1})

Experiment	r_c	r_r	r_p	r_s	r_a	r_g	r_h
EXP1	5.0	2.5	3.0	0.35	0.4	0.1	6.0
EXP2	5.0	2.5	3.5	0.05	0.35	0.05	7.0
EXP3	1.0	4.5	1.5	0.05	0.05	0.05	9.0
EXP4	8.5	0.0	7.0	1.0	2.2	3.9	2.0
EXP5	0.5	6.0	0.5	0.0	0.05	0.05	9.0
EXP6	5.0	2.5	1.5	0.4	0.5	1.8	7.0
EXP7	5.0	2.5	1.5	0.4	0.5	1.5	7.0

is a consequence of the smaller diagnosed diameters in the 2 moment predictive scheme (Fig. 3.4). Another striking feature is the spatial variability of the structure of the mean diameter field across the domain. The diameters are fixed in the one moment scheme. Therefore the diameter cannot be adjusted by the varying microphysical conditions which can potentially modify the diameter structure. The greatest difference between EXP1 and EXP2 is in the precipitation distribution (Fig. 3.16). Coincident with the relatively larger diameters in EXP2, precipitation amounts are nearly four times higher in EXP2 than found in EXP1. Nearly 70% of this precipitation falls in the form of hail (note that hail may be a mixed phased hydrometeor). The smaller hydrometeor diameters produced in EXP1 result in cloud precipitation processes which are less efficient, and more hydrometeor mass is injected into the upper regions of the cloud. The diameters and the resultant terminal velocities in EXP2 are fixed to very high values which enhances precipitation collection and fallout.

Table 3.3: Maximum concentrations (l^{-1})

Experiment	n_r	n_p	n_s	n_a	n_g	n_h
EXP1	2.0	9×10^4	500	100	0.5	0.2
EXP3	7.5	9×10^4	300	50	0.05	2.3
EXP4	0.0	9×10^4	900	300	24	3.1
EXP5	30.0	9×10^4	0.0	0.0	72.0	0.2
EXP6	2.0	4×10^4	2100	400	950	1.4
EXP7	2.0	6×10^4	2300	400	850	1.5

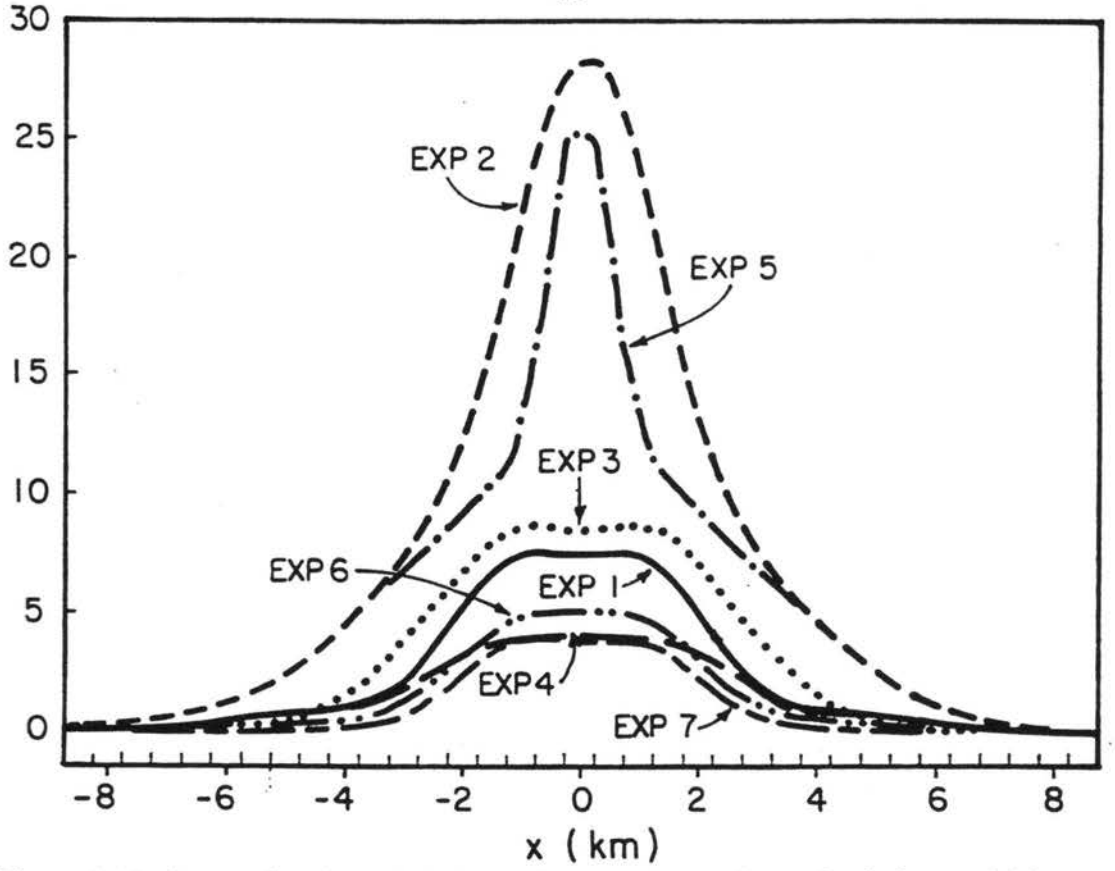

Figure 3.16: Accumulated precipitation after 30 minutes for each of the sensitivity runs. Units are in mm.

The set of experiments which modified the cloud droplet number concentrations (EXP3 and EXP4) had a large influence on the resultant microphysical fields. These tests, which basically investigated the sensitivity of warm rain processes, showed how important the auto-conversion of cloud droplets to rain was to the initiation of hydrometeor development in the middle troposphere in these environmental conditions. In EXP3, where the cloud droplet concentration was set to 60 cm^{-3}, the rain field was nearly doubled compared to EXP1. Consequently, hydrometeor collection of the smaller ice categories dramatically increased. This feedback resulted in much more hail mass being produced due to collection of the lower density ice crystals by rain in EXP3, decreasing low density ice mass amounts in the anvil region of the cloud. Interestingly, however, precipitation amounts increased only slightly in EXP3 over EXP1 (Fig. 3.16). This slight increase was due to the smaller hydrometeor diameters found EXP3. Even though much more hail mass was produced by collection, the interacting hydrometeors were relatively small snow, aggregate, and graupel particles. These collections resulted in a smaller collected hail category as compared to

EXP1. With smaller sizes, precipitation efficiencies were decreased, but since more mass was converted over to hail in EXP3, more precipitation was produced. Warm rain processes were effectively eliminated, with the cloud droplet concentration set to 1500 cm^{-3}. Therefore, much more cloud water remained and was made available for the low density ice categories, with most of the mass being injected into the anvil. Hail mixing ratios were nearly one-third of EXP1. Precipitation effeciencies were drastically reduced and the total precipitation produced in this experiment was the lowest.

One problem with the ν parameter is that there are not many observationals of hydrometeor size distibutions. Also, the exponential assumption, which is used widely by modelers, may not be correct in many situations. These experiments show that the microphysical structure is very sensitive to different ν. First, warm rain processes are more efficient with a higher specified ν of cloud droplets since the mean diameter of cloud droplets is increased by nearly 40% (W94) which enhances the autoconversion of cloud droplets to rain. The increased collection kernel of rain collects much more snow, aggregate, and graupel mass (with a ν of 3 for all variables the collection kernel of these categories are also increased), and this collection results in more hail mass produced lower in the cloud. With an increased collection kernel of snow, aggregates and cloud droplets, and in the absence of rain, more conversion to graupel occurs higher in the cloud resulting in much higher graupel concentrations near 10 km AGL. Increasing ν also has a profound impact on the precipitation processes of the simulated cloud (Fig. 3.16). In EXP5, precipitation is more than three times greater than in EXP1, due to the increased diameters of the hydrometeors. However, less than 10% of the precipitation falls in the form of hail, as opposed to EXP2 where nearly 70% of the precipitation is in the form of hail. Rain precipitation dominates the total precipitation in EXP5 since much more rain is produced at lower altitudes and these droplets are larger in size.

The final sensitivity tests investigated the role of diagnosing the crystal habit on the microphysical structure of the cloud. As opposed to EXP1, EXP6 allows for variable habit diagnosis. The greatest impact of habit diagnosis in this convective environment is seen in the upper cloud region. The pristine ice crystals growth rates for needles, columns and

rosettes are much greater than for hexagonal plates, and therefore more mass and number is converted to the snow categories in EXP6. EXP6 shows pristine ice crystal mixing ratios and number concentrations are nearly half those found in EXP1 due to conversion to the snow category. With more snow and aggregates available, more conversion to graupel due to riming is facilitated by the columnar crystals in this region. Therefore, graupel masses and number concentrations are much greater in EXP6 than Experiment 1. The sensitivity of changing the habit diagnosis based on a vertical dependence (EXP7) shows little change from EXP6. Precipitation amounts for EXP6 and 7 are slightly less than EXP1 (Fig. 3.16), possible due to more mass being partitioned to the anvil.

In summary, two-moment prediction allows more freedom on the size distribution by predicting on both mixing ratio and concentration of each hydrometeor and allowing the mean diameter to evolve more realistically than in a 1-moment scheme. Modelers, however, need to recognize the potential sensitivity of some of these input parameters on the evolution of cloud processes in a simulated storm. Parameters such as cloud droplet concentrations are usually measured during field programs and have a good climatological database. These values should be understood for a given case environment due to the strong sensitivity of the model to this parameter. The shape of the size distribution ν, however, is not easily applied by modelers since these measurements are not typically conducted for various types of weather phenomena. More recent field projects such as WISP and FIRE, have specifically looked at the size distribution where the breadth of the distribution can be inferred, but many more measurements are needed. This argument is reinforced by the sensitivity of the simulated cloud structure to the ν parameter discussed in this chapter. In the following chapters, case study simulations are examined. In the WISP case, most of the input parameters are inferred from observations which facilitates the model spinup time. Conversely, in the summertime case, many of the input parameters were based on climatology or intuition which lead to a more difficult startup time which is discussed in the following chapters.

Chapter 4

28-29 JANUARY 1991 WISP SIMULATIONS

4.1 Introduction

To exercise the model with a wintertime case, the 28-29 January 1991 orographic wintertime upslope case study from Winter Icing and Storm Project (WISP) (Rasmussen et al., 1992) is numerically investigated. A map of the WISP91 project area is shown in Fig. 4.1. This case was characterized by a strong cold front which moved across the project area during the evening hours of the 28th and widespread light snow which fell across the area following frontal passage. Previous modeling efforts (Wesley and Pielke, 1990; Cotton et al., 1994) have numerically examined Colorado Front Range snowstorms with RAMS in a 1-moment microphysical framework. The case study represents an excellent opportunity to examine the 2-moment scheme in a weakly forced ice-phase dominated event. These weakly forced storms are quite prevalent across the High Plains of the United States.

4.2 Case study

A dense mesonet of instruments in place for WISP recorded data for this case. This network included 61 automated surface stations, 4 Doppler radars, a network of volunteer snow observers (Bernstein et al., 1992) as shown in Fig. 4.2, and the University of Wyoming King Air research aircraft.

The storm was characterized by a strong cold front from the north which was preceded by moderate westerly downslope winds (10 m s^{-1}). Temperatures were mostly 5–10°C ahead of the front on 28 January, but dropped to less than –10°C behind the front. Widespread light to moderate snow fell across most of the region. The synoptic conditions

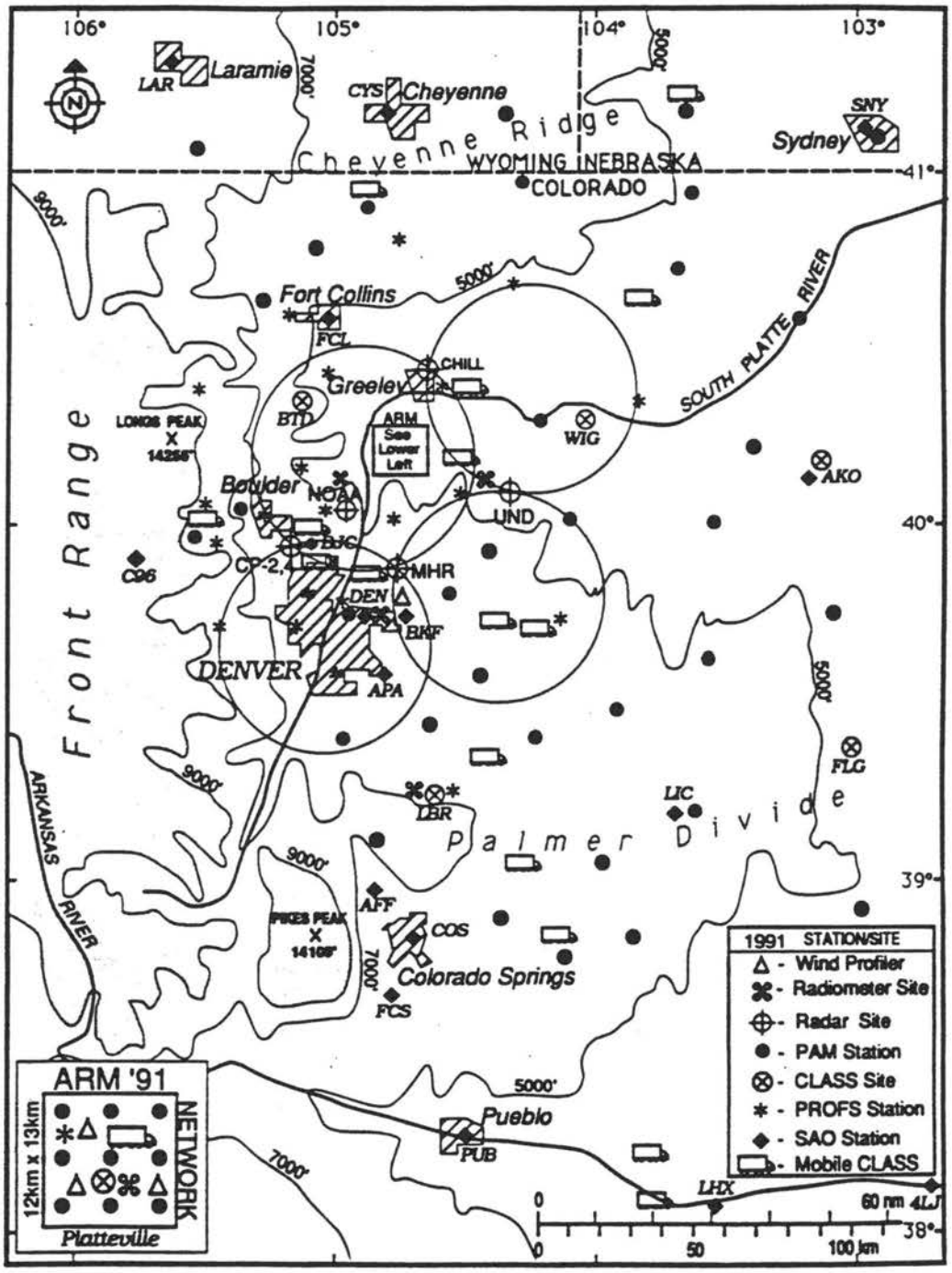

Figure 4.1: Winter Icing and Storm Project (WISP91) network of instruments showing location of Doppler radars, CLASS stations, PAM and PROFS mesonet stations, radiometer sites, wind profiler sites, and SAO stations. Topographic contours are given every 2000 ft. The shaded region represents terrain above 9000 ft. (From Rasmussen et al., 1992)

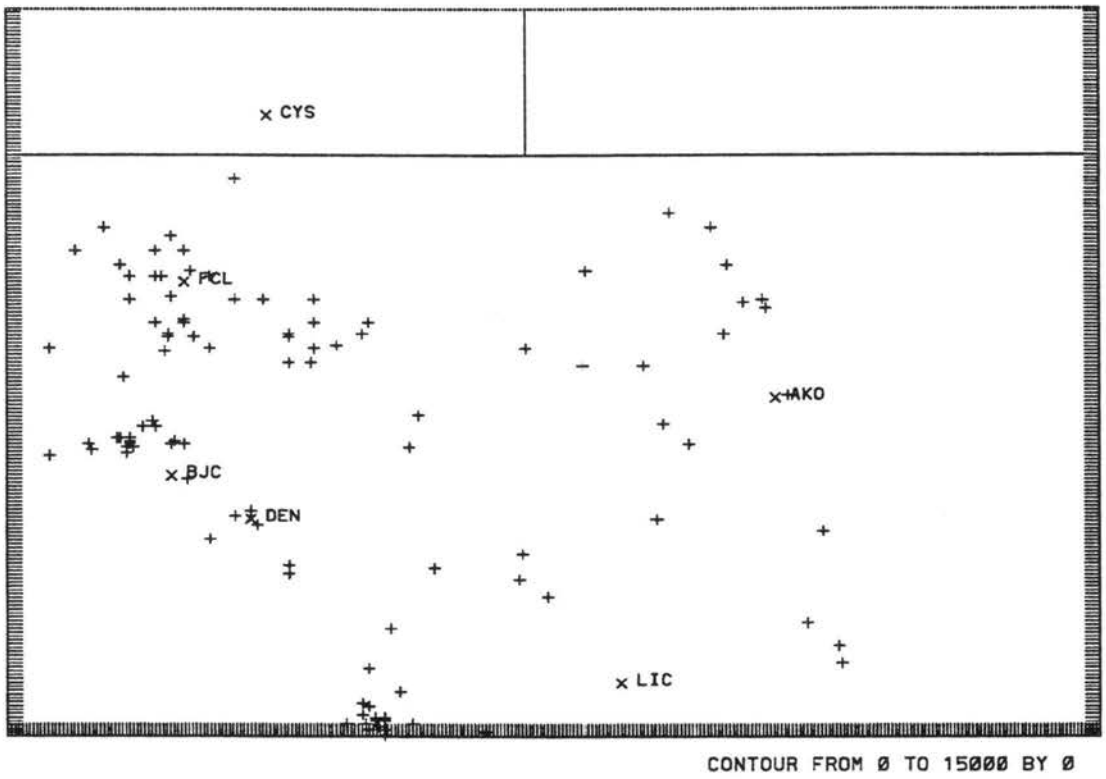

Figure 4.2: A map of the snow observation network.

at 1200 UTC 28 January show that the surface forcing is driven by a 1032 HPa high pressure area over southwestern Canada with a cold front extending across northern Wyoming. (Fig. 4.3). The 500 HPa pattern at 0000 UTC (Fig. 4.4) shows a weak trough over the intermountain West with an embedded shortwave over southwestern Idaho, however, most of the dynamics moved south of the project area. By 0000 UTC on 29 January the upslope gradient had developed over northern Colorado and precipitation developed behind the front. The upslope continued overnight, and by 1200 UTC on 29 January (Fig. 4.5) the surface high pressure moved southeastward to South Dakoka (1028 HPa) and the resultant upslope gradient had progressed south of the WISP area.

4.3 Numerical simulations

4.3.1 Model setup

The numerical model used in this study is a version of the RAMS cloud model developed at CSU (Tripoli and Cotton 1982; Cotton *et al.* 1982; 1986; Pielke *et al.*, 1992).

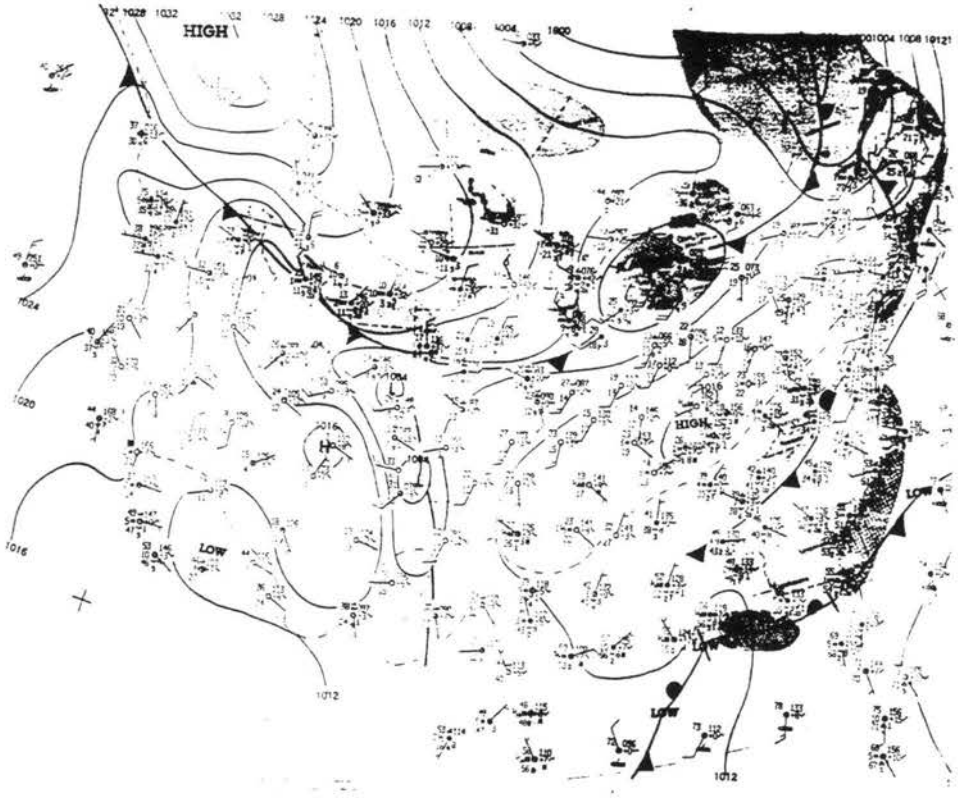

Figure 4.3: Surface analysis for 1200 UTC 28 January 1991.

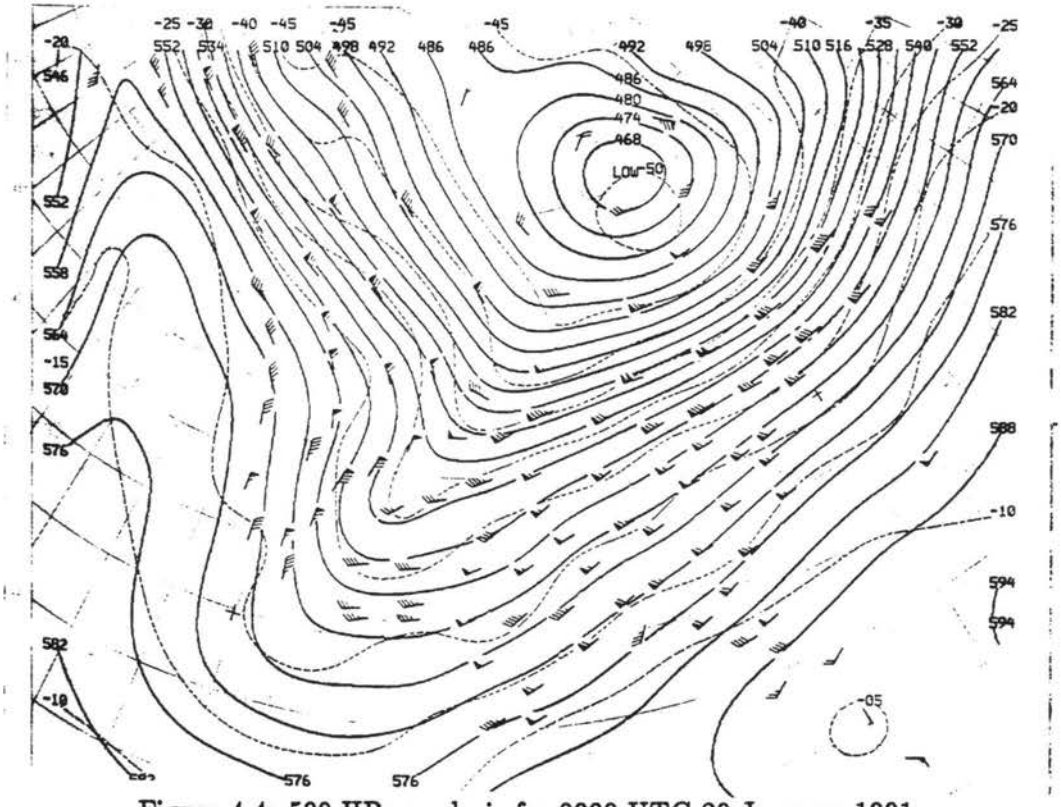

Figure 4.4: 500 HPa analysis for 0000 UTC 29 January 1991.

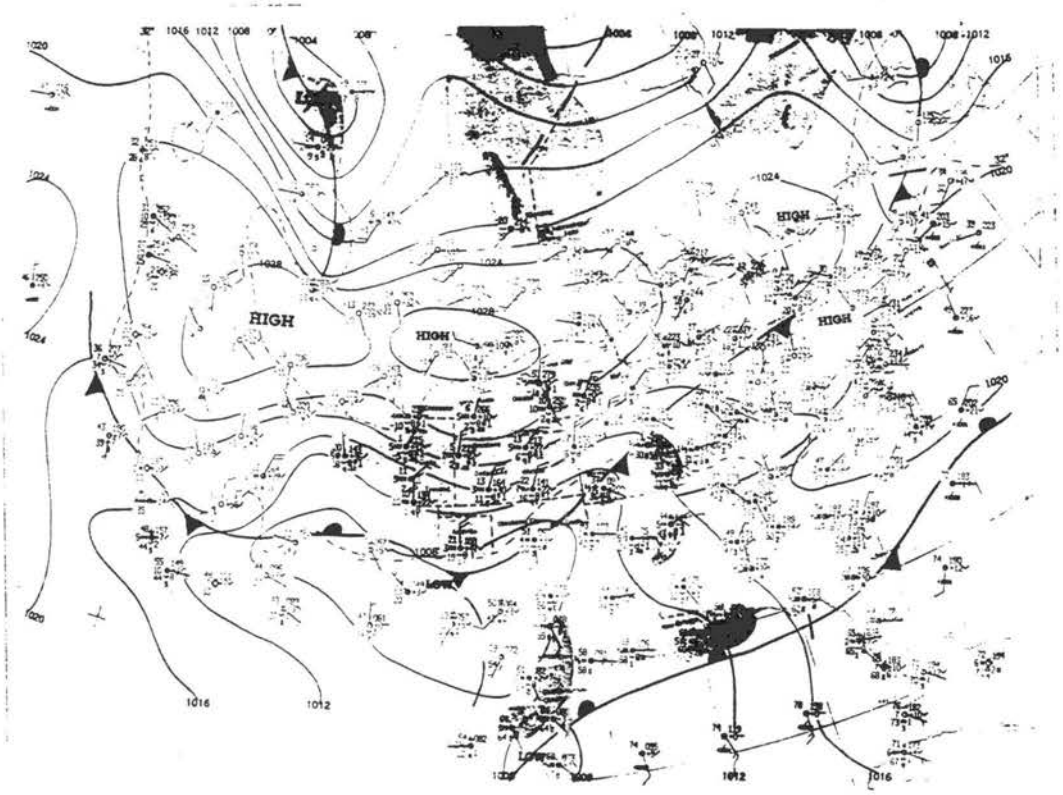

Figure 4.5: Surface analysis for 1200 UTC 29 January 1991.

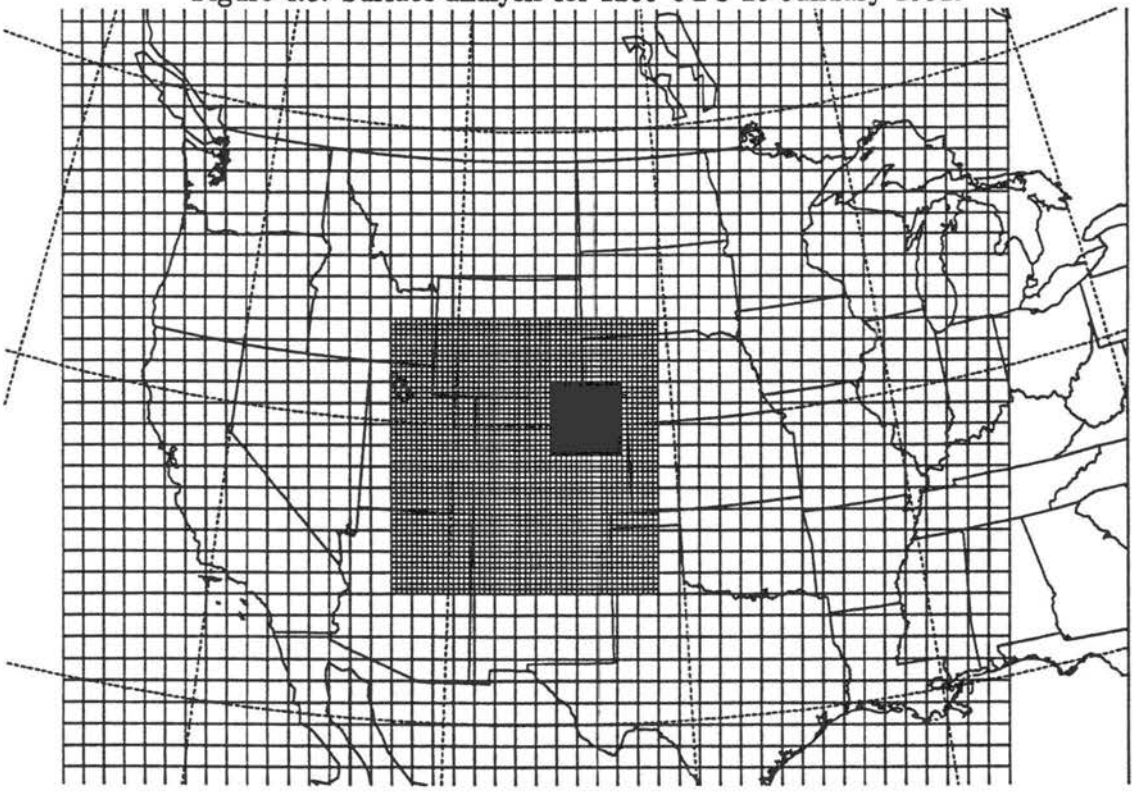

Figure 4.6: Grid Configuration of 3D nested-grid model.

RAMS is configured using the non-hydrostatic, fully compressible momentum equations, a thermodynamic energy equation, and equations for liquid and ice phase precipitation processes. The predicted variables include the three velocity components, the Exner function (π), the ice-liquid water potential temperature (θ_{il}) (Tripoli and Cotton, 1981). Potential temperature, temperature, cloud droplet mixing ratio, water vapor mixing ratio, and pressure are calculated diagnostically (Tripoli and Cotton, 1982). Horizontal and vertical turbulence are parameterized using an eddy viscosity closure scheme, as described by Tripoli and Cotton (1982). The Klemp and Wilhelmson (1978) radiative-type lateral boundary condition is used. "A wall on top" top boundary condition is used in conjunction with a modified Rayleigh friction layer (Cram, 1990) which provides a damping mechanism at the boundary top. The radiation scheme follows Chen and Cotton (1983) which includes shortwave and longwave radiative transfer in both clear and cloudy atmospheres. A two-way interactive grid nesting scheme following Clark and Farley (1984) is used. The microphysical scheme is described in Chapter 2, however, the hail category is turned off in these simulations. The coefficients for the heterogeneous ice nucleation parameterization are shown in Fig. 2.1 for the High Plains wintertime environment. All of these runs assume that the shape of the distribution (ν=1) follows an exponential structure based on measurements from WISP91 (personal communication, R. Rasmussen).

The grid configuration used for these simulations is shown in Fig. 4.6. The domain is 48X48X32 on Grid #1, 54X54X32 on Grid #2 and 58X58X32 on Grid #3. The horizontal grid spacing is 80 km on Grid #1 and the model incorporates a four to one nest ratio yielding 20 km grid spacing on Grid #2 and 5 km grid spacing on Grid #3. The vertical grid spacing is stretched from 150 m near the surface to 750 m at the top the model. The equations are integrated numerically by a time-splitting procedure for a non-hydrostatic, compressible system (Tripoli and Cotton 1982) with a large timestep of 60 seconds on the coarse grid and 15 seconds on Grid #3. A 30 s topography dataset is employed in Grid #2 and Grid #3. Time dependent lateral boundary conditions were used to variably initialize the simulations. The lateral boundary conditions were nudged to the National Meteorological Center (NMC) upper air analysis, rawinsonde data, and surface

airway observations (SAO) at 900 second intervals using the Davies (Davies, 1983) nudging algorithm.

4.3.2 Two-moment results

Kinematic and Thermal structure

The kinematic structure of the storm shows that the simulated front progressed through northern Colorado between 0100 UTC and 0700 UTC on 29 January. Temperature and flow fields are shown in Fig. 4.7 for 0100 UTC. The simulated temperatures and flow fields compare quite well with observations at this early simulation time. The simulated flow pattern shows strong northeasterly winds occurring over northern Colorado behind the front with strong east to southeasterly flow ahead and along the front just south along a line from east of Brighton (BRI) to Akron (AKO). Strong westerly flow exists along the foothills where downslope flow is observed. There is also evidence of a cyclonic-type circulation east of Denver (DEN) and Brighton which is located near the cold front. This type of circulation is also evident in the observed 0100 UTC surface field near 39.30 N and 104.40 W. The temperature field at 0100 UTC is predicted well, with temperatures ranging from -12°C across the Wyoming and Nebraska, to near 0°C east of Limon (LIC).

By 0700 UTC (Fig. 4.8a) the simulated cold front has not progressed south as quickly as observations. The simulated wind field has a more easterly component south of Akron than the observations which show a predominantly north and northeast flow pattern across the project area. However, the cold front has accelerated along the foothills in response to the strong northeasterly winds indicative of blocked flow. The simulated temperature gradient across the region is more than 10°C with the coldest temperatures north of Cheyenne Wyoming (CYS) (Fig. 4.8a), with a 7°C gradient observed from Cheyenne to Limon (Fig. 4.8b). Temperatures are consistently 2°C warmer in the simulation as compared to the observations. Colder temperatures exist in the observations at the foothill locations but this area is outside the Grid #3 domain.

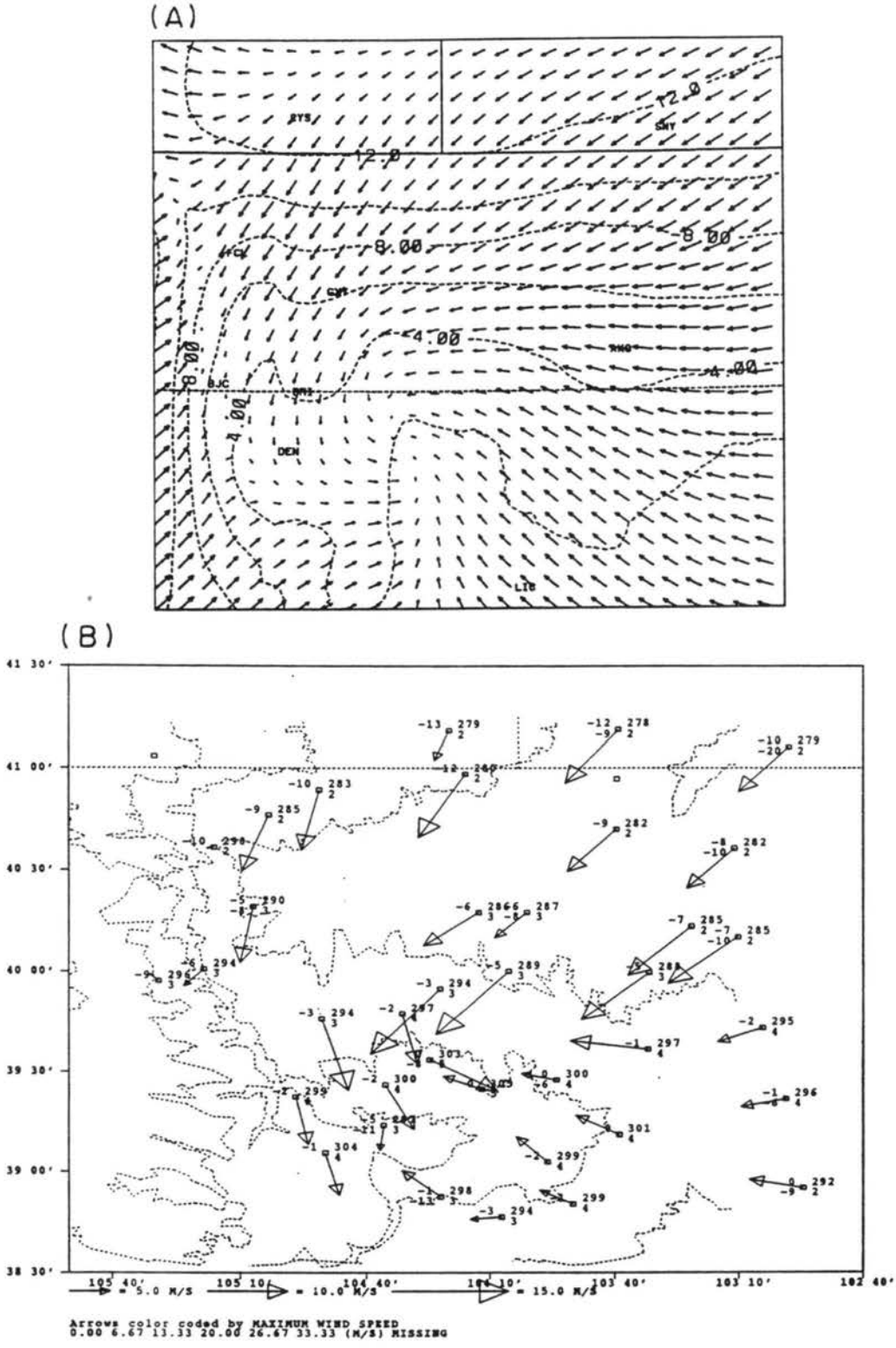

Figure 4.7: (A) Simulated (Grid #3) and (B) observed temperatures and wind vectors at 0100 UTC. Temperature contour is 2°C, and maximum wind vector is 7.6 m s^{-1}.

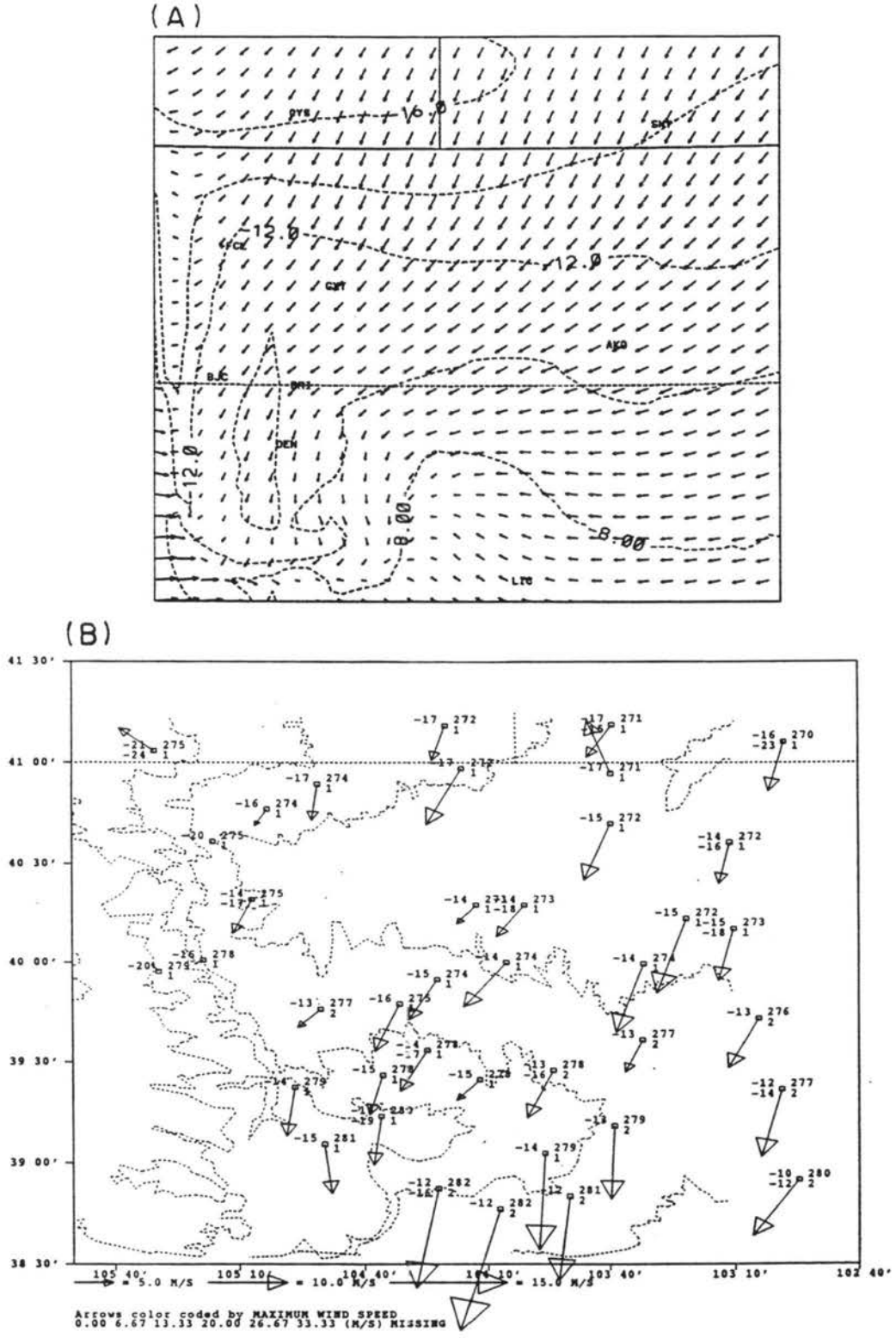

Figure 4.8: (A) Simulated (Grid #3) and (B) observed temperatures and wind vectors at 0700 UTC. Temperature contour is 2°C, and maximum wind vector is 12.1 m s^{-1}.

Radar reflectivity structure

The radar structure observed for this case is shown in Fig. 4.9b– 4.14b, using the Mile High Radar CAPPI at 2.5 km MSL (nearly 0.9 km AGL at the radar site). At 0121 UTC (Fig. 4.9b), the first radar echoes develop nearly 100 km north of the radar with peak reflectivities around 10 dBZ. Reflectivities increased towards the northern foothills with peak reflectivities near 15 dBZ. Only negligible reflectivities are simulated at 0100 UTC (Radar reflectivity calculations used in the model are described in Appendix A). By 0219 UTC (Fig. 4.10b) the areal extent of precipitation was more widespread as the surface front moved southward from CYS, and more intense reflectivities (25 dBZ) developed 110 km NNW of the radar. A secondary region of echoes also developed in a 80 km line NE from the radar with peak reflectivities less than 20 dBZ. The simulated reflectivities at 0200 UTC (Fig. 4.10a) also show weak reflectivities across the northeastern border of Colorado just behind the simulated cold front. These echoes are dominated by smaller-sized hydrometeors producing reflectivities less than 5 dBZ. Another region of reflectivity had also developed along the northern foothills with stronger reflectivities (greater than 20 dBZ).

The precipitation continued to expand by 0317 UTC (Fig. 4.11b) with some enhanced reflectivities (up to 30 dBZ) evident 120 km north of the radar. The simulated reflectivities at 0300 UTC (Fig. 4.11a) do not extend as far south and are weaker than the observations. This is likely due to the slight lag of the simulated cold front behind the observed cold front, however both the observed and simulated reflectivity regions formed behind the cold front. Peak reflectivities of 15 dBZ are predicted in the northeastern portion of the grid, and over 25 dBZ are predicted along the foothills west of Boulder. By 0405 UTC (Fig. 4.12b) the reflectivity pattern across northern portion of the network weakened. A fairly high reflectivity region was positioned south and east of the radar, where peak reflectivities exceeded 30 dBZ. Figure 4.12a shows that the simulated reflectivity fields at 0400 UTC had widespread echoes on a line north from Denver to Akron with peak reflectivities near 20 dBZ north of Sydney, (SNY) Nebraska. Another reflectivity peak was present over the foothills south of Fort Collins (FCL) with peak values near 30 dBZ.

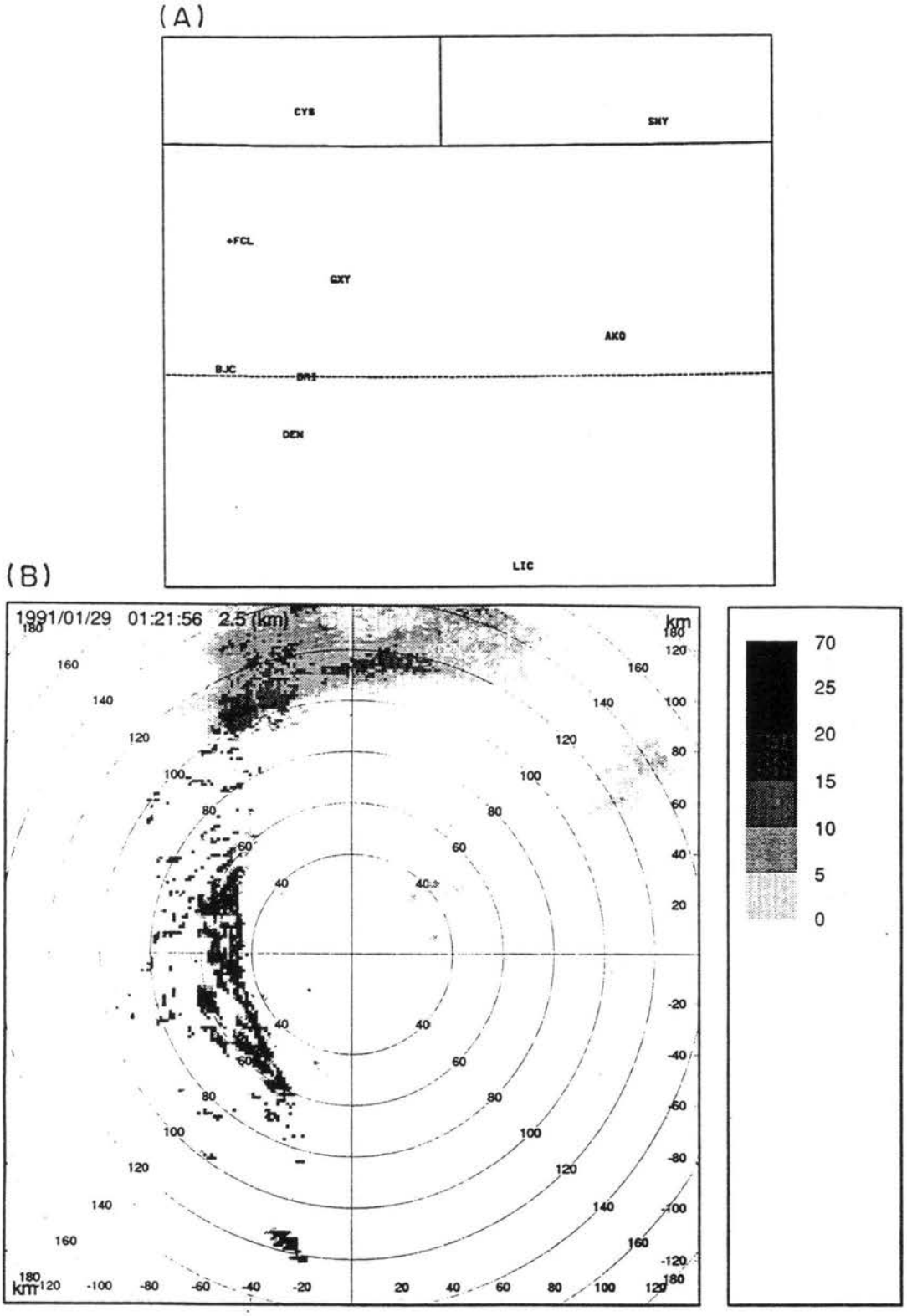

Figure 4.9: (A) Simulated and (B) observed radar reflectivity fields at 0100 UTC and 0121 UTC, respectively for 2.5 km MSL.

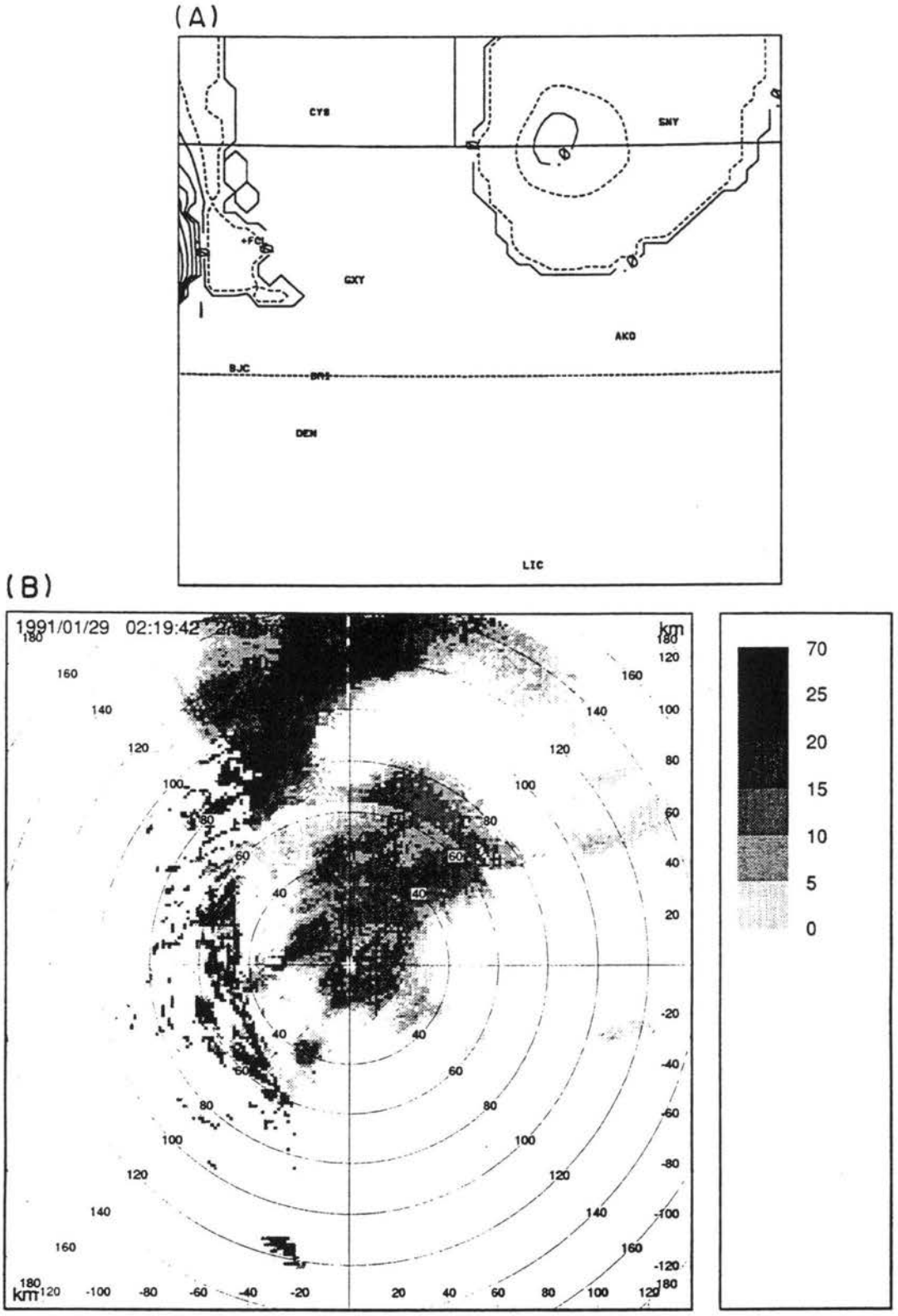

Figure 4.10: (A) Simulated and (B) observed radar reflectivity fields at 0200 UTC and 0220 UTC, respectively for 2.5 km MSL. Contour interval on simulated plot is 5 dBZ, where dashed lines denote negative values and solid lines denote positive values.

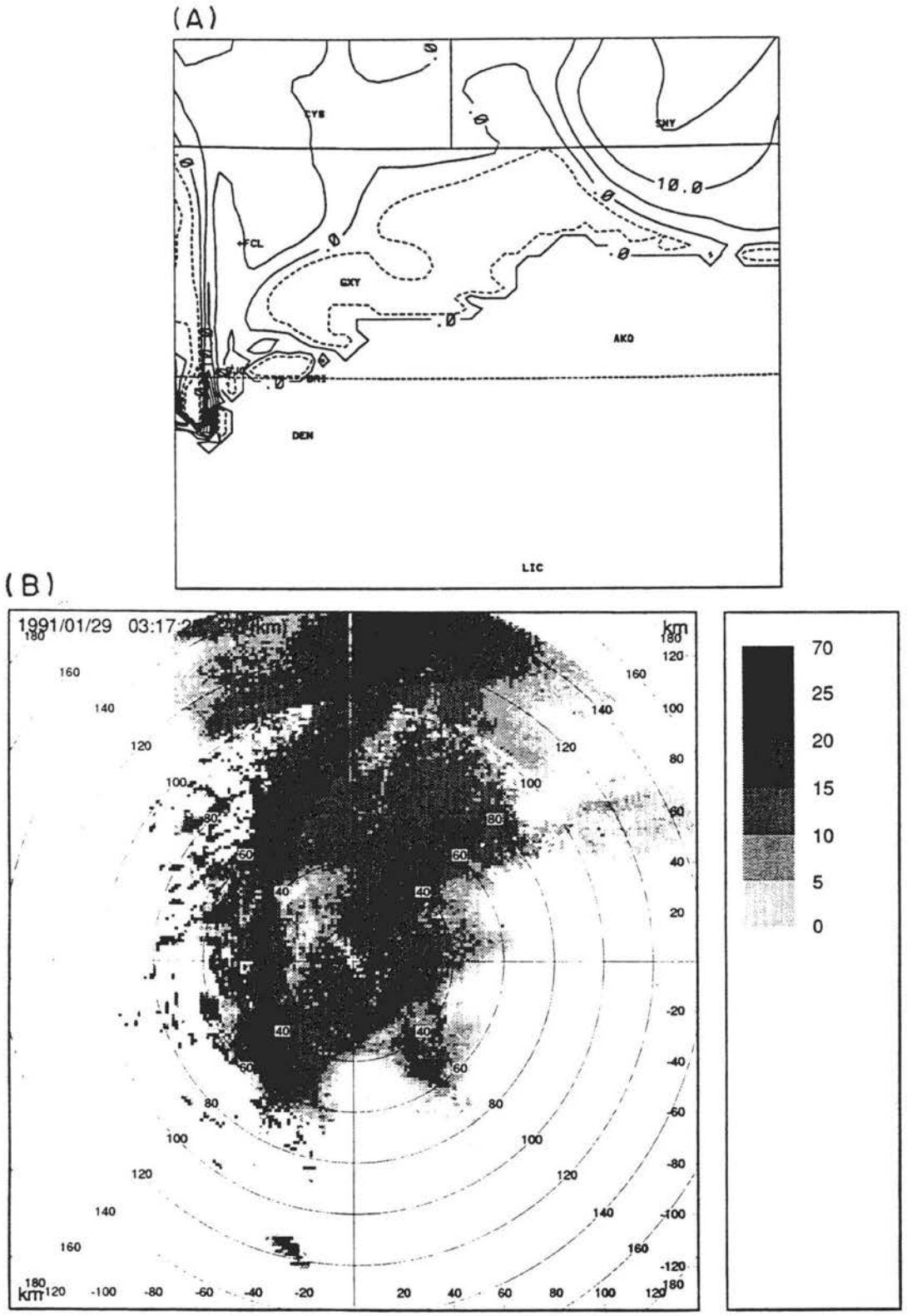

Figure 4.11: (A) Simulated (Grid #3) and (B) observed radar reflectivity fields at 0300 UTC and 0317 UTC respectively for 2.5 km MSL. Contour interval on simulated plot is 5 dBZ, where dashed lines denote negative values and solid lines denote positive values.

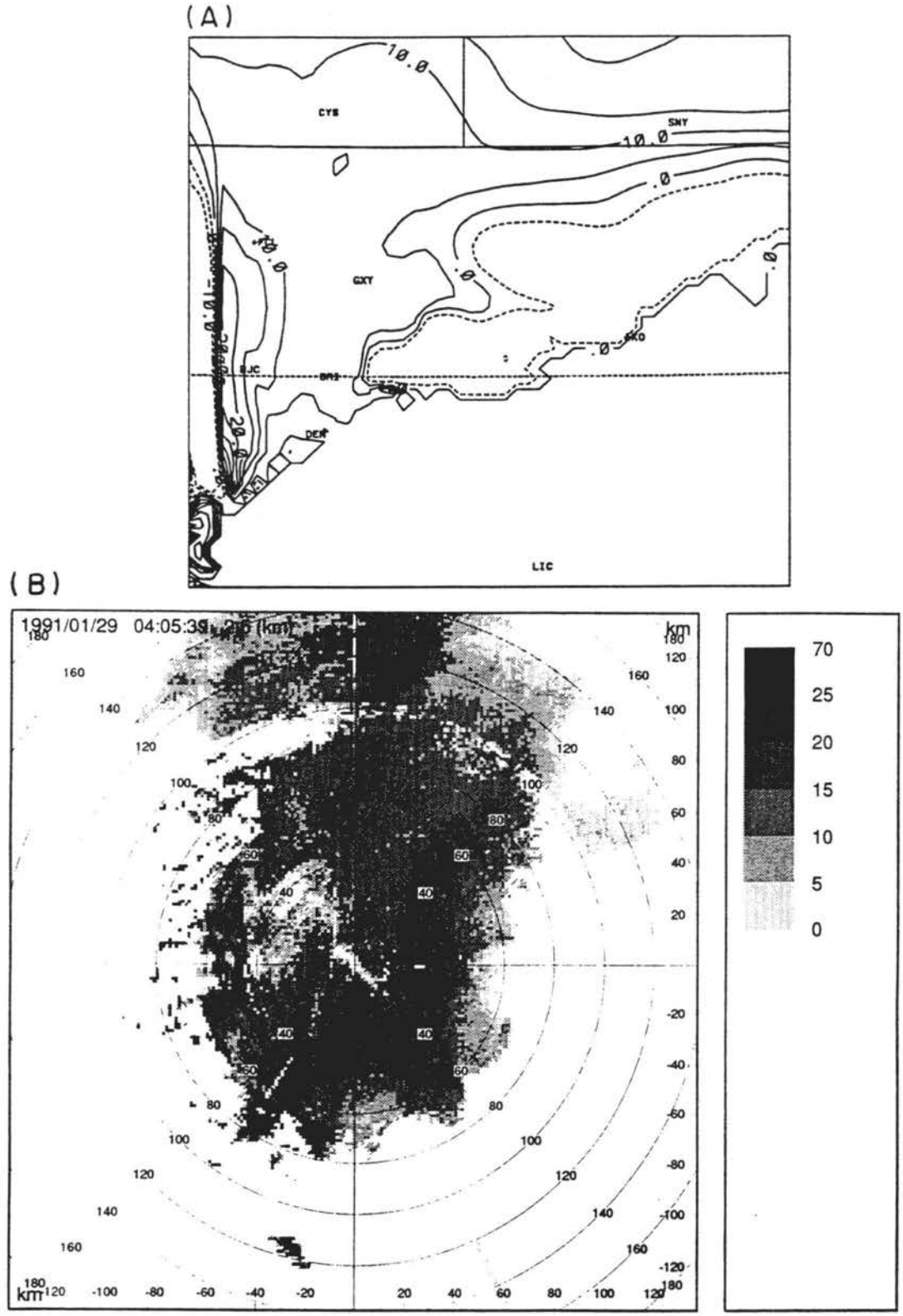

Figure 4.12: (A) Simulated (Grid #3) and (B) observed radar reflectivity fields at 0400 UTC and 0406 UTC, respectively for 2.5 km MSL. Contour interval on simulated plot is 5 dBZ, where dashed lines denote negative values and solid lines denote positive values.

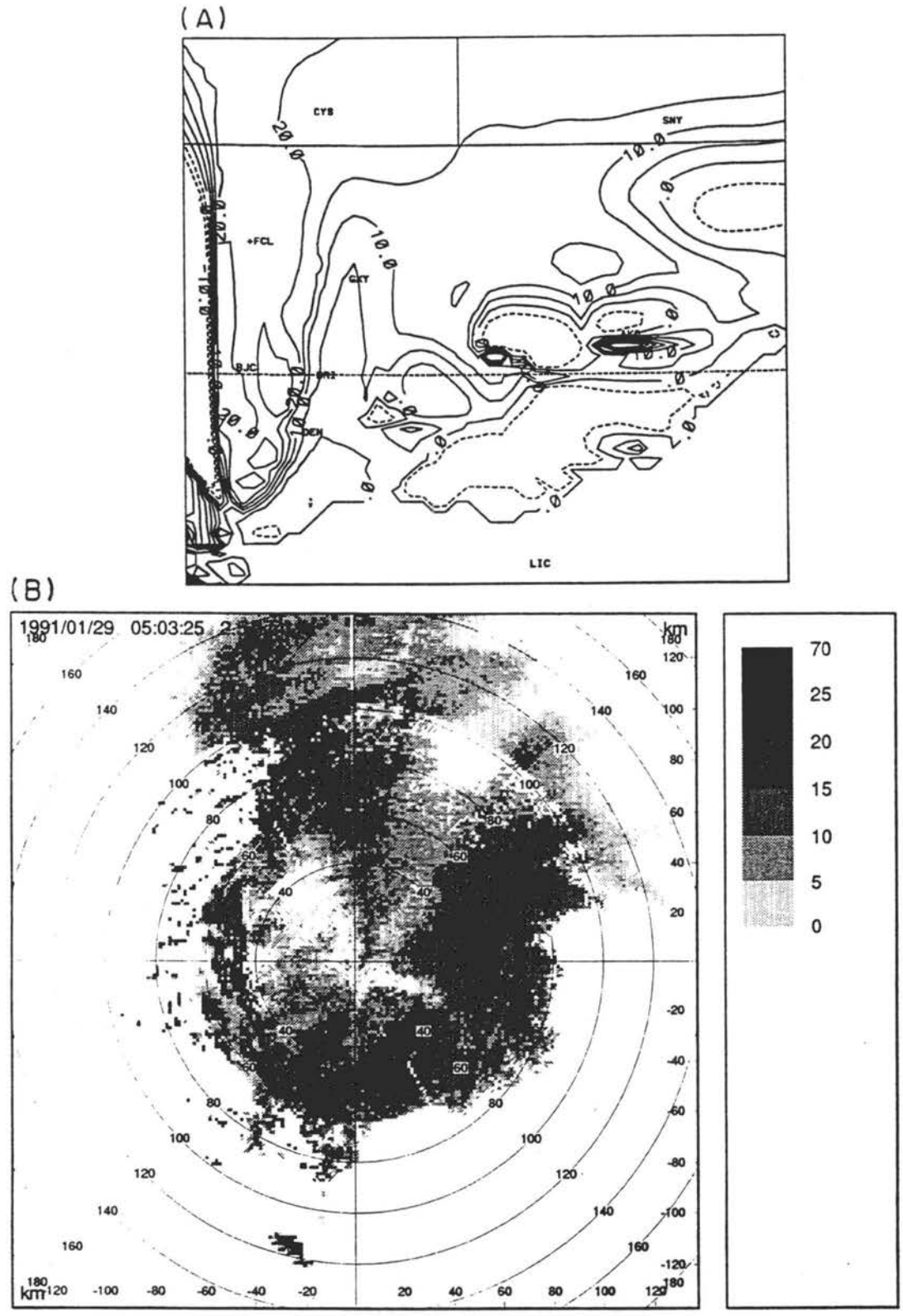

Figure 4.13: (A) Simulated and (B) observed radar reflectivity fields at 0500 UTC and 0503 UTC, respectively for 2.5 km MSL. Contour interval on simulated plot is 5 dBZ, where dashed lines denote negative values and solid lines denote positive values.

The observed reflectivity pattern (Fig. 4.13b) shifted eastward during the next hour (0503 UTC). Peak reflectivities were 20 dBZ and 30 dBZ approximately 50 km east of the radar. The simulated structure (Fig. 4.13a) also shows peak values extending southward along the northern foothills with peak reflectivities of 25 dBZ. Echoes extend farther south across the eastern Plains of Colorado with peak values near 35 dBZ, however, most simulated reflectivities were less than 10 dBZ. By 0551 UTC (Fig. 4.14b) precipitation is occurring over two distinct regions, 30-100 km north and east of the radar. Peak reflectivities in these regions were 25 dBZ. The simulated reflectivity (Fig. 4.14a) also shows two distinct regions of reflectivity with an eastern reflectivity peak located near Akron (AKO), and a broad region over the northern part of Grid #3 with reflectivity echoes near 30 dBZ.

Aircraft and crystal observations

The Wyoming King Air flew from 0455-0655 UTC as indicated by Fig. 4.15a. The flight track originated in Laramie Wyoming, and flew southeast towards the CSU-CHILL radar. Number concentrations of cloud ice and precipitating ice were measured from 2DC and 2DP probes. Measurements from the aircraft microphysical probes are compared to similar model predicted fields. Simulated ice crystal concentrations for 0500-0700 UTC are shown in Fig 4.16. These fields are the total number concentration of snow, aggregates, and graupel (pristine ice crystals are not included, and the simulation produced only negligible amounts of pristine ice for this region). A horizontal slice was taken across an altitude (4 km MSL) of the aircraft flight path. Concentrations during these times ranged from 16 l^{-1} at 0500 UTC which is predicted north of the aircraft flight path, to 12 l^{-1} at 0700 UTC co-located with the observation from the aircraft. These values are quite similar to concentrations of 10 l^{-1} (peak values were measured near 40 l^{-1}) measured by the 2DP probe (Fig. 4.15b). The 2DP probe measured precipitation particles similar to those described here for the model simulations. Figure 4.17a shows a cross section of total ice number concentrations which shows that the simulated cloud top extends up to 8 km MSL. This cross section is taken across the center of the domain at the same latitude as Greeley (GXY). Peak values of all simulated ice particles are 45 l^{-1} in this region similar to the peak observed values. Figure 4.17b shows that only a small portion of these crystals

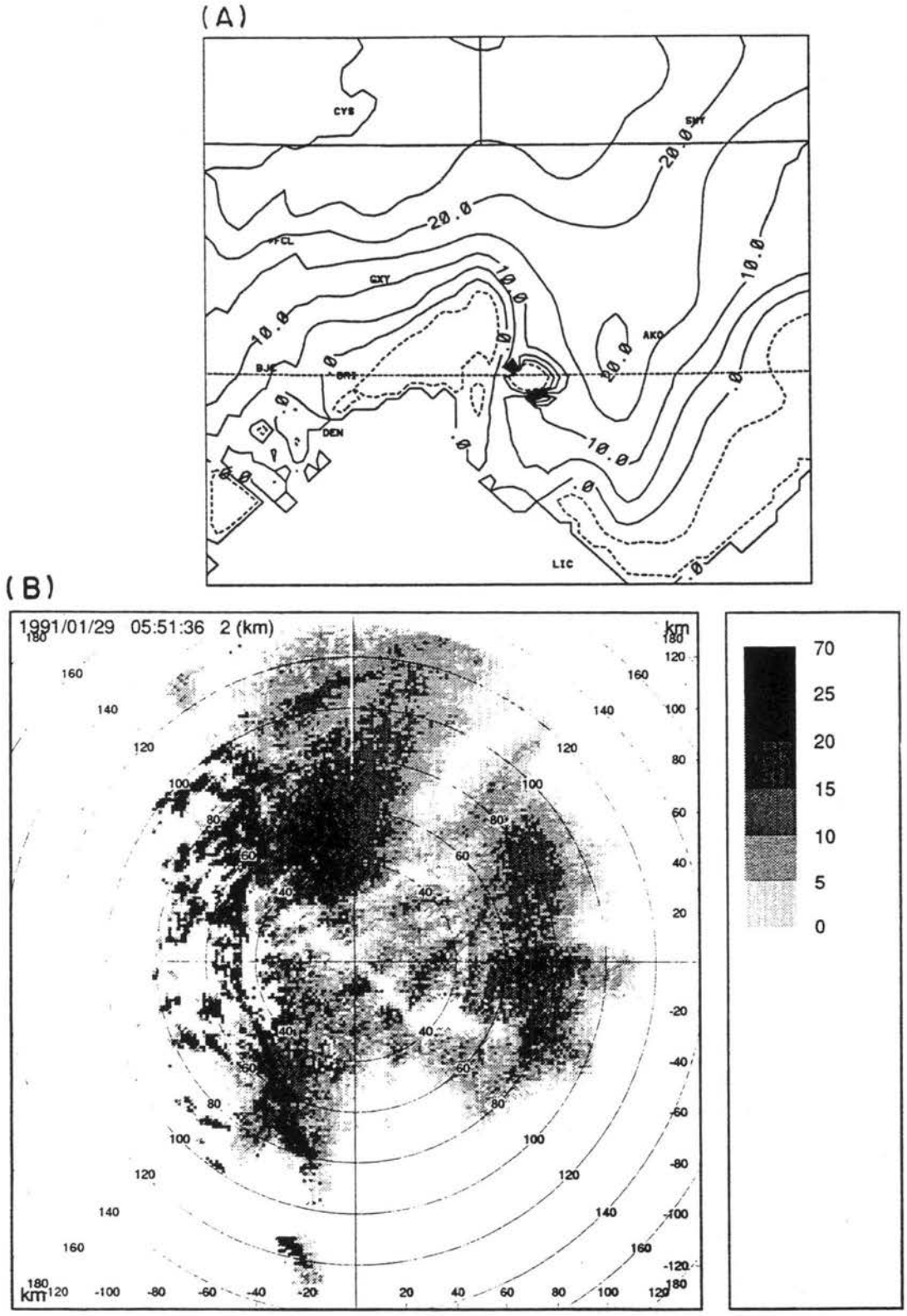

Figure 4.14: (A) Simulated and (B) observed radar reflectivity fields at 0600 UTC and 0551 UTC, respectively for 2 km MSL. Contour interval on simulated plot is 5 dBZ, where dashed lines denote negative values and solid lines denote positive values.

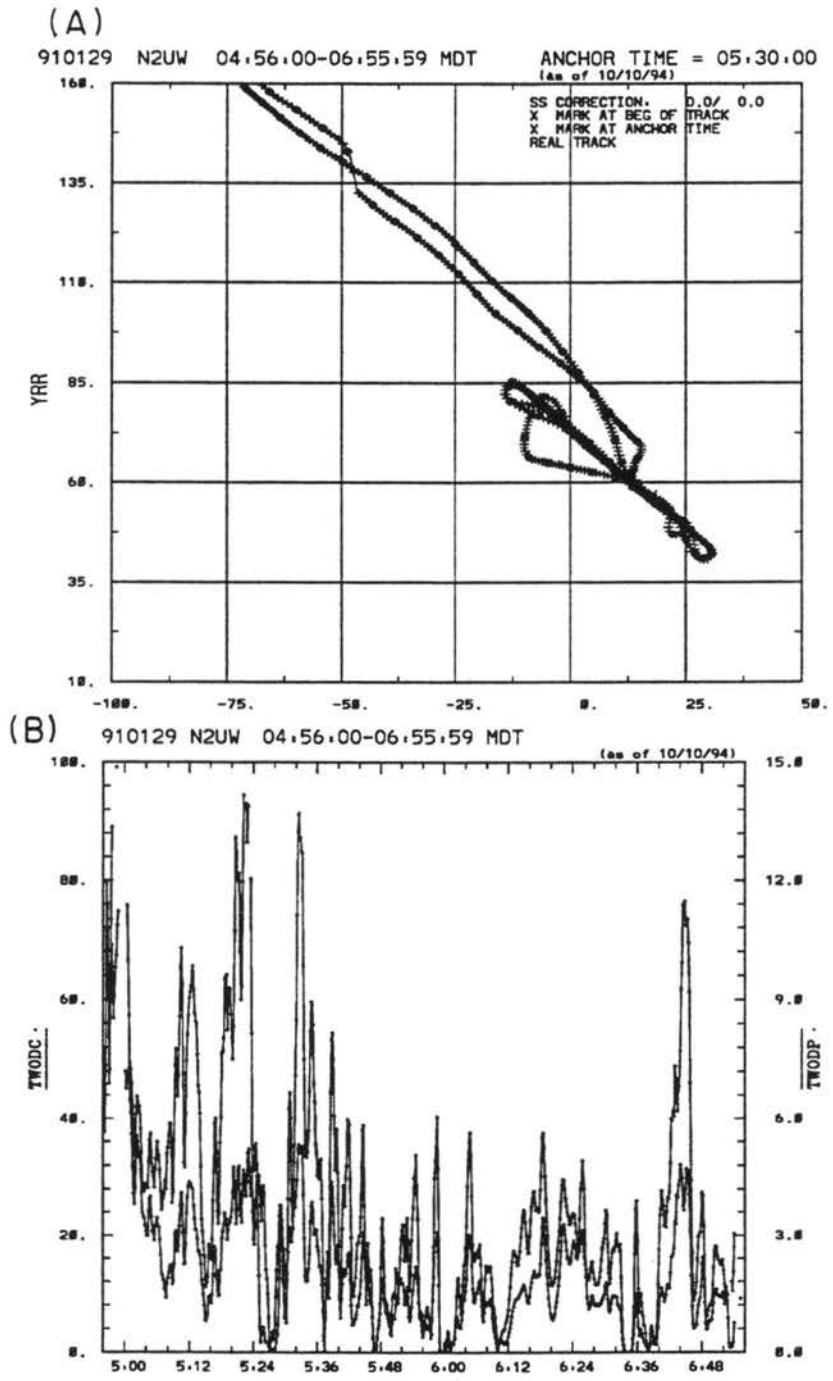

Figure 4.15: (A)Wyoming King Air flight path during 28-29 January 0455-0655 UTC including (B) 2DC scaled on the left ordinate and 2DP measurements scaled on the right ordinate (l^{-1}), with times scaled on the abscissa.

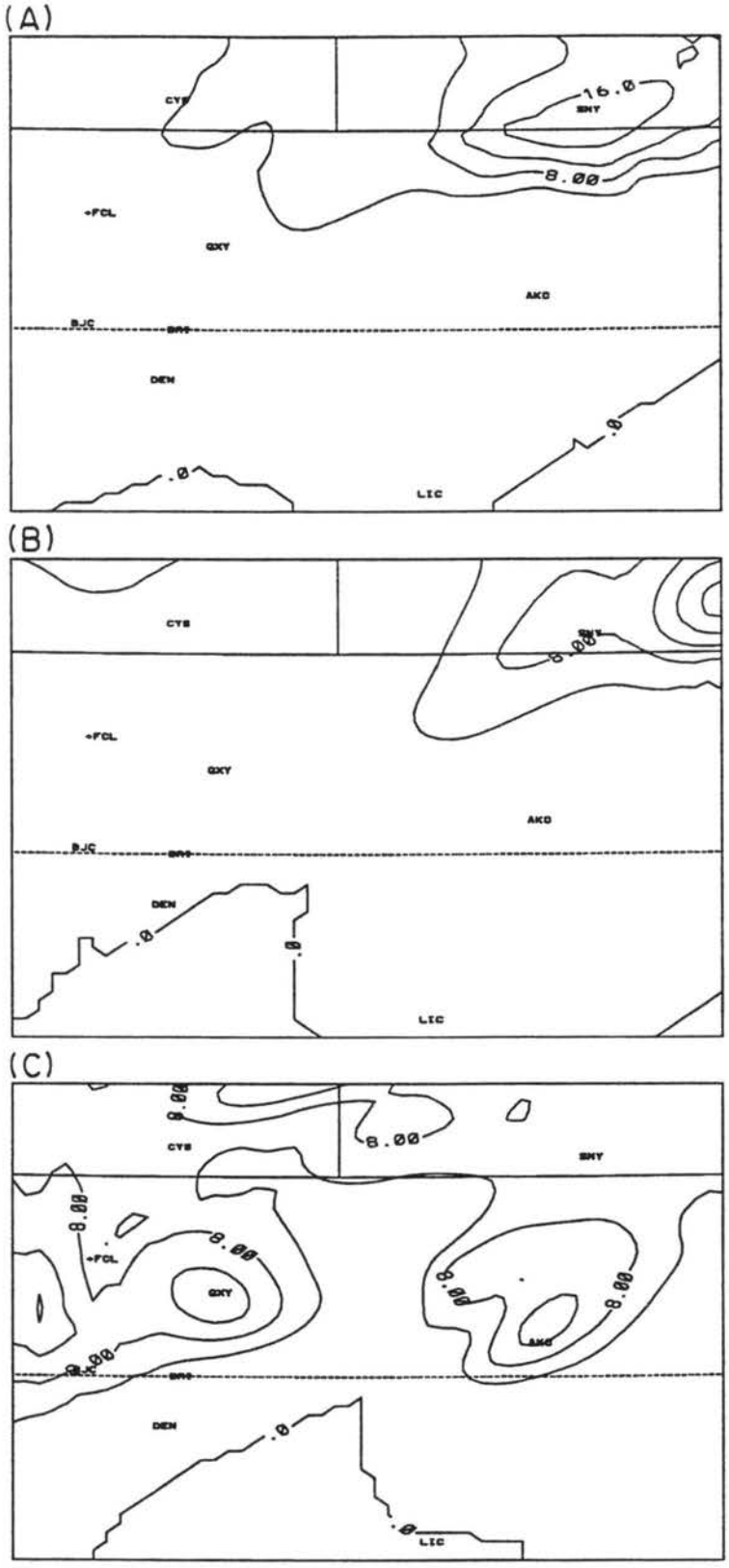

Figure 4.16: Simulated total ice number concentrations at 4000 m MSL for (A) 0500 UTC, (B) 0600 UTC, and 0700 UTC on Grid #3. Contour intervals are 4 l^{-1}.

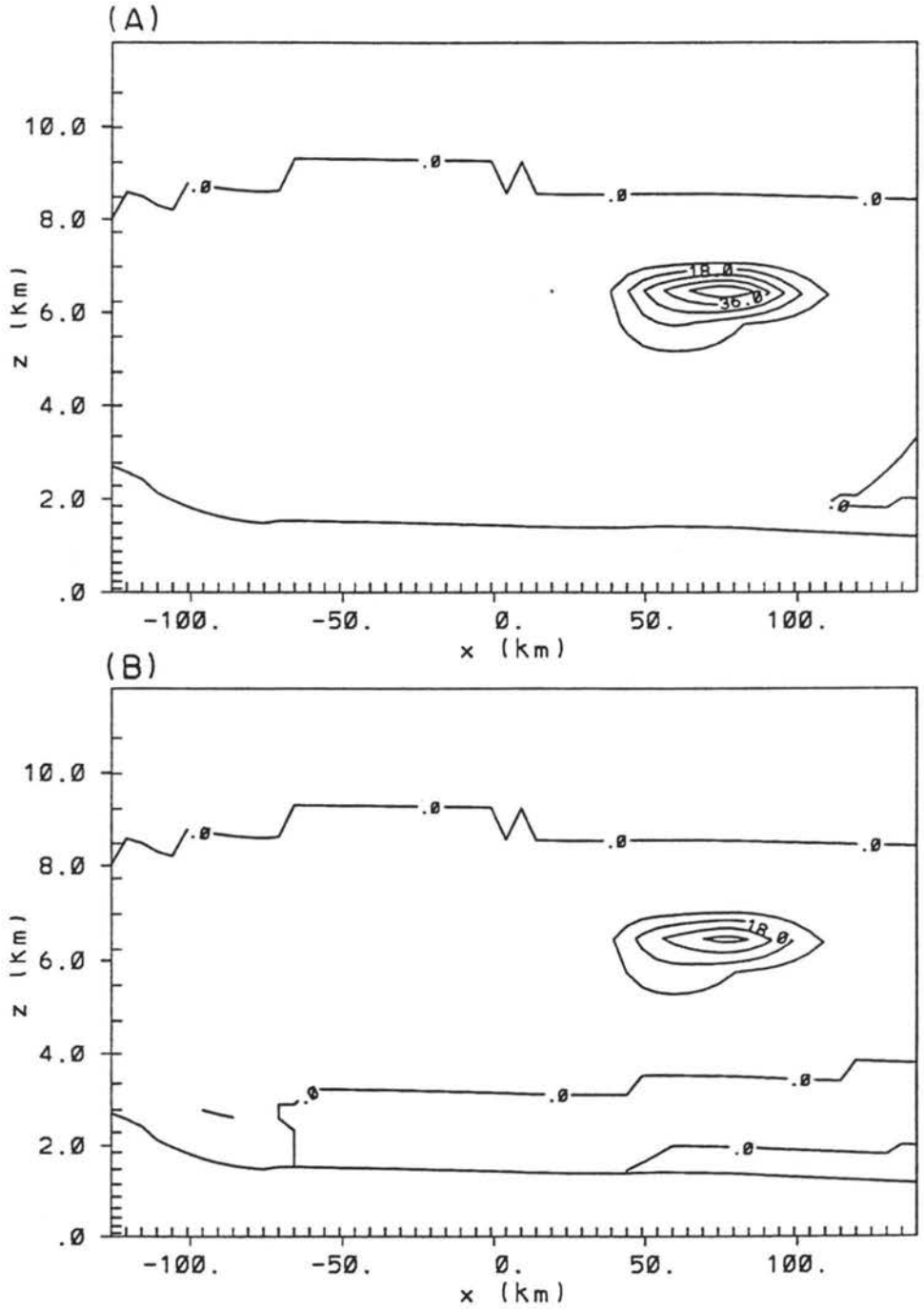

Figure 4.17: X-Z cross section of simulated (A) total ice number concentrations (max=45 l^{-1}) and (B) snow number concentrations (max=36 l^{-1}) for 0500 UTC. Cross section is placed east-west through Greeley Colorado. Contour intervals are 9 l^{-1}.

are the very small pristine ice crystals (mean diameters near 25 μm) which are at the lower end of the 2DP size measuring window, and may have been too small to be properly measured by the 2DP PMS probes. Most of the crystals predicted are snow (35 l^{-1}) which have grown, initially as pristine ice crystals, from vapor deposition and converted to snow within a cloud deck above the upslope wind layer. This upper cloud developed early in the simulation, and generated "seeding" crystals which fell into the lower upslope cloud (Rutledge and Hobbs, 1983).

Figure 4.18a shows that most of the upward vertical velocities were in and near the foothills, with peak values near 0.27 m s^{-1}. The next two cross-sections Fig. 4.18b,c show the location of the ice water and liquid water clouds. The aircraft only measured small amounts of cloud water during their flight, however, the model produced significant amounts of liquid water near the surface. Peak values of LWC were 0.24 g m^{-3}. The ice water content shown in Fig. 4.18c shows an ice mass peak found near 6 km MSL and a secondary peak of ice mass is also predicted in the lowest kilometer above the surface in response to the upslope flow.

A table summarizing the surface crystal observations taken by members of the volunteer observer network is shown in Table 4.1. This table summarizes the location of the station, the amount of riming, observation of graupel, the size of the aggregates (if observed). The crystal observation network shows that a large amount of riming is observed even in this relatively cold airmass. Nearly all the crystal observers noted the occurrence of significant riming, with a large percentage of the network observing graupel (very heavy graupel). Also, heavy riming was especially evident during the onset of the snow, however, heavy riming and graupel were observed at many locations for several hours after the onset. Another trend noted by the observers was the temporal evolution of aggregates. Aggregates made up primarily of dendrites were observed by many of the observers. The sizes of these aggregates were very large, with mean aggregate diameters of 2-4 mm, with the largest aggregates up to 10 mm. The largest aggregates were observed near the cold front and smaller aggregates were observed farther behind the front.

The simulated microphysical fields near the surface are shown in Fig. 4.19. Most of the cloud water is located near the southern boundary of Grid #3, behind the location

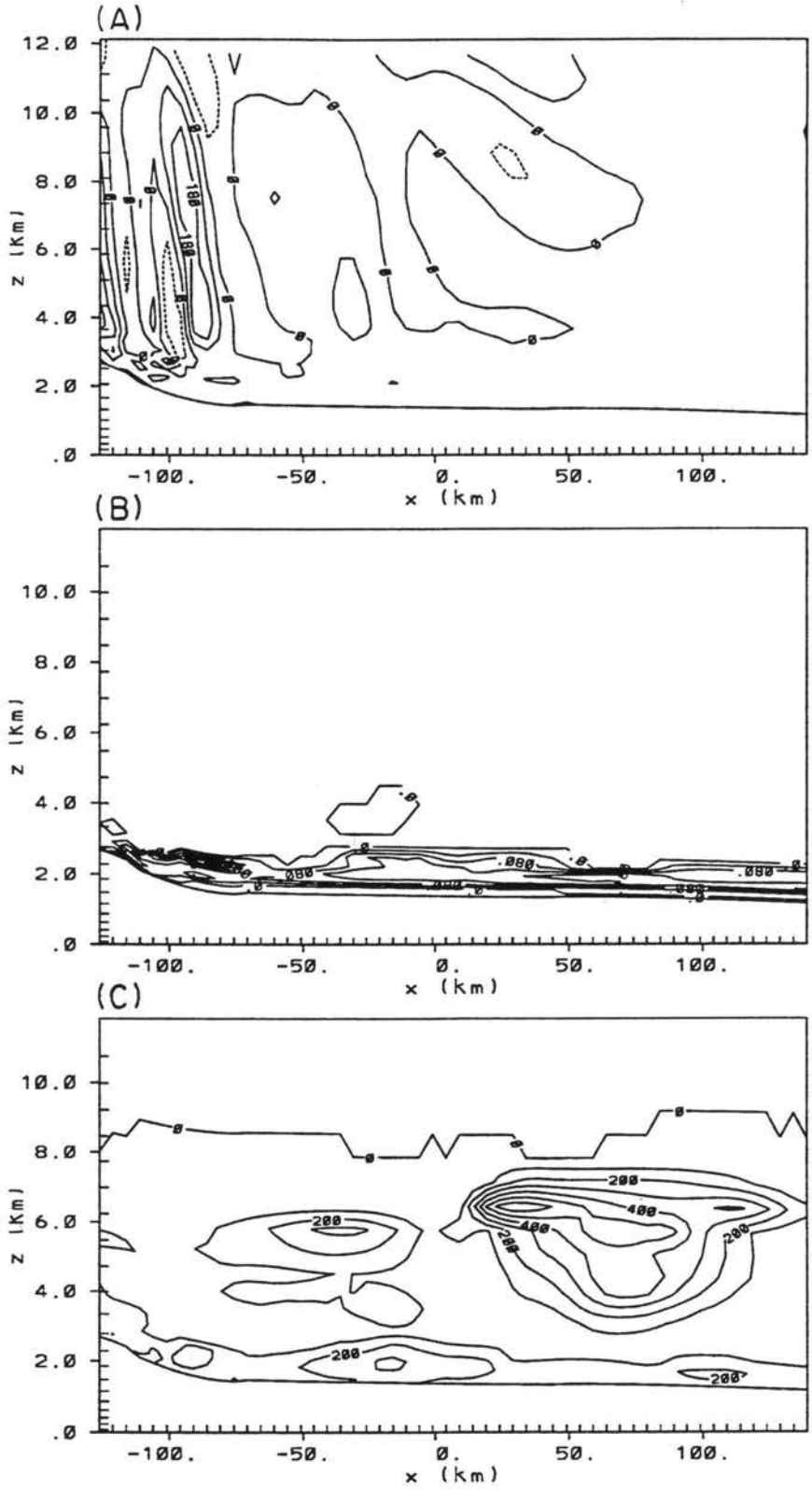

Figure 4.18: Simulated vertical cross-sections of (A) vertical velocity (0.09 m s^{-1}, 0.27 m s^{-1}), (B) liquid water content (0.04 g m^{-3}, 0.24 g m^{-3}), and (C) ice water content (0.01 g m^{-3}, 0.06 g m^{-3})on Grid #3 at 0500 UTC. Vertical slice is taken at same latitude as Denver Colorado, which is behind the cold front. Contour intervals are 4 l^{-1}.

Table 4.1: Summary of crystal observations from 0000–0700 UTC 29 January

Location	amount of riming	graupel	aggregates D_{mean}, D_{max} (mm)	crystal habit
Agate	heavy	yes	1, 8	dendrites
Berthoud	light	no	1, 3	plates
Boulder1	light	yes	5, 10	dendrites
Boulder2	heavy	no	5, 5	dendrites
Boulder3	light	no	7, 10	dendrites
Boulder4	light	no	6, 9	dendrites
W. Boulder	heavy	no	missing	stellars
Carr	heavy	yes	3, 6	dendrites
Denver	heavy	yes	missing	plates
Elbert	light	no	6, 9	plates
Flagler	heavy	yes	missing	dendrites
Fort Collins	heavy	yes	5, 20	dendrites
Ft. Morgan	heavy to light	yes	1, 5	plates
Gunbarrel	heavy	yes	1, 3	plates
Kersey	heavy	yes	3, 10	dendrites
LaSalle	light	no	missing	dendrites
Loveland1	heavy	yes	5, 5	stellars
Loveland2	heavy to light	yes	2, 2	plates
Merino	light to heavy	yes	missing	columns
New Raymer	heavy	no	1, 2	dendrites
New Raymer2	heavy	no	5, 5	dendrites
Strasburg	heavy	yes	1, 1	dendrites

of the simulated cold front, and along the foothills, with peak mixing ratios near 0.4 g kg^{-1}. The snow field (Fig. 4.19b) shows small amounts of snow mass being produced in the simulation at this time. A potential sink for snow is aggregation and, especially in this simulation, riming-produced graupel, as both aggregates and graupel are prevalent across the domain as shown in Figs. 4.19c,d. Graupel is predicted near the surface over most of the domain and is produced by riming and subsequent conversion of snow farther behind the front. Immediately behind the front, more cloud water exists (greater than 0.1 g kg^{-1}), and this occurs since there is no significant ice mass in this region to scavenge the cloud water. Peak total ice number concentrations at this time are nearly 10 l^{-1} (Fig. 4.19e). Figs. 4.19f-h show the snow, aggregate, and graupel mean diameters in an assumed gamma distribution. Snow and graupel mean diameters are fairly small

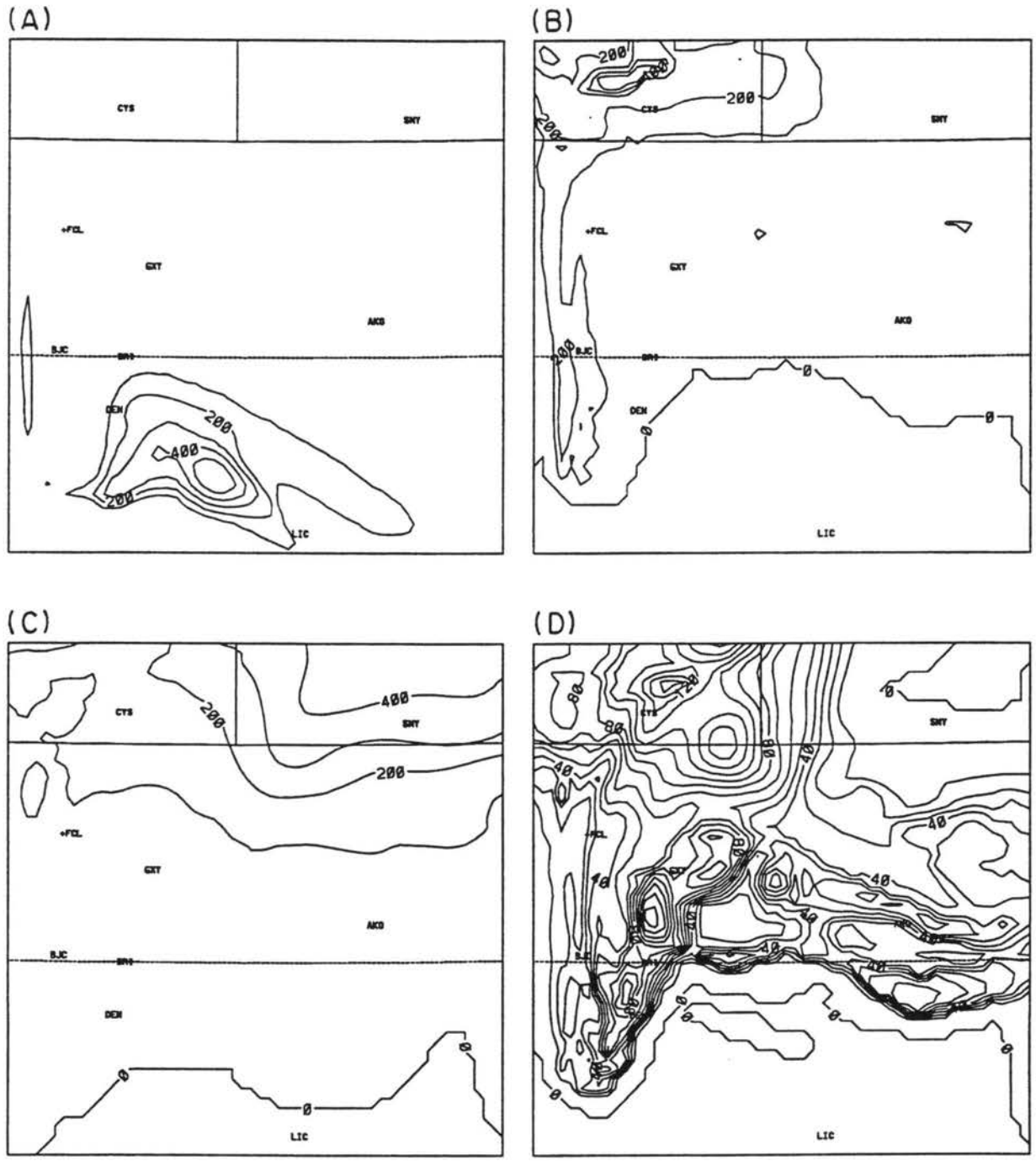

Figure 4.19: Simulated microphysical field at 75 m AGL at 0500 UTC including (contour interval, maximum) of (A) cloud mixing ratio (0.1 g kg^{-1}, 0.5 g kg^{-1}), (B) snow mixing ratio (0.0005 g kg^{-1}, 0.0025 g kg^{-1}), (C) aggregate mixing ratio (0.01 g kg^{-1}, 0.06 g kg^{-1}), (D) graupel mixing ratio (0.001 g kg^{-1}, 0.007 g kg^{-1}), (E) total ice number concentration (0.5 l^{-1}, 3.0 l^{-1}) (F) mean snow diameter (0.05 mm, 0.4 mm), (G) mean aggregate diameter (0.3 mm, 3.0 mm), (H) mean graupel diameter (0.05 mm, 0.65 mm).

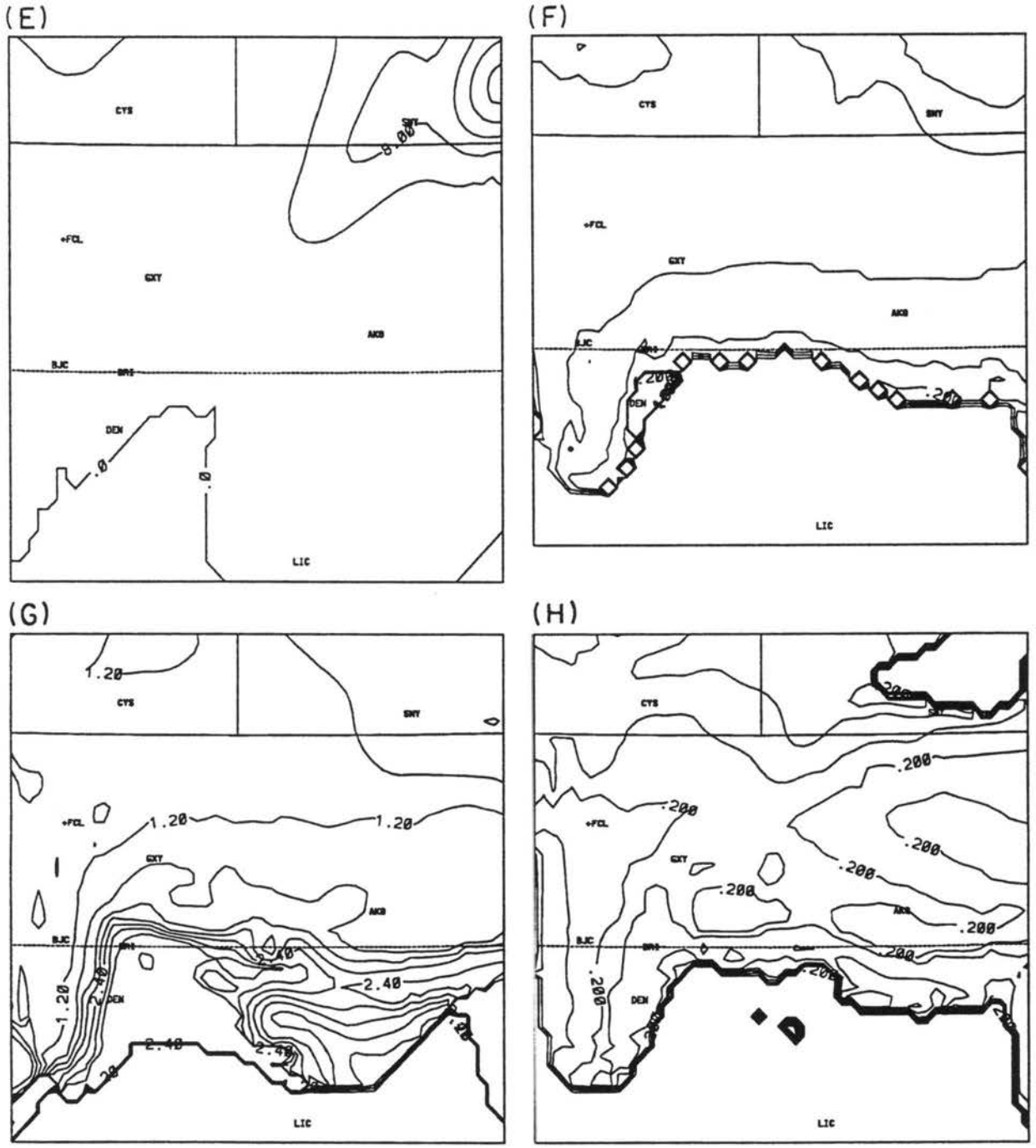

Figure 4.19: Continued.

with most mean diameters less than 0.3 mm. Since the collection kernel increases as the mean diameter increases, most of the larger snow crystals are converted to aggregates and graupel. Snow crystals, which convert to graupel are fairly small, which accounts for the small graupel diameters. However, snow which converts to aggregates, continues to grow to larger sizes due to aggregate self-collection and aggregate collection of snow, producing quite large mean diameters ranging from 1-2 mm near and behind the cold front. Another feature shown in the predicted aggregate diameter field is the decrease in the mean sizes farther north away from the cold front which was observed by the snow crystal network. The aggregates near the front grew to larger sizes due to the availability of cloud water and warmer temperatures which enhanced aggregate growth rates. Behind the front, available liquid water is much less, and as a result, aggregate diameters are decreased.

Precipitation distribution

The overall trend in the observed precipitation structure (Fig. 4.20b) shows heaviest precipitation occurred in a N/S line along the foothills with over 3 mm of liquid precipitation. Another peak occurs across the northeastern Plains of Colorado where over 2 mm of liquid precipitation occurred. The simulated precipitation amounts (Fig. 4.20a) compare well with the observed spatial distribution of precipitation with peak amounts predicted over the foothills and the northeastern portion of the domain. However, predicted precipitation amounts are lower than the observed values. Peak values from the 2-moment simulation was nearly 1 mm near the foothills and over the northeastern portion of the domain. Lesser amounts seen in the model may be due to unresolved convective components since the grid spacing was 5 km. Also, the simulated cold front was slightly slower than in the observations, and the pre-existing downslope episode was slow to erode over the foothills which may have lessened precipitation amounts. For the most part differences between 1 and 3 mm are quite small, and the model did handle the spatial distribution of the precipitation quite well.

4.3.3 One-moment results

In the 1-moment microphysical scheme a prescribed mean diameter for each hydrometeor species is assumed, and the mixing ratio is predicted. The prescribed mean diameters

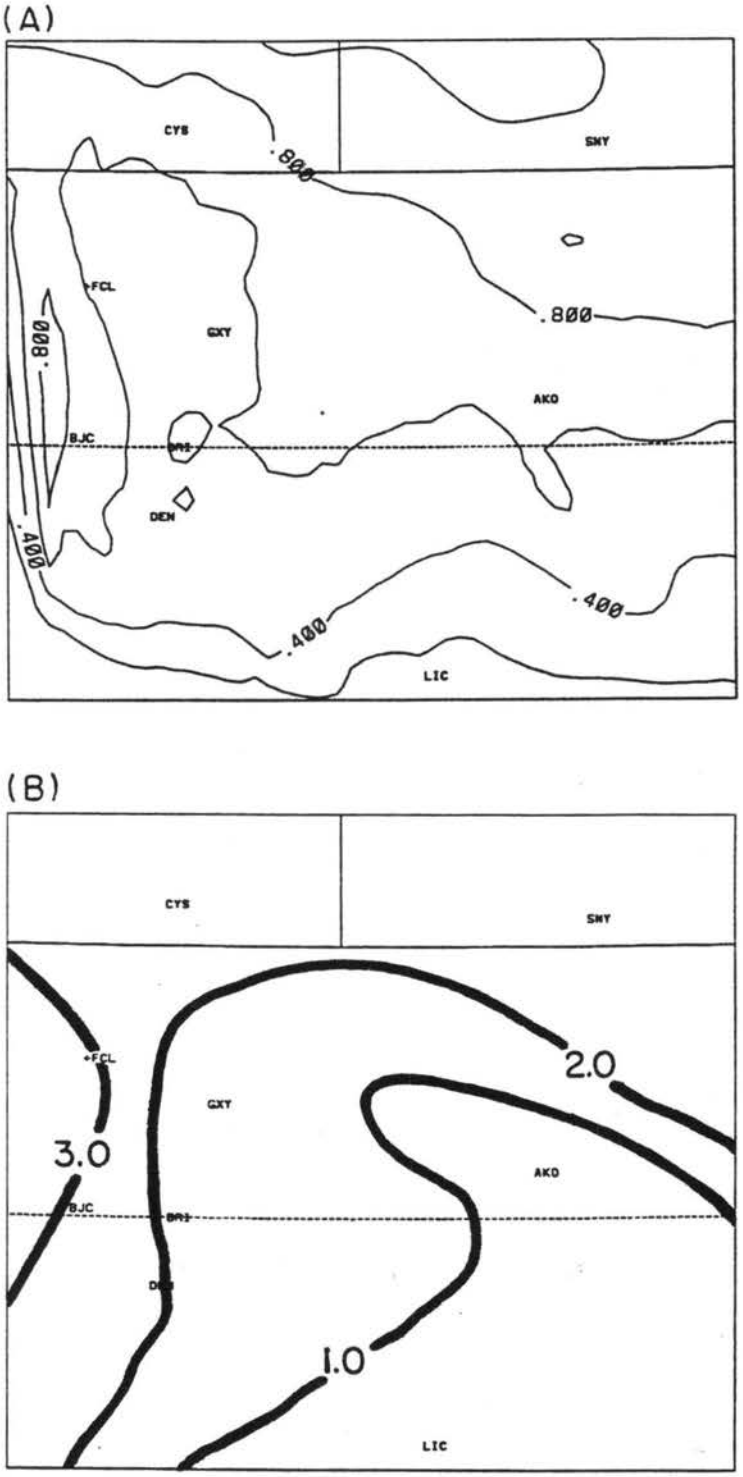

Figure 4.20: (A) Simulated (Grid #3) and (B) observed total precipitation distribution as of 1200 UTC 29 January 1991. Precipitation is liquid equivalent in millimeters.

used in the simulation include, 0.5 mm for rain, 0.5 mm for snow, 1.0 mm for aggregates, and 1.0 mm for graupel. Two-moments are predicted for the pristine ice crystal category. Otherwise, everything is set up similar to the 2-moment simulation.

The overall kinematic structure was nearly identical to the 2-moment simulation. The major difference between the 1-moment scheme and the 2-moment scheme is that the diameter cannot vary in the 1-moment scheme, which impacts hydrometeor growth and evolution. Figure 4.21a shows a similar cloud water mixing ratio structure over the Plains, however, less cloud water is evident over the foothills. In the 1-moment simulation, the snow diameter is prescribed at 0.5 mm, which is much larger than diameters predicted in the 2 moment simulations (Fig. 4.19f). With larger snow diameters in the 1-moment scheme, the collection kernel of snow increases, resulting in more snow mass (Fig. 4.21b), which enhances aggregation processes. Conversely, in the 2-moment simulation, aggregation of snow is not as prevalent over the foothills at this time, so the largest conversion sink of the snow category is to graupel due to the collection of cloud water. In the 1-moment scheme, more aggregate mass is produced (Fig. 4.21c) which is less likely to be converted to graupel.

The overall effect on the precipitation distribution is insignificant. Slightly more precipitation occurs in the 1-moment scheme (Fig. 4.22) with peak amounts near 1.2 mm, however, the overall structure is similar to the 2-moment simulations.

4.4 Discussion

In this chapter a shallow wintertime upslope event along the Front Range of Colorado has been examined with both a 2-moment and 1-moment microphysical predictive scheme. Both simulations did handle the kinematic structure of the storm and evolution of the cold front fairly well except that the simulated cold front was a bit slower than the observed cold front. The microphysical structure of the storm was handled quite well in the 2-moment simulation. The predicted radar reflectivity structure showed similarities to both the spatial distribution and intensities of the observed reflectivity pattern, however, observed peak echoes were not always predicted by the model. Comparisons with aircraft data showed

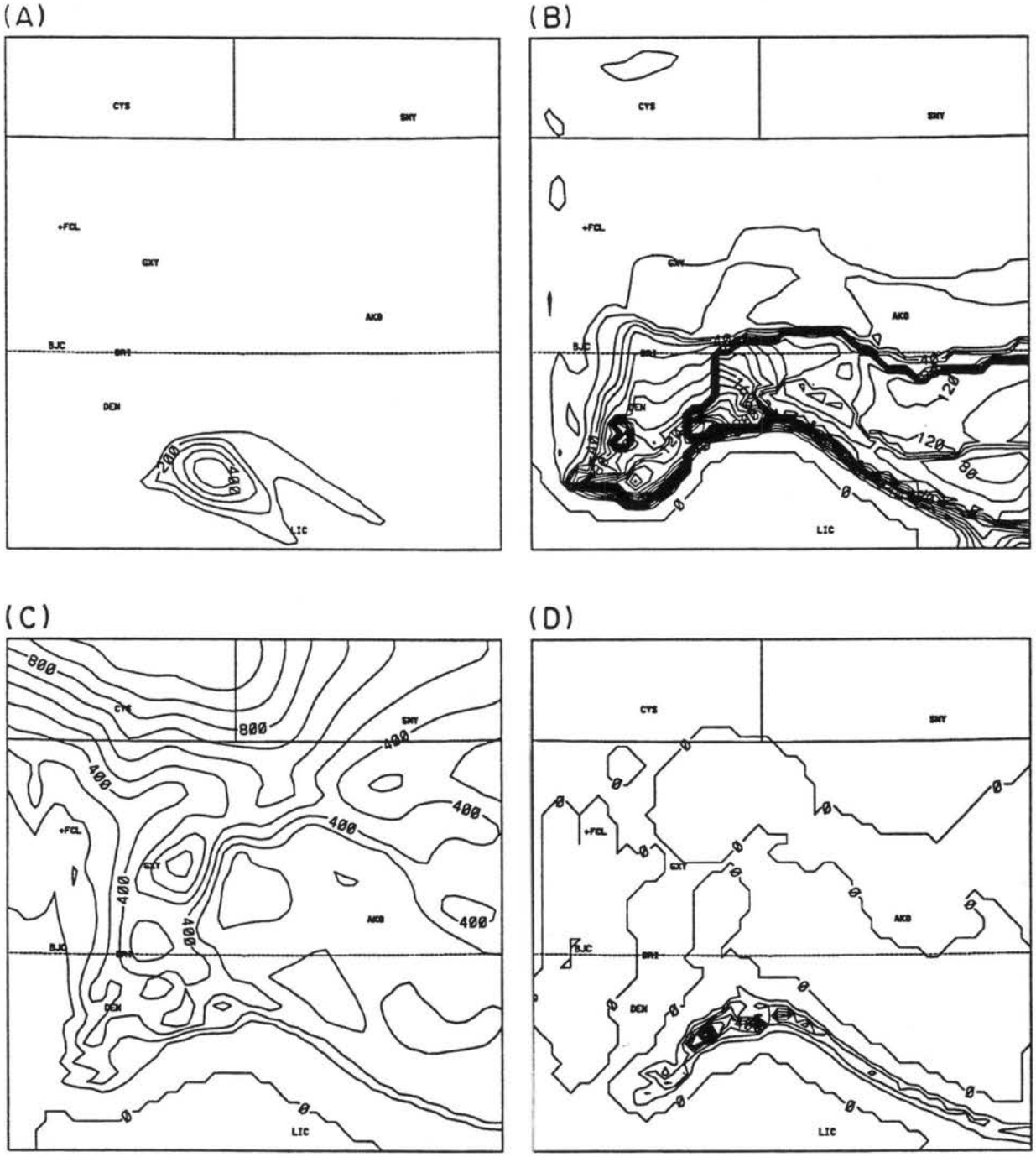

Figure 4.21: Simulated microphysical field using the 1-moment scheme at 75 m AGL at 0500 UTC of (A) cloud mixing ratio (0.1 g kg^{-1}, 0.4 g kg^{-1}), (B) snow mixing ratio (0.0005 g kg^{-1}, 0.03 g kg^{-1}), (C) aggregate mixing ratio (0.01 g kg^{-1}, 0.6 g kg^{-1}), (D) graupel mixing ratio (0.001 g kg^{-1}, 0.006 g kg^{-1}).

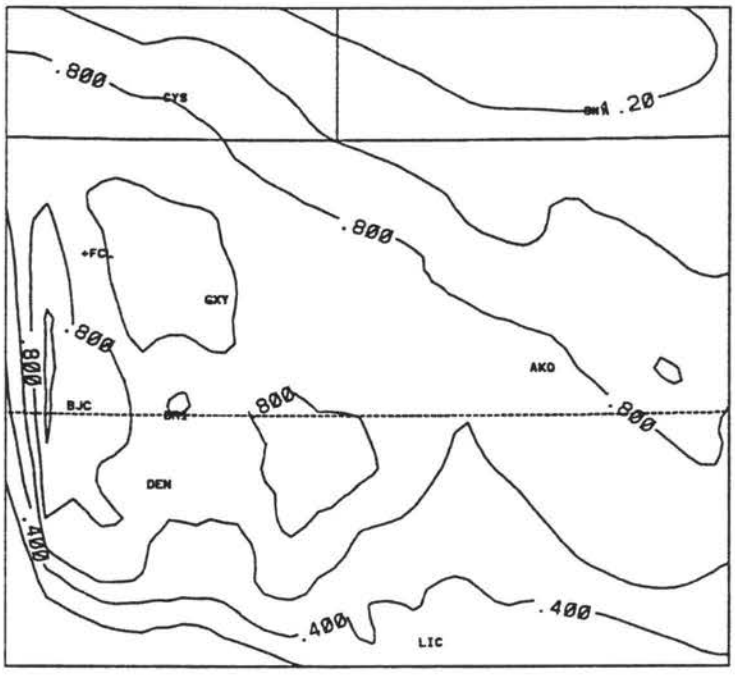

Figure 4.22: Simulated (Grid #3) total precipitation distribution as of 1200 UTC 29 January 1991 for 1-moment simulation. Precipitation is liquid equivalent in millimeters.

that model predicted number concentrations of 10-20 l^{-1} were observed. Observations of the distribution (temporal/spatial) of graupel, riming and aggregation were also consistent with predicted fields, especially near the front. The model also predicted that the sizes of the aggregate diameters decreased steadily away from the cold front, which was observed. Finally, although aircraft data only reported negligible cloud water, the snow crystal network observed a great deal of riming on the crystals, as well as graupel. The model predicted low level cloud water values up to 0.4 g kg^{-1} which resulted in widespread graupel precipitation near the surface. The simulated cloud water was well below the aircraft minimum heights. Also, the model liquid water was near the front, which was south of the aircraft flight path. The spatial distribution of total precipitation was predicted well by the models, however, predicted amounts were more than 2 mm under-predicted near the foothills. This discrepancy may be attributed to the cold front being slower than observed which allowed the downslope flow to persist longer near the foothills. This difference does not appear to be related to the microphysical scheme but, instead, to either the

initialization of the model or the inability of the model to resolve fine-scale topographic forcing.

Comparison between the 2-moment scheme and the 1-moment scheme showed general agreement between the overall kinematic structure in both simulations. With two moments predicted on each hydrometeor, the diameters of each hydrometeor were allowed to vary depending on the environmental conditions. A great deal of variability of aggregate diameters were observed and these were predicted with the 2-moment scheme, however, in the 1-moment scheme the diameter is held fixed which is an unrealistic constraint. Another difference between the two schemes is the evolution of precipitation processes. In the 2-moment scheme the snow crystals were predicted to be much smaller than the prescribed 0.5 mm mean diameters in the 1-moment simulations, which enabled more graupel mass to be produced in the 2-moment scheme. This result is contrary to 1-moment scheme, in which the larger snow crystals were more readily converted to aggregates instead of graupel. Both aggregates and graupel were predicted by both schemes, and both species were observed. The 2-moment scheme allowed the crystals to evolve without a fixed diameter constraint, and for the most part, predicted the microphysical structure better than the 1-moment scheme. The 2-moment scheme also allows for verification of more observable parameters such as reflectivity and crystal diameters and these predicted fields compared favorably to the observed features.

Chapter 5

1 AUGUST 1981 CCOPE SIMULATIONS

The purpose of these numerical simulations is to exercise the microphysical scheme in a convective environment which is dominated by strong vertical velocities, high liquid water contents and hail. It is desired that the case be well documented for microphysical and precipitation verification. This examination focuses on an intense and well studied, supercell storm which passed through the Cooperative Convective Precipitation Experiment (CCOPE) field network in Montana on 1 August 1981.

Extensive observational analysis and modeling studies have been performed on this storm. Miller et al. (1990) performed a thorough observational investigation of this event detailing the air motions and precipitation growth mechanisms of the storm. Rasmussen and Heymsfield (1987c) examined the role of melting and shedding of graupel and hail for hail embryo development in this case through observational analysis and diagnostic modeling. Kubesh et al. (1988) examined T-28 aircraft data as well as other observations, to verify two-dimensional modeling results of the storm. Their simulation used both a bulk water model and a detailed hail category model. The dynamical evolution of the storm was not well reproduced, but the microphysical structure agreed fairly well with the observations. Finally, Wang and Chang (1993) modeled the storm using a three-dimensional 2-moment microphysical predicted scheme. Their simulations produced steady state updrafts which were weaker than observed values. However, other predicted fields based on microphysics, such as the radar reflectivity factors were close to the observed data.

In the following sections, the observational background, and the RAMS modeling results of this case study are presented. Detailed analysis of the simulated microphysical structure is performed which highlights the hydrometeor production and depletion during

the evolution of the storm. Comparisons between the 2-moment and 1-moment simulations are performed with comparisons between the results and observations to validate the reliability of the model. The sensitivity of the model to the shape parameter of hydrometeors and to collection processes is also examined.

5.1 Case study

5.1.1 Environmental background

A detailed observational description of this storm has been presented by several authors (Rasmussen and Heymsfield, 1987; Kubesh et al., 1988; Miller et al., 1990; and Wang and Chang, 1993). The storm developed in moderate shear and very unstable conditions. The surface synoptic conditions (Fig. 5.1) featured a stationary front across the CCOPE domain. Southeasterly moist flow existed to the south of the front, having circulated around the low over Wyoming, and replaced pre-existing drier air over the project area. As the southeasterly flow developed over southeastern Montana, surface moisture mixing ratios increased from 7 to 13 g kg^{-1} in some areas. This flow produced an environment which was conducive for severe thunderstorms as evident by the 1330 MDT Miles City sounding shown in Fig. 5.2. The lifted index for the storm was –8 (based on the Miles City sounding) which is typical for severe hailstorms (Marwitz, 1972 a,b). The convective bulk Richardson number was 22, which is within the range for supercells according to Weissman and Klemp (1984). However, Kubesh et al. (1988) point out that the wind shear for the layer between 3-12 km was found to be characteristic of multicellular storms.

5.1.2 Storm characteristics

Two storms developed over the CCOPE domain during this episode. Although there exists the possibility that the storms developed from a splitting supercell, Miller et al. (1990) cautions that it is uncertain whether the storms developed from splitting of a single updraft or from two separate updrafts. Figure 5.3 shows the evolution of Storms I and II across the CCOPE domain. Both storms moved parallel to each other during the first hour of development, and eventually moved rapidly away from each other as the rapid growth commenced. The right moving storm moved eastward at 8.1 m s^{-1},

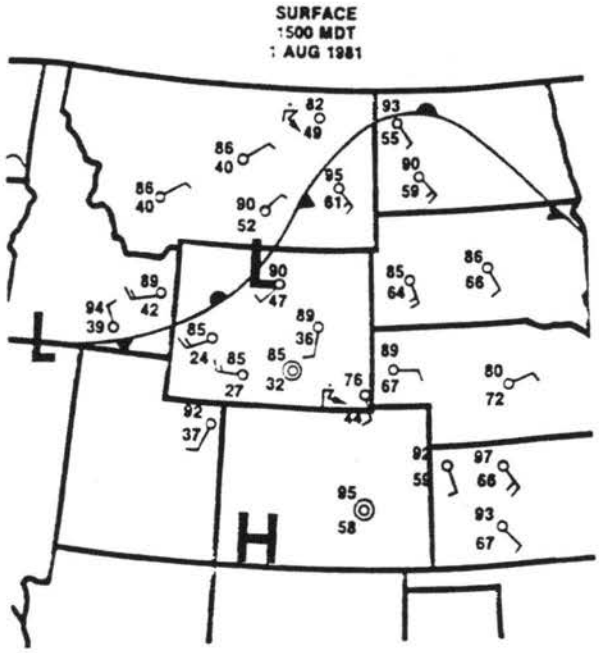

Figure 5.1: Surface synoptic map depiction for 1500 MDT on 1 August 1981 (from Kubesh et al., 1988)

and the left moving storm progressed northeastward at 21 m s^{-1} (Kubesh et al., 1988). The observational network concentrated on the right moving storm due to its prolonged intensity and proximity to the project area.

The storm was characterized by both supercell and multicell characteristics. It developed a long-lived updraft (peak values of 47 m s^{-1}) typical of supercells, but the updraft was vertical, unlike more traditional supercells which have tilted updrafts. The storm traveled along the average cloud-layer wind; unlike typical supercells which tend to travel to the right or left of the mean tropospheric wind. Kubesh et al. (1988) point out that the size of the midlevel area exceeding 45 dBZ radar echo was not quite large enough to qualify for a supercell according to criteria set by Foote and Mohr (1989).

The storm developed two echoes by 1503 MDT separated by 10 km apart (Fig. 5.3). By 1535 Storm II moved rapidly northeastward out of the project area. By 1600 MDT, Miller et al. (1990) point out that a short-lived large cell followed in the path of Storm II giving the resemblance of a splitting storm. Storm I finally reached a steady state

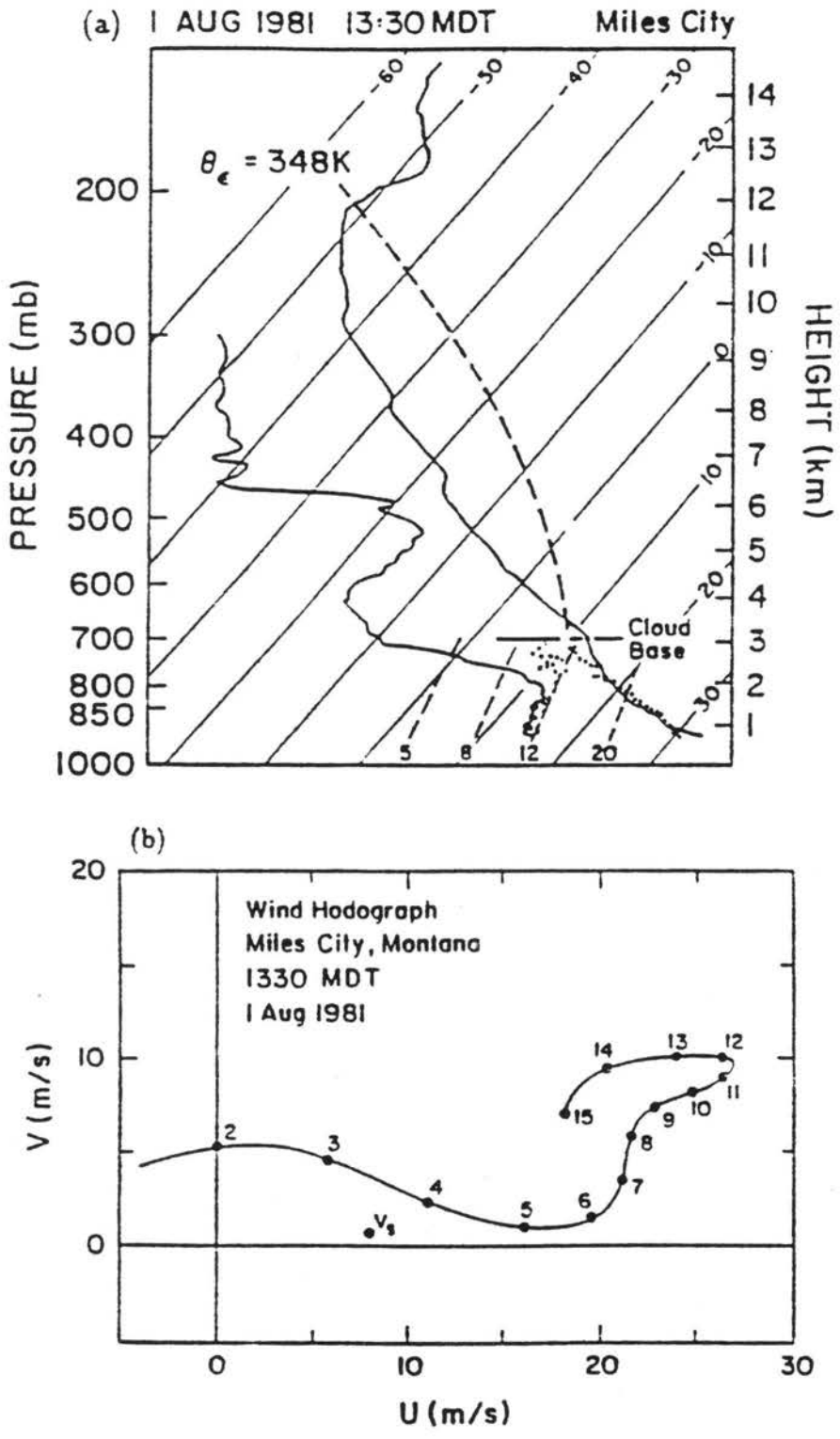

Figure 5.2: 1330 MDT 1 August 1981 Miles City Montana (a) thermodynamic diagram including temperature and dew point. The 1415 Queen Air N306D (heavy dotted lines) of temperature and dew point are also included. A parcel ascending from cloud base would follow the heavy dashed line (equivalent potential temperature of 348°K). (b) Wind hodograph including storm motion as indicated by the dot marked V_s. (From Wang and Chang, 1993)

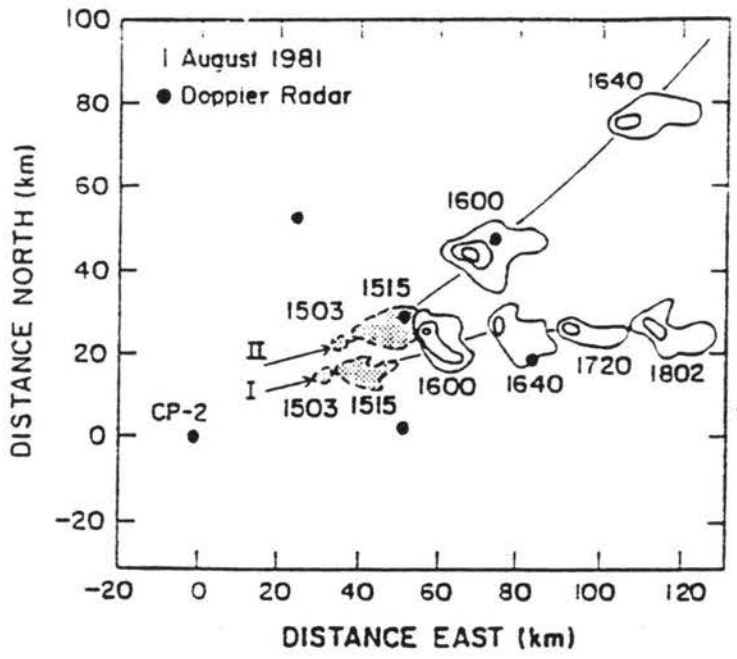

Figure 5.3: Movement of Storms I and II from selected scans by the Bureau of Reclamation Skywater radar. The Doppler radar network is shown in bold dots. The origin of the coordinate system is the CP-2 site. (From Miller et al. 1990)

structure by 1615 MDT. The peak reflectivity was reached at 1630 MDT, and the T-28 research aircraft penetrated the updraft around 1650 MDT. Most of the model simulations are compared to the observed structure during the steady-state period from 1630–1650 MDT.

5.2 Numerical simulations

5.2.1 Model setup

The RAMS model is thoroughly discussed in Section 4.3.1. The microphysical scheme is described in Chapter 2. The coefficients for the heterogeneous ice nucleation parameterization are shown in Fig. 2.1 for the High Plains summertime environment. The control run assumes that the shape of the distribution of each hydrometeor follows an exponential structure (ν=1). However, a sensitivity test which varies ν is conducted. The domain is 16X16X44 on Grid #1 and 42X42X44 on Grid #2, with a horizontal grid spacing of 5 km

on Grid #1 and 1 km on Grid #2. The vertical grid spacing is stretched from 200 m near the surface to 750 m at the top the model. The equations are integrated numerically by a time-splitting procedure for a non-hydrostatic, compressible system (Tripoli and Cotton, 1982) with a large timestep of 10 seconds on the coarse grid and 5 seconds on Grid #2. A flat topography of 800 meters elevation is assumed. A horizontally homogeneous initialization is employed using the 1330 MDT Miles City sounding (Fig. 5.2). To follow the modeled storm, a mean environmental wind of 8.3 m s^{-1} is removed to keep the storm within Grid #2 boundaries. To initiate convection a 1.5°C warm bubble (10X10X2.5 km^3) is introduced into the initial field. The simulation is run for 90 minutes.

The numerical experiments performed are summarized in Table 5.1. The control run is a 2-moment prediction run where ν=1 for all hydrometeors. SENS1 is the same as the control run except that only one moment of each hydrometeor category, the mixing ratio, is

Table 5.1: Experimental design of numerical experiments for 1 August 1981 case study

Experiment	Description
Control run	2-moment run with ν=1 for all hydrometeors
SENS1	1-moment run with D_m specified
SENS2	1-moment run with N_0 specified
SENS3	sensitivity to hydrometeor collection of rain
SENS4	sensitivity to $\nu = 3$ for all hydrometeors
SENS5	sensitivity to $\nu = 3$ for hail only, all others $\nu = 1$

predicted (except 2-moments for pristine ice crystals). The prescribed mean particle mass has a diameter of 0.1 cm for rain, snow, aggregates, and graupel, and 0.5 for hail. SENS2 is also a one-moment run (except 2-moments for pristine ice crystals) but N_0 is specified. The prescribed values are 8×10^6 m^{-4} for rain, 3×10^6 m^{-4} for snow, 1.8×10^6 m^{-4} for aggregates, 1.1×10^6 m^{-4} for graupel and 4×10^4 m^{-4} for hail. SENS3 is a sensitivity test to examine the hydrometeor collection of rain. As was noted in Section 2.6.5, ice collecting raindrops will most likely be converted to hail at sub-freezing temperatures in the model. As a sensitivity to this collection process, this experiment examines the effect of changing the collection path of ice collecting rain from hail in all other simulations to graupel in this experiment. Otherwise there are no changes from the control run. SENS4

and SENS5 are two-moment simulations in which the sensitivity of the model to variations in the ν parameter is examined while all other parameters are unchanged from the control run. SENS4 experiment assumes all hydrometeors have a $\nu = 3$ and SENS5 experiment assumes that only the hail category has a $\nu = 3$, while all other species have a ν=1.

It must be emphasized that the convection initiated in this simulation is artificially produced. Since a horizontally-homogeneous initialization is employed, the simulated environment is restricted to a single sounding which is assumed over the entire domain. Inhomogeneities such as outflow boundaries from nearby convection which may have influenced the observed storm, cannot impact this simulation. Also, the type of convection produced by the warm bubble is dependent on the prescribed environment. For the given environment conditions, the simulation should produce a splitting supercell which may or may not have occurred. The intent of this simulation is to generate a quasi-steady convective storm which is similar to the observed case. The quasi-steady environment is desirable for two reasons. First, this steady period of the storm was well observed by the project. Secondly, the steady-state characteristic of the storm facilitates comparisons between the observed microphysical structure of the storm to the model results, which should test the performance of the new microphysical model.

5.2.2 Control run

As was shown in Fig. 5.3, two storms moved across the CCOPE project area during this operations period. The dominant storm moved in a eastward direction and the weaker storm moved rapidly northeastward. The simulation produced a similar scenario as shown in Fig. 5.4. These figures are shown at 9 km AGL, since the vertical velocity field is very strong at this level. After 30 minutes of simulation, the updraft has begun to split, with two distinct updrafts (peak values 25 m s^{-1}) developing from the initial convective pulse. The accompanying total ice mixing ratio field also shows two distinct peaks, with the northern storm (5 g kg^{-1}) a bit stronger than the southern storm (4 g kg^{-1}). The two storms have separated further by 60 minutes of simulation time. The northern storm has moved northeastward to the northern border of the domain with peak vertical velocities of 35 m s^{-1} (Fig. 5.4c). This simulated northern storm moves much slower than the observed

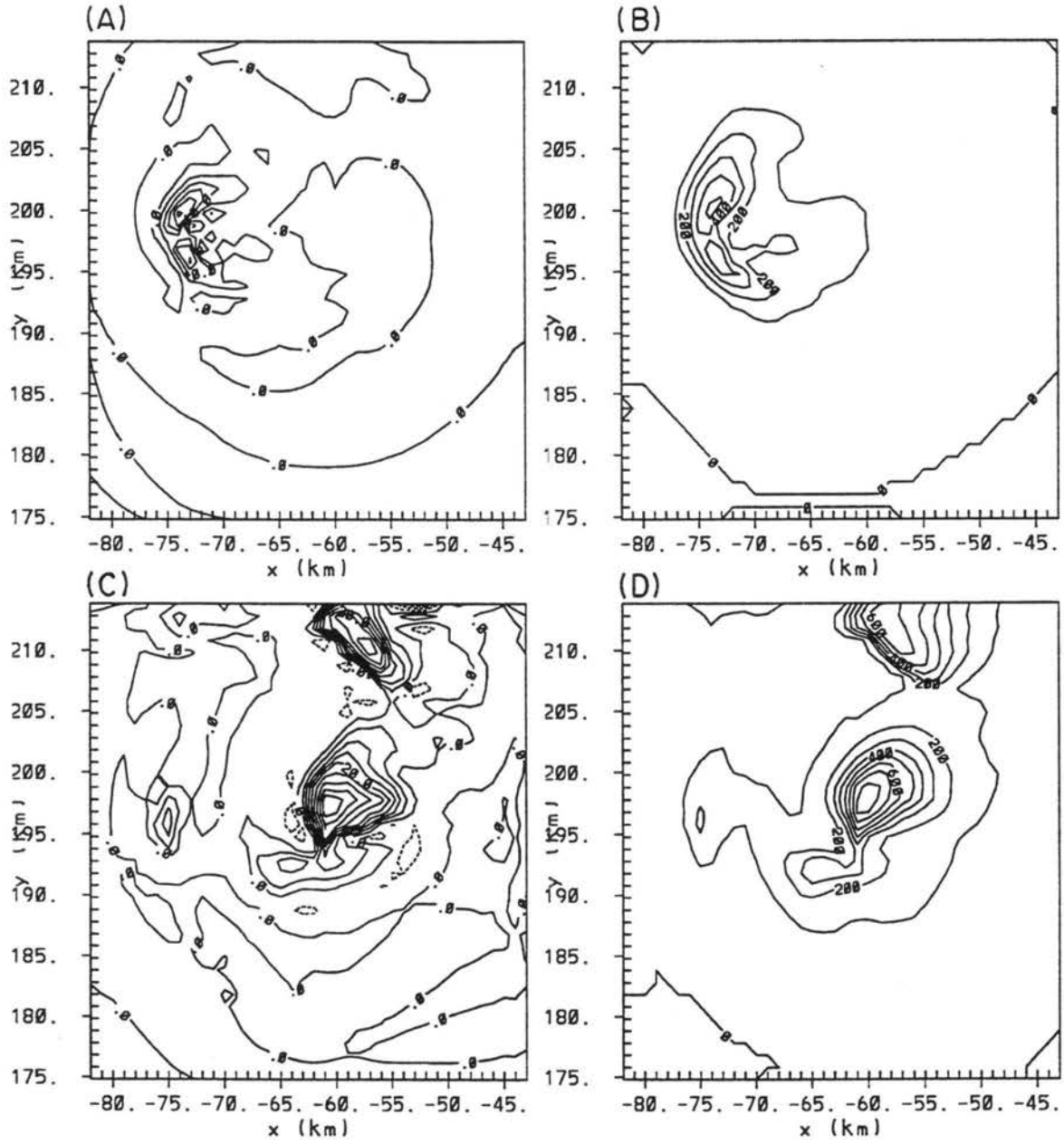

Figure 5.4: Simulated vertical velocities and total ice mixing ratios (contour interval, maximum) at 9000 m AGL for the control run after 30 minutes of simulation time for (A) vertical velocity (5 m s^{-1}, 25 m s^{-1}) and (B) total ice mixing ratio (1 g kg^{-1}, 5 g kg^{-1}), and after 60 minutes of simulation time for (C) vertical velocity (5 m s^{-1}, 40 m s^{-1}) and (D) total ice mixing ratio (1 g kg^{-1}, 8 g kg^{-1}).

northern storm, and remains in the model domain through the lifetime of the simulation. The storm of interest, located in the center of the domain, has a peak updraft of 40 m s^{-1}. The total ice field at this time (Fig. 5.4d) shows a peak mixing ratio of 6 g kg^{-1} for the northern storm and 8 g kg^{-1} for the storm of interest. This southern storm maintains a fairly steady structure during the next 30 minutes, and this simulation period is compared to the steady-state observed period from 1630-1650 MDT.

A vertical cross-section of the simulated (60 minutes simulation time) and observed airflow (1630-1650 MDT) is shown in Fig. 5.5. The comparison highlights several important features which the model was able to simulate which occurred in the observed structure. The simulated updraft is quite similar to the observed structure. The orientation of the simulated updraft is nearly vertical which was observed. Also, the placement of the simulated updraft maxima is centered between 8–10 km MSL with peak values of 43 m s^{-1} near 10 km MSL, which was close to the observed magnitude (peak updrafts in the storm were 47 m s^{-1}). The width of the simulated updraft is slightly less than the observed updraft. Areas of downdrafts occur in the simulation, between 10 and 12 km MSL east of the updraft, and between 2–4 km MSL just east and west of the main updraft. These downdraft regions were also observed, but the magnitudes of the simulated downdrafts found between 10 and 12 km MSL are 3 m s^{-1} greater than the observations. The simulated flow pattern also looks consistent with the observations, except in the lowest 2 km east of the updraft. Here, the simulated flow shows strong easterly winds of 10 m s^{-1} where the observed structure showed weak flow. However, strong easterly inflow in the lowest levels was observed during the lifetime of the storm.

The observed updraft, flow field, and reflectivities at 5.6 km MSL for the control run at 1630 MDT are shown in Figs. 5.6 and 5.7. These horizontal cross-sections are compared to the simulated fields after 60 minutes and 90 minutes as shown in Fig. 5.8. The simulated main updraft is very similar to that observed (Fig. 5.6) at both simulation times. The simulated peak updraft is 25 m s^{-1} at 60 minutes (Fig. 5.8a) and 19 m s^{-1} at 90 minutes (Fig. 5.8c). The orientation of the simulated updraft is southwest/northeast at 60 minutes but rotates to a more west/east orientation by 90 minutes which is shown in the

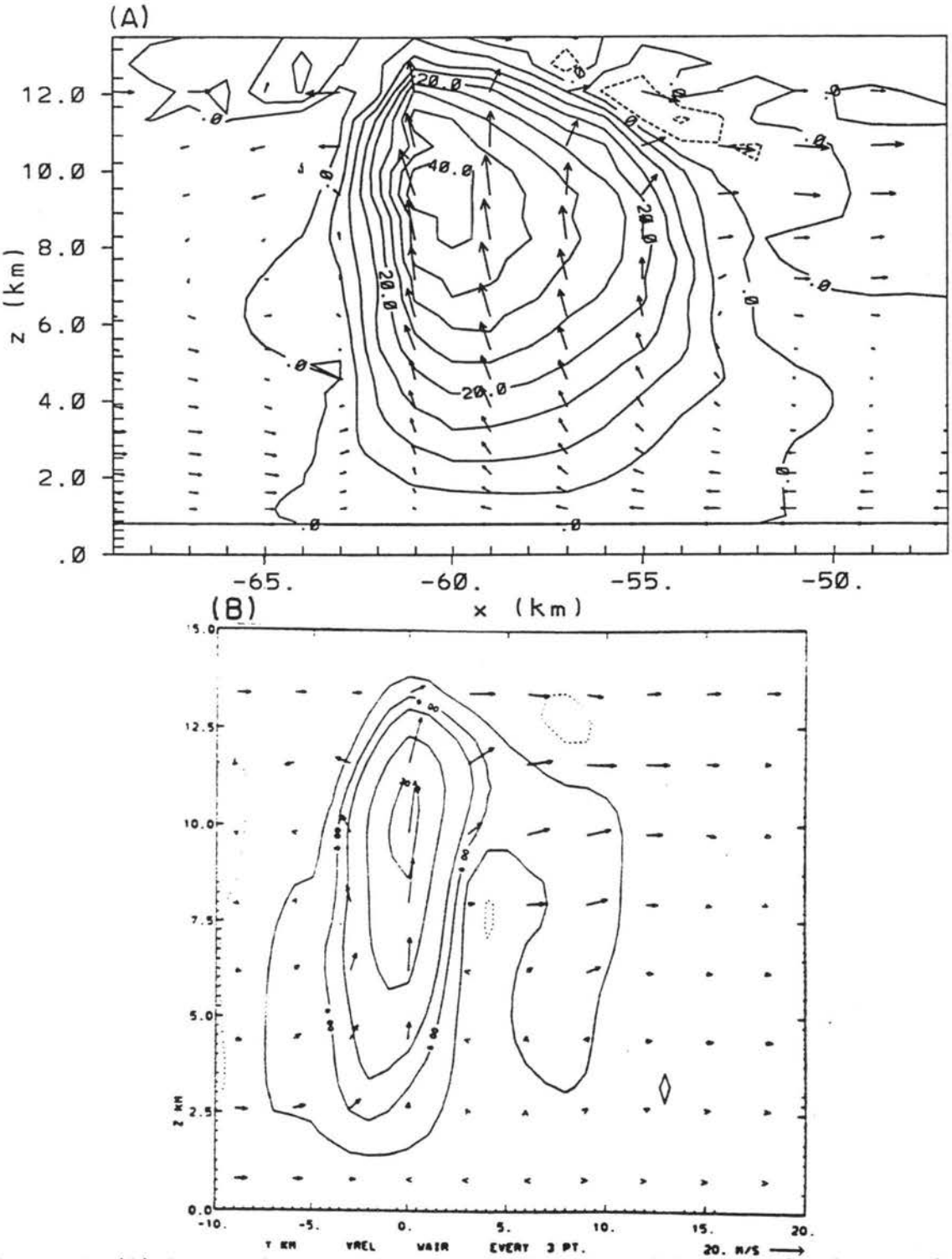

Figure 5.5: (A) A vertical cross-section through the center of the storm for the control run with simulated vertical velocities (5 m s^{-1}, 43 m s^{-1}) with solid contours denoting positive values and negative contours denoting negative values. Wind vectors are also included with maximum vector of 43 m s^{-1}. This and vertical cross-sections subsequent figures are "windowed in" to isolate the main updraft. (B) Airflow in the 1 August storm, based on multiple Doppler, aircraft, surface, and rawinsonde measurements from the period 1630–1650 MDT. Winds are relative to the storm reflectivity core. The solid contours represent updrafts of 2, 6, 10, 20, and 30 m s^{-1}; and dashed contours represent downdrafts of 2 m s^{-1}. (from Kubesh et al., 1988)

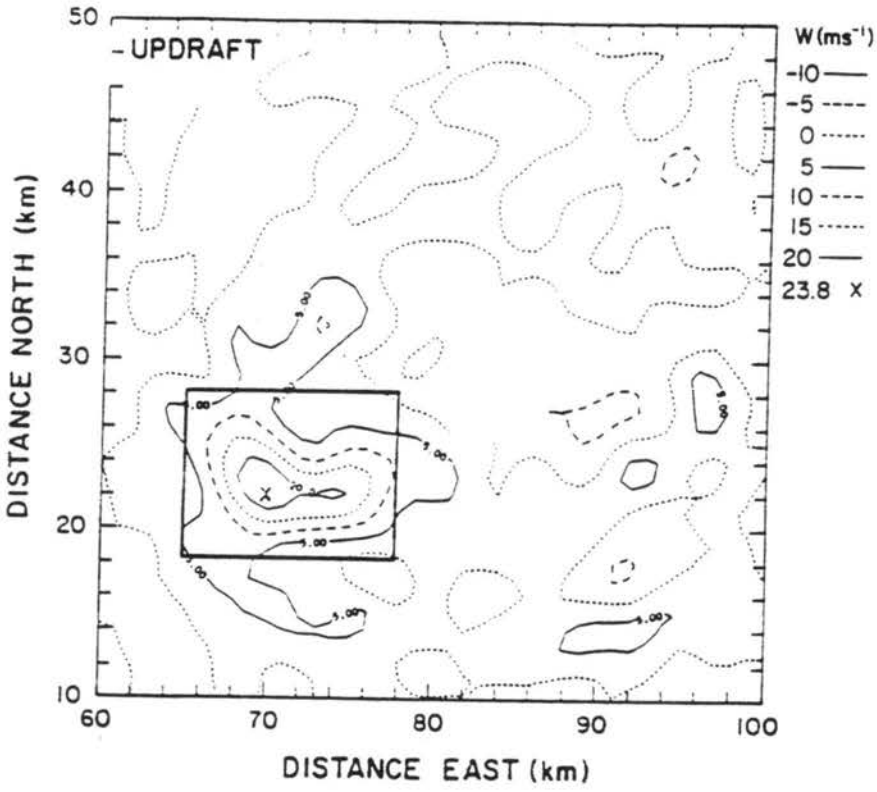

Figure 5.6: Doppler derived updraft velocity at 5.6 km MSL at 1630 MDT. (from Rasmussen and Heymsfield, 1987c)

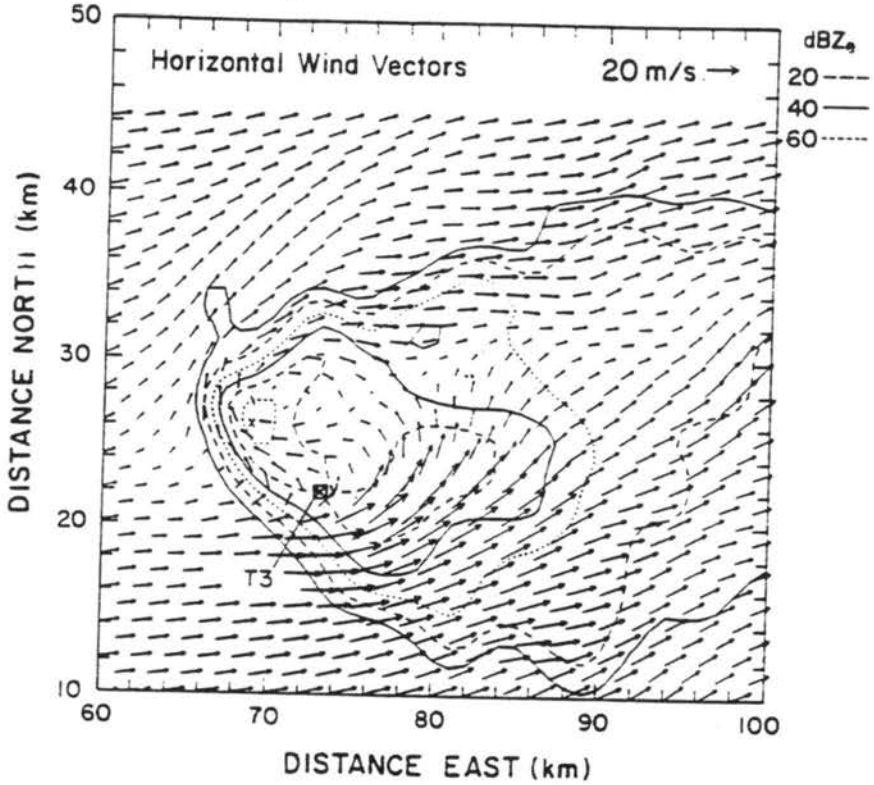

Figure 5.7: Horizontal wind vectors from the Doppler wind field at 5.6 km MSL, with the 1630 to 1650 MDT time averaged radar reflectivity superimposed. (from Rasmussen and Heymsfield, 1987c)

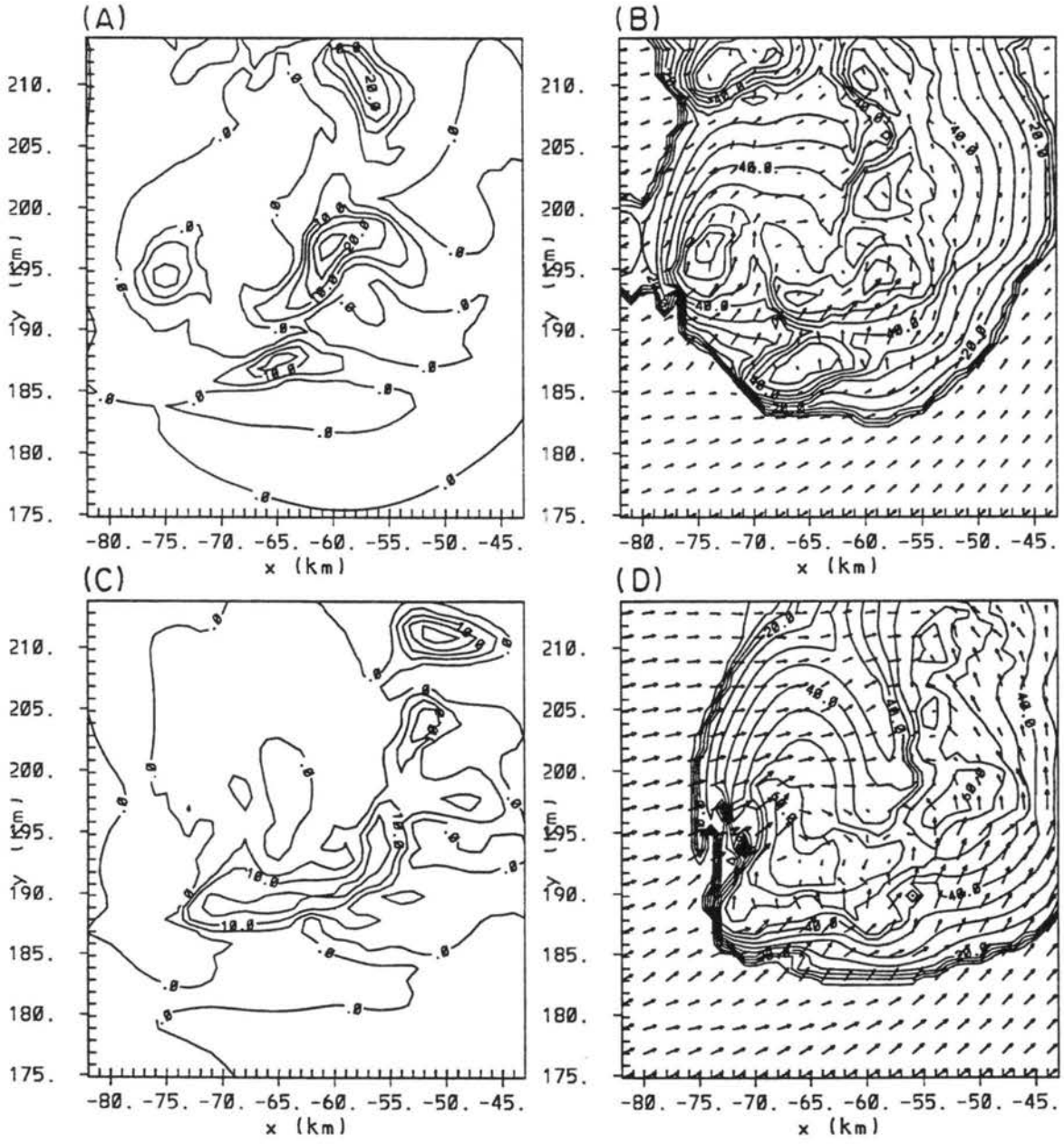

Figure 5.8: Simulated vertical velocities and reflectivity (contour interval, maximum) at 5.6 km MSL for the control run after 60 minutes of simulation time for (A) vertical velocity (5 m s^{-1}, 25 m s^{-1}) and (B) reflectivity (5 dBZ, 60 dBZ) and wind vectors (maximum value 25 m s^{-1}), and after 90 minutes of simulation time for (C) vertical velocity (5 m s^{-1}, 21 m s^{-1}) and (D) reflectivity (5 dBZ, 65 dBZ) and wind vectors (maximum value 21 m s^{-1}).

observed field. The simulated vertical velocity fields also shows another updraft near the northern section of the domain in response to the northern storm. At 60 minutes there are also weaker updrafts south of the main updraft (15 m s^{-1}) and west of the main updraft (10 m s^{-1}), however, these become incorporated into the main updraft by 90 minutes. The observed reflectivity pattern and flow fields are shown in Fig. 5.7. Observed peak reflectivities (60 dBZ) were found in and to the east of the updraft. Another feature of the reflectivity pattern was a strong reflectivity gradient found on the western boundary of the storm. At 60 minutes, the simulated reflectivity (Fig. 5.8b) has many small scale peaks in the structure which are responding to the isolated peaks in the vertical velocity field producing larger hydrometeors in these locations. Peak values are found near the western boundary of the reflectivity core near an isolated updraft, and another one is found near Y=185 km and X=-65 km which is forced by the weaker updraft to the south of the main updraft. A broad region of reflectivities greater than 50 dBZ is co-located with the main updraft near Y=195 km and X=-60 km. Another difference between the model results and the observations is found on the northern boundary where strong reflectivity is produced in response to the simulated northern storm.

By 90 minutes the reflectivity pattern (Fig. 5.8d) becomes more coherent and similar to the observed structure. Peak reflectivities are near the main updraft with values up to 65 dBZ, and a strong reflectivity gradient is present on the western boundary, similar to observations. The observed flow pattern showed prevailing westerly flow south of the storm with more southwesterly flow northwest of the storm. A weak circulation was evident near the updraft. The simulated flow field features mostly west to southwest flow outside of the storm. The flow field at 60 minutes has a more southerly wind component northwest of the main updraft. A disorganized circulation pattern is also evident near the main updraft. The flow pattern is modified by the northern simulated storm which was not observed since it was well north of this area at this time.

The T-28 aircraft observations are shown in Fig. 5.9. This figure shows FSSP, 2-D, hail foil impactor, and hail sensor concentration measurements, as well as vertical velocities as the aircraft traversed the updraft. A cross-section of some of the microphysical fields is

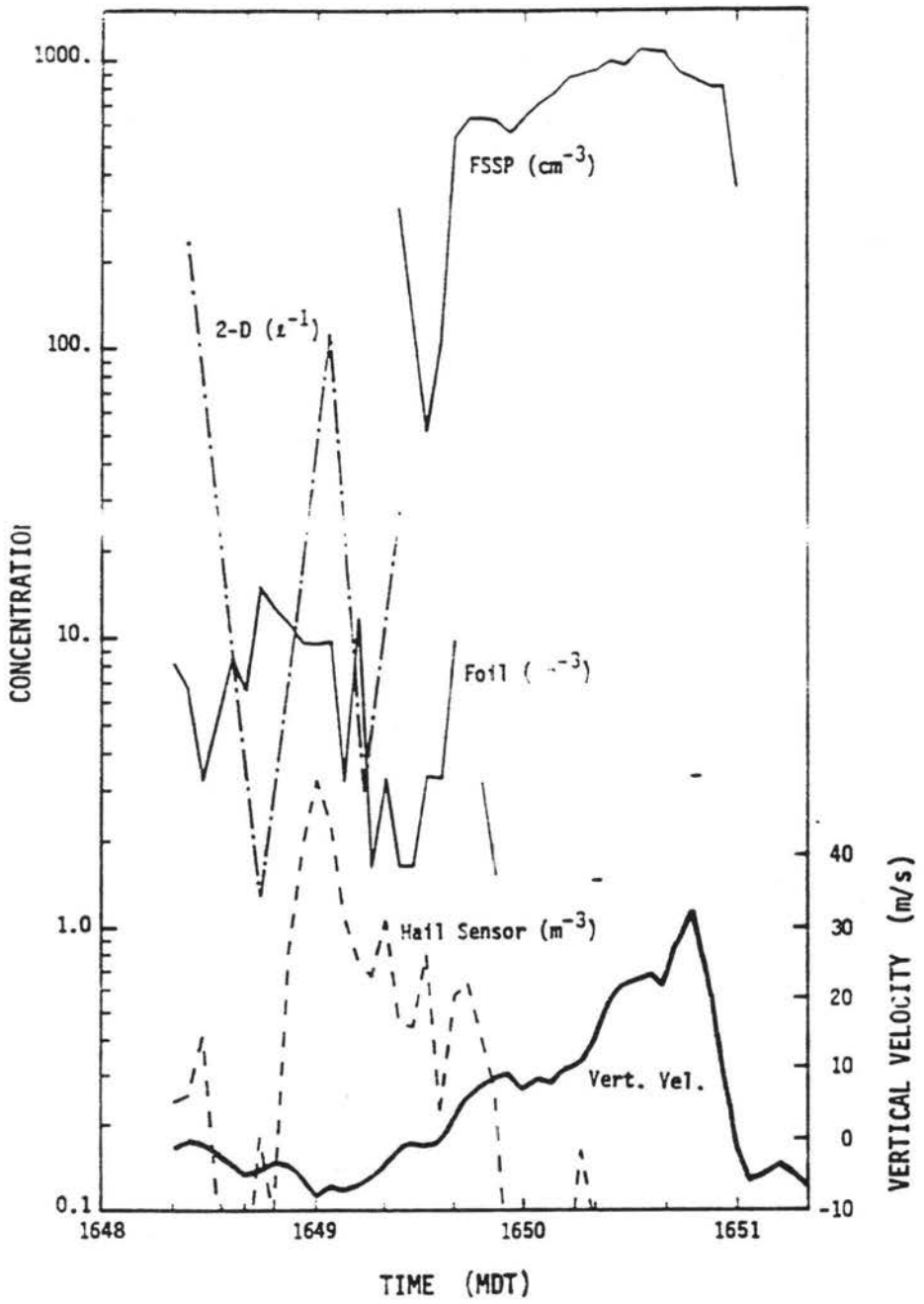

Figure 5.9: Particle concentrations measured by the T-28: FSSP, particles from 3 to 45 μm; 2-D, 31 to 1000 μm; foil, 1 to 5 mm; hail sensor 4.5 to 50 mm. The vertical velocity is also shown. (From Kubesh et al., 1988)

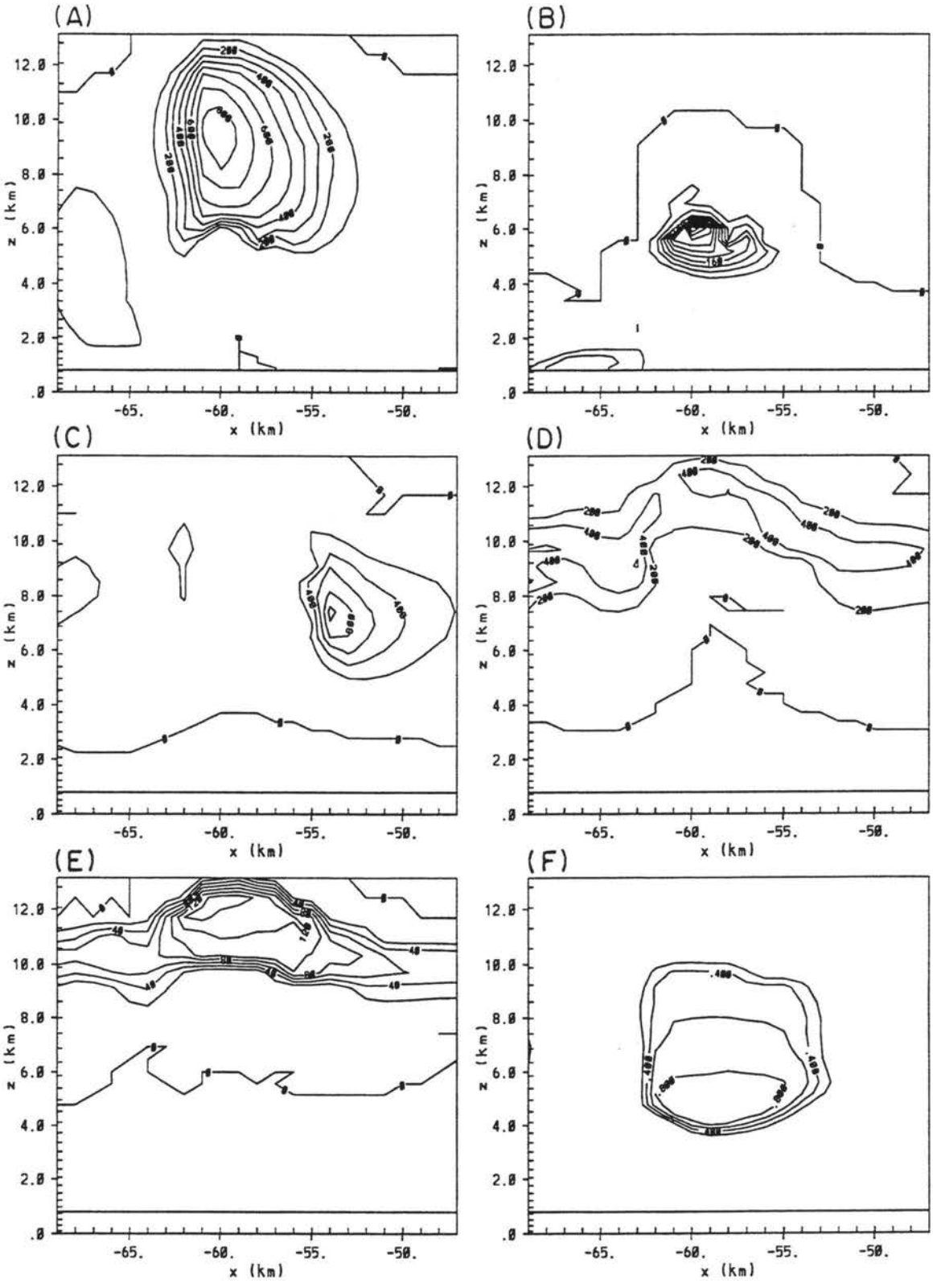

Figure 5.10: The control run fields of (A) hail mixing ratio (1 g kg^{-1}, 8 g kg^{-1}), (B) rain mixing ratio (0.4 g kg^{-1}, 4.2 g kg^{-1}), (C) graupel mixing ratio (0.2 g kg^{-1}, 1.0 g kg^{-1}) and (D) aggregate mixing ratio (0.2 g kg^{-1}, 0.6 g kg^{-1}), (E) pristine ice crystal mixing ratio (0.2 g kg^{-1}, 1.4 g kg^{-1}) and (F) liquid water content (0.2 g m^{-3}, 0.8 g m^{-3}). Contour intervals and maxima are shown in brackets. All fields are at 60 minutes of simulation time.

shown in Fig. 5.10. These fields are valid at 60 minutes simulation time. The hail mixing ratio field shows a broad region of hail mass centered near 9 km MSL (peak values 8 g kg^{-1}). This hail peak is found in the updraft core and peripheral regions of the updraft which was observed by the T-28 aircraft (Rasmussen and Heymsfield, 1987c). Both the observed and simulated hail in the updraft experienced wet growth. Rain mixing ratios (Fig. 5.10b) show 2 distinct peaks in the simulated results. One area is found near 5.5 km MSL with a 4.2 g kg^{-1} peak. Table 5.2 quantifies the sources for rain mass at this location at 60 minutes of simulation time. Most of these drops form by melting and shedding from the hail category, which was observed to be prevalent at this level and was suggested by Rasmussen and Heymsfield (1987c) to be a dominant source of hail embryos. The rain in this region is also being generated by autoconversion of cloud droplets to rain and to a smaller degree due to collection of cloud water by raindrops. The percentage of converted mass due to collection by other ice categories such as pristine ice, snow, aggregates and graupel is low since the model will most likely convert this mixed-phased mass to hail before converting it completely to rain. The other peak near the surface (0.9 g kg^{-1}) has formed from a

Table 5.2: Conversion sources for rain at 5.5 km MSL

Conversion process	percentage of mass transferred to rain
melting and shedding	61%
autoconversion	30%
rain collection of cloud droplets	8%
rain collection of other categories	1%

combination of melting and shedding of drops from the hail category which has fallen out in the downdraft west of the main updraft. The graupel mixing ratio field (Fig. 5.10c) shows a broad region of graupel mass above 5 km MSL with most of graupel mass east of the main updraft (peak values 1.0 g kg^{-1}). This eastern region of graupel mass is co-located with an enhanced region of liquid water content (Fig. 5.10f) forced by the eastern periphery of the updraft as shown in Fig. 5.5a. Graupel mass in and near the updraft is relatively lower than its surrounding altitudes due to the large amounts of rain near 6 km MSL which optimizes the transfer to hail due to collection. Pristine ice crystal and aggregate

mass (Fig. 5.10 d,e) are confined to higher altitudes of the cloud making up most of the mass in the anvil. Aggregation was observed by Heymsfield and Palmer (1986) to be very active in the anvil of the cloud. Aggregates and snow crystals which exist in the anvil fall into this higher liquid water region quickly converting to graupel. Predicted peak liquid water contents (0.8 g m^{-3}) are nearly half as much as observed values. Possible reasons for this difference is that autoconversion from cloud to rain may have been overpredicted, and hydrometeor collection of cloud water is too efficient in the model. Cloud top extends to 14.5 km MSL which is slightly lower than the observed cloud top (15 km MSL).

Number concentrations and mean diameters of selected hydrometeor fields are shown in Fig. 5.11. The number concentration of hail (D >5.0 mm) (Fig. 5.11a) shows that peak values (14 m^{-3}) are higher than the observed peak hail number concentrations of 3.0 m^{-3} (Kubesh et al., 1988). The mean hail diameter field in an assumed gamma distribution is shown in Fig. 5.11b. This field shows most of the mean hail diameters are approximately 1.4 mm, with larger diameters at lower altitudes where peak mean diameters are over 2.0 mm. As is highlighted by Fig 5.11a, since the model assumes a gamma distribution for hail, these mean diameters imply that larger hailstones even greater than 10 mm exist. The rain number concentration field shows a distinct peak near the updraft at 6 km MSL. Peak values of rain number concentration are close to 4 l^{-1} due to a combination of melting and shedding from hail and autoconversion from cloud droplets. Peak values of rain concentration were observed to be 2 l^{-1} near 5-6 km MSL. Elsewhere in the domain, rain number concentrations are less than 0.1 l^{-1}. The mean diameters of rain show values are below 0.5 mm above 6 km MSL, but increase over lower altitudes with most values over 0.8 mm below 4 km MSL; observations showed rain diameters between 0.2 and 0.6 mm above 4 km and larger drops greater than 1 mm were found below 4 km. Graupel number concentrations (Fig. 5.11e) are mostly in the 1–6 l^{-1} range and exist above 6 km MSL, however, diameters in and near the updraft are 0.5 to 1.0 l^{-1}. Observed peak values of graupel were 1 l^{-1} near 6 km in and near the updraft. Pristine ice crystal number concentrations (Fig. 5.11f) are predicted up to 54000 l^{-1} at temperatures colder than -40°C which may be over-predicted in the model. A very strong updraft is producing

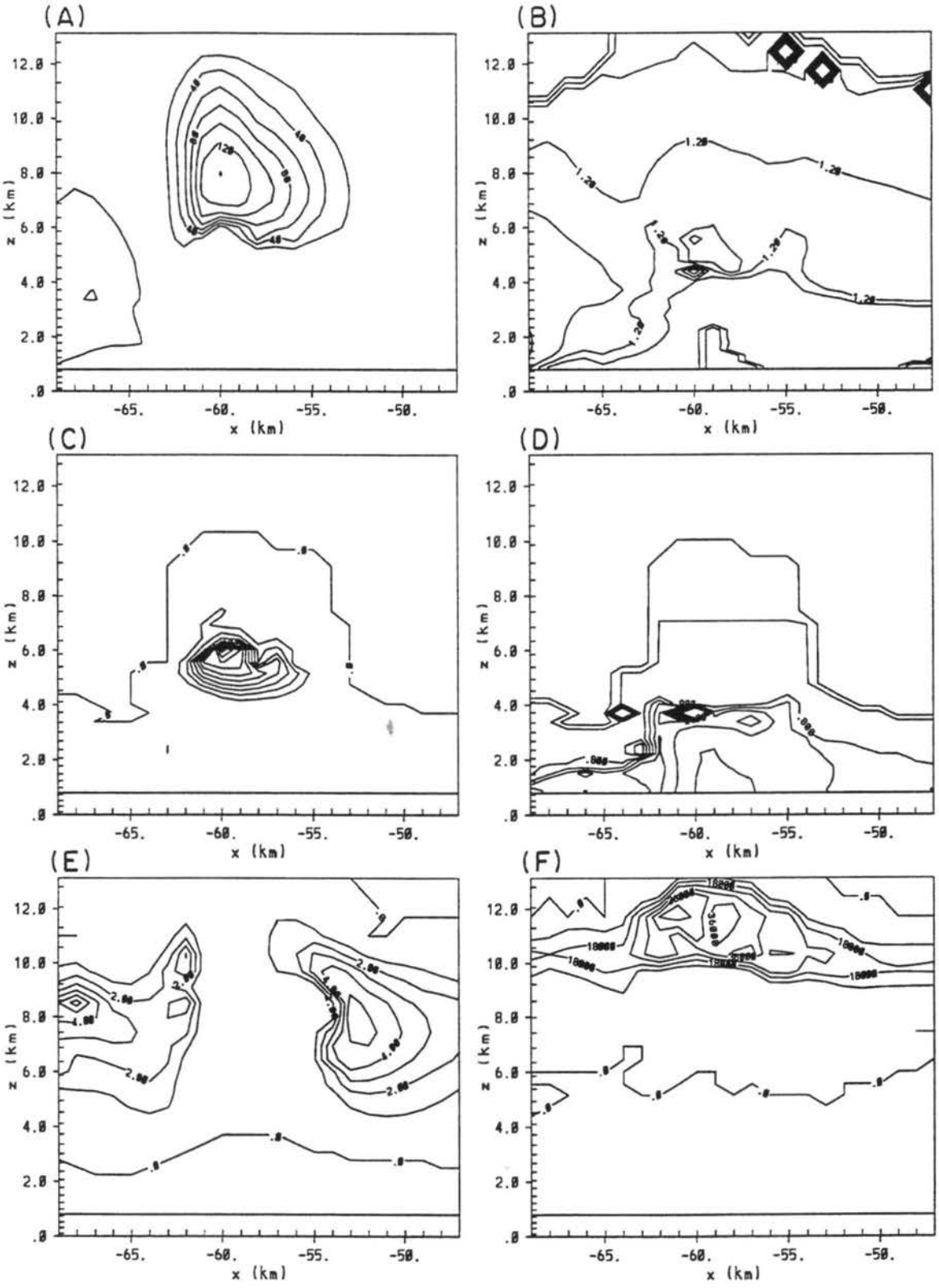

Figure 5.11: Simulated fields for the control run of (A) hail number concentration (2 m^{-3}, 14 m^{-3}), (B) hail mean diameter (0.3 mm, 2.1), (C) rain number concentration (0.4 l^{-1}, 4.0 l^{-1}) and (D) rain mean diameter (0.3 mm, 2.1 mm), (E) graupel number concentration (1 l^{-1}, 6 l^{-1}) and (F) pristine ice crystal number concentrations (9000 l^{-1}, 54000 l^{-1}). Contour intervals and maxima are shown in brackets. All fields at 60 minutes of simulation time.

large amounts of cloud water and nearly saturated conditions above 9 km MSL. At these altitudes, both homogeneous freezing of cloud water and haze particles are occurring. Since the aerosol and cloud number concentrations are not predicted, a potentially large number of ice crystals are produced, which is based on the fixed number concentrations of aerosols and cloud droplets prescribed in the model. A solution to this potential problem would be to predict the number concentrations of aerosols and cloud droplets.

5.2.3 SENS1–sensitivity to 1-moment prediction (D_m specified)

Results of the 1-moment simulation with D_m specified are discussed in this section. This experiment predicts on one moment for each hydrometeor category (except 2-moments for pristine ice crystals), and assumes a fixed mean diameter for each species. The mean particle mass has a diameter of 0.1 cm for rain, snow, aggregates, and graupel, and 0.5 cm for hail.

The evolution of the vertical velocities and total ice field (Fig. 5.12) is very similar to the control run. The major difference is that the northern storm is slightly more north than in the control run. A vertical cross-section of the vertical velocity field is shown in Fig. 5.13. This figure shows only slight differences from the control run. The updraft is slightly weaker (35 m s^{-1} peak updraft) and not as wide as the control run. The simulated vertical velocity and reflectivity fields at 5.6 km MSL are shown in Fig. 5.14. These vertical velocity fields show a similar structure after 60 minutes of simulation time compared to the control run, however, after 90 minutes of simulation time, the main updraft (15 m s^{-1}) is slightly weaker than the control run and there exists two strong updrafts (greater than 15 m s^{-1}) to the north. The reflectivity pattern shows some similarities to the control run, but the major difference is that the area of reflectivity over 60 dBZ is much greater than the control run. Also, peak values in SENS1 are over 80 dBZ which is much greater than the control run (65 dBZ). This difference is due to the diameter dependence of reflectivity, and in this 1-moment simulation a prescribed diameter of 0.5 cm is assumed which dominates the reflectivity pattern.

The mixing ratios at 60 minutes of simulation time for SENS1 are shown in Fig. 5.15. The hail mixing ratio shows a similar structure to the control run with slightly larger

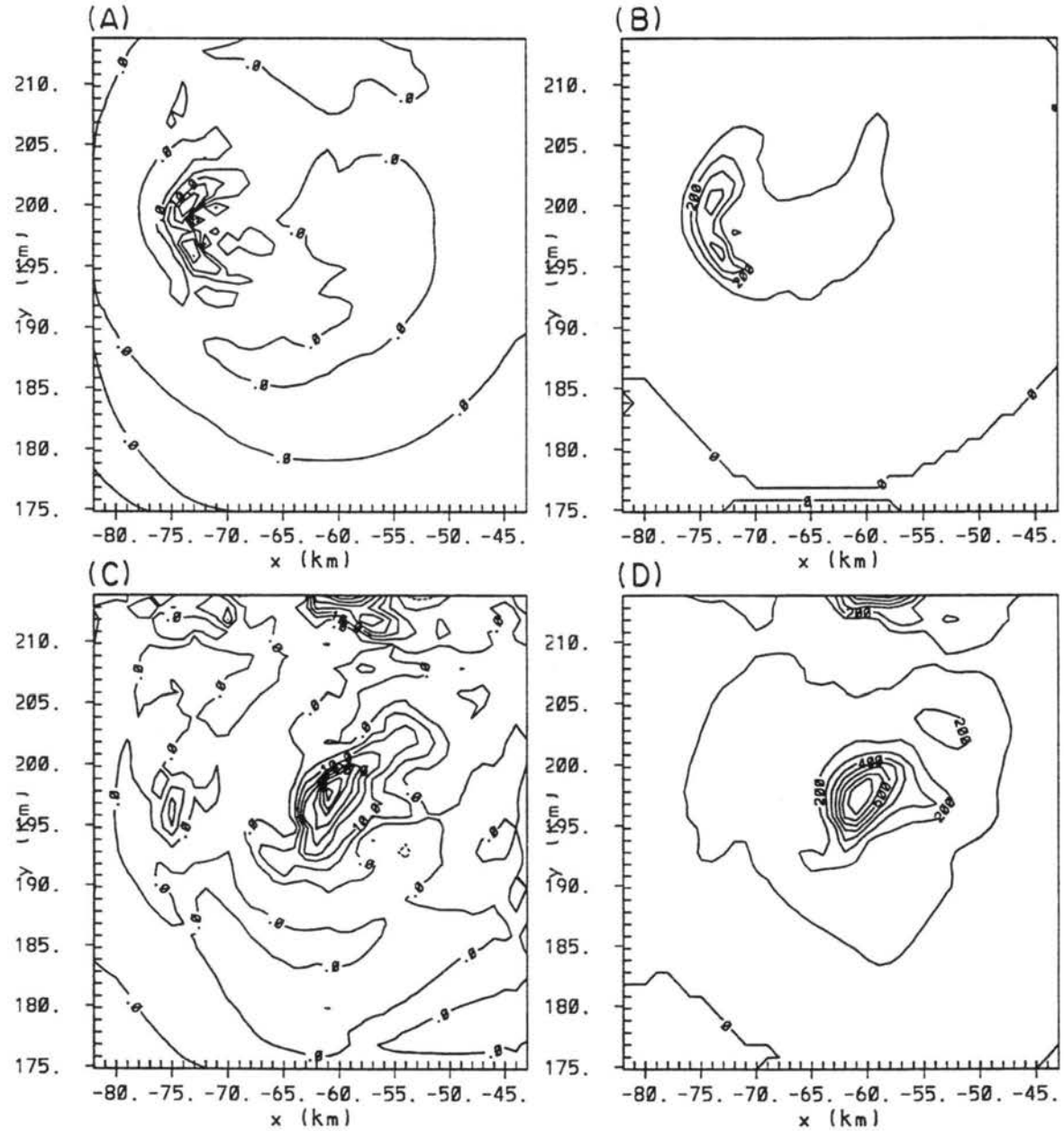

Figure 5.12: Simulated vertical velocities and total ice mixing ratios (contour interval, maximum) at 9000 m AGL for SENS1 after 30 minutes of simulation time for (A) vertical velocity (5 m s^{-1}, 25 m s^{-1}) and (B) total ice mixing ratio (1 g kg^{-1}, 5 g kg^{-1}), and after 60 minutes of simulation time for (C) vertical velocity (5 m s^{-1}, 40 m s^{-1}) and (D) total ice mixing ratio (1 g kg^{-1}, 8 g kg^{-1}).

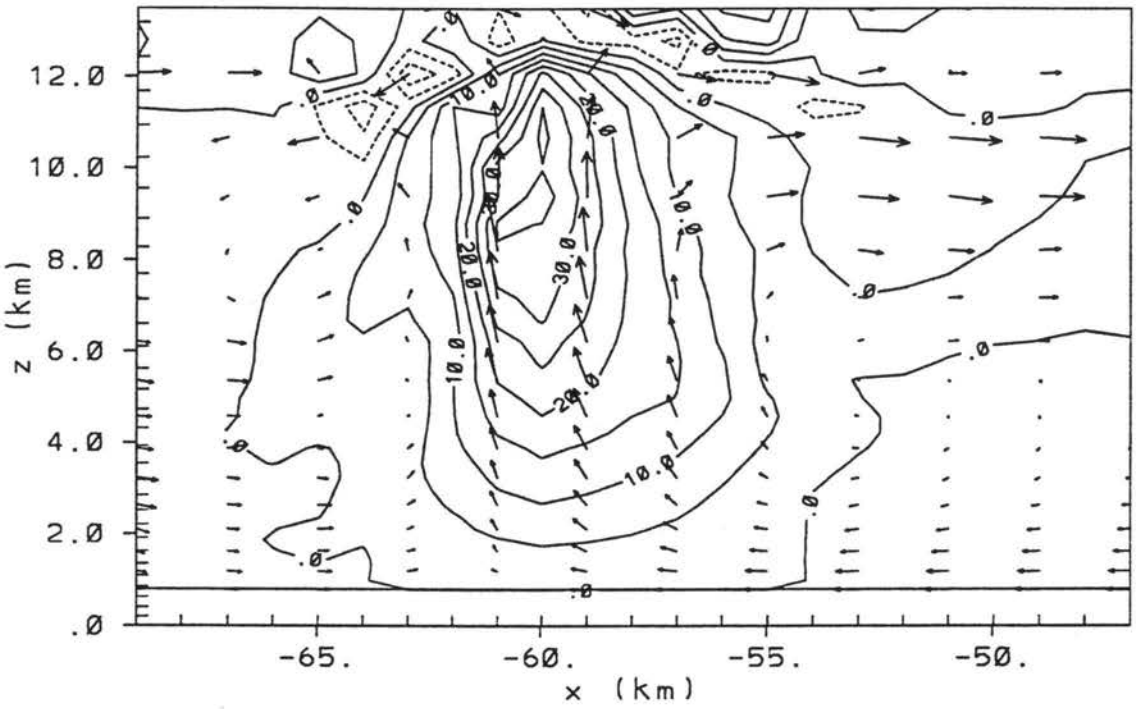

Figure 5.13: A vertical cross-section through the center of the storm for SENS1 with simulated vertical velocities (5 m s^{-1}, 35 m s^{-1}) with solid contours denoting positive values and negative contours denoting negative values. Wind vectors are also included with maximum vector of 35 m s^{-1}.

peak values found near 8 km MSL. The peak is displaced about 1 km lower than the control run in response to the larger hail particles in SENS1 which have larger fallspeeds. The rain mixing ratio field shows peak values of 4.5 g kg^{-1} found at 4–6 km MSL which is slightly greater than the control run. No significant rain mass is found elsewhere in this cross-section unlike the control run which has a secondary peak of rain found at the surface west of the main updraft. Both graupel and aggregate mixing ratios have increased at the expense of rain in this sensitivity run. Graupel mass is found to the east of the main updraft, with peak values of 1.6 g kg^{-1}. The graupel mass field is more widespread and greater than the control run in response to the higher prescribed diameters used in this simulation than is diagnosed in the control run (mostly between 0.4 and 0.7 mean diameters). The aggregate mass field also extends to lower altitudes than the control run with significant mass existing above 6 km MSL with peak values of 1.0 g kg^{-1} which is nearly twice as much as the control run. The pristine ice crystal mixing ratio field is confined above 9 km MSL. Liquid water contents are similar to the control run.

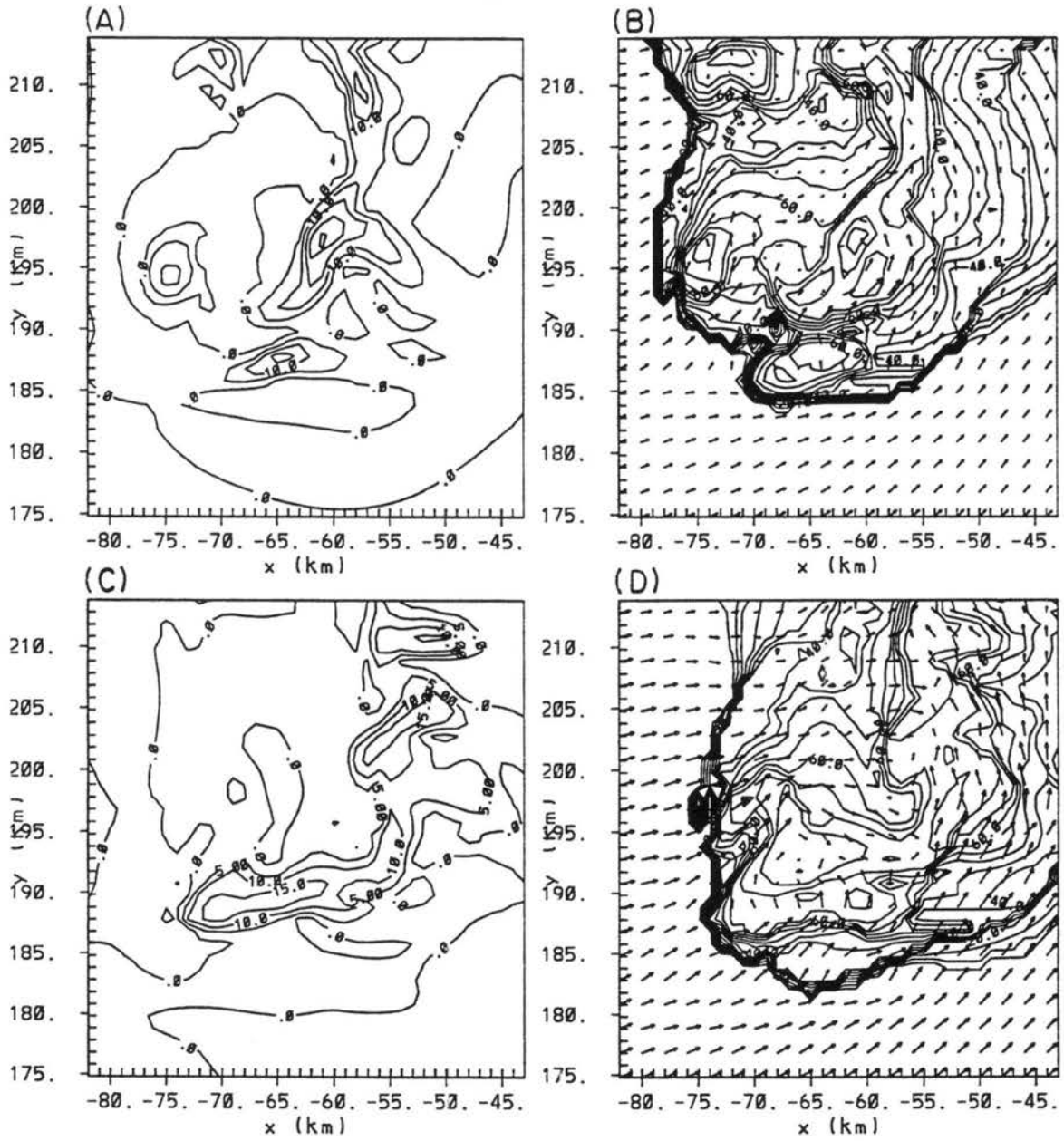

Figure 5.14: Simulated vertical velocities and reflectivity (contour interval, maximum) at 5.6 km MSL for SENS1 after 60 minutes of simulation time for (A) vertical velocity (5 m s^{-1}, 15 m s^{-1}) and (B) reflectivity (5 dBZ, 80 dBZ) and wind vectors (maximum value 24 m s^{-1}), and after 90 minutes of simulation time for (C) vertical velocity (5 m s^{-1}, 15 m s^{-1}) and (D) reflectivity (5 dBZ, 80 dBZ) and wind vectors (maximum value 20 m s^{-1}).

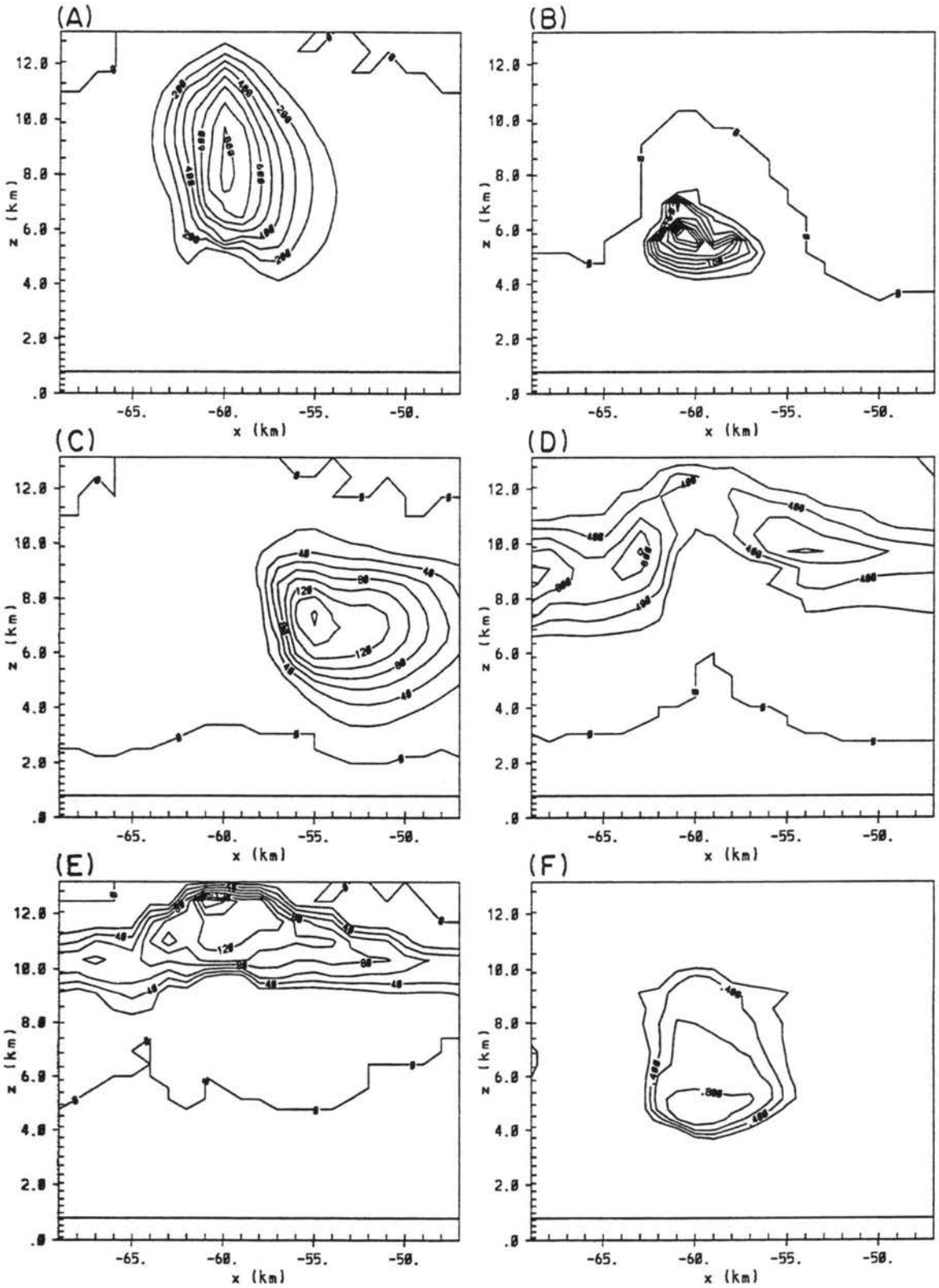

Figure 5.15: Simulated fields for SENS1 of (A) hail mixing ratio (1 g kg^{-1}, 8 g kg^{-1}), (B) rain mixing ratio (0.4 g kg^{-1}, 2.8 g kg^{-1}), (C) graupel mixing ratio (0.2 g kg^{-1}, 1.6 g kg^{-1}) and (D) aggregate mixing ratio (0.2 g kg^{-1}, 1.0 g kg^{-1}), (E) pristine ice crystal mixing ratio (0.2 g kg^{-1}, 1.6 g kg^{-1}) and (F) liquid water content (0.2 g m^{-3}, 0.9 g m^{-3}). Contour intervals and maxima are shown in brackets. All fields are at 60 minutes of simulation time.

5.2.4 SENS2–sensitivity to 1-moment prediction (N_0 specified)

In this experiment one moment of the distribution is predicted (except 2-moments for pristine ice crystals) with N_0 being specified. The prescribed N_0 for each hydrometeor species are 8×10^6 m^{-4} for rain, 3×10^6 m^{-4} for snow, 1.8×10^6 m^{-4} for aggregates, 1.1×10^6 m^{-4} for graupel and 4×10^4 m^{-4} for hail.

The evolution of the vertical velocities and total ice field (Fig. 5.16) is very similar to the control run. The predicted vertical velocity field at 60 minutes of simulation time (Fig. 5.16c) is slightly more elongated and weaker than the control run. A vertical cross-section of the vertical velocity field is shown in Fig. 5.17. This figure shows some minor differences from the control run. The updraft is slightly weaker (35 m s^{-1} peak updraft) and not as wide as the control run. The location of the peak updraft is near 8 km MSL which is simulated lower than the control run. SENS2 also has stronger negative velocities (15 m s^{-1}) east of the main updraft at 11-12 km AGL.

The simulated vertical velocity and reflectivity fields at 5.6 km MSL are shown in Fig. 5.18. These vertical velocity fields show a similar structure after 60 minutes. After 90 minutes of simulation time the vertical velocity field is similar in structure but slightly stronger than the control run. The reflectivity pattern is very similar to the control run, and contrary to the high reflectivities found in SENS1, peak reflectivity values in SENS2 are near 65 dBZ. The areal coverage of reflectivity greater than 60 dBZ in SENS2 is greater than the control run north of the main updraft. The microphysical fields at 60 minutes of simulation time for SENS2 are shown in Fig. 5.19. The hail mixing ratio field shows that the hail mass extends to lower levels than in the control run. Peak values of hail mass are located near 8 km MSL which is nearly 1 km lower than the control run which may be partly due to the lower location of the peak updraft (Fig. 5.17) and to the larger hail mean diameters found above 5 km in SENS2 (Fig. 5.19e). The rain mixing ratio shows much less mass between 4 and 6 km MSL compared to the control run. With the larger hail diameters found in SENS2, the hail category has a longer residence time and is slower to melt completely than in the control run, and consequently is slower to convert to rain. Graupel mixing ratio values are very small, with a region of 0.2 g kg^{-1} found east of the

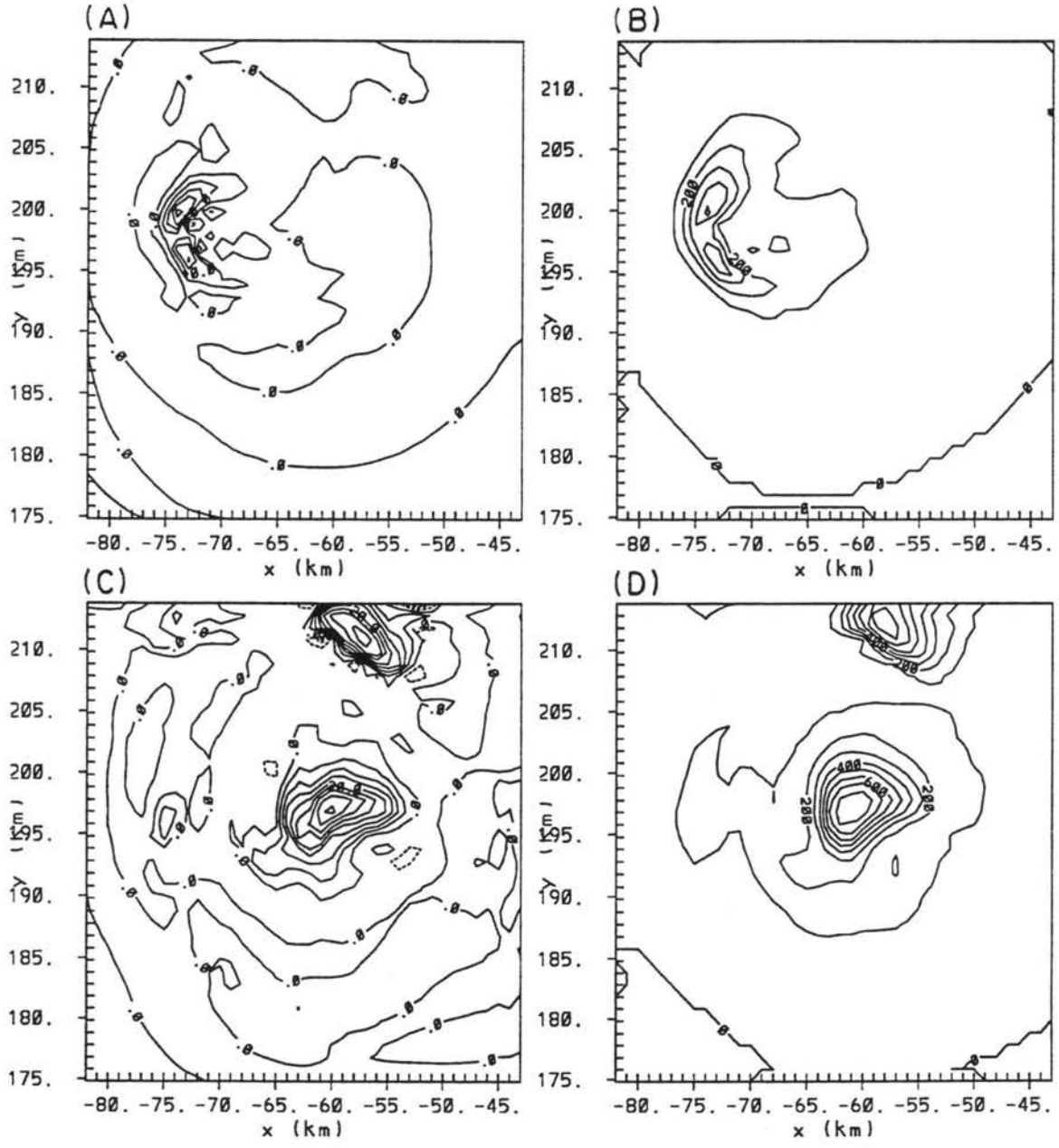

Figure 5.16: Simulated vertical velocities and total ice mixing ratios (contour interval, maximum) at 9000 m AGL for SENS2 after 30 minutes of simulation time for (A) vertical velocity (5 m s^{-1}, 25 m s^{-1}) and (B) total ice mixing ratio (1 g kg^{-1}, 5 g kg^{-1}), and after 60 minutes of simulation time for (C) vertical velocity (5 m s^{-1}, 40 m s^{-1}) and (D) total ice mixing ratio (1 g kg^{-1}, 8 g kg^{-1}).

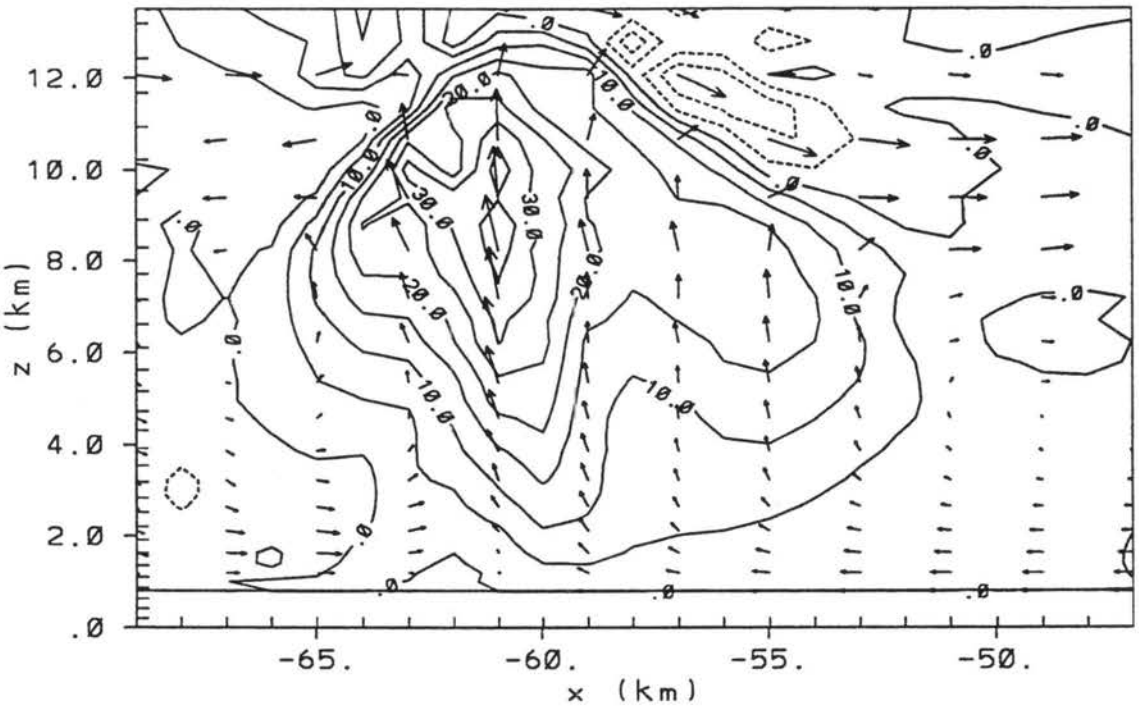

Figure 5.17: A horizontal cross-section through the center of the storm for SENS2 with simulated vertical velocities (5 m s^{-1}, 35 m s^{-1}) with solid contours denoting positive values and negative contours denoting negative values. Wind vectors are also included with maximum vector of 35 m s^{-1}.

main updraft. These results are contrary to the observations in which graupel precipitation was quite active in the storm. Pristine ice crystal and aggregate mass (not shown) is very similar to the control run. The liquid water content field extends over a wider area than the control run with slightly less liquid water found in SENS2. The hail diameter field is very different than the control run with peak values slightly larger (2.4 mm) than in the control run. Largest hail mean diameters are found near 8 km MSL, with diameters less than 1 mm below 4 km MSL over the eastern half of the domain. The rain mean diameter field is also quite different than the control run and the observations, with peak values less than 0.5 mm nearly four times less than the control run.

5.2.5 SENS3–sensitivity to collection

This sensitivity test examines the effect of modifying the mechanism of raindrop freezing. As was noted in Section 2.6.5, ice collecting raindrops would most likely be converted

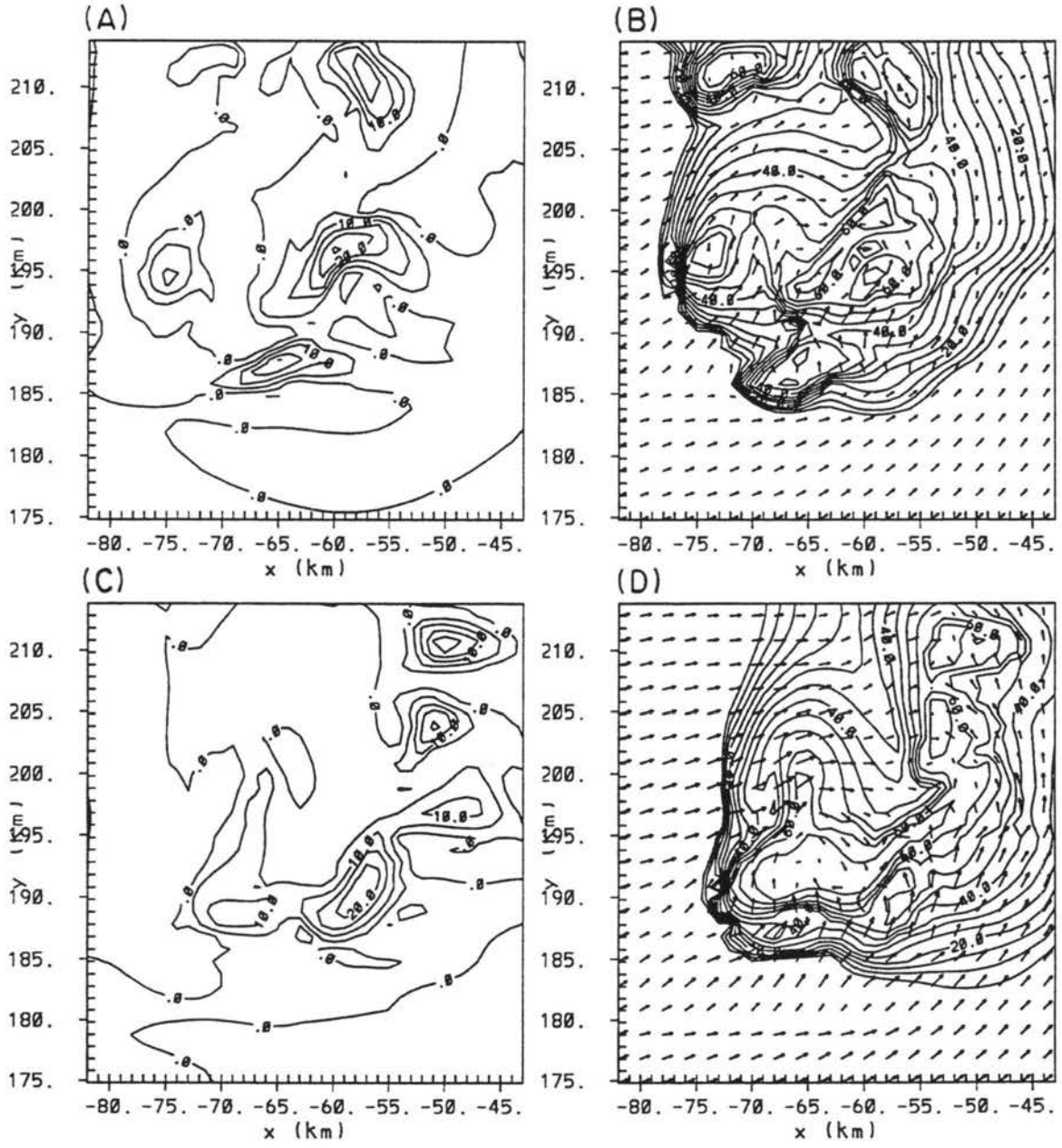

Figure 5.18: Simulated vertical velocities and reflectivity (contour interval, maximum) at 5.6 km MSL after 60 minutes of simulation time for SENS2 of (A) vertical velocity (5 m s^{-1}, 28 m s^{-1}) and (B) reflectivity (5 dBZ, 60 dBZ) and wind vectors (maximum value 24 m s^{-1}), and after 90 minutes of simulation time for (C) vertical velocity (5 m s^{-1}, 21 m s^{-1}) and (D) reflectivity (5 dBZ, 65 dBZ) and wind vectors (maximum value 20 m s^{-1}).

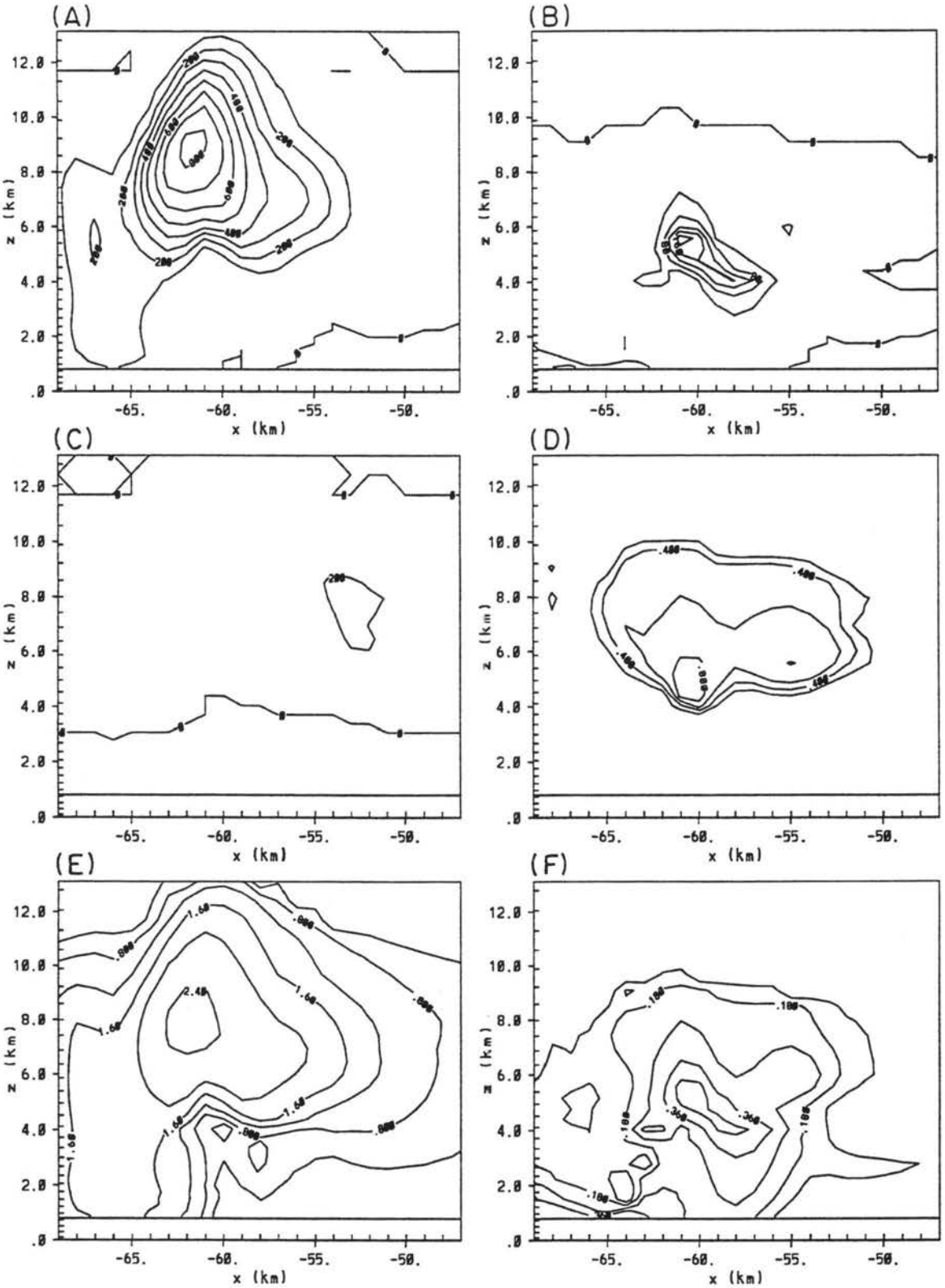

Figure 5.19: Simulated fields for SENS2 of (A) hail mixing ratio (1 g kg^{-1}, 8 g kg^{-1}), (B) rain mixing ratio (0.4 g kg^{-1}, 2.1 g kg^{-1}), (C) graupel mixing ratio (0.2 g kg^{-1}, 0.2 g kg^{-1}) and (D) liquid water content (0.2 g m^{-3}, 0.8 g m^{-3}), (E) hail mean diameter (0.4 mm, 2.4 mm) and (F) rain mean diameter ((0.09 mm, 0.45 mm)). Contour intervals and maxima are shown in brackets. All fields are at 60 minutes of simulation time.

to hail at sub-freezing temperatures in the model. As a sensitivity to this collection process, this experiment examines the effect of changing the collection path of ice collecting rain from hail (as in the other simulations) to graupel (in this experiment). One simulated feature not represented well by the control run was the relatively high hail concentrations. Even though the hail category is defined as a combination of all frozen drops and hail particles, there is a possibility that more frozen drops are converted to the hail category which may increase hail concentrations. This sensitivity, therefore, defines the hail category as being produced solely by the conversion of graupel to hail by collection of liquid water.

The vertical velocity and total ice fields at 9 km for SENS3 are shown in Fig. 5.20. These fields exhibit little changes from the control run. A vertical cross-section of the simulated vertical velocity field (60 minutes simulation time) is shown in Fig. 5.21. Comparison to the control run shows that the peak updraft is slightly less (peak values 35 m s^{-1} in SENS3) and that the width of the updraft is much less than in SENS3. The orientation of the simulated updraft is nearly vertical which was observed. Another weak updraft is found near X=-68, between 7 and 10 km MSL, which is not simulated by the control run. Areas of downdrafts occur in the simulation, between 10 and 12 km MSL east of the updraft, between 2–4 km MSL just east of the updraft, and west of the main updraft. These downdraft regions were observed, but the magnitudes are much stronger than the control run and the observations. The structure also picks up the downdraft to east of the main updraft which splits the main updraft from a secondary updraft to the east, which was observed (Fig. 5.5b). The simulated flow pattern also appears consistent with the control run. The simulated vertical velocity and reflectivity fields at 5.6 km MSL for SENS3 after 60 minutes and 90 minutes are shown in Fig. 5.22. The simulated main updraft is very similar to the control run structure (Fig. 5.6) at both simulation times. The simulated peak updraft is 25 m s^{-1} at 60 minutes (Fig. 5.22a) and 21 m s^{-1} at 90 minutes (Fig. 5.22c) which is slightly stronger than the control run. The orientation of the simulated updraft is southwest/northeast at 60 minutes but rotates to a more west/east orientation by 90 minutes which is shown in the observed field. At 60 minutes, the simulated reflectivity pattern (Fig. 5.22a) has many small scale peaks in the structure, which are co-located with

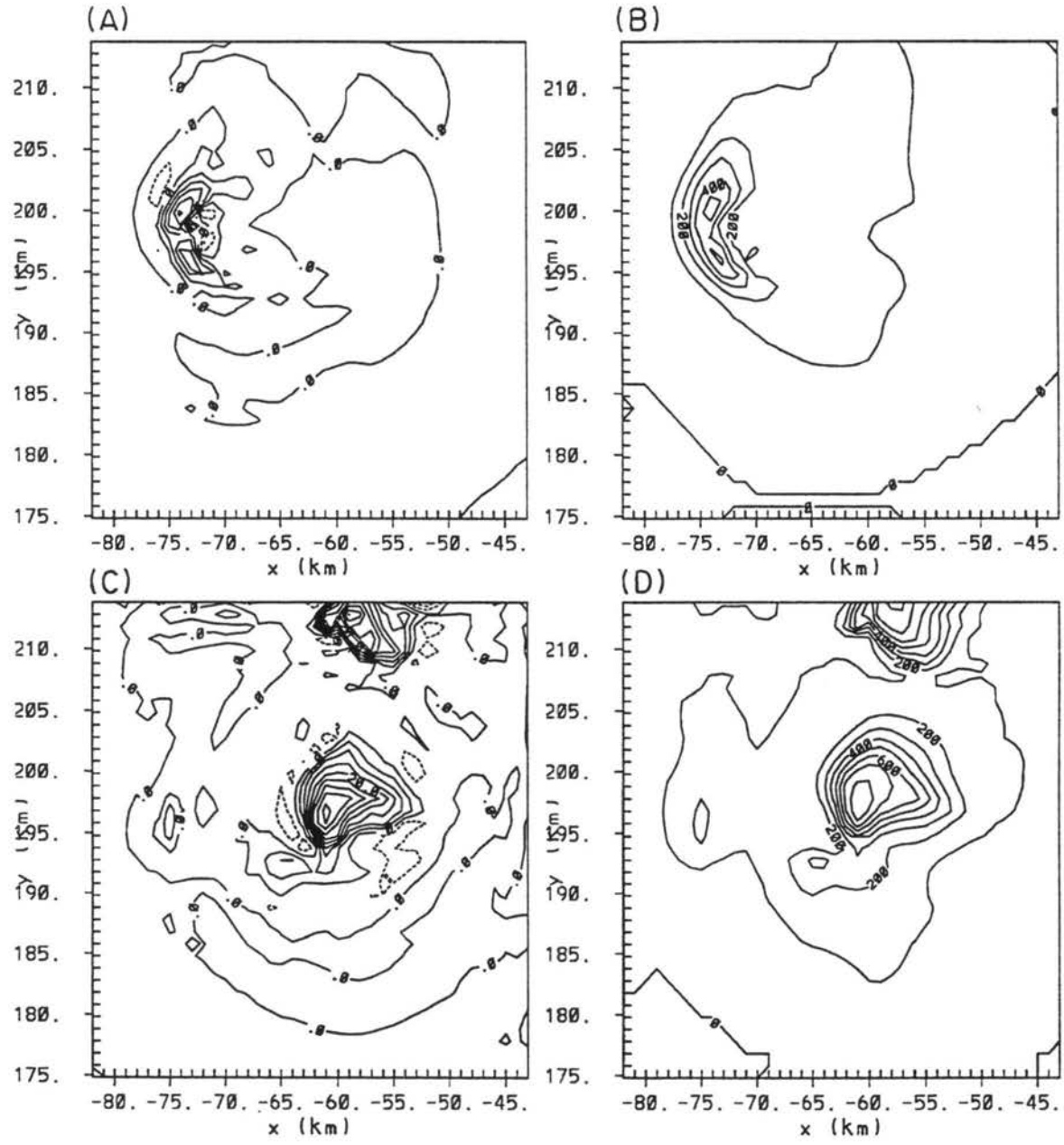

Figure 5.20: Simulated vertical velocities and total ice mixing ratios (contour interval, maximum) at 9000 m AGL for SENS3 after 30 minutes of simulation time for (A) vertical velocity (5 m s^{-1}, 25 m s^{-1}) and (B) total ice mixing ratio (1 g kg^{-1}, 5 g kg^{-1}), and after 60 minutes of simulation time for (C) vertical velocity (5 m s^{-1}, 40 m s^{-1}) and (D) total ice mixing ratio (1 g kg^{-1}, 8 g kg^{-1}).

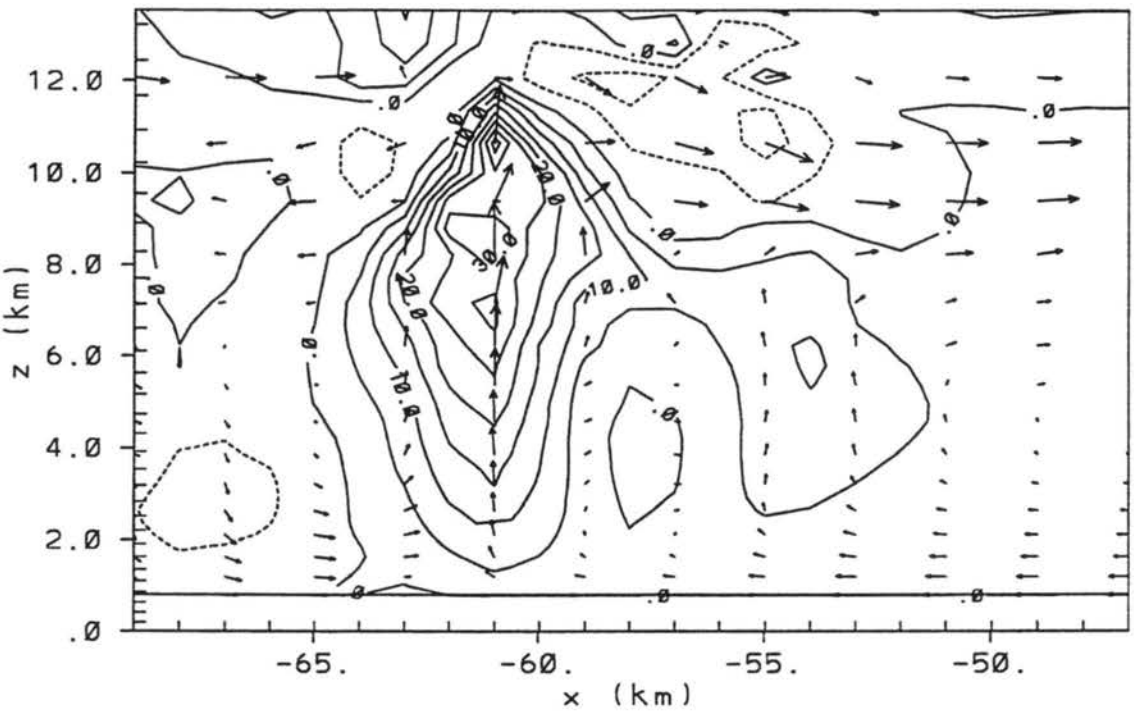

Figure 5.21: A horizontal cross-section through the center of the storm for SENS3 with simulated vertical velocities (5 m s^{-1}, 35 m s^{-1}) with solid contours denoting positive values and negative contours denoting negative values. Wind vectors are also included with maximum vector of 35 m s^{-1}.

isolated updrafts. Peak values are found near the western boundary of the reflectivity core near an isolated updraft, and another one is found near Y=198 km and X=-58 km which is co-located with the main updraft. By 90 minutes the reflectivity pattern (Fig. 5.22d) becomes more coherent and similar to the control run. Peak reflectivities are near the main updraft with peak values of 65 dBZ, and there exists a strong reflectivity gradient on the western boundary which is found in the control run.

A vertical cross-section of certain microphysical fields at 60 minutes is shown in Fig. 5.23. The hail mixing ratio field shows a broad region of hail mass centered over 8 km MSL (peak values 7 g kg^{-1}). A secondary peak exists west of the main updraft with a 2 g kg^{-1} peak, which may be forced by a weaker updraft simulated in this region (Fig. 5.21). The hail mixing ratio field is less widespread than the control run since rain-water collected by ice hydrometeors is first converted to graupel instead of hail, unlike the other simulations. The hail structure has also shifted to lower altitudes than in the control

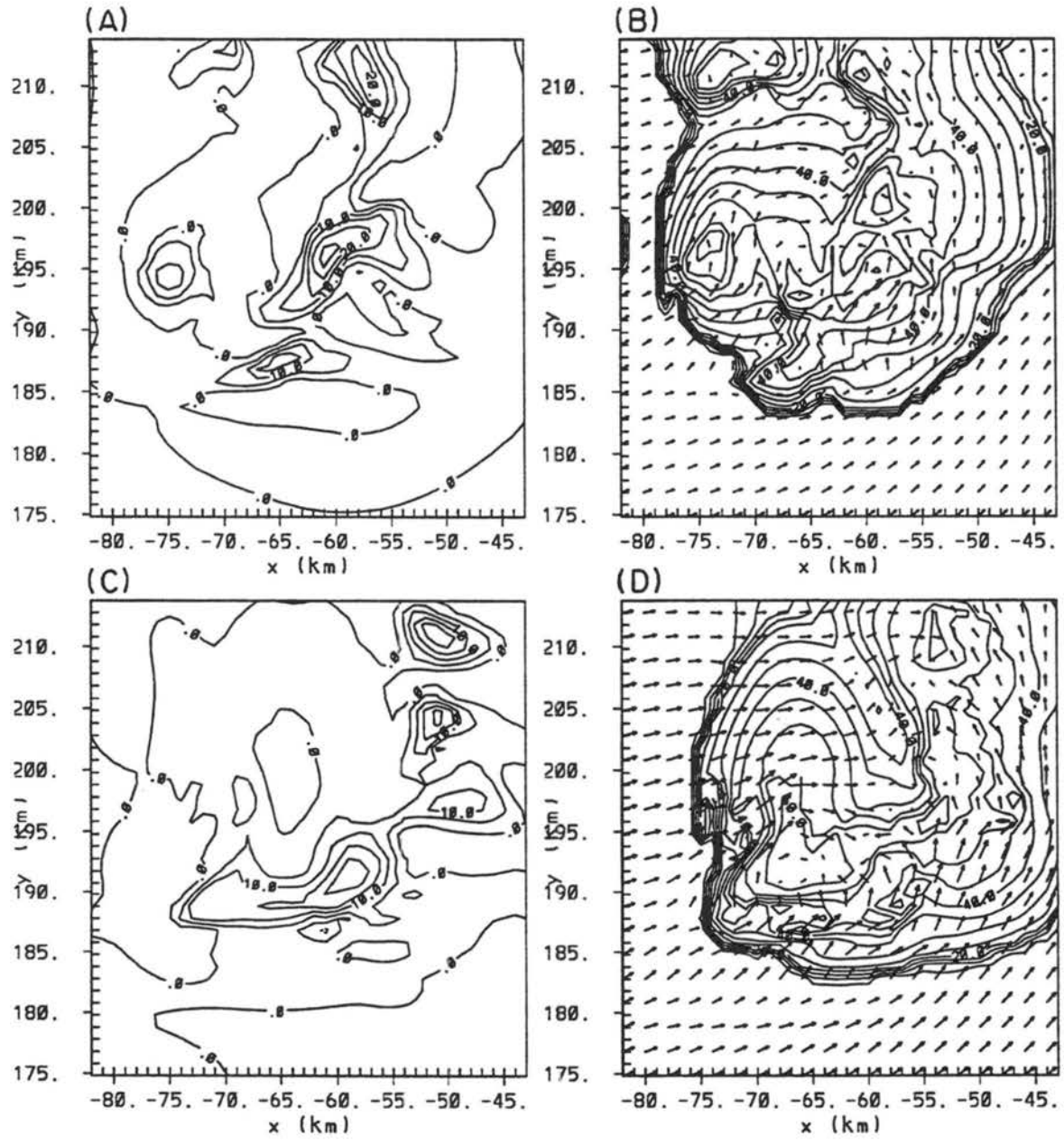

Figure 5.22: Simulated vertical velocities and reflectivity (contour interval, maximum) at 5.6 km MSL after 60 minutes of simulation time for SENS3 of (A) vertical velocity (5 m s^{-1}, 25 m s^{-1}) and (B) reflectivity (5 dBZ, 65 dBZ) and wind vectors (maximum value 24 m s^{-1}), and after 90 minutes of simulation time for (C) vertical velocity (5 m s^{-1}, 21 m s^{-1}) and (D) reflectivity (5 dBZ, 65 dBZ) and wind vectors (maximum value 20 m s^{-1}).

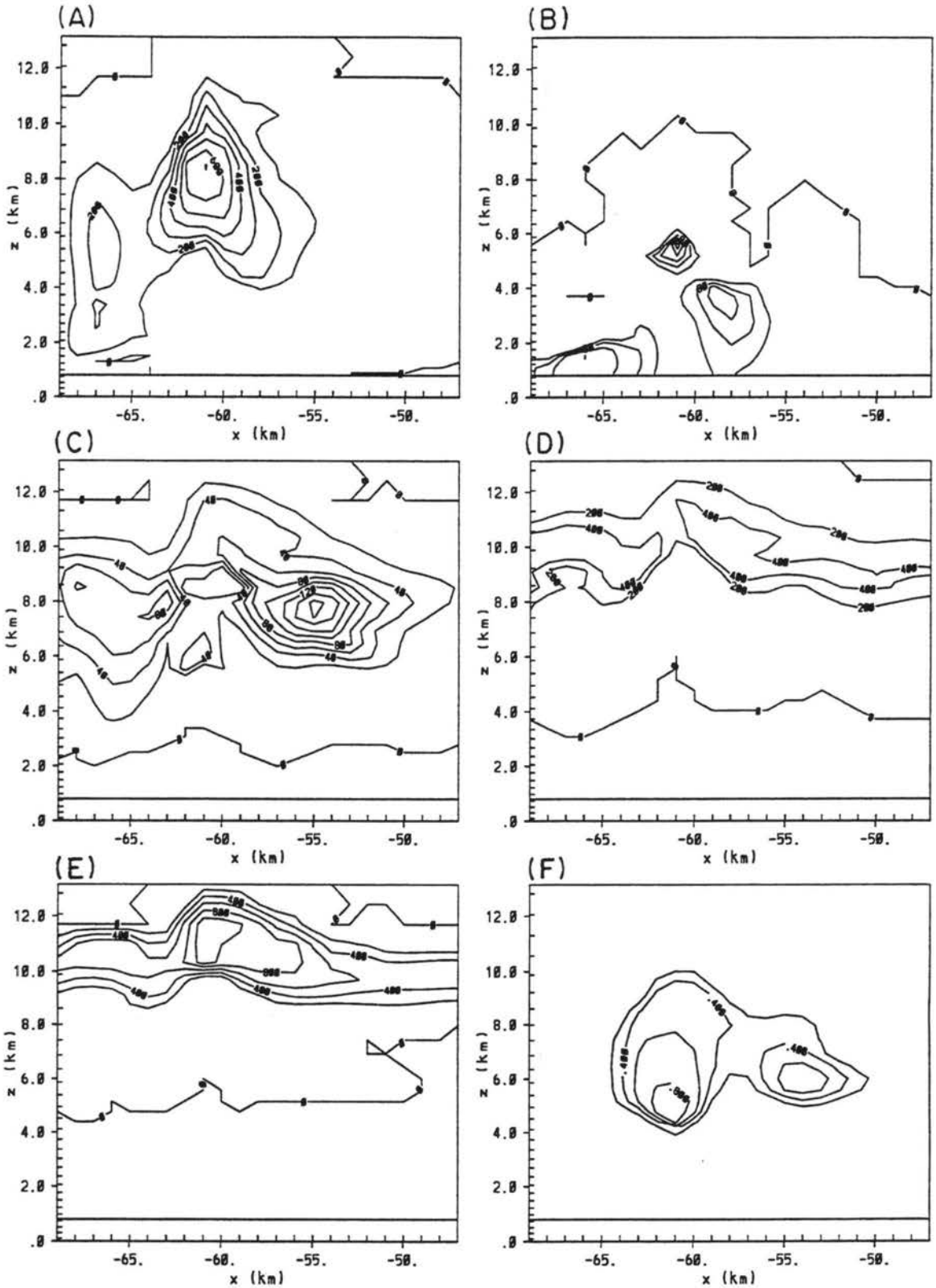

Figure 5.23: Simulated fields for SENS3 of (A) hail mixing ratio (1 g kg^{-1}, 7 g kg^{-1}), (B) rain mixing ratio (0.4 g kg^{-1}, 2.2 g kg^{-1}), (C) graupel mixing ratio (0.2 g kg^{-1}, 1.6 g kg^{-1}) and (D) aggregate mixing ratio (0.2 g kg^{-1}, 0.4 g kg^{-1}), (E) pristine ice crystal mixing ratio (0.2 g kg^{-1}, 1.0 g kg^{-1}) and (F) liquid water content (0.2 g m^{-3}, 0.8 g m^{-3}). Contour intervals and maxima are shown in brackets. All fields are at 60 minutes of simulation time.

run due to the higher prescribed diameters and resultant higher fallspeeds of hail in SENS3. Rain mixing ratios (Fig. 5.23b) show 3 distinct peaks in the simulated results. One area is found near 5 km MSL with a 2.1 g kg^{-1} peak, where most of these drops form by melting and shedding from the hail category and from autoconversion of cloud droplets. The other 2 peaks near 3 km MSL (1.2 g kg^{-1}) and near the surface (1.5 g kg^{-1}) have formed by a combination of melting and shedding of drops from the hail and graupel categories. More rain is being produced by melting graupel in this simulation since graupel exists at lower altitudes than the control run. This structure is quite different from the control run with more rain being collected between 4 and 6 km MSL by hail and graupel. More rain is produced between 4 km and the surface due to melting of graupel and hail than in the control run. The graupel mixing ratio field (Fig. 5.23c) shows a much broader region of graupel mass above 5 km MSL than in the control run, with highest values of graupel mass east of the main updraft (peak values 1.6 g kg^{-1}). This eastern region of graupel mass is co-located with an enhanced region of liquid water content (Fig. 5.23f) which is forced by the secondary updraft as shown in Fig. 5.21. Unlike the control run, graupel also exists in the updraft region. Graupel amounts are higher than in the control run due to the larger diameters prescribed in SENS3 which allow the graupel particles to grow to larger sizes before converting to hail. Aggregates and pristine ice crystal categories are quite similar to the control run, except that ice crystal mass is less than the control run. Pristine ice crystal mass is lower due to less mass reaching the anvil region of the cloud, due to much larger conversion of mass to graupel in the middle troposphere.

Number concentrations and mean diameters of selected hydrometeor fields for SENS3 are shown in Fig. 5.11. The number concentration of hail (D >5.0 mm) (Fig. 5.24a) shows that peak values are 14 m^{-3}, which is still higher than observed values. The mean hail diameter field in an assumed gamma distribution is shown in Fig. 5.24b. This field shows that most of the mean hail diameters are approximately 1.2 mm, with larger diameters west of the main updraft where peak mean diameters are over 2.0 mm. This result is surprising since raindrop freezing being converted to hail instead of graupel was hypothesized as a potential reason for the production of smaller hail particles and higher hail number

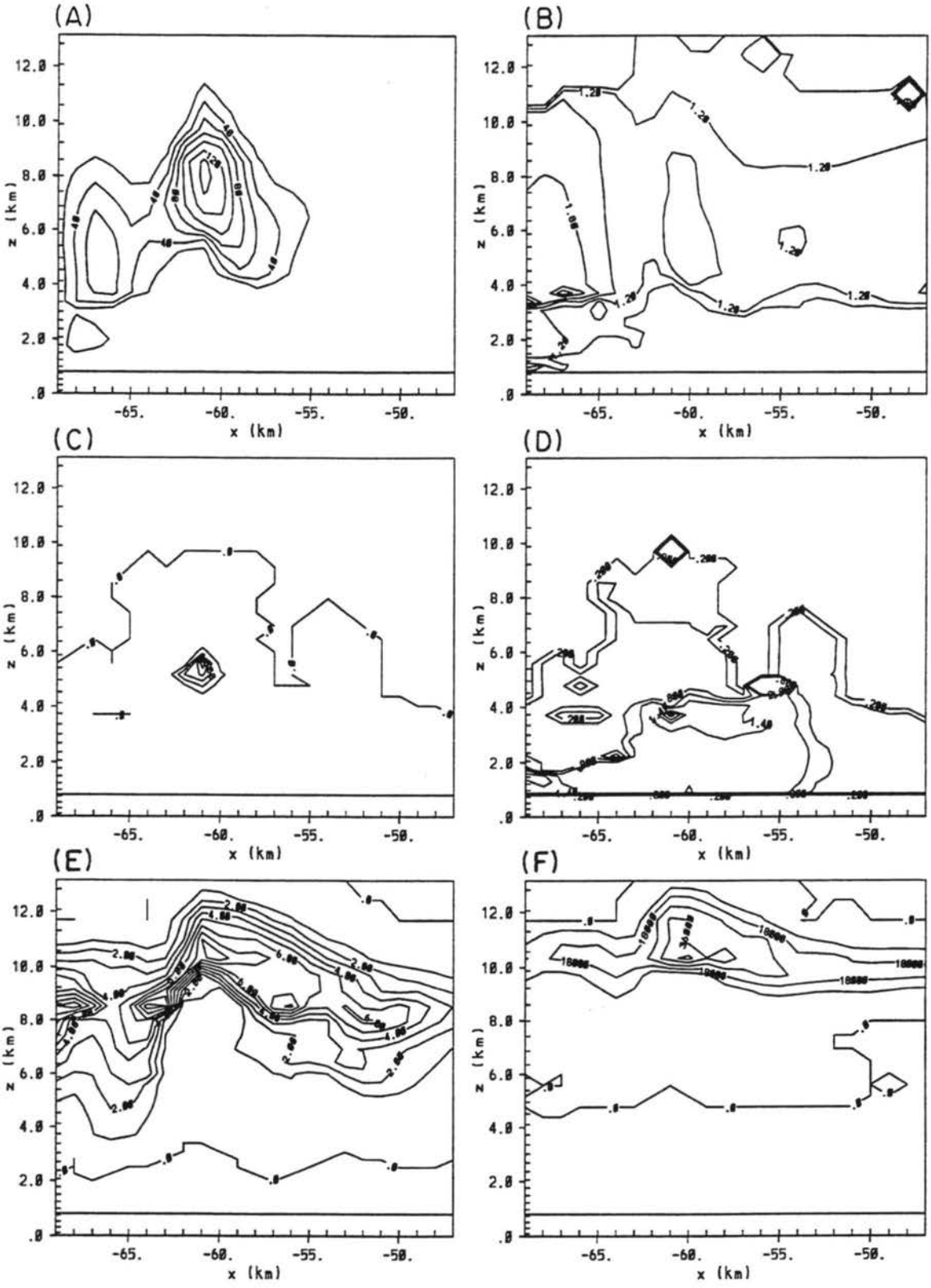

Figure 5.24: Simulated fields for SENS3 of (A) hail number concentration (2 m^{-3}, 14 l^{-1}), (B) hail mean diameter (0.3 mm, 2.4), (C) rain number concentration (0.4 l^{-1}, 2.0 l^{-1}) and (D) rain mean diameter (0.3 mm, 2.4 mm), (E) graupel number concentration (1 l^{-1}, 9 l^{-1}) and (F) pristine ice crystal number concentrations (9000 l^{-1}, 45000 l^{-1}). Contour intervals and maxima are shown in brackets. All fields at 60 minutes of simulation time.

concentrations in the control run. The rain number concentration field shows a distinct peak near the updraft at 5 km MSL. Peak values of rain number concentration are close to 2 l^{-1}. These peak values of rain concentration are less than the control run and rain concentrations were observed to be 2 l^{-1} near 5-6 km MSL. Elsewhere in the domain, rain number concentrations are less than 0.1 l^{-1}. The mean diameters of rain show values are below 0.8 mm above 4 km MSL, but increase over lower altitudes with most values over 1.0 mm below 4 km MSL which is slightly greater than the control run. Graupel number concentrations (Fig. 5.24e) are mostly in the 1–9 l^{-1} range and exist predominantly above 6 km MSL, however, concentrations in and near the updraft are 0.5 to 1.0 l^{-1}. These values are slightly greater than the control run. Pristine ice crystal number concentrations (Fig. 5.24f) are predicted up to 45000 l^{-1} near 10 km MSL which is less than the control run due to a sink of available mass to graupel in the middle troposphere.

5.2.6 SENS4–sensitivity to all hydrometeors; ν=3

This sensitivity examines the effect of changing the shape parameter of all hydrometeors. This effectively increases the mean diameter of each species as was shown by Fig. 2.1. All other model parameters are similar to the control run.

A horizontal cross-section of the vertical velocity and total ice fields at 9 km for SENS4 is shown in Fig. 5.25. The evolution of the storms at this altitude is very similar to the control run. A vertical cross-section of the simulated vertical velocity field for SENS3 (60 minutes simulation time) is shown in Fig. 5.26. Comparison to the control run shows that the peak updraft in SENS3 is slightly less (41 m s^{-1}) but overall, the structure is very similar. The simulated fields for SENS4 after 60 minutes and 90 minutes are shown in Fig. 5.27. The simulated main updraft is very similar to the control run at both simulation times. The simulated peak updraft is 25 m s^{-1} at 60 minutes (Fig. 5.27a) and 21 m s^{-1} at 90 minutes (Fig. 5.27c). The orientation of the simulated updraft is southwest/northeast at 60 minutes but rotates to a more west/east orientation by 90 minutes like the control run. The updraft at 90 minutes, however, extends farther northeastward than the control run. The reflectivity pattern for SENS4 shows much higher reflectivities at both times than in the control run. Most of the reflectivity is greater than 60 dBZ, with large regions

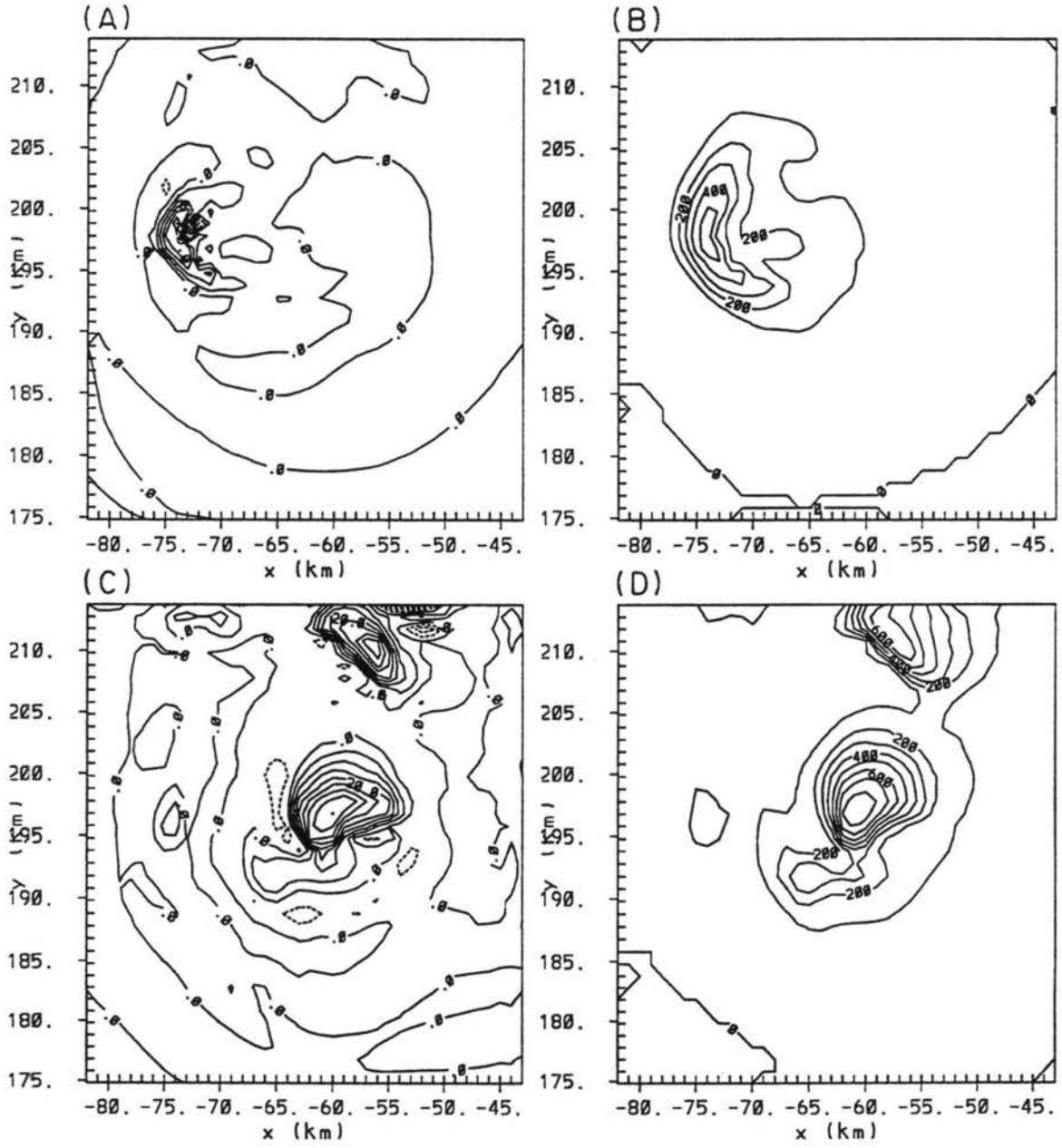

Figure 5.25: Simulated vertical velocities and total ice mixing ratios (contour interval, maximum) at 9000 m AGL for SENS4 after 30 minutes of simulation time for (A) vertical velocity (5 m s^{-1}, 25 m s^{-1}) and (B) total ice mixing ratio (1 g kg^{-1}, 4 g kg^{-1}), and after 60 minutes of simulation time for (C) vertical velocity (5 m s^{-1}, 40 m s^{-1}) and (D) total ice mixing ratio (1 g kg^{-1}, 5 g kg^{-1}).

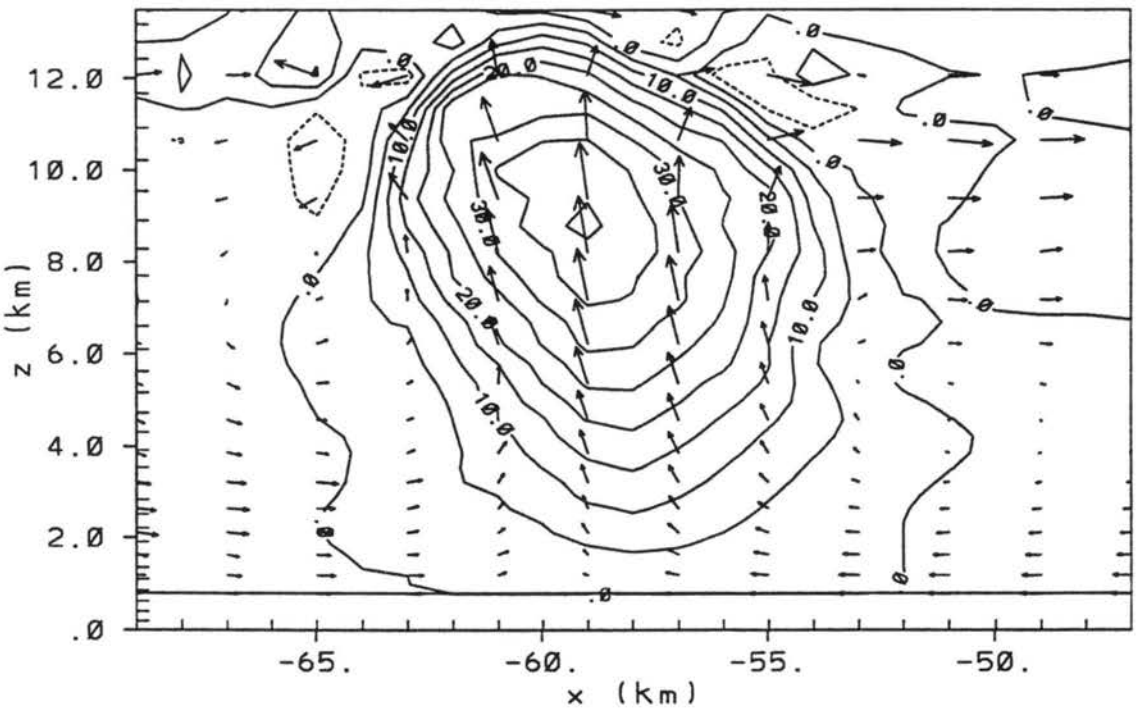

Figure 5.26: A horizontal cross-section through the center of the storm for SENS4 with simulated vertical velocities (5 m s^{-1}, 41 m s^{-1}) with solid contours denoting positive values and negative contours denoting negative values. Wind vectors are also included with maximum vector of 41 m s^{-1}.

of over 80 dBZ at both times. These high reflectivities are due to the higher value of ν for each hydrometeor which effectively shifts the mean diameter of the distribution to larger sizes. These reflectivities are much higher than observed values. A cross-section of some of the microphysical fields for SENS4 is shown in Fig. 5.28. The hail mixing ratio field is very similar to the control run, with a peak value of 8 g kg^{-1} centered near 9 km MSL. Rain mixing ratios (Fig. 5.28b) are similar to the control run with peak values near 4.0 g kg^{-1}. No significant rain mass is found near the surface as in the control run. The graupel mixing ratio field (Fig. 5.28c) shows only negligible amounts since most ice-liquid collections result in conversion to the hail category. The aggregate mixing ratio field is smaller than the control run with 0.4 g kg^{-1} found in SENS4. Pristine ice crystals are similar to the control run. The liquid water content field shows lower amounts than the control run with 0.6 g m^{-3} found at 4 km MSL. These values are less than the control run due to hydrometeor collection and autoconversion to rain.

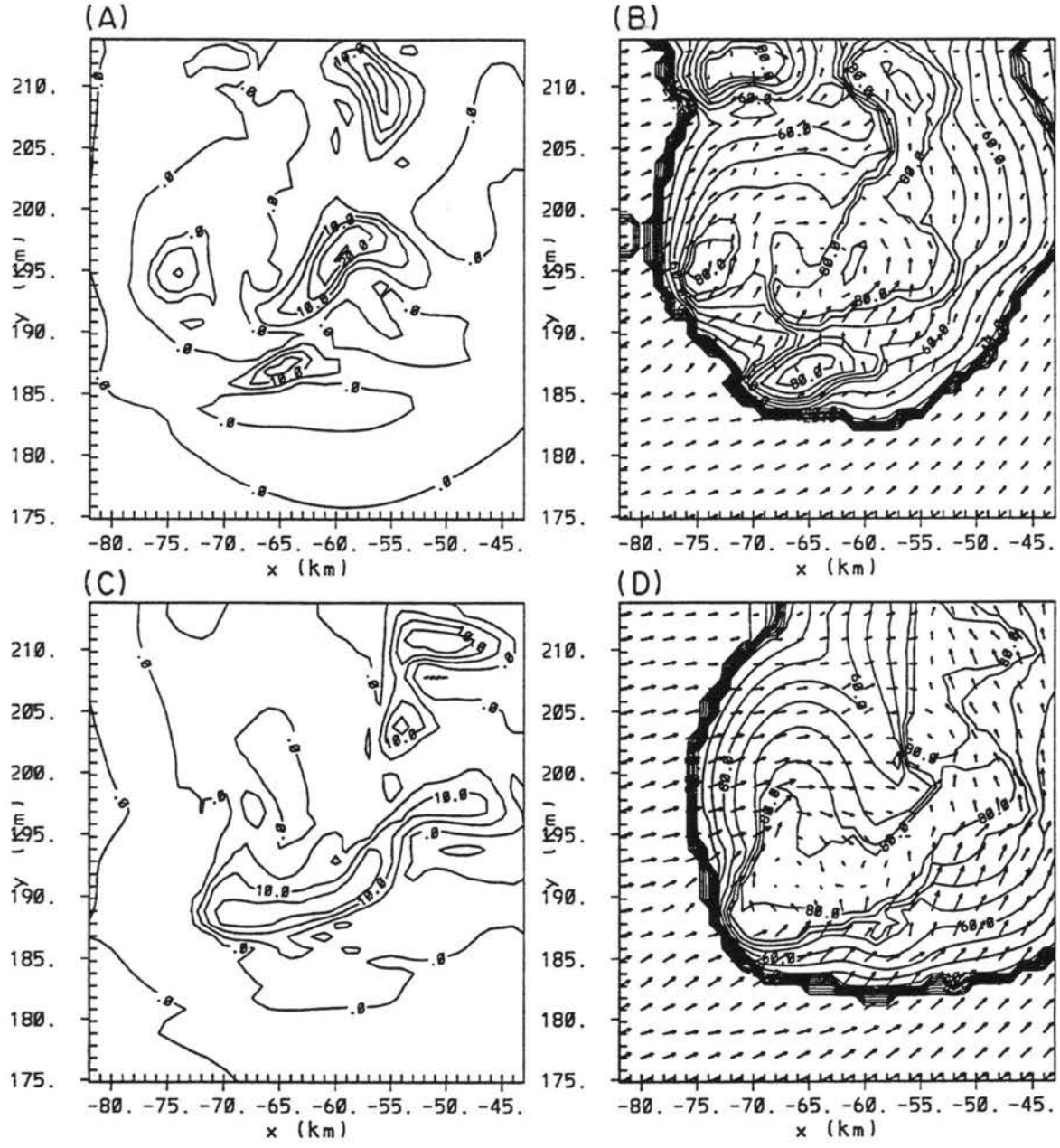

Figure 5.27: Simulated vertical velocities and reflectivity (contour interval, maximum) at 5.6 km MSL for SENS4 after 60 minutes of simulation time for (A) vertical velocity (5 m s^{-1}, 25 m s^{-1}) and (B) reflectivity (5 dBZ, 70 dBZ) and wind vectors (maximum value 24 m s^{-1}), and after 90 minutes of simulation time for (C) vertical velocity (5 m s^{-1}, 18 m s^{-1}) and (D) reflectivity (5 dBZ, 75 dBZ) and wind vectors (maximum value 20 m s^{-1}).

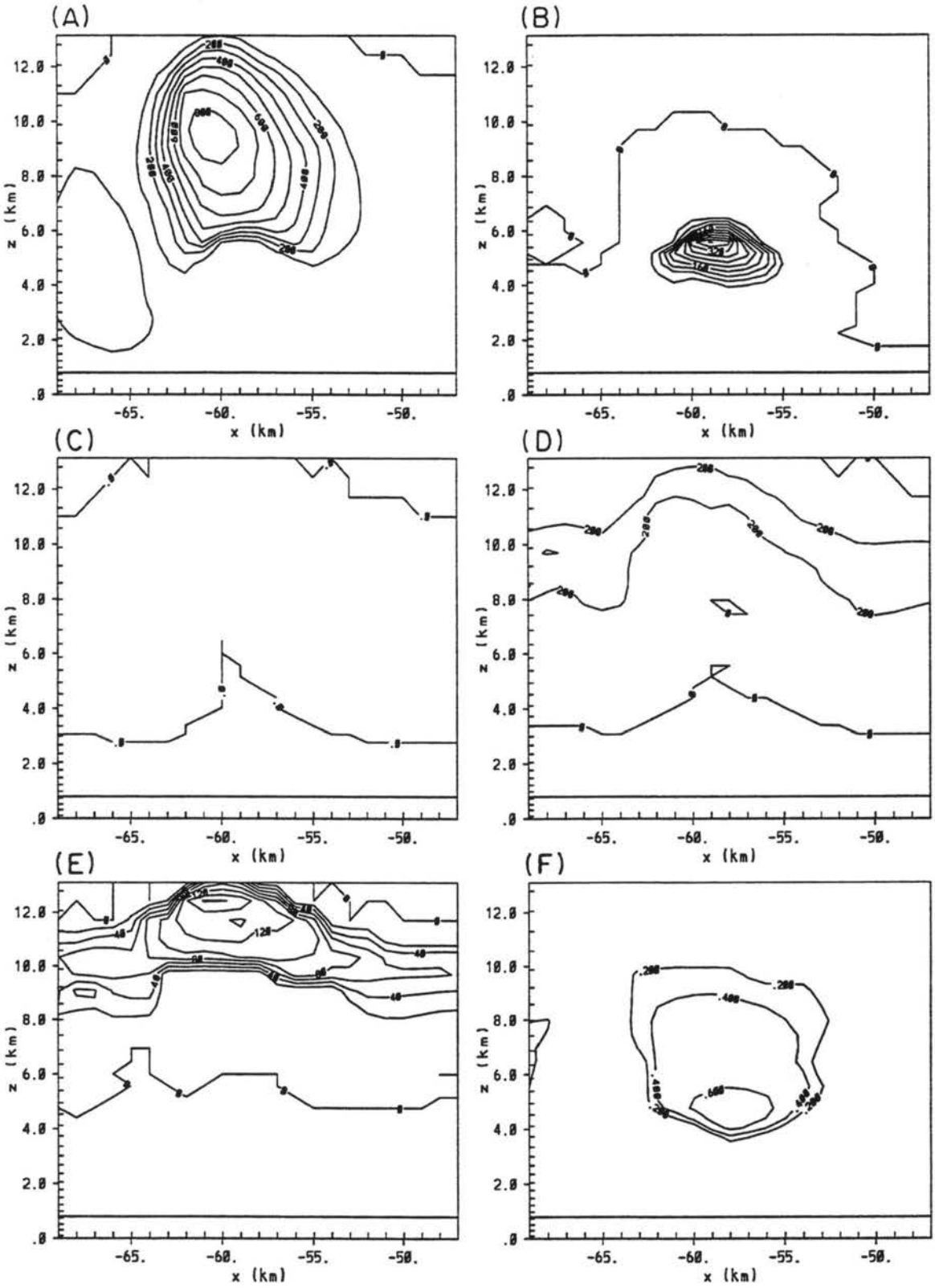

Figure 5.28: Simulated fields for SENS4 of (A) hail mixing ratio (1 g kg^{-1}, 8 g kg^{-1}), (B) rain mixing ratio (0.4 g kg^{-1}, 4.0 g kg^{-1}), (C) graupel mixing ratio (0.2 g kg^{-1}, 0.0 g kg^{-1}) and (D) aggregate mixing ratio (0.2 g kg^{-1}, 0.4 g kg^{-1}), (E) pristine ice crystal mixing ratio (0.2 g kg^{-1}, 1.6 g kg^{-1}) and (F) liquid water content (0.2 g m^{-3}, 0.6 g m^{-3}). Contour intervals and maxima are shown in brackets. All fields are at 60 minutes of simulation time.

Number concentrations and mean diameters of selected hydrometeor fields for SENS4 are shown in Fig. 5.29. The number concentration of hail (D >5.0 mm) (Fig. 5.29a) shows peak values of 16 m^{-3}, which are greater than in the control run. The mean hail diameter field in an assumed gamma distribution is shown in Fig. 5.29b. This field shows that most of the mean hail diameters are much larger than the control run with peak values of 6 mm found near the surface, which is due to the higher value of ν for hail. The rain number concentration field shows values of less than 0.2 l^{-1} over the domain. The mean diameter of rain field shows values that are below 1.5 mm where the small rain mass is located, which is much greater than the control run at this altitude due to larger ν values for rain. Graupel number concentrations (Fig. 5.29e) are negligible. Pristine ice crystal number concentrations (Fig. 5.29f) are predicted up to 54000 l^{-1} which is similar to the control run.

5.2.7 SENS5–sensitivity to ν=3 for hail only

This sensitivity test examines the role of the shape parameter on the hail distribution, while all other species have a $\nu = 1$. Increasing the ν of hail should produce larger hail particles, and possibly lower number concentrations which were not handled well in the control run.

The vertical velocity field and total ice field at 9 km for SENS5 are shown in Fig. 5.30. The evolution of the storm at this altitude is very similar to the control run. A vertical cross-section of the simulated vertical velocity and flow fields for SENS5 (60 minutes simulation time) is shown in Fig. 5.31. The peak velocities in the updraft (37 m s^{-1} in SENS5) and the width of the updraft are less in SENS5 than in the control run. The other basic features are quite similar to the control run. The simulated vertical velocity and reflectivity fields at 5.6 km MSL for SENS5 after 60 minutes and 90 minutes are shown in Fig. 5.32. The simulated vertical velocity fields at both times are nearly identical to the control run. The reflectivity fields for SENS5 are also quite similar to the control run. Some differences between the two simulations are that the peak reflectivities are nearly 5 dBZ higher in SENS5 and the area of greater than 60 dBZ is greater in SENS5 than in the control run. These increases are due to the higher value of ν for hail in SENS5. A cross-section of

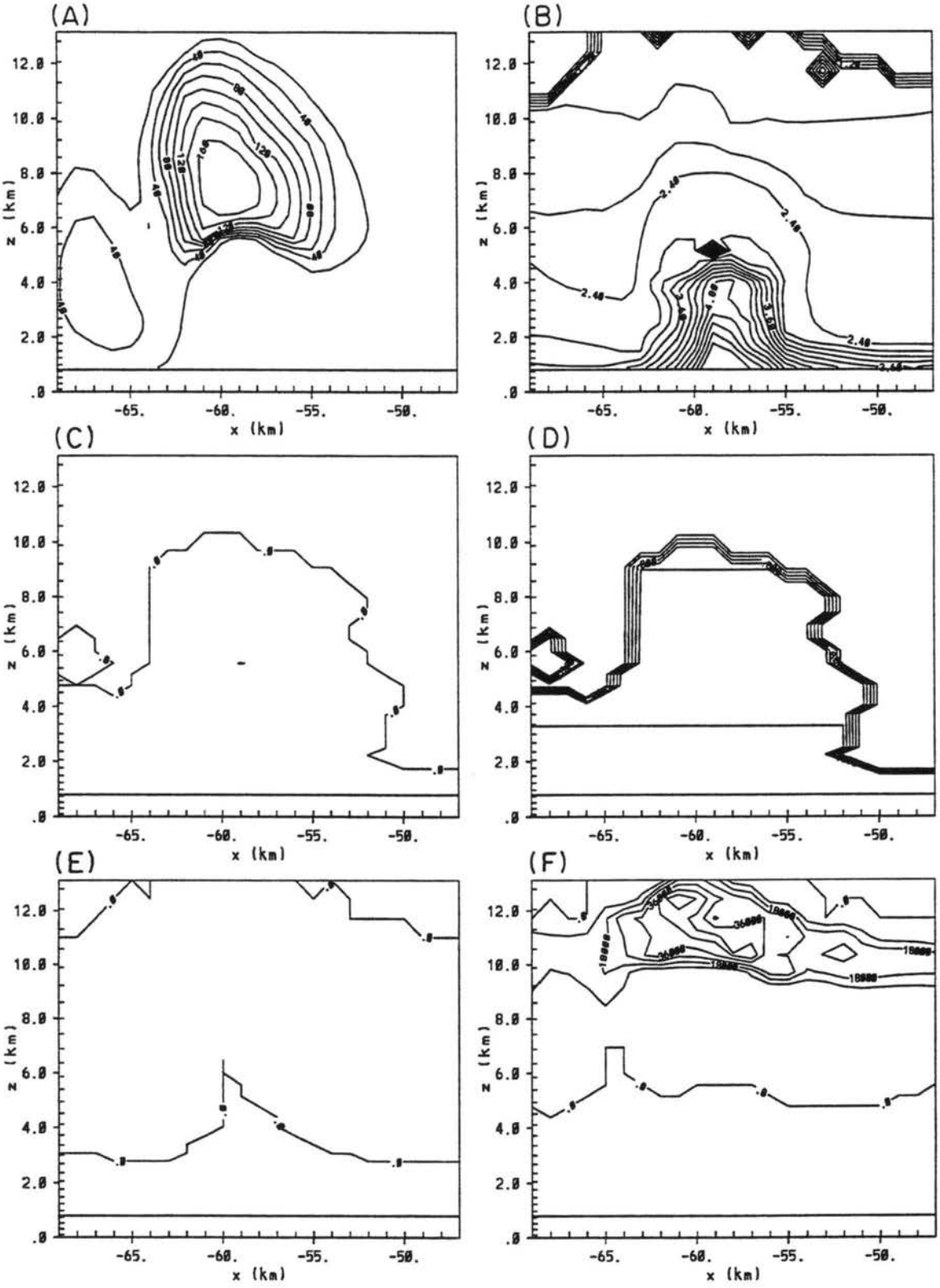

Figure 5.29: Simulated fields for SENS4 of (A) hail number concentration (2 m^{-3}, 16 m^{-3}), (B) hail mean diameter (0.3 mm, 6.0 mm), (C) rain number concentration (0.4 l^{-1}, less than 0.4 l^{-1}) and (D) rain mean diameter (0.3 mm, 1.6 mm), (E) graupel number concentration (1 l^{-1}, 0 l^{-1}) and (F) pristine ice crystal number concentrations (9000 l^{-1}, 72000 l^{-1}). Contour intervals and maxima are shown in brackets. All fields at 60 minutes of simulation time.

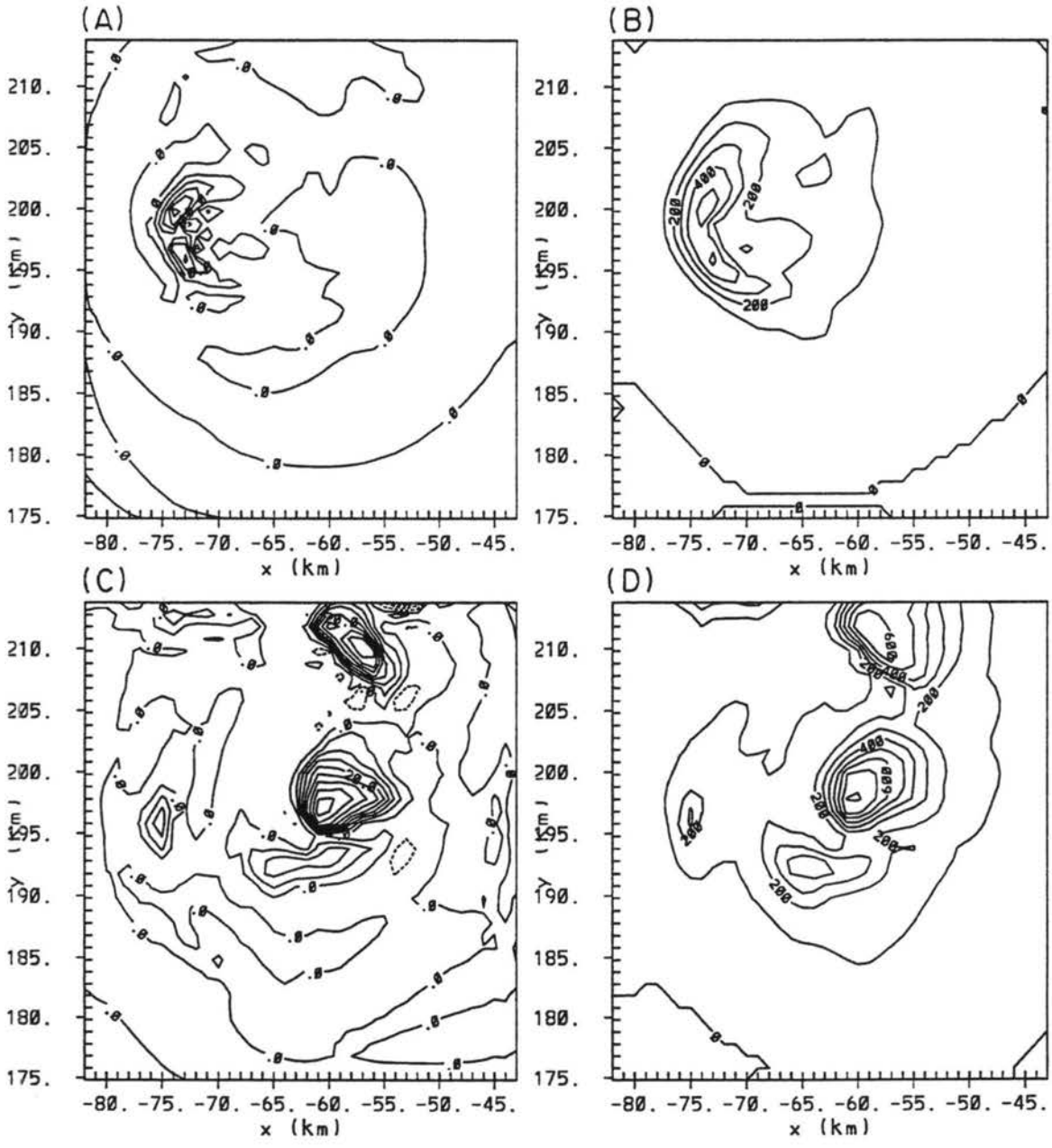

Figure 5.30: Simulated vertical velocities and total ice mixing ratios (contour interval, maximum) at 9000 m AGL for SENS5 after 30 minutes of simulation time for (A) vertical velocity (5 m s^{-1}, 25 m s^{-1}) and (B) total ice mixing ratio (1 g kg^{-1}, 5 g kg^{-1}), and after 60 minutes of simulation time for (C) vertical velocity (5 m s^{-1}, 40 m s^{-1}) and (D) total ice mixing ratio (1 g kg^{-1}, 8 g kg^{-1}).

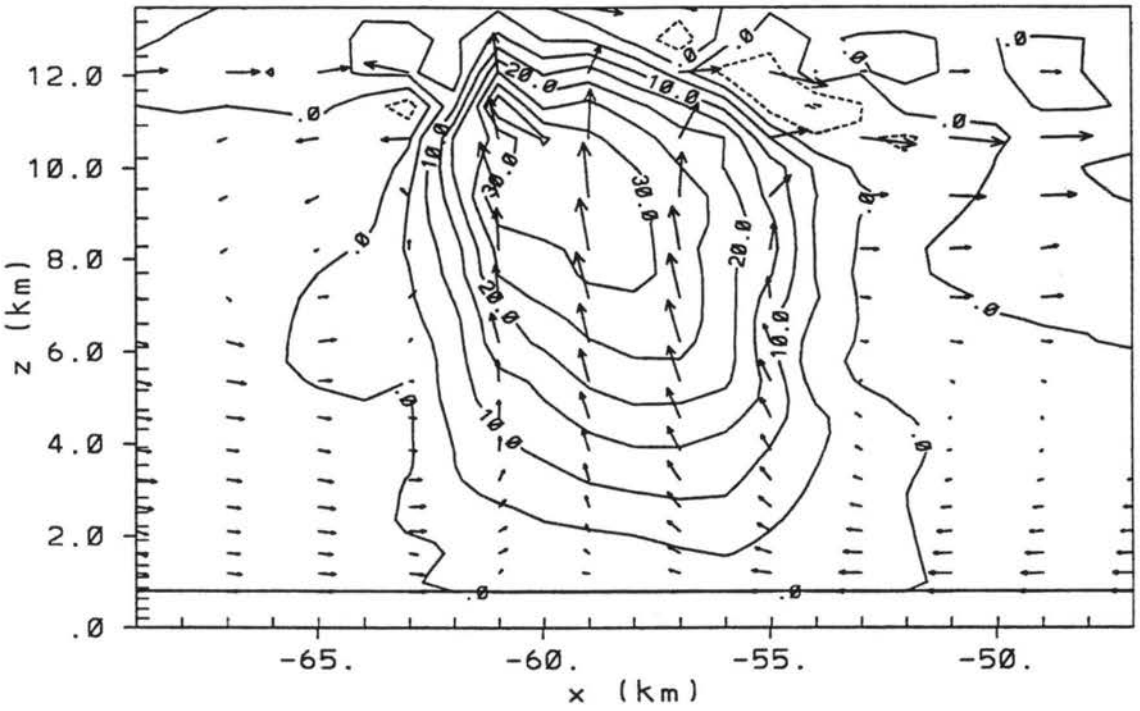

Figure 5.31: A horizontal cross-section through the center of the storm for SENS5 with simulated vertical velocities (5 m s^{-1}, 37 m s^{-1}) with solid contours denoting positive values and negative contours denoting negative values. Wind vectors are also included with maximum vector of 37 m s^{-1}.

some of the microphysical fields for SENS5 is shown in Fig. 5.33. These fields are valid for 60 minutes simulation time. The hail mixing ratio field shows a broad region of hail mass centered over 9 km MSL (peak values 8 g kg^{-1}). A secondary peak exists west of the main updraft with a 1 g kg^{-1} peak. The overall structure of the hail mixing ratio field is very similar to the control run with slightly less hail mass found in SENS5. The rain mixing ratio field (Fig. 5.33b) shows only one peak near 5 km MSL (1.6 g kg^{-1}). The other peak found near the surface (1.6 g kg^{-1}) in the control run is not predicted in SENS5. Peak rain mixing ratios are much less than the control run. The graupel mixing ratio field (Fig. 5.33c) shows a broader region of graupel mass above 4 km MSL than in the control run, with much higher values of graupel mass found in SENS5, which have grown at the expense of the rain category. Aggregate and pristine ice mixing ratios are slightly greater than the control run. The liquid water content field in SENS5 is similar to the control run.

Number concentrations and mean diameters of selected hydrometeor fields for SENS5 are shown in Fig. 5.34. The number concentration of hail (D >5.0 mm) (Fig. 5.34a) shows

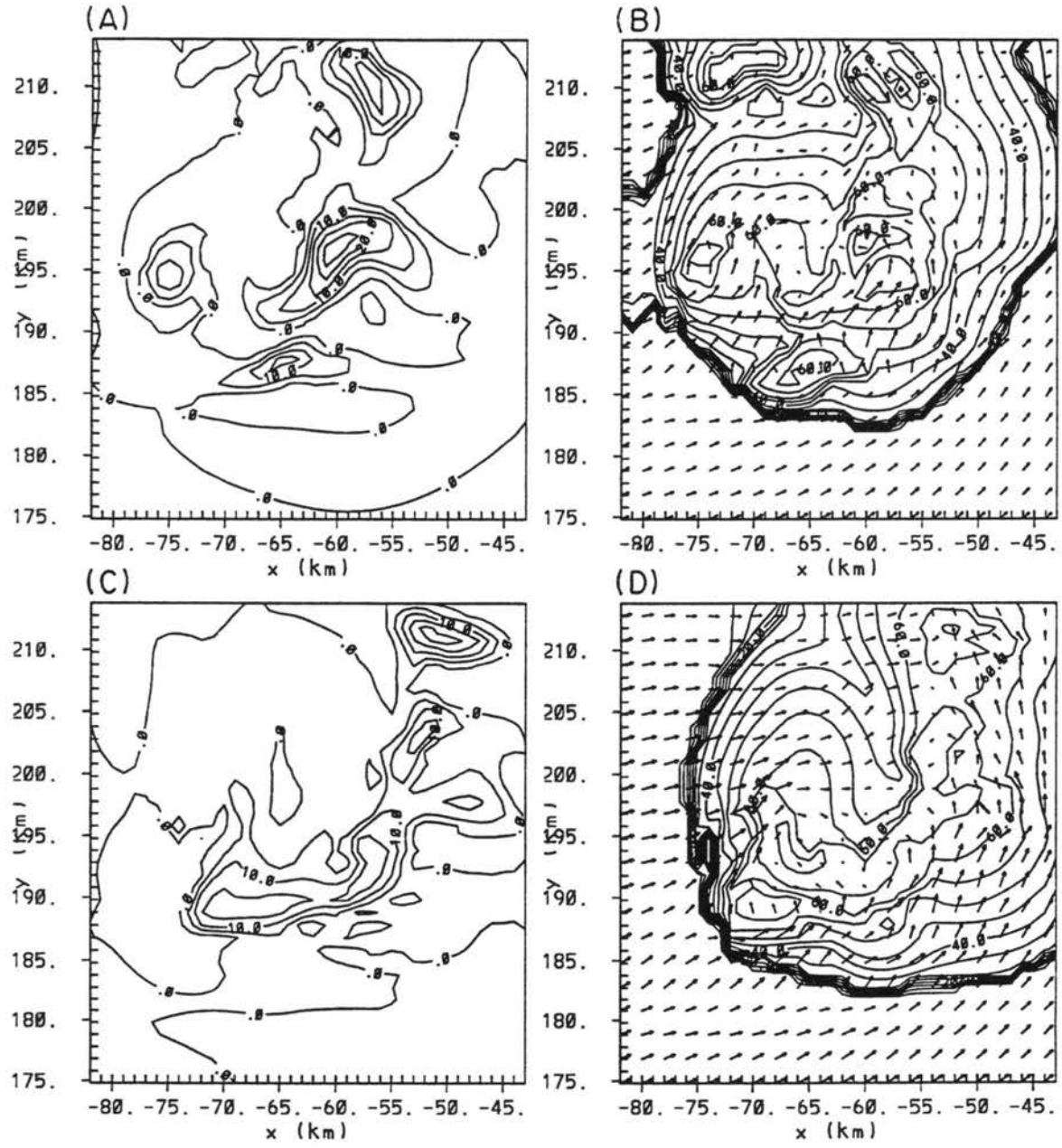

Figure 5.32: Simulated vertical velocities and reflectivity (contour interval, maximum) at 5.6 km MSL for SENS5 after 60 minutes of simulation time for (A) vertical velocity (5 m s^{-1}, 25 m s^{-1}) and (B) reflectivity (5 dBZ, 65 dBZ) and wind vectors (maximum value 24 m s^{-1}), and after 90 minutes of simulation time for (C) vertical velocity (5 m s^{-1}, 15 m s^{-1}) and (D) reflectivity (5 dBZ, 70 dBZ) and wind vectors (maximum value 20 m s^{-1}).

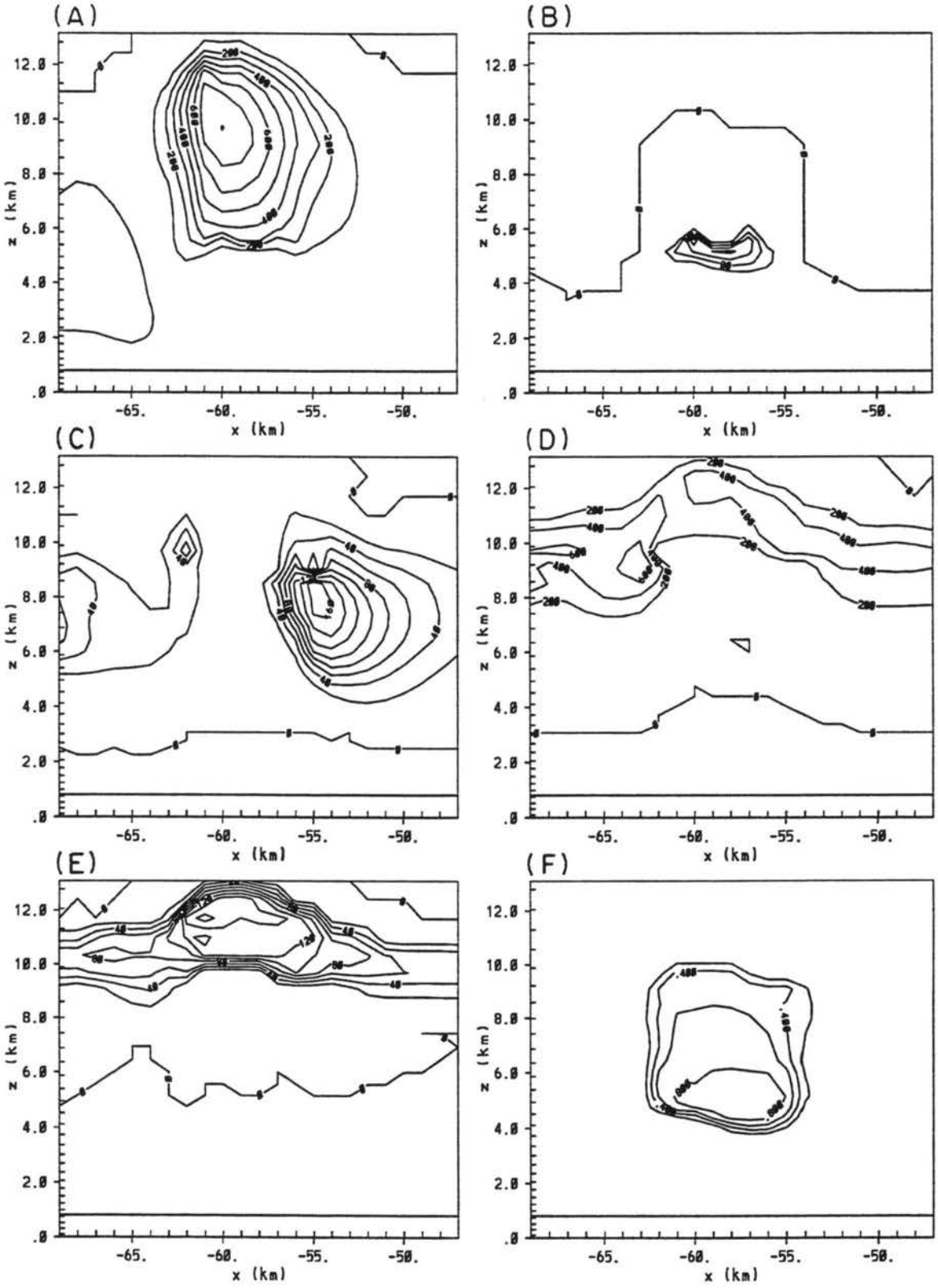

Figure 5.33: Simulated fields for SENS5 of (A) hail mixing ratio (1 g kg^{-1}, 7 g kg^{-1}), (B) rain mixing ratio (0.4 g kg^{-1}, 1.5 g kg^{-1}), (C) graupel mixing ratio (0.2 g kg^{-1}, 1.6 g kg^{-1}) and (D) aggregate mixing ratio (0.2 g kg^{-1}, 0.6 g kg^{-1}), (E) pristine ice crystal mixing ratio (0.2 g kg^{-1}, 1.6 g kg^{-1}) and (F) liquid water content (0.2 g m^{-3}, 0.8 g m^{-3}). Contour intervals and maxima are shown in brackets. All fields are at 60 minutes of simulation time.

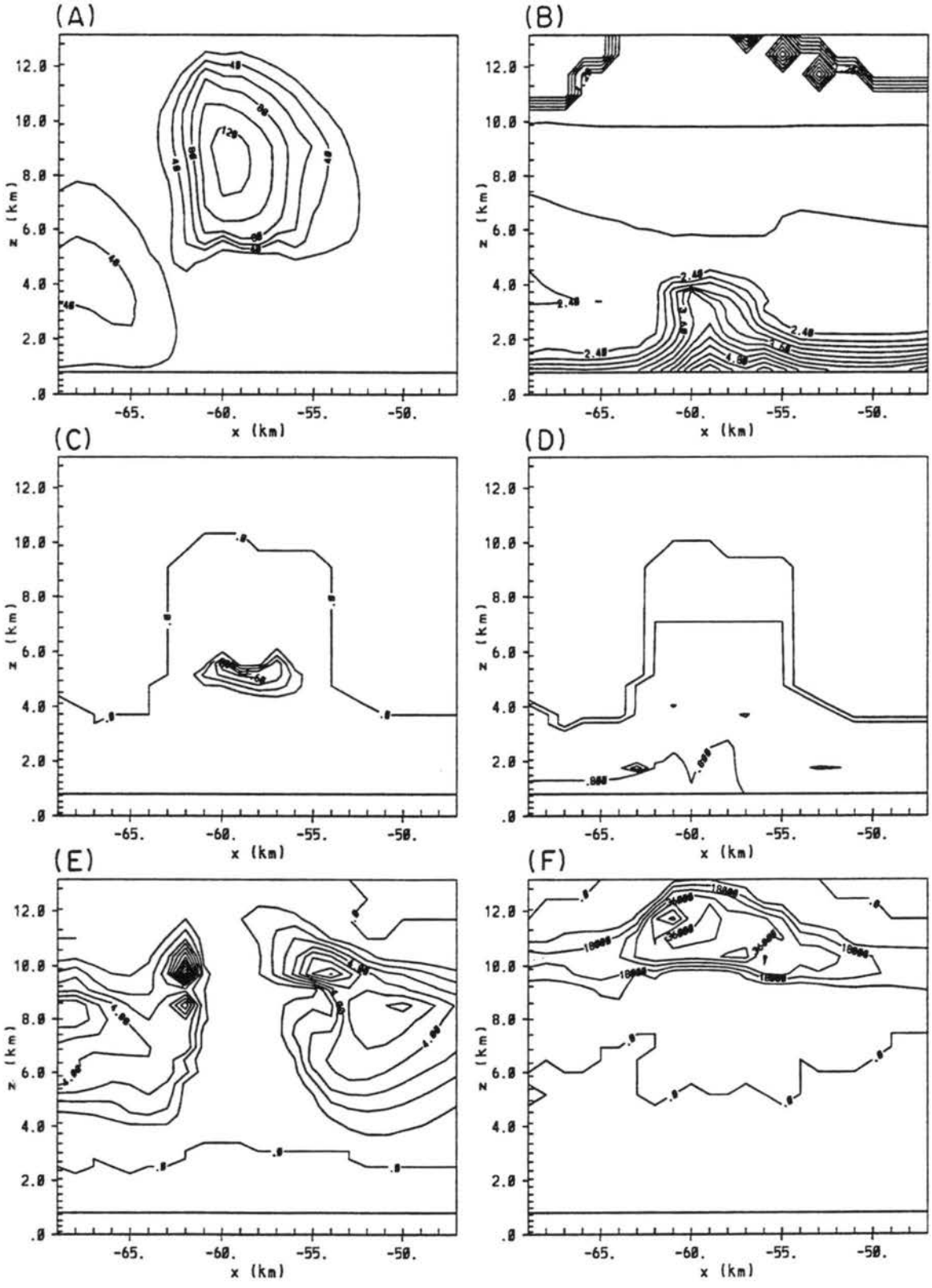

Figure 5.34: Simulated fields for SENS5 of (A) hail number concentration ($2\,m^{-3}$, $12\,m^{-3}$), (B) hail mean diameter (0.3 mm, 6.0), (C) rain number concentration ($0.4\,l^{-1}$, $2.0\,l^{-1}$) and (D) rain mean diameter (0.3 mm, 0.8 mm), (E) graupel number concentration ($1\,l^{-1}$, $10\,l^{-1}$) and (F) pristine ice crystal number concentrations ($9000\,l^{-1}$, $63000\,l^{-1}$). Contour intervals and maxima are shown in brackets. All fields at 60 minutes of simulation time.

peak values of 12 m^{-3}, which is less than the control run, but still higher than observed values. The mean hail diameter field in an assumed gamma distribution is shown in Fig. 5.34b. This field shows that the mean hail diameters are much larger than the control run with peak values of 6 mm found near the surface. Mean hail diameters above 6 km MSL are near 2 mm, which is near the location of higher hail number concentrations. The rain number concentration field shows values of 2.0 l^{-1} which is similar to the observed values. The mean diameters of rain show values are between 0.5 and 0.8 mm which is slightly less than the control run. Graupel number concentrations (Fig. 5.34e) are mostly from 1–6 l^{-1} similar to the control run. Pristine ice crystal number concentrations (Fig. 5.34f) are predicted up to 63000 l^{-1} which is slightly higher than in the control run due to more moisture reaching the anvil region of the cloud in SENS5.

5.3 Discussion

A strong convective storm that occurred during the CCOPE field project on 1 August 1981 has been numerically investigated with RAMS. The convection was artificially initiated with a warm bubble in a horizontally homogeneous initialization. Five simulations were performed: a control run which included the new 2-moment hydrometeor prediction scheme; a 1-moment sensitivity run; a sensitivity run which examined the effect of hydrometeor collection of rain; and sensitivity tests which modified the shape parameter of each hydrometeor ($\nu = 3$); and for hail ($\nu = 3$) only. Each of these simulations exhibited a splitting updraft which developed after 30 minutes of simulation time, and quasi-steady characteristics existed from 60 to 90 minutes of simulation time.

The control run reproduced many features of the observations. The simulated strength, orientation, and width of the updraft compared well to the observations. Simulated peak updrafts were 43 m s^{-1} which was close to the observed peak updraft of 47 m s^{-1}. The simulated updraft also reproduced the width and the vertical orientation of the updraft from the observations. The simulated storm generated a weak circulation pattern at 5.6 km which was similar to the observations. The reflectivity structure was well reproduced by the model, with peak reflectivities and a strong gradient on the western

edge, both similar to the observations. Some small scale variations in the vertical velocity and reflectivity fields were found in the model results which were not found in the observed fields. The northern storm modified kinematic and microphysical structure on the northern border of the domain and this storm was actually observed to be well north of the simulated location.

The microphysical structure of the storm was compared to T-28 aircraft data, which traversed the updraft between 5 and 7 km during a steady state time period of the storm. The predicted and observed hail mass was found in and near the updraft with maximum simulated values near 8 km MSL. Rain mass was simulated to be primarily produced by melting and shedding between 4 and 6 km MSL which was suggested by Rasmussen and Heymsfield (1987c) to be a primary source of hail embryos. Another source of rain was due to autoconversion from cloud droplets which may have been overpredicted by the model and rain rain collection of cloud water. These processes represented potential sinks of the liquid water field. Pristine ice crystal, aggregate, and graupel hydrometeors were predicted at higher altitudes and were a possible source for hail categories as these crystals grew and collected liquid water which resulted in conversion to hail. Liquid water content predicted by the model was nearly half of observed values. This discrepancy may be due to fact that hydrometeor collection of cloud water is too efficient in the model. Ice production mechanisms are quite efficient at these temperatures, and in the presence of high ice mass, depletion of cloud water by collection is enhanced. Also, autoconversion of cloud water may have been overpredicted by the model. This process may have decreased liquid water values in the region of the updraft.

In a two-moment framework, examination of hydrometeor concentrations and mean diameters are permitted, and the model results were encouraging. Hail number concentrations for diameters greater than 5 mm were simulated to be 14 m^{-3}, however these values were greater than peak values of observed hail number concentrations (3 m^{-3}). These relatively high hail number concentration provided some of the impetus for sensitivity testing of the hydrometeor collection and the shape parameter of the hydrometeor distribution. Hail mean diameters in an assumed gamma distribution were mostly around 1.2 mm with

mean diameters of 2 mm near the surface. The rain number concentrations were 4 l^{-1} which was close to the observed values of 2 l^{-1}. Raindrop mean diameters were primarily less than 0.8 mm above 4 km MSL which was observed, and values increased to near 1.4 mm near the surface. Graupel concentrations were 1 to 6 l^{-1} outside of the updraft core which was slightly greater than aircraft measurements, however, graupel concentrations were less than 1 l^{-1} in and near the updraft, similar to the observations. Aggregation was also evident in the anvil region of the cloud, similar to the observations. Pristine ice concentrations were predicted up to 54000 l^{-1} which may be over-predicted in the model. A very strong updraft produced large amounts of cloud water and nearly saturated conditions above 9 km MSL. At these altitudes, both homogeneous freezing of cloud water and haze particles are occurring. Since the aerosol and cloud number concentrations are not predicted, a potentially large number of ice crystals are produced, which is based on the fixed number concentrations of aerosols and cloud droplets prescribed in the model. Plans are currently underway to predict the number concentrations of aerosols and cloud droplets in RAMS. Cloud top height was 14.5 km which was 0.5 km less than the observations.

Peak precipitation rates for each of the experiments are shown in Table 5.3. Since the storm relative winds were subtracted out of the mean winds, verification of precipitation rates to the observed values would be fortuitous. However, the amount of ice and liquid precipitation can be determined from this table. Peak precipitation amounts for the control run were 15 mm h^{-1}, with most of the precipitation falling as rain. Peak hail amounts fell earlier in the simulation. These results are consistent with Crow et al. (1976) which found that only a small percentage of the total precipitation (4%) from High Plains thunderstorms fell as hail.

The sensitivity of predicting one-moment of the distribution for each hydrometeor while specifying the mean diameter exhibited a slight weakening in the strength of the updraft compared to the control run. A major difference was noted in the reflectivity fields which were unrealistically high (80 dBZ) in some regions. These high reflectivities were a result of the larger prescribed hydrometeor diameters in the one-moment simulation. With larger prescribed diameters, more mass was predicted in the aggregate, graupel and

Table 5.3: Precipitation rates (mm h^{-1}) for CCOPE experiments

Experiment	all categories	rain only	hail only
Control run	15	15	9
SENS1	15	3.8	15
SENS2	15	8	10
SENS3	15	15	9
SENS4	14	2.5	12
SENS5	12	2	10

hail categories at the expense of rain. This feature resulted from higher collection kernels for these hydrometeors which depleted liquid water more rapidly than the control run. Precipitation rates for this simulation (Table 5.3) fell primarily as hail with only small amounts of rain precipitation predicted. The precipitation rates for hail are much higher due to the larger prescribed hail diameters.

In the sensitivity of predicting one-moment of the distribution for each hydrometeor while specifying N_0 also generated a weaker updraft than in the control run as seen in SENS1. By prescribing N_0 the hail mean diameters were not fixed and the resultant reflectivity pattern was better simulated. However, other microphysical parameters such as graupel mass and rain diameters did not compare well with the observations, possibly due to variations in the N_0 in the storm. Liquid water contents were still lower than observed similar to the control run. SENS2 produced more rain precipitation than in SENS1, however, a greater percentage of the precipitation still fell as hail, which was not observed.

The sensitivity experiment of changing the production of raindrops interacting with ice particles from hail to graupel resulted in some modifications of the updraft structure. The main updraft was weaker and narrower than the updraft in the control run. A more pronounced downdraft was also located below 6 km MSL east of the main updraft. This downdraft resulted due to more precipitation occurring in this region. More graupel and hail existed at lower altitudes producing much more rain due to melting and shedding east of the updraft. Surprisingly, hail concentrations greater than 5 mm were unaffected by

this change in the collection formulation. Precipitation rates and precipitation type (Table 5.3) were the same as the control run.

The sensitivity of making ν=3 for all hydrometeors had little effect on the kinematic fields and the updraft was nearly as strong as the updraft in the control run. Reflectivity measurements were dramatically different than the control run. Large regions of 60 dBZ were found at 5.6 km, and peak values were 80 dBZ, more than 15 dBZ greater than the control run. With larger mean diameters found in this sensitivity experiment due to the increased ν, reflectivities were increased. The mixing ratio fields were similar to the control run with the exception of the graupel category, which only showed negligible amounts due to efficient conversion to hail due to collection of liquid water. Peak hail concentrations for diameters greater than 5 mm were 16 m^{-3}, which was greater than values predicted in the control run. Hail mean diameters were much greater than the control run with values greater than 6 mm. Rain number concentrations were much smaller than the control run due to hydrometeor collection of the smaller raindrops. Precipitation rates (Table 5.3) for this simulation were slightly less than the control run, but were dominated by the hail precipitation due to the increased ν for hail, even though the ν value for the other categories was increased.

The sensitivity of making ν=3 for hail generated little effect on the kinematic fields with the exception that the updraft was slightly weaker in the control run. Reflectivity measurements were spatially similar to the control run, however, values were nearly 5 dBZ higher in the sensitivity experiment, possibly due to the increase ν for hail. The microphysical fields showed a dramatic increase in the graupel mass which occurred at the expense of the rain category which was much lower than the control run. Hail concentrations were unaffected by the change in ν but hail mean diameters near the surface were dramatically higher with peak values near 6 mm. Hail diameters at higher altitudes, where high hail concentrations were found, were less than 2 mm. Precipitation rates for this simulation are slightly less than the control run but with a higher ν for hail, more hail precipitation is predicted.

Chapter 6

CONCLUSIONS AND SUGGESTIONS FOR FUTURE RESEARCH

6.1 Summary of research results

A two-moment hydrometeor prediction scheme has been implemented into RAMS. This development includes physics based on the most recent observations and parameterizations. The scheme predicts the mixing ratio and number concentration of rain, pristine ice crystals, snow, aggregates, graupel, and hail. Some added features of this new microphysical scheme include:

- the use of a generalized gamma size-spectrum where the ν parameter can be prescribed by the user as opposed to a fixed Marshall Palmer spectrum
- the introduction of ice-liquid mixed phase graupel and hail categories categories with non-thermal equilibrium for the rain, graupel and hail classes
- new heterogeneous and homogeneous ice nucleation parameterizations
- approximate solutions to the stochastic collection equation rather than the continuous accretion model approach
- breakup of rain droplets is formulated into the collection efficiency
- analytical flux equations predict mixing ratio and number concentration conversion from pristine ice crystals to snow due to deposition and vice-versa due to sublimation (no riming of the pristine ice category)
- predictive equations for ice nuclei (IN)
- crystal habit is diagnosed dependent on temperature and saturation

- evaporation and melting of each species assumes that the smallest particles completely disappear first
- more complex shedding formulations which take into account the amount of water mass on the coalesced hydrometeor.

Preliminary tests in an idealized convective environment as discussed in Chapter 3, showed that the two-moment prediction scheme allowed more freedom on the size distribution by predicting on both the mixing ratios and concentrations of each hydrometeor distribution. This freedom allowed the size spectra to evolve more realistically than in a one-moment scheme. One of the unique problems of predicting both the number concentration and mixing ratio of a hydrometeor is that diagnosed diameters could be unrealistically small or large. A diameter bounds check is therefore needed to keep the distributions realistic. A diagnosis was performed on these idealized convective simulations and it was found that these limits were exceeded less than 5% of the time, which is acceptable. The bounds were usually exceeded in large gradient regions of the cloud where mixing ratios were low, and evaporation was taking place. The simulations also showed that the model is very sensitive to some of the input parameters, which are prescribed by the user. Parameters such as the cloud droplet number concentration and the shape parameter ν of the distribution can significantly impact the model results, and therefore need to be observed and understood, especially for modeling purposes. The computational costs of predicting on the additional moment is not excessive, being nearly 15% greater than with the one-moment scheme. Moreover, the code is currently being optimized to make it more efficient.

Model verification was performed on two separate case studies which exercised the model in both a wintertime and summertime deep-convective environment. The wintertime case was a shallow, post-frontal upslope case over the High Plains of Colorado that occurred during the WISP field project on 28-29 January 1991. Comparisons between 2-moment scheme and the 1-moment scheme showed general agreement in the overall kinematic structure. Total precipitation for both simulations was under-predicted by up to a factor of 3 near the foothills. The microphysical structure, however, of both simulations differed. In the two-moment simulation, the diameters of each hydrometeor were allowed

to evolve depending on the environmental conditions, which was especially evident in the aggregate diameter field. Simulated and observed aggregate mean diameters were much larger immediately behind the front, and the sizes decreased farther north behind the front. In the 1-moment scheme, the diameter is held fixed which is an unrealistic constraint and does not allow variations of the hydrometeor spectra. Another difference between the two schemes is the evolution of precipitation processes. Both simulations produced significant cloud water near the surface. This liquid mass was an important source of growth for snow, aggregates and graupel, however, the hydrometeor evolution due to this growth was different for both simulations. In the 2-moment scheme the snow crystals were predicted to be much smaller than the prescribed 0.5 mm mean diameters in the 1-moment simulations, which enabled more graupel mass to be produced in the 2-moment scheme. This result is contrary to the 1-moment scheme, in which the larger snow crystals were more readily converted to aggregates instead of graupel. Both aggregates and graupel were predicted by both schemes, and both species were observed. However, since the two-moment scheme predicted the sizes of aggregates and graupel to be similar to the observations, the two-moment simulation handled the observed microphysical evolution more realistically.

The summertime case that was numerically investigated was a strong convective storm that occurred during the CCOPE field project on 1 August 1981. The convection in this simulation was initiated with a warm bubble and a horizontally homogeneous initialization was employed. The control run simulated the strength, orientation, and width of the updraft quite well. Some small scale features in the vertical velocity field, however, were produced which were not seen in the observations. Also, the simulation moved the northern storm too slowly out of the domain. Peak reflectivities were simulated close to the observed values with a strong reflectivity gradient on the western edge of the storm reproduced in the simulation. Comparisons to aircraft measurements showed that the qualitative microphysical structure produced by the simulations compared well to the observations: hail mass was found in and near the updraft, shedding was predicted to be a dominant source of rain between 4 to 6 km, aggregation processes were active in the anvil, and cloud top height was 14.5 km which was 0.5 km less than the observations. Some features not

handled as well in the simulation were that hail number concentrations were over-predicted by a factor of 4, and liquid water content was under-predicted by 50%. Precipitation analysis of the simulation showed that most of the precipitation fell as rain, while significant hail precipitation occurred earlier in the simulation.

Two sensitivity experiments using the one-moment scheme (with D_m or N_0 specified) showed somewhat similar kinematic structure as the control run, however, magnitudes of the updraft were slightly weaker in the both one-moment runs. The one-moment runs produced more ice mass at the expense of rain. However, these results are forced by the constraints of the user-prescribed parameters, rather than allowed to evolve more realistically as in the control run. In both 1-moment runs the diameters for each hydrometeor species above the freezing level were larger than those diagnosed in the two-moment scheme. These larger diameters resulted in a larger collection kernel of each ice category which depleted more rain mass than in the control run. Consequently, the ratio of hail precipitation relative to rain was over–predicted in the one-moment runs. With a one-moment scheme, the user is forced to speculate what is the typical mean diameter or slope intercept of each hydrometeor. Also, if there are measurements available for a given environment, the measurements that are made in one region of the storm may not be characteristic of another region. Therefore, a compromise must be made by the user in a one-moment framework.

The second sensitivity test examined the importance of converting raindrops which freeze due to collection by ice, into graupel rather than hail as was done for the other simulations. The impetus for this experiment was due to the concern that too much small ice mass was being converted to the hail category, producing relatively small mean diameters of hail and relatively high hail number concentrations. The sensitivity experiment, however, had little effect on the microphysical structure of the simulated storm. As in the idealized convective simulations from Chapter 3, the model was very sensitive to the shape of the distribution. With $\nu = 3$ for all hydrometeors, the microphysical structure was drastically modified. The collection kernel for each hydrometeor was enhanced, which eventually led to more hail production at the expense of the other ice species. In the sensitivity test in which ν was only increased for hail from 1 to 3, the results were very similar

to the control run. However, more graupel was produced since more ice mass was injected into the anvil, which was a source for graupel formation away from the main updraft. The total precipitation rates were very similar for each experiment except for a decrease noted in the sensitivity to ν of hail. Unlike the control run, the one-moment simulation and the sensitivity experiments to ν predicted most of the precipitation to be in the form of hail, due to the larger hail diameters in these experiments.

In summary, the new two-moment microphysical scheme was tested in both a wintertime and summertime environment. The two-moment scheme allowed the hydrometeors to evolve without a fixed diameter constraint, and for the most part, predicted the microphysical structure better than the one-moment scheme. The two-moment scheme also allowed for verification of more observable parameters such as reflectivity and crystal diameters, and these predicted fields compared favorably to the observed features.

6.2 Future research topics

The modeling results indicated some of the problems with not predicting on the aerosol and cloud droplet spectra. First, prediction of aerosols and cloud condensation nuclei (CCN) would allow for a more realistic prediction of the cloud droplet spectra. This prediction would impact warm rain autoconversion processes and collection of cloud water. Another implication for predicting on the aerosol and CCN populations would be with the homogeneous nucleation of cloud water and haze particles. Currently, this parameterization assumes fixed concentrations of cloud droplets and haze particles which may lead to overprediction of pristine ice crystals produced by homogeneous freezing mechanisms. Since there is, in essence, a sustained supply of these freezing sites. A more explicit prediction of their concentrations should allow a more realistic simulation.

Since two moments are predicted in the new scheme, it provides the capability for remote sensing comparisons by the model. Currently, multi-parameter algorithms are being developed (personal communication, V. Bringi) which will be implemented in RAMS. Also, a more detailed test of the microphysical scheme would be to develop diagnostic tendency algorithms to examine sources and sinks of each conversion process.

It would be desirable to test a MCS in a cloud resolving simulation. The one-moment scheme would be expected to have difficulty simulating both the deep convective regions and the stratiform-anvil region with the same user-specified parameters. Finally, these simulations showed the sensitivity of the model to the shape (ν) of each hydrometeor distribution. The shape of the size distribution, however, is not easily applied by modelers since these measurements are not typically conducted for various types of weather phenomena. More recent field projects such as WISP and FIRE, have specifically looked at the size distribution where the breadth of the distribution can be inferred, but many more measurements are needed. There is also a need to test the effects of varying ν in a variety of environments and storms.

Appendix A

REFLECTIVITY CALCULATIONS

Using (2.6), the reflectivity or the 6th moment of the distribution can be solved as

$$Z = N_t D_n^6 \frac{\Gamma(\nu+6)}{\Gamma(\nu)} (mm^6 m^{-3}). \tag{A.1}$$

For one-moment calculations where D_n is specified, N_t was diagnosed from the predicted mixing ratio. In the case when N_0 was specified, D_n was defined as

$$D_n = (\frac{\pi \rho N_0}{\rho_a r}). \tag{A.2}$$

and N_t is diagnosed from D_n and N_0.

For ice-phased particles the above value for Z must be multiplied by a dialectric constant adjustment which is parameterized by

$$(\frac{|K|^2(ice)}{|K|^2(liquid)}) = \rho^2/4.335, \tag{A.3}$$

where ρ is in g cm^{-3}. In the case of mixed-phased graupel or hail particles, a mixed-phase dielectric constant is assumed.

Bibliography

Al-Naimi, R. and C. Saunders, 1985: Measurements of natural deposition and condensation–freezing ice nuclei with a continuous flow chamber. *Atmos. Environ.*, **19**, 1871—1882.

Arnott, W. P., Y. Y. Dong, and J. Hallett, 1992: Cirrus microphysics observations made during FIRE II: Small particles, high concentrations, and probe comparisons. In *Preprints FIRE Cirrus Science Conf. June 14-17, 1993, Breckenridge Colorado*, 5—8.

Beheng, K., 1994: A bulk parameterization of warm cloud microphysical conversion processes. *Atmos. Phys.*, **33**, 193—206.

Bernstein, B. C., I. Baker, D. Wesley, J. Smart, L. Wharton, and J. Wirshborn, 1992: The utility of a high resolution volunteer snow observer network. In *Preprints 11th Intl. Conf. on Clouds and Precipitation, Montreal, Canada*, IAMAP, 991—994.

Berry, E. X. and R. L. Reinhardt, 1974a: Analysis of cloud drop growth by collection: Part I. Double distributions. *J. Atmos. Sci.*, **31**, 1814—1824.

Berry, E. X. and R. L. Reinhardt, 1974b: Analysis of cloud drop growth by collection: Part II. Single initial distributions. *J. Atmos. Sci.*, **31**, 1825—1831.

Berry, E. X. and R. L. Reinhardt, 1974c: Analysis of cloud drop growth by collection: Part III. Accretion and self-collection. *J. Atmos. Sci.*, **31**, 2118—2126.

Berry, E. X. and R. L. Reinhardt, 1974d: Analysis of cloud drop growth by collection: Part IV. a new parameterization. *J. Atmos. Sci.*, **31**, 2127—2135.

Brazier-Smith, P., S. Jennings, and J. Latham, 1973: Raindrop interactions and rainfall rates within clouds. *Quart. J. Roy Meteor. Soc.*, **99**, 260—272.

Chen, C. and W. R. Cotton, 1983: Numerical experiments with a one-dimensional higher order turbulence model: Simulation of the wangara day 33 case. *Bound. Lay. Meteorol.*, **25**, 375—404.

Chong, S. and C. Chen, 1974: Water shells on ice pellets and hailstones. *J. Atmos. Sci.*, **31**, 1384–1391.

Clark, T. L. and R. D. Farley, 1984: Severe downslope windstorm calculations in two and three spatial dimensions using anelastic interactive grid nesting: A possible mechanism for gustiness. *J. Atmos. Sci.*, **41**, 329—350.

Cotton, W. R., G. Tripoli, R. M. Rauber, and E. A. Mulvihill, 1986: Numerical simulation of the effects of varying ice crystal nucleation rates and aggregation processes on orographic snowfall. *J. Climate Appl. Meteor.*, **25**, 1658—1680.

Cotton, W. R., G. Thompson, and P. Mielke, 1994: Real-time mesoscale prediction on workstations. *Bull. Amer. Met. Soc.*, **75**, 349—362.

Cram, J. M., 1990: *Numerical simulation and analysis of the propagation of a prefrontal squall line.* Ph.D. dissertation, Dep. of Atmos. Sci., Colorado State University, Ft Collins, CO 80523. 332 pp.

Crow, E. L., P. W. Summers, A. B. Long, C. A. Knight, G. B. Foote, and J. E. Dye, 1976: "Experimental results and overall summary" Vol. I, Final Rep. Natl. Hail Res. Exp. Randomized Seeding Exp. 1972–1974. Technical report, Natl. Center Atmos. Res., Boulder, CO.

Davis, H. C., 1983: Limitations of some common lateral boundary schemes used in regional NWP models. *Mon. Wea. Rev.*, **111**, 1002–1012.

DeMott, P. J., M. P. Meyers, and W. R. Cotton, 1994: Parameterization and impact of ice initiation processes relevant to numerical model simulations of cirrus clouds. *J. Atmos. Sci.*, **51**, 77–90.

DeMott, P. J., J. L. Stith, and D. C. Rogers, 1995: Studies of cloud-active aerosols and ice initiation in north dakota cumuli. In *Preprints AMS Conference on Clouds Physics, 15-20 January, Dallas, TX.*

Doms, G. and K. Beheng, 1986: Mathematical formulation of self-collection, autoconversion and accretion rates of cloud and raindrops. *Meteorol. Rdsch.*, **39**, 98—102.

Farley, R. D., 1987: Numerical modelling of hailstorms and hailstone growth. Part III: Simulation of an Alberta hailstorm-natural and seeded cases. *J. Appl. Clim. Met.*, **26**, 789—812.

Feingold, G., S. Tzivion, and Z. Levin, 1988: Evolution of raindrop spectra. Part I: Solution to the stochastic collection/breakup equation using the method of moments. *J. Atmos. Sci.*, **45**, 3387—3399.

Feingold, G., B. Stevens, W. Cotton, and R. Walko, 1994: An explicit cloud microphysics/LES model designed to simulate the Twomey effect. *J. Atmos. Res.*, **33**, 207–233.

Ferrier, B. S., 1994: A double-moment multiple-phase four class bulk ice scheme. Part I: Description. *J. Atmos. Sci.*, **51**, 249–280.

Flatau, P. J., G. J. Tripoli, J. Verlinde, and W. R. Cotton, 1989: The CSU-RAMS cloud microphysical module: General theory and code documentation. Dept. of Atmos. Science Paper 451, Colorado State University, Ft Collins, CO 80523.

Fletcher, N. H., 1962: *Physics of rain clouds.* Cambridge University Press. 386 pp.

Fraile, R., A. Castro, and J. Sanchez, 1992: Analysis of hailstone size distributions from a hailpad network. *Atmos. Res.*, **28**, 311–326.

Gordon, G. L. and J. D. Marwitz, 1981: Secondary ice crystal production in stable orographic clouds over the sierra nevada. In *Eighth Conf. on Inadvertent and Planned Weather Modification*, Amer. Meteor. Soc., 62—63.

Hall, W., 1980: A detailed microphysical model within a two-dimensional dynamical framework: Model description and preliminary results. *J. Atmos. Sci.*, **37**, 2486–2507.

Hallet, J. and S. C. Mossop, 1974: Production of secondary ice particles during the riming process. *Nature*, **249**, 26—28.

Harrington, J. L., 1994: Parameterization of ice crystal conversion processes in cirrus clouds using double-moment basis functions. Master's thesis, Department of Atmospheric Science, Fort Collins, CO 80523. Atmospheric Science Paper No. 554.

Harrington, J. L., M. P. Meyers, R. L. Walko, and W. R. Cotton, 1995: Parameterization of ice crystal conversion processes in cirrus clouds using double-moment basis functions. Part I: Basic formulation and one-dimensional tests. *J. Atmos. Sci.*, **54**. In press.

Heymsfield, A., 1983: Case study of a hailstorm in Colorado. Part IV: Graupel and hailstone growth mechanisms deduced through particle trajectory calculations. *J. Atmos. Sci.*, **40**, 1482–1509.

Heymsfield, A. J., 1978: The characteristics of graupel particles in northeastern Colorado cumulus clouds. *J. Atmos. Sci.*, **35**, 284—295.

Heymsfield, A. J. and M. Hjelmfelt, 1984: Processes of hydrometeor development in Oklahoma convective clouds. *J. Atmos. Sci.*, **41**, 2811—2835.

Heymsfield, A. J. and A. G. Palmer, 1986: Relationships for deriving thunderstorm anvil ice mass for CCOPE storm water budget estimates. *J. Climate Appl. Meteor.*, **25**, 691—702.

Kidder, R. and A. Carte, 1964: Structures of artificial hailstones. *J. Rech. Atmos.*, **1**, 169–181.

Klemp, J. B. and R. B. Wilhelmson, 1978: Simulations of right– and left–moving storms produced through storm splitting. *J. Atmos. Sci.*, **35**, 1097—1110.

Knight, N. and A. Heymsfield, 1983: Measurement and interpretation of hailstone density and terminal velocity. *J. Atmos. Sci.*, **40**, 1510—1516.

Kogin, Y., 1991: The simulation of a convective cloud in a 3-D model with explicit microphysics. Part I: Model description and sensitivity experiments. *J. Atmos. Sci.*, **48**, 1160–1189.

Kopp, F., H. Orville, R. Farley, and J. Hirsh, 1983: Numerical simulation of dry ice cloud seeding experiment. *J. Climate Appl. Meteor.*, **22**, 1542–1556.

Kubesh, R. J., D. J. Musil, R. D. Farley, and H. D. Orville, 198: The 1 August 1981 CCOPE storm: Observations and modeling results. *J. Appl. Met.*, **27**, 216–243.

Lesins, G. and R. List, 1986: Sponginess and drop shedding of gyrating hailstones in pressure-controlled icing wind tunnel. *J. Atmos. Sci.*, **43**, 2813—2825.

Lesins, G., R. List, and P. Joe, 1980: Ice accretions. Part I: Testing of new atmospheric icing concepts. *J. Rech. Atmos.*, **14**, 347—356.

Lin, Y.-L., R. D. Farley, and H. D. Orville, 1983: Bulk parameterization of the snow field in a cloud model. *J. Atmos. Sci*, **22**, 1065—1089.

List, R. and R. Schemenauer, 1971: Free-fall behavior of planar snow crystals, conical graupel and small hail. *J. Atmos. Sci.*, **28**, 110—115.

Low, T. and R. List, 1982: Collision, coalescence and breakup of raindrops. Part I: Experimentally established coalescence efficiencies and fragment size distributions in breakup. *J. Atmos. Sci.*, **39**, 1591—1606.

Lupkes, C., K. Beheng, and G. Doms, 1989: A parameterization scheme for simulating collision/coalescence of water drops. *Beitr. Phys. Atmosph.*, **62**, 289—306.

Macklin, W., 1962: The density and structure of ice formed by accretion. *Quart. J. Roy. Meteor. Soc.*, **92**, 297–300.

Marwitz, J. D., 1971a: The structure and motion of severe hailstorms. Part I: Supercell storms. *J. Appl. Met.*, **11**, 127–135.

Marwitz, J. D., 1971b: The structure and motion of severe hailstorms. Part II: Multicell storms. *J. Appl. Met.*, **11**, 180–188.

Matson, R. and A. Huggins, 1980: The direct measurements of the sizes, shapes and kinematics of falling hailstones. *J. Atmos. Sci.*, **37**, 1107–1125.

McCumber, M., W. Tao, J. Simpson, R. Penc, and S. Soong, 1991: Comparison of ice-phase microphysical parameterization schemes using numerical simulations of tropical convection. *J. Appl. Met.*, **30**, 985–1004.

Meyers, M. P. and W. R. Cotton, 1992: A wintertime orographic quantitative precipitation forecast with an explicit cloud model. Part I: Two-dimensional sensitivity experiments. *J. Appl. Met.*, **31**, 26—50.

Meyers, M. P., P. J. DeMott, and W. R. Cotton, 1992: New primary ice nucleation parameterizations in an explicit cloud model. *J. Appl. Met.*, **31**, 708—721.

Miller, J. L., J. D. Tuttle, and G. B. Foote, 1990: Precipitation production in a large Montana hailstorm: Airflow and particle growth trajectories. *J. Atmos. Sci.*, **47**, 1619–1646.

Murakami, M., 1990: Numerical modeling of dynamical and microphysical evolution of an isolated convective cloud–The 19 July 1981 CCOPE cloud. *J. Met. Soc. Jap.*, **68**, 107—128.

Nickerson, E. C., E. Richard, R. Rosset, and D. R. Smith, 1986: The numerical simulation of clouds, rain, and airflow over the Vosges and Black Forest Mountains: A meso-β model with parameterized microphysics. *Mon. Wea. Rev.*, **114**, 398—414.

Orville, H. D. and F. J. Kopp, 1977: Numerical simulation of the life history of a hailstorm. *J. Atmos. Sci.*, **34**, 1596—1618.

Pflaum, J. and H. Pruppacher, 1979: A wind tunnel investigation of the growth of graupel initiated from frozen drops. *J. Atmos. Sci.*, **36**, 680–689.

Pflaum, J., J. Martin, and H. Pruppacher, 1978: A wind tunnel investigation of the hydrodynamic behavior of growing, freely falling graupel. *Quart. J. Roy. Meteor. Soc.*, **104**, 179–187.

Pielke, R. A., W. R. Cotton, R. L. Walko, C. J. Tremback, W. A. Lyons, L. D. Grasso, M. E. Nicholls, M. D. Moran, D. A. Wesley, T. J. Lee, and J. H. Copeland, 1992: A comprehensive meteorological modeling system–RAMS. *Meteorol. Atmos. Phys.*, **49**, 69–91.

Pitter, R., 1977: A reexamination of riming on thin ice plates. *J. Atmos. Sci.*, **34**, 684–685.

Prodi, F., 1970: Mesurements of local density in artificial and natural hailstones. *J. Appl. Met.*, **9**, 903–910.

Pruppacher, H. R. and J. D. Klett, 1978: *Microphysics of clouds and precipitation.* D. Reidel, 714 pp.

Rasmussen, R., M. Politovich, J. Marwitz, W. Sand, J. McGinley, J. Smart, R. Pielke, S. Rutledge, D. Wesley, G. Stossmeister, B. Bernstein, K. Elmore, N. Powell, E. Westwater, B. B. Stankov, and D. Burrows, 1992: Winter Icing and Storms Project WISP. *Bull. Amer. Met. Soc.*, **73**, 951–974.

Rasmussen, R. M. and A. J. Heymsfield, 1987a: Melting and shedding of graupel and hail. Part I: Model physics. *J. Atmos. Sci.*, **44**, 2754–2763.

Rasmussen, R. M. and A. J. Heymsfield, 1987b: Melting and shedding of graupel and hail. Part II: Sensitivity study. *J. Atmos. Sci.*, **44**, 2764–2782.

Rasmussen, R. M. and A. J. Heymsfield, 1987c: Melting and shedding of graupel and hail. Part III: Investigation of the role of shed drops as hail embryos in the 1 August CCOPE Severe Storm. *J. Atmos. Sci.*, **44**, 2783–2803.

Rasmussen, R. M., V. Levizzani, and H. R. Pruppacher, 1984: A wind tunnel and theoretical study on the melting behavior of atmospheric ice particles III: Experiment and theory for spherical ice particles of radius > 500μm. *J. Atmos. Sci.*, **41**, 381–388.

Rogers, D. C., 1993: Measurements of natural ice nuclei with a continuous flow diffusion chamber. *Atmos. Res.*, **29**, 209—228.

Rogers, D. C. and P. J. DeMott, 1995: Measurements of natural ice nuclei, CCN, and CN in winter clouds. In *Preprints AMS Conference on Clouds Physics, 15-20 January, Dallas, TX.*

Rutledge, S. A. and P. V. Hobbs, 1983: The mesoscale and microscale structure and organization of clouds and precipitation in midlatitude cyclones. VIII: A model for the "seeder-feeder" process in warm-frontal rainbands. *J. Atmos. Sci.*, **40**, 1185—1206.

Rutledge, S. A. and P. V. Hobbs, 1984: The mesoscale and microscale structure and organization of clouds and precipitation in midlatitude cyclones. XII: A diagnostic modeling study of precipitation development in narrow cold-frontal rainbands. *J. Atmos. Sci.*, **41**, 2949—2972.

Schlamp, R. and H. Pruppacher, 1977: On the hydrodynamic behavior of supercooled water drops interacting with columnar ice crystals. *Pure Appl. Geophys.*, **115**, 805—843.

Schlamp, R., H. Pruppacher, and A. Hamielec, 1975: A numerical investigation of the efficiency with which simple columnar ice crystals collide with supercooled water drops. *J. Atmos. Sci.*, **32**, 2330—2337.

Srivastava, R., 1978: Parameterization of raindrop size distributions. *J. Atmos. Sci.*, **35**, 108—117.

Tripoli, G. J. and W. R. Cotton, 1981: The use of ice-liquid water potential temperature as a thermodynamic variable in deep atmospheric models. *Mon. Wea. Rev.*, **109**, 1094—1102.

Ulbrich, W. and D. Atlas, 1982: Hail parameter relations: A comprehensive digest. *J. Appl. Met.*, **21**, 22–43.

Verlinde, J. and W. R. Cotton, 1990: A mesoscale vortex couplet observed in the trailing anvil of a multi-cellular convective complex. *Mon. Wea. Rev.*, **118**, 993—1010.

Verlinde, J. and W. Cotton, 1993: Fitting microphysical observations of non-steady convective clouds to a numerical model: An application of the adjoint technique of data assimilation to a kinematic model. *Mon. Wea. Rev.*, **121**, 2776—2793.

Vittori, O. and G. di Caporiacco, 1959: The density of hailstones. *Nubila*, **2**, 51—57.

Walko, R., W. R. Cotton, M. P. Meyers, and J. L. Harrington, 1995: New RAMS cloud microphysics parameterization Part I: The single–moment scheme. *Atmos. Res.*, **34**. In Press.

Wang, P. K. and J. S. Chang, 1993a: A three dimensional numerical model of cloud dynamics, microphysics, and chemistry 1. Concepts and formulations. *J. Geophys. Res.*, **98**, 14827—14844.

Wang, P. K. and J. S. Chang, 1993b: A three dimensional numerical model of cloud dynamics, microphysics, and chemistry 2. A case study of the dynamics and microphysics of a severe local storm. *J. Geophys. Res.*, **98**, 14845—14862.

Weisman, M. L. and J. B. Klemp, 1984: The structure and classification of numerically simulated convective storms in directionally varying wind shears. *Mon. Wea. Rev.*, **112**, 2479—2498.

Wesley, D., J. Weaver, and R. Pielke, 1990: Heavy snowfall during an arctic outbreak along the Colorado Front Range. *Nat. Wea. Dig.*, **15.3**, 2–19.

Young, K. C., 1974a: A numerical simulation of wintertime, orographic precipitation. II: Comparison of natural and AgI-seeded conditions. *J. Atmos. Sci.*, **31**, 1749—1767.

Young, K. C., 1974b: The role of contact nucleation in ice phase initiation in clouds. *J. Atmos. Sci.*, **31**, 768—776.

Ziegler, C. L., 1985: Retrieval of thermal and microphysical variables in observed convective storms. Part I: Model development and preliminary testing. *J. Atmos. Sci.*, **42**, 1487—1509.